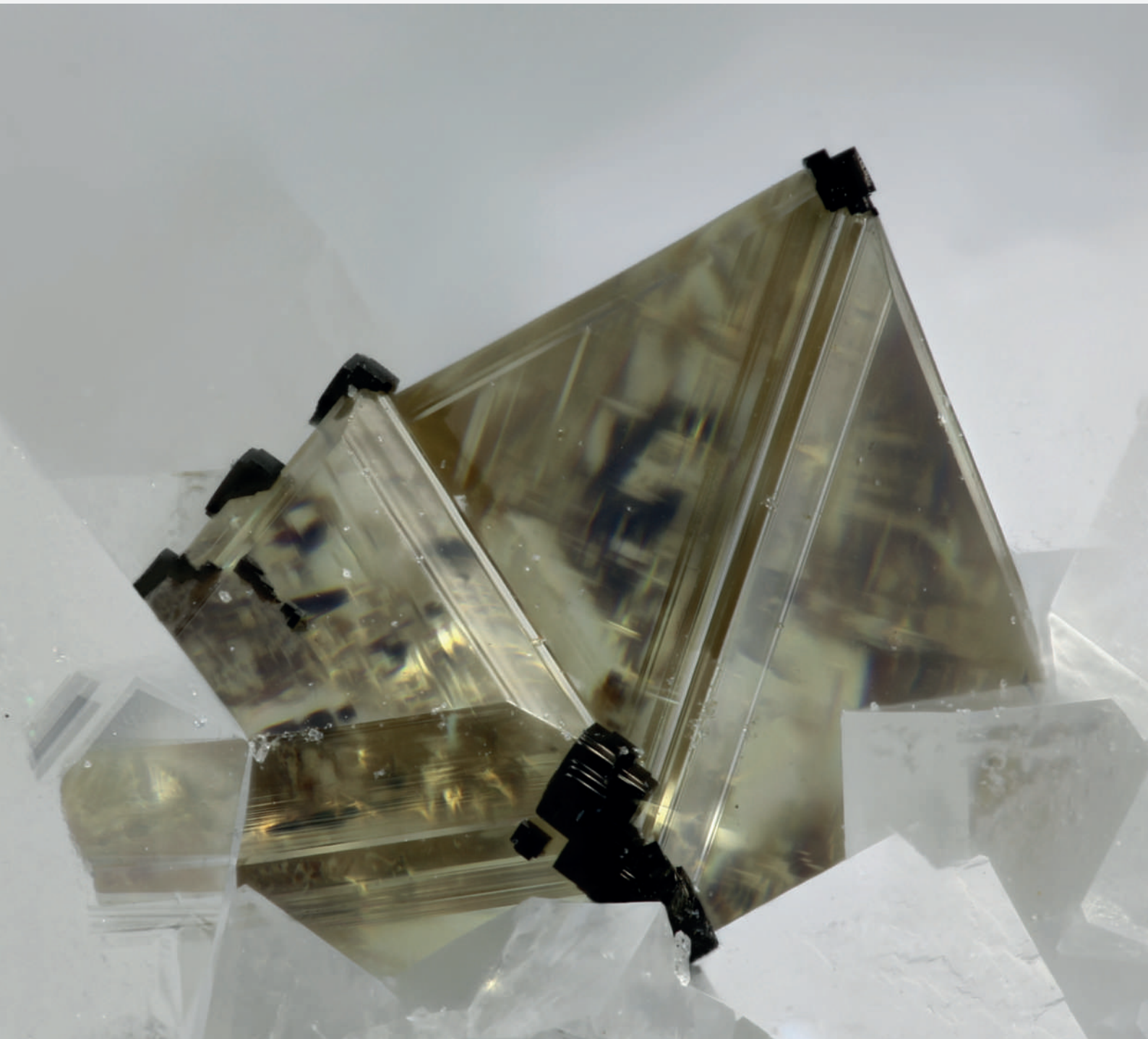


PLINIUS



Società Italiana di Mineralogia e Petrologia
c/o Dipartimento di Scienze della Terra
Via S. Maria 53 - 56126 PISA



Contents

- 3 Plinius Editorial Board**
- 5 Senior's Interviews**
6 *Prof. Piergiulio Cappelletti*
9 *Prof. Bernardo Cesare*
- 12 Awards Interviews**
13 *Ferrando Carlotta*
14 *Mauro Daniela*
15 *Murri Mara*
16 *Capriolo Manfreda*
17 *Finocchiaro Claudio*
18 *Corvò Stefania*
19 *Fugazzotto Maura*
20 *Mingardi Giulia*
21 *Fantini Riccardo*
- 22 Ph.D. Theses Extended Abstracts**
23 *Altieri Alessandra*
30 *Cantaluppi Marco*
37 *Carnevale Gabriele*
44 *Corno Alberto*
52 *D'Agostino Alberto*
60 *De Matteis Chiara*
68 *Yikai Liu*
76 *Magnani Lorenzo*
79 *Pagliaro Francesco*
86 *Petroccia Alessandro*
95 *Randazzo Antonio*
103 *Verde Maria*
- 110 BeGeo Extended Abstract**
111 *Scanu et alii*
- 116 Photo Contest**

Rivista Annuale SIMP - Società Italiana di Mineralogia e Petrologia | Numero 49 | 2023

SOCIETÀ ITALIANA DI MINERALOGIA E PETROLOGIA

c/o Dipartimento di Scienze della Terra, Università di Pisa, Via S. Maria 53 - 56126 Pisa

www.socminpet.it | <https://www.socminpet.it/344/plinius.html>

Direttore Editoriale: Concetta Rispoli (concetta.rispoli@unina.it)

Comitato Editoriale: Concetta Rispoli, Virginia Marchionni, Alessandro Petroccia, Maria Verde, Andrea Maffei, Stefania Corvò, Lorenza Fascio, Nadia Malaspina

Gli articoli e le note firmate esprimono solo l'opinione dell'autore e non impegnano la Società Italiana di Mineralogia e Petrologia né la redazione del periodico.

FOTO COPERTINA: Matteo Chinellato | Sfalerite con Sulvanite

Plinius Editorial Board

Concetta Rispoli

Researcher (RTD-A)
Università degli Studi di
Napoli - Federico II

Virginia Marchionni

SIMP Secretariat &
Communication

Alessandro Petroccia

Post-Doc Researcher
Università di Torino

Maria Verde

Post-Doc Researcher
Università degli Studi di
Napoli - Federico II

Andrea Maffeis

Post-Doc Researcher
Università di Torino

Stefania Corvò

Post-Doc Resercher
Università degli Studi di
Pavia

Lorenza Fascio

SIMP Secretariat

Nadia Malaspina

Associate Professor
Università degli Studi di
Milano - Bicocca




CONCETTA RISPOLI
UNIVERSITÀ DI NAPOLI - FEDERICO II



VIRGINIA MARCHIONNI
SECRETARIA SIMP



ALESSANDRO PETROCCIA
UNIVERSITÀ DI TORINO



MARIA VERDE
UNIVERSITÀ DI NAPOLI - FEDERICO II



ANDREA MAFFEIS
UNIVERSITÀ DI TORINO



STEFANIA CORVÒ
UNIVERSITÀ DI PAVIA



LORENZA FASCIO
SECRETARIA SIMP



NADIA MALASPINA
UNIVERSITÀ DEGLI STUDI DI MILANO - BICOCCA

From the Editorial Board

Dear Members, the editorial transformation of our magazine continues. In recent years the journal has been moved to the web, which allowed the introduction of the DOI for published contributions. The consolidated sections of the Extended Abstracts of the Juniors SIMP's Ph.D. Thesis and the SIMP Activities will be maintained and accompanied, down the line, by new sections. These will be aimed at enhancing the cultural, didactic and dissemination activity that involves the Society and its Members. All of this will be framed in a new graphic design aimed at reviving the magazine.

To achieve these objectives, the editorial committee composed of Concetta Rispoli, Nadia Malaspina and Lorenza Fascio has been expanded, adding four young SIMP members: Post-Docs Stefania Corvò and Andrea Maffeis, and two members of the BeGeo organizing committee, Alessandro Petroccia and Maria Verde. They are joined by Virginia Marchionni, the new component of the SIMP secretariat and communication team.

We hope that this initiative will give our magazine a new impetus and that, with the contribution of all the Members, PLINIUS will continue to be a reference point for all those who wish to learn about the themes, the research and the dissemination activities in the fields of Mineralogical and Petrological Sciences.

The history of the SIMP logo and *PLINIUS* emblem

In the early 1980s the SIMP planned to institute a prize to be awarded to scientists for their outstanding contribution to the Mineralogical sciences

Early 1980s

Renato Guttuso and Marcello Carapezza
(Courtesy Archivi Guttuso Association)



Marcello Carapezza (SIMP president '82-'83) asks Renato Guttuso (Italian painter) to engrave a medal with a scientist considered a "myth" of natural sciences

Early 1980s

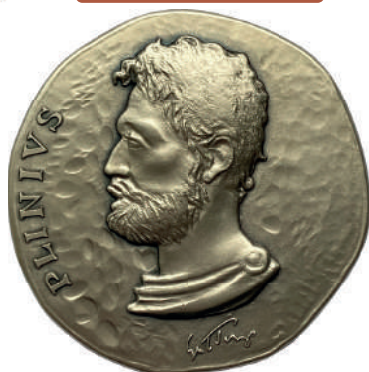


The medal portrays Gaius Plinius Secundus (the Elder), a philosopher, a historian and a scientist, regarded as one of the fathers of Mineralogy

Since 1983

▲ The original sketch by Guttuso
(Courtesy Archivi Guttuso Association)

▶ The Plinius Medal



The official bulletin of the SIMP, the *Rendiconti della Società Italiana di Mineralogia e Petrologia* (1967-1988), previously *Rendiconti della Società Mineralogica Italiana* (1941-1966), becomes *PLINIUS* and the Guttuso Medal is since featured on the cover of the journal

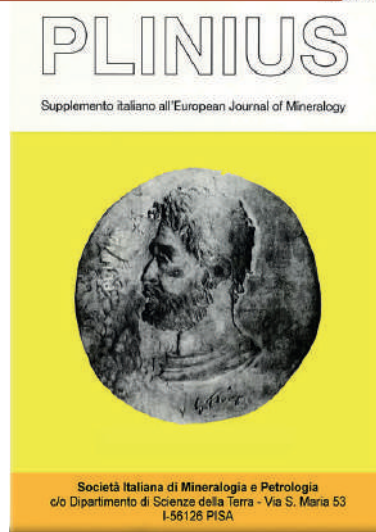
1972-1988

Plinius Medal becomes the SIMP logo

1983



1989



2014

The SIMP logo is digitised and renewed, inspired by the original design of Guttuso

2019



2023

The journal *PLINIUS* is being renewed and Guttuso's Plinius silhouette has been now sketched out and embeded within the journal name



Senior's Interviews

Cappelletti Piergiulio.....6

Cesare Bernardo.....9

Cappelletti Piergiulio

Parma 2019
SIMP Meeting



Piergiulio Cappelletti

is a Professor of Mineral Georesources and Mineralogical-Petrographic applications for the Environment and Cultural Heritage at University of Naples. Director of the Department of Earth Sciences, Environmental and Resources (DiSTAR) from 2015 to 2016. President of the Società Italiana di Mineralogia e Petrologia (SIMP) from 2018 to 2019 and has also held the position as Director of the Museum Center of Natural and Physical Sciences since 2018.

The Center for Natural Sciences Museums

The Center for Natural Sciences Museums was established in 1992 and consists of the Mineralogy, Zoology, Anthropology, Palaeontology museums, and since 2012, also the Physics Museum. Soon, the Chemistry Museum will also be added to them.

The high scientific and historical value of the various collections, combined with the significant artistic and cultural interest of the exhibition halls, make it a prominent institution among other national

What does SIMP represent for the scientific community?

First, I would like to congratulate the whole new Plinius team for this new way of approaching the SIMP community, I would have loved to experience this kind of relationship between the senior member of the mineropetrographic community. SIMP represents in my opinion the natural interface for young students and researchers from different Universities and Research Institution that operate in the specific field of the mineralogical sciences (*sensu lato*); with its annual congresses, and along with workshops, schools and seminars, in which the results of scientific research are presented and discussed, SIMP promotes the development in sciences and is the natural place for constructive confrontations among scientists, no matter what their age (academic and not) is.

As a museum director, what are the most fascinating and complicated aspects of your role?

I have to admit my role as Museum Director represents a new challenge for me, since my academic career was totally devoted to field and laboratory activities, beside teaching, and only in 2018 I began this new adventure, that I have been heavily involved in, and it is not always easy to reconcile the two aspects mentioned above, but I try my best not to let one of the two activities be negatively affected. Undoubtedly, being Director of the *Centro Musei* (there are five museums: Mineralogy, Palaeontology, Zoology, Anthropology and Physics, and a sixth is on the way, Chemistry) is certainly a stimulating challenge but also one dense with responsibility; one only has to think of the importance of the collections housed and the names of my predecessors, in various capacities, to make one's wrists quiver...

What qualities are essential?

Patience is the fundamental quality, as well as the ability to mediate in order to obtain results that might seem easy, but that conceal an enormous amount of work behind them; it is obvious that without all the staff of the Museum Center, the Director alone could never have achieved the results achieved so far, both at the level of representativeness in the

and international museums.

The aim is to make the sciences, particularly the natural and physical sciences, accessible to the general public, involving scholars, educational institutions, and the community in the appreciation of the beauty and importance of spreading scientific knowledge.

The Museums in the Center actively engage with the community by promoting exhibitions, conferences, seminars, and activities aimed at schools, through guided tours, workshops, and field trips.

A recent walk (2023) in the Royal Mineralogical Museum (Federico II University), along with the Italian famous science disseminator, Alberto Angela.

territory but also with regard to Third Mission activities, which constitutes a very important challenge for all Italian universities, now and in the years to come.

When you were a student what triggered the engine of interest that led you to these important achievements?

The main engine that has driven me throughout my career is undoubtedly the passion for Geology in its various fields, and since I was a boy even before enrolling in university, the interest in the explanation of the natural phenomena affecting our planet. On the other hand, I cannot deny that having been born and raised in Campania (and more precisely in the city of Pozzuoli, mentioned by both Vitruvius and Pliny the Elder - does this last name ring a bell?) it came natural for me to indulge this passion. Then, I was certainly lucky during my career as a student, having met professors who were able to raise in me the awareness of having made the right choice but who above all taught me work ethics and gave me the opportunity to continue my journey.

What age groups visit museums most frequently and what are the reasons that motivate them to occupy their halls?

Visitors to the Museum Center belong to a wide range of age groups, and although the main number of guests belong to schoolchildren of all levels in the Campania region (but not only), there are numerous visitors from the entire citizenry who join the ranks of science enthusiasts of all ages. The uniqueness of the architectural heritage (pertaining to the oldest secular Athenaeum in Italy, and which this year celebrates its 799th anniversary since its founding) is combined with the very considerable importance of the collections housed in the five museums, and makes the Museum Center an exceedingly representative institution, not only of the city of Naples, as a reference for the history of the evolution of the scientific method, helping to organize events and seminars of both a popular and scientific nature. Finally, there are numerous occasions on which temporary exhibitions, cultural events and classical music concerts are hosted in the prestigious halls.



Today, it is very difficult to stimulate the younger generation, who are increasingly interested in finding better-paid university paths in the future. What can the natural and physical sciences give young people?

Well, this consideration is true up to a point, because despite everything I continue to see young scholars animated by passion and "holy fury" in regard to scientific disciplines, even if economic aspects are undeniably to be taken into consideration. I believe that in any case being able to be fortunate enough to do something you are passionate about goes beyond what may be mere career expectations, and if in life you are able to indulge your work-type aspirations, then it can be even more fulfilling and satisfying than a job that allows you to earn a very good salary level materially.

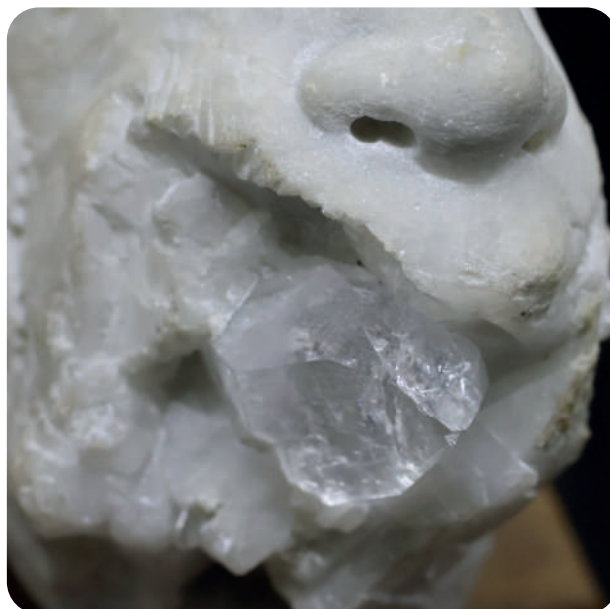
With such an extensive collection of natural and physical science specimens, which ones do you believe capture the essence of the museum's mission and purpose?

Among the many exhibits in the Museum Center, the choice is extremely complex, but I would like to dwell on one of them, which in my opinion combines the true essence of what an university science museum may be able to convey. The presence of a small Satyr's head (labelled as quartz on Carrara marble) attributed to Antonio Canova within the collections of the Royal Mineralogical Museum of Naples offers an opportunity to highlight the layering of meanings an object becomes the bearer of when it is part of a museum display. The object dates from the famous collection of naturalist Teodoro Monticelli largely acquired by the Royal Mineralogical Museum in 1851. Canova and Monticelli had met during one of the artist's Neapolitan sojourns, and had become particularly close, as evidenced by correspondence between the two, who also exchanged rock specimens. The small Satyr, then, represents not only an interesting mineralogical essay, but also a work of art and material evidence of the museum's history, and its importance, which helps to understand how the Museums also had the role of research centers over the centuries. Indeed, a number of complex meanings are layered on it, ranging from mineralogy to art history and history tout court, which are revealed, however, only if the history of the museum and the collecting history of the object are kept in mind. Antonio Scherillo, the museum's director from 1939 to 1972, and my most illustrious predecessor (he was also president of SIMP from 1968 to 1969) also points out that the attribution to the great sculptor was tied exclusively to an oral tradition handed down from director to director.

Do you have any advice for young people who want to study geological sciences (min-pet-geochemistry)?

Aside from the ever-valid suggestion to follow your passions, regardless of external conditioning and fashions of the moment, I like to recall a phrase that has always made me think a lot: "Civilization exists by geological consent, subject to change without notice". This is a quote from William James Durant, an American historian and philosopher, best known for his 11-volume work, *The Story of Civilization*, which contains and details the history of Eastern and Western civilizations, and in my humble opinion many of the reasons for this "geological consent" for civilization could be described and explained through mineralogical and petrographical studies; and for this purpose we need only think of the many georesources that have been used over the millennia, and that enable the continuous development of increasingly advanced technologies (metals, glass, ceramics, ligands, building stones and so on).

Canova's Satyr:
head in Carrara marble from whose mouth emerges like a hyaline quartz crystal. Collection of the Royal Mineralogical Museum of Naples, dating back to the collection of the naturalist Teodoro Monticelli, acquired by the Neapolitan museum in 1851.



Cesare Bernardo

On the Archean granulites of the Lewisian Complex, Scotland



Bernardo Cesare is a Professor of Petrology at the Department of Geosciences at the University of Padua and President of the Società Italiana di Mineralogia e Petrologia (SIMP) from 2014 to 2015. His research includes metamorphic rocks, the origin of granitic magmas, minerals and their inclusions. He extensively employs photography, both micro and macro, to document his research and describe the morphological features of minerals.

About MicROCKScopica - Rock Art (since 2009)

As a photographer with artistic intent, my rock photomicrographs have been displayed in photo galleries, at mineralogical and scientific exhibits and in Natural Sciences Museums in Italy, France, Germany, Hungary, Poland, Spain, Switzerland, UK and USA, and published in photographic and popular magazines, and in geological journals.

I won the MicroGeo2008 photo contest of the Russian Mineralogical Society, the 2nd

What does SIMP represent for the scientific community?

SIMP is, or should be, the reference Society for the Italian mineralogical s.l. community. Under the current circumstances - shrinkage of affiliates or potential members at national level; widening of the international perspective and interests of early-stage researchers - SIMP is facing some difficulties to maintain such reference role. Initiatives such as the rejuvenation of Plinius and its editorial board are definitely on the right track, and should be supported and followed by many others.

How was MicROCKScopica - Rock Art born?

MicROCKScopica developed in parallel to my scientific activity, as I realized that rocks under the microscope may have an important aesthetic value, and are pleasing to viewers. At the beginning, working with transparencies film, photomicrography was time-consuming and expensive, and results somehow unpredictable: often times, after developing the film, I had to throw it away due to bad exposure or lack of focus. Digital photography made everything faster and cheaper, but most of all you could see the results in real time. My first digital camera on a microscope marked the serious beginning of MicROCKScopica.

Did it start from a simple passion or after attending photography or similar courses?

I never attended photography courses even though at the time of Ph.D. I was interested in reportage and macro photography - necessary for fieldwork - and studied some theory on books. For photomicrography I could learn many of my skills from a couple of excellent teachers: the managers of the photography lab of my Department.

When you created this page, did you imagine that it would become so famous?

Is MicROCKScopica really famous? Actually the main web page needs a major update, but I always postpone... I think the main reason why my aesthetic photomicrographs attract a fairly wide audience (mostly of non-geologists) on Twitter or Facebook is because viewers find the photos appealing but do not know what they are looking at. There's an element

and 3rd place at the 2008-9 Art in Crystallography Prize of the American Crystallographic Association, the 9th place at Nikon Small World contest 2009, the 8th in 2011. Runner up at Bilder der Forschung 2010 and at WPGA 2010 - The Pollux Awards, and at Chasing the light - Patterns in Nature 2011. Merit award a WPGA 2011 - Beauty Around Us. I won the IPA-2012 Awards (micro - non pro category).

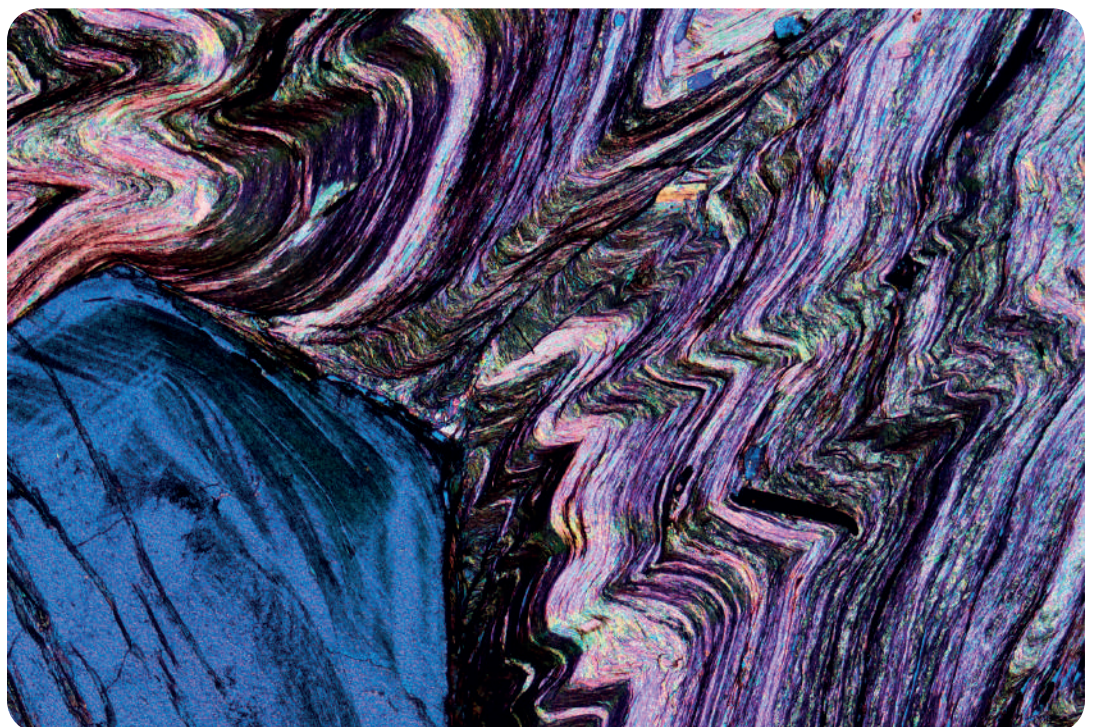
of surprise in MicROCKScopica that, fortunately, was not explored before. And, yes, I take some prizes having been featured in calendars, exhibits and books alongside people like Michael Davidson, Felice Frankel or Martin Öggerli. Those are really the famous SciArtist!

How long does it take to create one of your masterpieces? From choosing the object to depict to the final photo?

It depends. Some rocks are photogenic; some are just not (for me, of course). This means that with some thin sections I could stay for hours at the microscope (generally I quit before) looking for a good subject, without success. For the good ones it may be a matter of minutes. Then it comes to color, and also in this case even though I like the composition I may be unsatisfied with the combination of colors, and move to another subject. But once the right image has been prepared, shooting several others is very fast with digital equipment.

When you were a student, what sparked your interest that led you to the achievements of your career in geosciences?

Ah, let's move to more serious things! As a student I was quite unaware that I wanted to (would) become a scientist. I just wanted to learn, and do things well. With the master thesis I enjoyed working with crystalline rocks and the microscope, and decided it could be not a bad idea to give a try to a Ph.D. in petrography (actually I had little alternatives...). From then on, my scientific future was basically determined by a combination of luck, serendipity, curiosity and encounters with some of the best scientists in my field. A few names? During Ph.D.: Guidotti, Sassi, Trommsdorff, Connolly, Thompson, Hollister, Vernon. Many others followed. Moreover, I would have not discovered nanogranitoids, what I am probably known most for in geology, if I hadn't seen by pure chance some thin sections of xenoliths from El Hoyazo (Spain) belonging to the collection of late G. Zirpoli. Those incredible rocks marked the major change of direction in my scientific career. Thanks Giampiero Venturelli for making this happen!



Garnet in blue

Garnet porphyroblast in a graphitic schist from the upper Vize Valley.

Taking photomicrographs
of dried Aperol



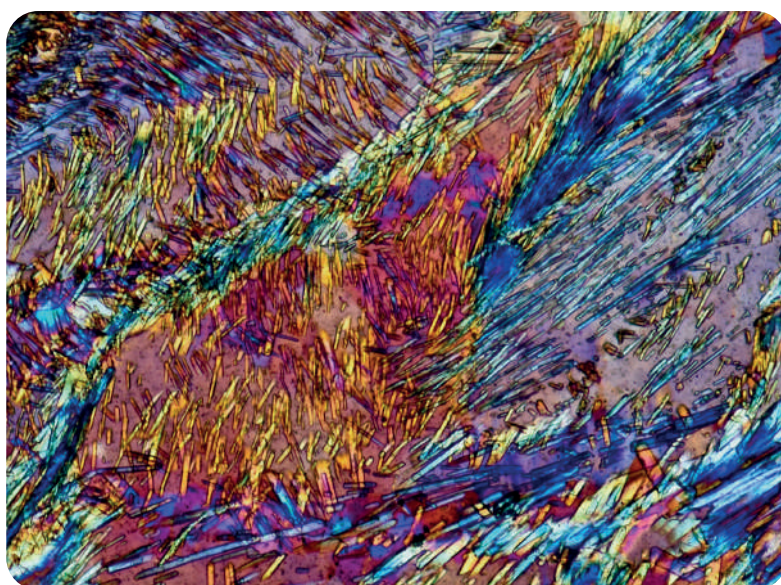
Which is your favourite photographed object or the one that surprised you the most once observed under the microscope?

The choice is really wide, both scientifically and aesthetically. Most thin sections I see for the first time have beautiful subjects for aesthetic photomicrography. Among my favorite rocks are agates, which provide a large variety of lovely microscapes despite being all made of silica. A non-geological jaw-dropping subject is callus remover, which allows to capture crystallization in real time. Scientifically speaking the most recent "wow" I said was looking at the tetragonal garnets (<https://doi.org/10.1038/s41598-019-51214-9>) of an eclogite under polychromatic polarization (<https://doi.org/10.1130/G49303.1>).

Do you have any advice to give to young people who want to undertake the study of geological sciences (especially in the min-pet-geochemistry field)?

Talking to Master or Ph.D. student what I can say is be curious, read/study a lot, think a lot and think you are learning how to address problems by asking the right questions rather than solve problems or answer questions. And for the specific MinPetGeochem fields, also keep in mind that the optical microscope is still fundamental!

Concerning follow-ups in research, Academia has changed a lot since I got my Ph.D., and my ideas and advice may be outdated or even counterproductive. But I still believe Ph.D. should be "training to research", whereas the current views are that a Ph.D. has to solve the major problems in Science. I know that one has to be successful in the job market, but early-stage researchers should not forget that research is not competition but the search for most likely answer to a scientific question. In this search I would recommend to be



**Needles which do
not sting**
Sillimanite needles in
cordierite. Metapelitic
granulite from
Klin Aus, Namibia

open minded, rigorous and humble, so as to evaluate most possible alternatives. All in all, as my Master advisor said reading the conclusions of my Thesis "potrebbe anche essere tutta un'altra cosa".

SIMP Grants Interviews

<i>Ferrando Carlotta</i>	13
<i>Mauro Daniela</i>	14
<i>Murri Mara</i>	15
<i>Capriolo Manfredo</i>	16
<i>Finocchiaro Claudio</i>	17
<i>Corvò Stefania</i>	18
<i>Fugazzotto Maura</i>	19
<i>Mingardi Giulia</i>	20
<i>Fantini Riccardo</i>	21

**PREMIO ANGELO
BIANCHI
2021**

Ferrando Carlotta



Area of Expertise:
Petrology

Current position:
Researcher (RTD-A)

Current Affiliation:
Dipartimento di Scienze della
Terra, dell'Ambiente e della Vita,
Università degli Studi di Genova
(Italia)

e-mail:
carlotta.ferrando@unige.it

What advice would you give to young members who are interested in studying geological sciences?

Follow your dreams and pursue your interests! Our field of research allows us to discover our Planet through different approaches, often ignored by many people although crucial to our understanding of Earth dynamics.

With a multidisciplinary methodological approach, from structural and microstructural investigations to geochemical analysis, my scientific research is focused on the understanding of the petrological processes involved in the formation of the oceanic lithosphere, from mantle melting at spreading centres to crystallization and cooling of the lower oceanic crust. This research aims at constraining the evolution of magmatic systems beneath spreading centres and the interplay among magmatism and hydrothermalism during the formation and exhumation of the lower oceanic crust, mainly in slow-spreading environments. I conduct petro-geochemical investigations on peridotites, pyroxenites and gabbroic sequences sampled at modern ridges (Mid-Atlantic Ridge and Southwest Indian Ridge) and analogue ophiolites (Erro-Tobbio, Ligurian Alps, Italy; Monte Maggiore, Alpine Corsica, France).

The continuous cycle of solid Earth begins at mid-ocean ridges where decompression melting and processes of melt migration and crystallization continuously build the oceanic crust. Understanding these processes that shape the outermost portion of our Planet provides fundamental constraints on the heat and masses exchanges between the interior and the exterior of the Earth. My scientific research and the multidisciplinary methodological approach I apply bring new insights into the processes behind these thermal and chemical exchanges, crucial for life in the deep oceans.



I received the SIMP award "Angelo Bianchi" based on my scientific activity and publication records. I presented 12 peer-reviewed published papers. These papers are the result of my ongoing international collaborations and involvement in oceanographic expeditions. These manuscripts are mainly focused on the accretion and evolution of the lower oceanic crust along present-day spreading centres, the Southwest Indian Ridge and the Mid-Atlantic Ridge.

**PREMIO MAZZI
(EX PANICHI)
2022**

Mauro Daniela



Area of Expertise:
Mineralogy

Current position:
Administrative Technician

Current Affiliation:
Museo di Storia Naturale,
Università degli Studi di Pisa
(Italia)

e-mail:
daniela.mauro@unipi.it

What advice would you give to young members who are interested in studying geological sciences?

Stay hungry. Stay foolish. I think that these words of Steve Jobs could summarize the advice I would like to give to young people. One of the take-at-home messages I learnt during my Ph.D. was that scientific research can be very exciting and the results totally unexpected. Every day a new discovery waits for you.

My main research topic is related to the crystal-chemical investigation of sulfate minerals through a multi-technique approach (X-ray diffraction, chemical analyses, and some spectroscopies). The aim was the understanding of the structural plasticity of sulfate minerals as well as their role as sinks for potentially toxic elements (PTE) during the alteration of primary ore deposits. Moreover, recently, I focused my attention on other topics, e.g., the OH content in garnets, and the mineralogy of the Peloritani Mountains (Sicily, Italy). Finally, due to my current position at the Natural History Museum of Pisa University, some research was devoted to the study of old mineral collections, with a particular focus on native copper from Tuscany and the sulfur specimens kept in our mineralogical collections.

The crystal-chemical investigation of sulfate minerals allowed an improvement of the understanding of their role in acid mine drainage systems, showing both their structural variability as well as their role in hosting some PTE (e.g., Tl) whose speciation was understood and described integrating data from different techniques. Moreover, some new mineral species were discovered (in some cases with novel crystal structures) adding further complexity to the sulfate mineralogy. Among current topics, I hope to be able to give a contribution to a better understanding of the role of H₂O in garnets. Finally, I would like to improve our knowledge of the mineralogy of the Peloritani Mountains, where several small deposits occur whose mineralogy (considering both primary and secondary phases) is scarcely known.



The SIMP award I received was a great honour. It deeply gratified me and it was a further stimulus in continuing my scientific research.

**PREMIO MAZZI
(EX PANICHI)
2022**

Murri Mara



Area of Expertise:
Mineralogy

Current position:
Researcher (RTD-A)

Current Affiliation:
Dipartimento di Scienze della
Terra e dell'Ambiente,
Università di Pavia (Italia)

e-mail:
mara.murri@unipv.it

What advice would you give to young members who are interested in studying geological sciences?

Be curious, careful and creative! The world of geological sciences is amazing and ready to be explored by young, motivated scientists! We still need to know and understand a lot of aspects of our planet. In our everyday life there is always something related to the geological science world, so if you want to discover more and be part of the future geological generation of scientists, find your favourite geological topic and pursue it!

I study the role of stress and strains in impact-shocked minerals and in minerals from ultra-high pressure metamorphic rocks to understand stress-driven processes occurring on the Earth's surface as impact shock events or deeper in the Earth, as subduction and exhumation. My research methods range from the application of intracrystalline geothermometry to unravel the thermal history of terrestrial and extraterrestrial bodies, to the development of Raman elastic geobarometry on mineral host-inclusion systems to assess the pressure and temperature conditions attained during metamorphism. I also study shock features in impact diamonds and the effects of space weathering processes in aqueous environments by performing liquid-phase nanosecond pulsed laser ablation on silicate and carbon phases.

The originality behind my research is the integration of methods from diverse fields which allows me to obtain new insights and results into geological processes. An example is the study of mineral host-inclusion systems by using Raman elastic geobarometry which can provide constraints about their formation conditions. However, most methods and theories available are developed for hydrostatic pressure conditions, while mineral inclusions often experience deviatoric stress. So, I developed the concept of the phonon-mode Grüneisen tensor to determine strains in inclusions from Raman spectroscopy measurements. This was only possible because I performed *ab initio* HF/DFT calculations to determine all the Grüneisen tensor components for each Raman active mode in quartz, which are almost impossible to achieve experimentally.



The SIMP award "Fiorenzo Mazzi" was extremely helpful for my research activities since it contributed to my attendance at one national conference and to the acquisition of laboratory equipment.

The SIMP award "Fiorenzo Mazzi" was extremely helpful for my research activities since it contributed to my attendance at one national conference and to the acquisition of laboratory equipment.

**PREMIO TESI DI
DOTTORATO
2022**

Capriolo Manfredo



Area of Expertise:
Igneous Petrology,
Geochemistry and Volcanology

Current position:
Post-Doc Researcher

Current Affiliation:
University of Birmingham
(United Kingdom)

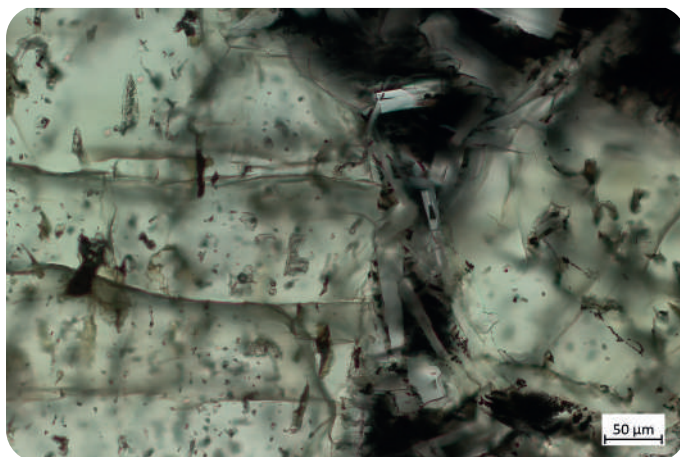
e-mail:
m.capriolo@bham.ac.uk

What advice would you give to young members who are interested in studying geological sciences?

My advice to all the young members interested in studying Geological Sciences is to be curious and to be driven by their curiosity in scientific research.

In Earth's history, the emplacement of Large Igneous Provinces (LIPs) coincided in time with the major mass extinction events. My Ph.D. thesis focussed on the carbon cycle in the Central Atlantic Magmatic Province (CAMP), whose activity was synchronous with the end-Triassic biotic crisis. Throughout a multi-analytical approach (combining optical microscopy, confocal Raman microspectroscopy, microthermometry, cathodoluminescence, SEM-EDS, EMP and Nano-SIMS), the investigation of melt and fluid inclusions within the magmatic minerals of CAMP basaltic rocks allowed characterizing and quantifying the volcanic and thermogenic emissions (CO_2 and CH_4 , respectively) from this LIP. Then, using a biogeochemical box model, the constraints on volcanic CO_2 from melt inclusions allowed assessing the impact of the main CAMP volcanic phase on the end-Triassic climate and environment.

My Ph.D. thesis presented a new protocol to detect and quantify the primary carbon species in LIPs. Since carbon is a volatile element and exsolves at high pressures (i.e., deep in Earth's crust), it was mostly degassed during LIPs activity. Hence, my Ph.D. research hinged on the analysis of melt and fluid inclusions preserving primary carbon within the magmatic minerals of both effusive and intrusive magmatic rocks from the end-Triassic CAMP. Potentially, this innovative and powerful approach may be applied to the study of any mass extinction-related LIP.



First of all, I am honoured to have received the SIMP award, which represents a great recognition for my Ph.D. research. Then, the SIMP award provided the economic support to attend an international conference, which is a great opportunity to present my current research and enlarge my academic network.

**PREMIO TESI DI
DOTTORATO
2022**

Finocchiaro Claudio



Area of Expertise:

Applied Mineralogy to Geo-resources and Cultural Heritage

Current position:

Researcher (RTD-A)

Current Affiliation:

Dipartimento di Scienze Biologiche, Geologiche ed Ambientali, Università di Catania (Italia)

e-mail:

claudio.finocchiaro@unict.it

What advice would you give to young members who are interested in studying geological sciences?

In general, the Earth sciences are wide and fascinating. I always suggest following and believing your own aspirations. Moreover, I invite the young students to follow political tendencies and to specialize in the applied sciences which have a high impact on the worldwide context

My research aims to provide innovation for the production of alternative and sustainable building materials, with the development of alkaline-activated materials, low-energy-consuming, using low-value natural raw materials or waste materials in view of the circular economy and environmental sustainability promoted by European policies for the ongoing Ecological Transition. In detail, the research was born with the chemical and mineralogical investigation of the volcanic ashes of Mt. Etna volcano (Italy), still a natural waste material with high management cost, for use in the alkaline activation process as a precursor. Their use is limited in traditional mortars and to the old leached deposits, since fresh volcanic products have an excessively high chloride and sulphate content due to their interaction with the volcanic gasses. The synthesized products were investigated, through a multidisciplinary approach, to assess their physical-mechanical features and useful durability test are in progress for further application tests in the restoration and building sectors.

My research aims to the valorisation of natural and industrial waste for the production of eco-friendly materials as an alternative to the traditional ones based on Portland cement, which are mostly responsible for CO₂ emissions in the industry sector. Moreover, it allows limiting the exploitation of natural resources for the environmental safeguard as requested by EU policies. In this way, the alkaline-activated materials represent a new potential georesource class to be investigated within the applied mineralogy and applied to building and restoration sectors. Considering the valorisation Mt. Etna volcanic deposits and the high interest already shown by several companies, this research could represent a great opportunity to create new industrial manufacturing lines of sustainable materials and thus boost the local economy in a circular way.



The "best Ph.D. thesis" award of SIMP gave me the opportunity to attend the prestigious XVIII Conference of the European Ceramic Society that took place in Lyon on 2-6 July 2023, where I have presented the results of durability tests of alkali-activated materials based on volcanic ashes, obtained during my abroad period at Department of Mineralogy and Petrology of Granada University (Spain).

**BORSE DI STUDIO
PER L'ESTERO
2022**

Corvò Stefania



Area of Expertise:
Petrology, Structural Geology

Current position:
Post-Doc Researcher

Current Affiliation:
Dip. di Scienze della Terra e
dell'Ambiente, Università degli
studi di Pavia (Italia)

e-mail:
stefania.corvo@unipv.it

What advice would you give to young members who are interested in studying geological sciences?

My main advice to young and future geoscientists is that, if there is such passion for what you do and curiosity to discover, then it means you are on the right track, so never give up! Always try! Because only with tenacity and determination, your sacrifices and efforts will be rewarded!

The research I conducted during my time abroad involved testing the U-Pb dating method on garnet in representative rocks of the continental crust. The aim was to investigate whether and how garnet can record magmatic, metamorphic and deformation processes in different lithotypes from distinct levels and sections of the continental crust exposed in famous and diverse locations in the Alps (and beyond). Thanks to the SIMP grant, I spent two months in one of the few laboratories in the world specialised in U-Pb dating of metamorphic garnet, the LERA (Laboratory for Environmental and Raw Materials Analysis) at the Karlsruhe Institute of Technology (KIT; Germany). Here, I was able to work closely with Dr. Aratz Beranoaguirre, an expert in the aforementioned technique. This was based on the use of modern laser ablation mass spectrometry instrumentation (LA-ICP-MS; ThermoFisher-Teledyne Proton Machine), which can successfully date metamorphic garnets containing less than 10 ng/g uranium and an accuracy of < 3 % for the lower intercept age.

During my stay, I tested the technique on a total of 50 thin sections of mafic, felsic, low- and high-grade metamorphic, deformed, and undeformed rocks. In summary, not all garnets are datable. The feasibility of dating garnet depends on several factors including the chemistry of the total rock, as well as the mineralogical assemblage. The rocks in which garnet is successfully dated are mainly skarn, garnetites, undeformed rocks and those poorer in accessory minerals (such as zircons, monazites, rutile etc.). Only in these particular cases, the garnet has a good chance of containing the right concentrations of U-Pb and thus being datable. With this research, I hope to provide important guidelines and a significant contribution to improving the method of U-Pb dating on metamorphic garnet, which is one of the main minerals contained in the rocks constituting the Earth's crust and whose study allows us to understand many geological processes.

This award gave me the occasion to do a new experience abroad and in a different university environment. This type of experience can only enrich you on several fronts, not only in your curriculum but above all from a cultural and social point of view. Receiving this award has given me more confidence in my work, motivation and energy to "take a challenge", as well as the opportunity to learn new knowledge to add to my wealth of experience.

**BORSE DI STUDIO
PER L'ESTERO
2022**

Fugazzotto Maura



Area of Expertise:

Georesources to mineralogy and petrology for the environment and cultural heritage

Current position:

Post-Doc Researcher

Current Affiliation:

Dipartimento di Scienze Biologiche, Geologiche ed Ambientali, Università di Catania (Italia)

e-mail:

maura.fugazzotto@unict.it

What advice would you give to young members who are interested in studying geological sciences?

It will appear prosaic, but I think that the best way to reach your objectives, in every field, not only in geology, is to focus on what you really like, definitely ignoring possible fear of failing. If you care about that thing, you will find the right path to reach it.

This project aimed to deeply investigate the chemical processes involved in binary alkali-activated materials (AAMs), which are linked in literature with hybrid gels. The research starts from the results of my Ph.D. Thesis, where a complex structure of the gel is developed in the binary AAMs based on ceramic waste and metakaolin (MK). Particularly, the obtained gel in a large set of AAMs was studied from molecular, mineralogical and microstructural points of view, by means of Infrared and Raman spectroscopies, X-ray Diffractometry and, extensively, by high-resolution Scanning and Transmission Electron Microscopies, coupled with Energy Dispersive X-ray Spectroscopy. To connect the characteristics of the gel to the used precursors, also the raw materials were studied, specifically by a reactivity test and chemical analysis.

The synthesis process of AAMs sees a series of reactions whose complexity depends on the whole system: alkaline liquid precursors, aluminosilicate powder precursors, synthesis conditions and so on. Overall, the scientific literature identifies two microstructural systems: low-Ca content three-dimensional gel and high-Ca content gel, basically bi-dimensional. But, a third, hybrid, system can also be formed, whose structure and reaction process is unclear. This study increases the available knowledge about the complex hybrid systems, particularly related to AAMs obtained by ceramics, highlighting as very small variations, also in only one parameter involved in the synthesis, can determine evident differences in the formation of the gel and possible secondary products.



Undoubtedly, the grant was useful for conducting research at the University of Granada and its Centro de Instrumentación Científica (CIC), where I had the opportunity to improve my skills both in investigation and in using analytical instrumentation, as, for example, high-resolution TEM analyses, a field in which the scientists in Granada are very expert.

**External Awards
to young SIMP
members:**

**PREMIO
Con.Sienze
MAGISTRALE
2021-2022**

Mingardi Giulia



Area of Expertise:
Rock Mechanics, Mineral Physics,
Planetology

Current position:
Ph.D. student

Current Affiliation:
Ecole Normale Supérieure,
Université PSL (France)

e-mail:
mingardi@geologie.ens.fr

**What advice would
you give to young
members who are
interested in stu-
dying geological
sciences?**

My advice is to be passionate and curious. I think that those two elements are fundamental to pushing us in our research and making new discoveries. Also, another important aspect of science is never give up. If the results you have are not what you expected just keep going. Maybe you will find explanations that are more interesting than the one you were expecting at the beginning.

With the Award Con.Sienze was awarded my Master thesis about the geochemical study of two Martian shergottites. I studied the chemical and isotopic compositions of two olivine-phyric shergottites, DaG 670 and NWA 4222, to determine their mantle source and geochemical evolution. To tackle this objective, I firstly measured in situ the Pb isotopic composition of 15 melt inclusions in olivine for each shergottite using SHRIMP (Sensitive High Resolution Ion Microprobe), instrument in KBSI (Ochang, South Korea). In addition to Pb isotopes, I measured trace element compositions of the pyroxenes in the matrix. They revealed significant Eu and Sr anomalies in the cores. Thanks to this study I was able to define the depleted mantle source origin of the two meteorites and the subsequent geochemical evolution.



as anorthositic levels, might have been partially reabsorbed in the melts. These results are in good agreement with a study performed on gabbroic rocks in the Ivrea Verbano Zone (Mazzucchelli et al., 1992) and it is the first case that this is documented for Martian shergottites.

From the analysis of Pb isotopes and trace elements, I determined that the source of the two samples was a depleted source. However, the simple melting and the consequent fractional crystallization could not have produced some characteristic features such as Eu and Sr positive anomalies in the analyzed pyroxenes of the matrix. These trace element patterns have been produced during the magma-chamber phase in the crust of Mars. In fact, during the intrusion in the crust of the melts produced in the depleted mantle, some plagioclase cumulates, such

**External Awards
to young SIMP
members:**

**PREMIO
Con.Sienze
MAGISTRALE
2021-2022**

Fantini Riccardo



Area of Expertise:
Mineralogy

Current position:
Post-Doc Researcher

Current Affiliation:
Dipartimento di Scienze Chimiche
e Geologiche,
Università di Modena e Reggio
Emilia (Italia)

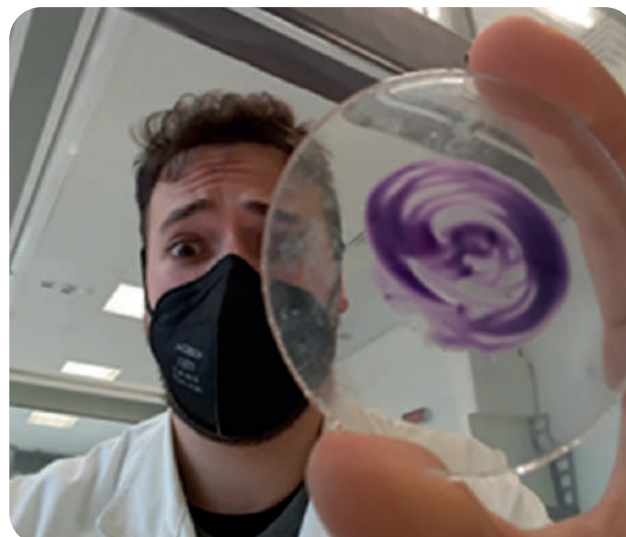
e-mail:
riccardo.fantini1@unimore.it

**What advice would
you give to young
members who are
interested in stu-
dying geological
sciences?**

The geological sciences are a complex mixture of entangled knowledge. Even if you have a specific interest in a particular subject, such as minerals or fossils or whatever, never be blind to other aspects. The mastery of a solid geological background can be a bargaining chip to face many challenges and projects in the research or business world.

With a multidisciplinary methodological approach, from structural and microstructural investigations to geochemical analysis, my scientific research is focused on the understanding of the petrological processes involved in the formation of the oceanic lithosphere, from mantle melting at spreading centres to crystallization and cooling of the lower oceanic crust. This research aims at constraining the evolution of magmatic systems beneath spreading centres and the interplay among magmatism and hydrothermalism during the formation and exhumation of the lower oceanic crust, mainly in slow-spreading environments. I conduct petro-geochemical investigations on peridotites, pyroxenites and gabbroic sequences sampled at modern ridges (Mid-Atlantic Ridge and Southwest Indian Ridge) and analogue ophiolites (Erro-Tobbio, Ligurian Alps, Italy; Monte Maggiore, Alpine Corsica, France).

The continuous cycle of solid Earth begins at mid-ocean ridges where decompression melting and processes of melt migration and crystallization continuously build the oceanic crust. Understanding these processes that shape the outermost portion of our Planet provides fundamental constraints on the heat and masses exchanges between the interior and the exterior of the Earth. My scientific research and the multidisciplinary methodological approach that I apply bring new insights into the processes behind these thermal and chemical exchanges, crucial for life in the deep oceans.



The ConScienze award I received shaded light on the results of our project, also attracting the attention of possible stakeholders. Moreover, the award strengthened the will of carrying on the project by seeking new collaborations.

Ph.D. Thesis Extended Abstracts

- 23 | Altieri Alessandra | Definition of a genetic model for the dark-colored overgrowths in pegmatitic gem tourmaline crystals
- 30 | Cantaluppi Marco | Advanced mineralogical and crystallographical techniques for understanding transformation processes in natural materials and their synthetic analogues. *Comparison between natural combustion pyrometamorphism and the synthetic analogous process of cement manufacture*
- 37 | Carnevale Gabriele | Petrology and geochemistry of Peri-Mediterranean carbonatite magmatism: case studies from Fuerteventura (Canary Islands) and Mt. Vulture Volcano (Southern Italy)
- 44 | Corno Alberto | Tectono-stratigraphic setting and metamorphic evolution of Ligurian-Piedmont Units in the Upper Susa and Chisone Valleys (Western Alps)
- 52 | D'Agostino Alberto | New frontiers of mineralogical and structural data analysis in the era of machine learning: tools for modern petrography
- 60 | De Matteis Chiara | Mineralogical and chemical characterization of Bottom Ashes from Municipal Solid Waste Incinerator. *A multi-techniques approach for an extremely complex and heterogeneous material*
- 68 | Yikai Liu | Geochemical modeling of solid waste-binder systems in stabilization/solidification applications
- 76 | Magnani Lorenzo | Lithium enrichment in anatectic pegmatites: new insights from the thermometamorphic aureole of the Adamello batholith
- 79 | Pagliaro Francesco | Crystal chemistry and physical-chemical behaviour of REE-bearing phosphates and arsenates. *The case study of Mt. Cervandone*
- 86 | Petroccia Alessandro | Unveiling the thermo-structural setting of collisional orogens. *Example from the Variscan chain in Sardinia*
- 95 | Randazzo Antonio | Biogeochemical processes affecting Volatile Organic Compounds (VOCs) in interstitial soil gases from geogenic sources and municipal waste landfills
- 103 | Verde Maria | Ceramic production in the *Ager Calenus* from the 3rd century BCE to early Imperial Period

Definition of a genetic model for the dark-colored overgrowths in pegmatitic gem tourmaline crystals

Alessandra Altieri

Dipartimento di Scienze della Terra, Università di Roma La Sapienza, Piazzale Aldo Moro 5, 00185, Roma, Italia

DOI: 10.19276/plinius.2023.01.001

RESEARCH'S INTRODUCTION AND AIM

Pegmatitic gem tourmaline crystals commonly display a sharp transition to dark color at the analogous termination; one of the best example is the so-called "Moor's head" textural type, which characterize the tourmaline crystals from Elba Island (Pezzotta, 2021). Such terminations show a wide range of morphological characteristics: they may occur as a narrow overgrowth with a sharp and lustrous pedion face terminating the crystal or as a thick overgrowth with rough pyramidal faces characterized by a fibrous texture that, occasionally, can be composed of an aggregate of long parallel needles (Fig. 1). However, in some tourmaline crystals, the dark overgrowth can extend all over the prismatic faces, including the antilogous pole. In all these cases, such dark-coloured overgrowths can be generally described as *colour anomalies*.

The formation of color anomalies, which are typically rich in Fe and/or Mn, is related to a dramatic physico-chemical change in the geochemical system during the latest-stages of tourmaline growth. However, the true se-

quence of events that led to the availability of such elements in the crystallization environment, resulting in the growth of late-stage tourmalines, was still unclear.

The goal of this Ph.D research is to constrain the formation mechanisms of tourmaline dark-colored terminations. To achieve this goal, selected gem-tourmaline crystals with dark overgrowths of different colors and textural features from several miarolitic Li-bearing pegmatites located in Elba Island (Italy), were studied with a multi-analytical approach. This approach includes chemical analysis with an electron microprobe and spectroscopic investigations using Mössbauer, OAS and FTIR analyses. Results obtained, combined with structural and paragenetic information of the cavities, were used to define a genetic model for the color anomalies observed in Elba gem-tourmaline crystals. This Ph.D research was further extended to several detrital tourmaline grains collected from the secondary deposit of Mavuco (Alto Ligonha pegmatite district, NE Mozambique). Gem-quality tourmalines from the Alto Ligonha district are among the most renowned for the combination of color and rarity.



Figure 1 a) Thin black overgrowth evidenced by a lustrous pedion face at the termination of a multicore tourmaline crystal on matrix. b) Thick black overgrowth with rough pyramidal faces at the termination of a multicore tourmaline crystal on matrix. c) Fibrous black overgrowth on a multicore tourmaline crystal. All specimens are from Elba Island (Italy). Private collection. A. Miglioli photo.

These features make them unique from a gemological viewpoint and therefore with a high commercial value, limiting the information regarding their crystal-chemical characteristics. To fill this gap, sixteen tourmaline grains provided by ongoing mining projects, were subjected to an in-depth analysis. Specifically, a detailed chemical characterization as well as a correlation study between compositional data and color displayed, was conducted. In addition, on selected grains with particular chromatic features, OAS analyses were performed. For all the tourmaline samples, the gemological variety was identified.

Besides their polychromatic features, most of these tourmaline grains are characterized by a dark overgrowth covering the prismatic faces. However, the genetic mechanisms responsible for these peculiar overgrowths have not been defined so far, as the pegmatitic source from which these tourmalines originated was still uncertain. This uncertainty was essentially due to the strong NYF (Niobium-Yttrium-Fluorine) geochemical affinity (Li and B-poor composition) of the Alto Ligonha pegmatites located quite close the secondary deposit of Mavuco, as well as the rudimentary excavation techniques, which did not allow the exploration of new pegmatitic deposits in the Alto Ligonha district. To gain information about the mechanisms that led to the formation of the prismatic dark overgrowths, selected tourmaline crystals from a recently discovered pegmatitic field, the so-called "Marina" pegmatite (Mavuco area), were analyzed. The "Marina" pegmatite has been hypothesized to be the source of the detrital tourmaline grains of the Mavuco area, given its proximity to the secondary deposit and its LCT geochemical signature. Studies on tourmaline crystals from the "Marina" pegmatite were carried out to confirm the above hypothesis; specifically through the comparison of the compositional data obtained from such tourmaline crystals with those obtained from the detrital tourmalines of the Mavuco area. The same studies allowed obtain detailed information on the genesis of the dark prismatic overgrowths, which also characterize most of the detrital tourmalines.

CRYSTAL-CHEMICAL STUDY OF PEGMATITIC GEM TOURMALINE CRYSTALS FROM ELBA ISLAND (TYRRHENIAN SEA, ITALY)

Main results

Eleven tourmaline samples that represent the variety of color anomalies at the termination of Elba tourmalines were collected from different miarolitic cavities occurring in the area of San Piero and Sant'Ilario in Campo villages, within four selected pegmatitic veins distributed along the eastern border of the Monte Capanne pluton. Compositional data were collected with electron microprobe along a straight traverse parallel to the c-axis from the base to the termination of each crystal using an average

step size of 300 μm , except at the overgrowths, where the step size was reduced to about 150 μm to capture more fine-scale details. A total of 400 spot analyses were collected. Iron oxidation state was determined in selected Fe-rich overgrowths by Mössbauer spectroscopy. On the basis of the chemical data and color displayed, each sample was divided in compositionally similar zones. For each zone, atoms per formula unit (apfu) were calculated and the relative empirical formula has been determined.

It is interesting to point out that during this chemical characterization, a new mineral species of the tourmaline supergroup was discovered: celleriite, ideally $\square(\text{Mn}^{2+}_2\text{Al})\text{Al}_6(\text{Si}_6\text{O}_{18})(\text{BO}_3)_3(\text{OH})_3(\text{OH})$. It was found in the Rosina pegmatite (San Piero in Campo, Elba Island, Italy) and occurs as chemically homogeneous, millimetric to

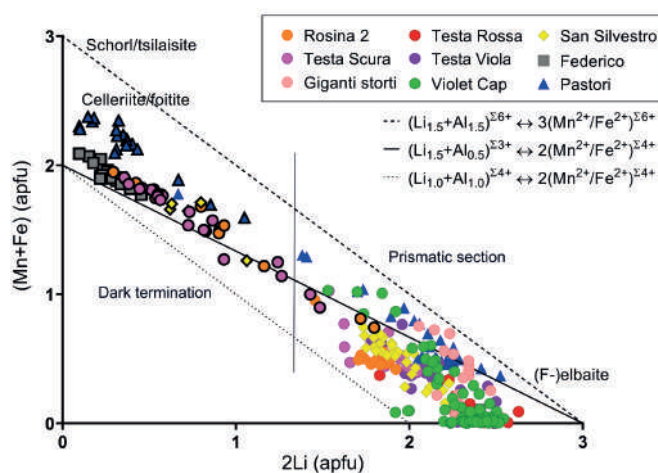


Figure 2 Plot of the content of 2Li vs. (Mn+Fe) at the Y site for each spot analysis of the tourmaline samples studied. The three lines (dashed, dotted and full) represent different degree of substitution. Symbols with black border indicate the compositions relative to the dark terminations of the different samples. For Pastori sample the Mg content was also considered. The vertical line distinguishes the compositions occurring at the crystal dark terminations (left) from those occurring in the prismatic sections (right).

sub-millimetric zones within the analogous pole of a zoned tourmaline crystal. This new mineral species was approved by the IMA-CNMNC, proposal n. 2019-089 (Bosi et al., 2022a).

In general, chemical analysis revealed that the termination of each crystal is characterized by a significant increase in Fe and/or Mn that is responsible for the color variation at the analogous pole. As expected, in the tourmaline crystals with the most significant Fe and/or Mn increase at the termination ($\text{MnO} > 5 \text{ wt\%}$ and $\text{FeO} > 2 \text{ wt\%}$), the color variation is more enhanced, and the species changes from initial elbaite/fluor-elbaite, to celleriite, foitite, or schorl (Fig. 2). Such increase in Fe/Mn suggests that a dramatic chemical variation in the crystallization environment, with a new supply in Fe/Mn during the latest stages of tourmaline growth, occurred. The increase in Fe and Mn is consistent with the substitution of Li and Al at the Y site of the tourmaline structure. However, this substitution can occur in different ways ac-

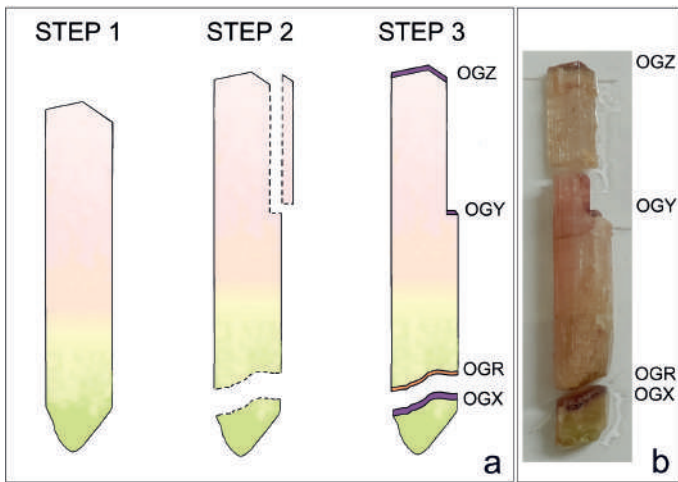


Figure 3 History of growth of the analysed tourmaline crystals. **a)** Schematic representation of the events that led to the collected samples. Step 1: tourmaline crystal growth from light green to pale pink in the direction of the analogous pole (c- side). Step 2: breakage of the crystal as a result of the pocket rupture event followed by changes in the chemical composition of the crystallisation environment. Step 3: generation of late-stage dark-coloured overgrowths at the analogous (OGZ, OGY, OGX) and at the antilogous (OGR) poles in a Mn-rich environment. **b)** Image of the tourmaline crystals analysed.

cording to whether Fe and Mn totally or partially replace Li and Al. In the crystals from Elba, a partial substitution occurred at Y, according to the simplified mechanism $(1.5\text{Li}^+ + 0.5\text{Al}^{3+}) \leftrightarrow 2(\text{Mn}^{2+}, \text{Fe}^{2+})$. As this substitution determines a total charge variation, it needs to be balanced by a cation vacancy (\square) replacing Na at the X site: $\text{Na}^+ + (1.5\text{Li} + 0.5\text{Al})^{3+} \leftrightarrow \square + 2(\text{Mn}, \text{Fe})^{2+}$.

Results obtained, along with structural and paragenetic observation of the cavities in which the tourmaline samples were collected, provide evidence that the formation of the observed dark overgrowths is the result of an opening of the geochemical system ascribable to an event of pocket rupture. This event is further supported by the crystal-chemical features of an elbaitic multicolored tourmaline crystal, found in a wide miarolitic cavity naturally broken in two fragments and characterized by Mn-rich dark overgrowths, respectively purplish-red at the analogous pole and yellow-orange at the antilogous pole (Altieri et al., 2023). Based on the results obtained from this peculiar tourmaline crystal, the pocket rupture was responsible for its breakage, allowing for the formation of new growth surfaces in the direction of the analogous and the antilogous pole (Fig. 3).

Consequently, this crystal represents a key witness of the pocket rupture event registering not only the compositional variations of the geochemical system through the formation of Mn-rich overgrowths, but also the mechanical events that led to the crystal breakage, thus allowing for the formation of an unusual overgrowth at the antilogous pole. In the same study, a comparison of the overgrowths at the analogous and antilogous poles provides evidence of a preferential incorporation of elements at growth surfaces. Beside the preferential uptake of Ca, F and Ti at the antilogous pole, already described in literature (e.g., Henry & Dutrow, 1992; van Hinsberg

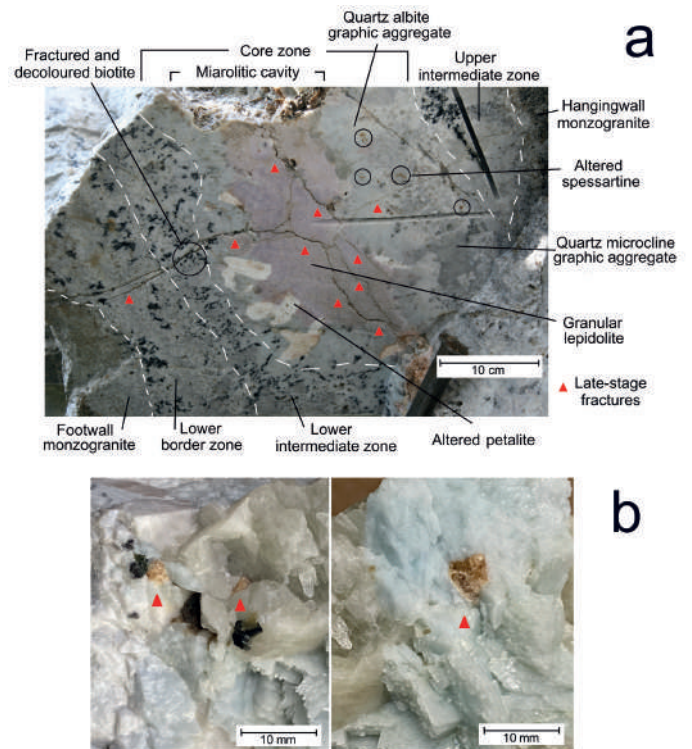


Figure 4 a) E-W section of the Rosina pegmatite (about 60 cm in thickness), with label for the different textures and mineralogical zonation. Altered cavity-lining minerals as well as late-stage fractures (red arrows) are also evidenced. Scale bar = 10 cm. **b)** Examples of heavily fractured and partially corroded spessartine crystals (red arrows) frozen in quartz and feldspars in proximity of cavities of the Rosina pegmatite. Crystals up to 6 mm in diameter. Scale bar = 10 mm.

et al., 2006), we report for the first time a further preference at level of the ionic charge of the same element. In fact, OAS data show a selective uptake of Mn^{2+} at the antilogous pole, even in the presence of a considerable amount of Mn^{3+} , which preferred the analogous one. This uneven uptake of Mn ions resulted in the yellow-orange coloration of the antilogous overgrowth (Mn^{2+} dependent) rather than the purple-reddish color of the analogous overgrowths (Mn^{3+} dependent; Altieri et al., 2023).

Overall data obtained, as well as structural and paragenetic observations of the cavities in which the studied tourmaline crystals were collected, allowed to clearly correlate structural information (i.e., fracturing of the pocket and breakage of tourmaline crystals) to the late-stage tourmaline growth, and thus permitting definition a genetic model for the dark overgrowths in Elba tourmaline crystals. A pocket rupture event, probably related to thermal contraction during the cooling of the rock, led to mechanical brittle deformations of the enclosing pegmatite through the formation of late-stage fractures (Fig. 4a). This situation allowed the highly reactive late-stage cavity fluids to permeate the fractures surrounding the cavity where the early-crystallized Fe- and Mn-rich cavity-lining minerals were formed. Then, the hydrothermal alteration of such minerals through leaching and corrosion processes by the late-stage cavity fluids, led to the release of Fe and Mn in the system, thus causing a sudden change in the chemical composition of the pocket environment. These processes are supported by the oc-

currence of fractured and altered biotite crystals, as well as corroded spessartine garnet in the intermediate and lower border zone of the pegmatites (Fig. 4b).

Based on the size of the cavity, the extent of the fracturing phenomena and the consequent leaching processes, as well as the relative abundance of different primitive minerals in the enclosing pegmatite, the chemical composition of the residual cavity fluids underwent a variation in concentration in Fe and Mn. This can result in a simple color change up to a chemical evolution from an initial elbaite/F-elbaite composition to foitite, cellerite or schorl at the termination of the tourmaline crystals.

For instance, in the case of the “blue-cap” tourmalines, found in small pockets ($\sim 10 \text{ dm}^3$) within the San Silvestro and the Fucili veins (San Piero in Campo locality), compositional analyses revealed that the blue coloration of these crystals is exclusively related to a slight enrichment in Fe^{2+} . In addition, the presence of Fe only in the divalent state, suggests persisting reducing conditions in the pocket environment. This interpretation is consistent with a partial opening of the cavity system associated to minor fracturing phenomena, which led to a limited leaching of biotite crystals in the enclosing pegmatite (Altieri et al., 2022).

In other cavities, more extensive fracturing phenomena associated with the presence of abundant Fe/Mn-rich primitive minerals in the enclosing pegmatite, allowed the release of high amounts of Fe/Mn to the residual cavity fluids. In these conditions, a chemical evolution at the analogous termination of the tourmaline crystal occurred. Depending on the prevalence of Mn or Fe, the overgrowth can result in cellerite, $\square(\text{Mn}^{2+}_2\text{Al})\text{Al}_6(\text{Si}_6\text{O}_{18})(\text{BO}_3)_3(\text{OH})_3(\text{OH})$, foitite, $\square(\text{Fe}^{2+}_2\text{Al})\text{Al}_6(\text{Si}_6\text{O}_{18})(\text{BO}_3)_3(\text{OH})_3(\text{OH})$ or schorl, $\text{NaFe}^{2+}_3\text{Al}_6(\text{Si}_6\text{O}_{18})(\text{BO}_3)_3(\text{OH})_3(\text{OH})$ compositions.

A similar scenario occurred in a wide miarolitic cavity ($\sim 80 \text{ dm}^3$) of the Rosina pegmatite where a peculiar tourmaline crystal, found naturally broken in two fragments and characterized by late-stage Mn-rich overgrowths at both analogous and antilogous poles, was collected. In this case, a partial pocket collapse occurred, which caused an intense leaching of the primitive Mn-rich minerals in enclosing pegmatite. Although the Mn increase at the overgrowths is confirming a significant chemical evolution (MnO up to 7 wt%), the mineralogical species remain elbaite/F-elbaite, due to the lower presence of spessartine garnet in the enclosing pegmatite. This scenario was also responsible for the crystal to break, with the consequent formation of dark-colored overgrowths of purple-reddish color at the analogous poles (Mn^{3+} dependent), and yellow-orange at the antilogous ones (Mn^{2+} dependent). The presence of Mn in both +3 and +2 redox states suggests relatively oxidizing conditions during overgrowths formation (Altieri et al., 2023).

COMPOSITIONAL AND SPECTROSCOPIC CHARACTERIZATION OF GEM-QUALITY TOURMALINES FROM THE ALTO LIGONHA PEGMATITE DISTRICT (MAVUCO AREA, NE MOZAMBIQUE)

Main results

Sixteen tourmaline grains collected from the secondary deposit of Mavuco in the Alto Ligonha pegmatite district were studied. The samples collected were found as waterworn grains with a sub-angular to sub-rounded shape and most of them show a dark-colored prismatic overgrowth that surrounds completely, or in part, a multicolored core ranging from blue, green, yellow to purple-red, even within the same crystal (Fig. 5a). Compositional data were collected with electron microprobe along a straight traverse perpendicular to the c-axis with an average step size of $300 \mu\text{m}$ for a total of 501 spot analyses. To gain information on the mechanisms underlying the color displayed by the core regions of the tourmaline grains, OAS analyses in the UV-Vis region were performed on selected samples with particular chromatic features. The in-depth study on these tourmaline grains allowed a detailed characterization of their chemical composition, which was correlated to the color displayed.

Chemical data indicate that all studied samples are characterized by a CuO content that never exceeds 1 wt%. Despite the moderate concentration, Cu is able to contribute as color-causing agent especially in those core zones where its value approaches 1 wt%. Furthermore, EMP data revealed that most of the detrital tourmalines are of F-elbaite composition (Fig. 5b). This is the evidence that the tourmalines from the secondary deposit of Mavuco do not belong only to elbaite species, as assumed in previous studies (e.g., Laurs et al., 2008), but also to different species, including fluor-liddicoatite. A correlation study between chemical composition and color displayed by the studied tourmaline samples, allowed identifying the gemological variety to which the core zone of these grains belong. Specifically, in the secondary deposit of Mavuco, tourmalines belonging to indicolite, canary tourmaline, Paraíba-type and “Cu-bearing rubellite” varieties were identified.

Compositional analysis was extended to two tourmaline crystals from the “Marina” granitic pegmatite (MAV 21 and MAV 22 samples).

The presence of Cu in MAV 21 sample, which amount is comparable with that of the detrital tourmalines, supports the hypothesis that the “Marina” pegmatite represents a source from which the tourmaline grains of the Mavuco area were originated. Thus, the “Marina” pegmatite can be considered a primary deposit for Cu-bearing (Paraíba-type) tourmalines and its further exploration can be economically advantageous.

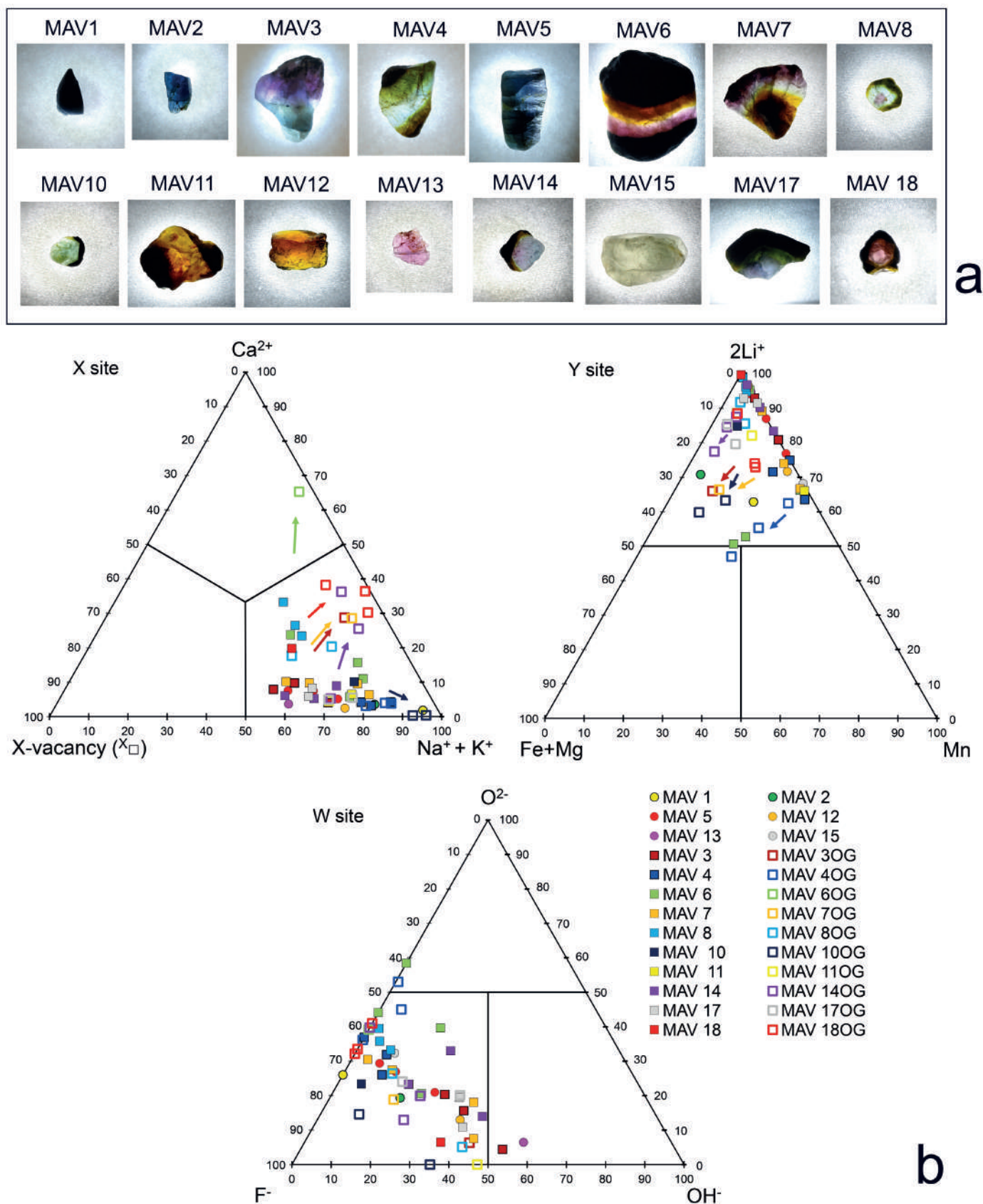


Figure 5 a) The tourmaline grains analyzed for this study. b) Compositional diagrams based on the X-, Y- and W-site occupancy determined by EMPA. Each point represents the result in apfu of the core and overgrowth zones analyzed. Arrows highlight the compositional evolution trend from the core zone to the overgrowth observed in some of the analyzed tourmaline grains.

The MAV 22 sample is characterized by a thick (up to 4 mm) black late-stage overgrowth developed all over the tourmaline surfaces, from the analogous to the antilogous pole, including the prism faces, which chemical and morphological features are similar to those obser-

ved in most of the detrital tourmalines from the secondary deposit of Mavuco (Fig. 6).

The presence of such an extended overgrowth further strengthen the hypothesis that “Marina” pegmatite is a primary source of the detrital tourmalines in the Mavuco area. Structural and paragenetic observations of the giant

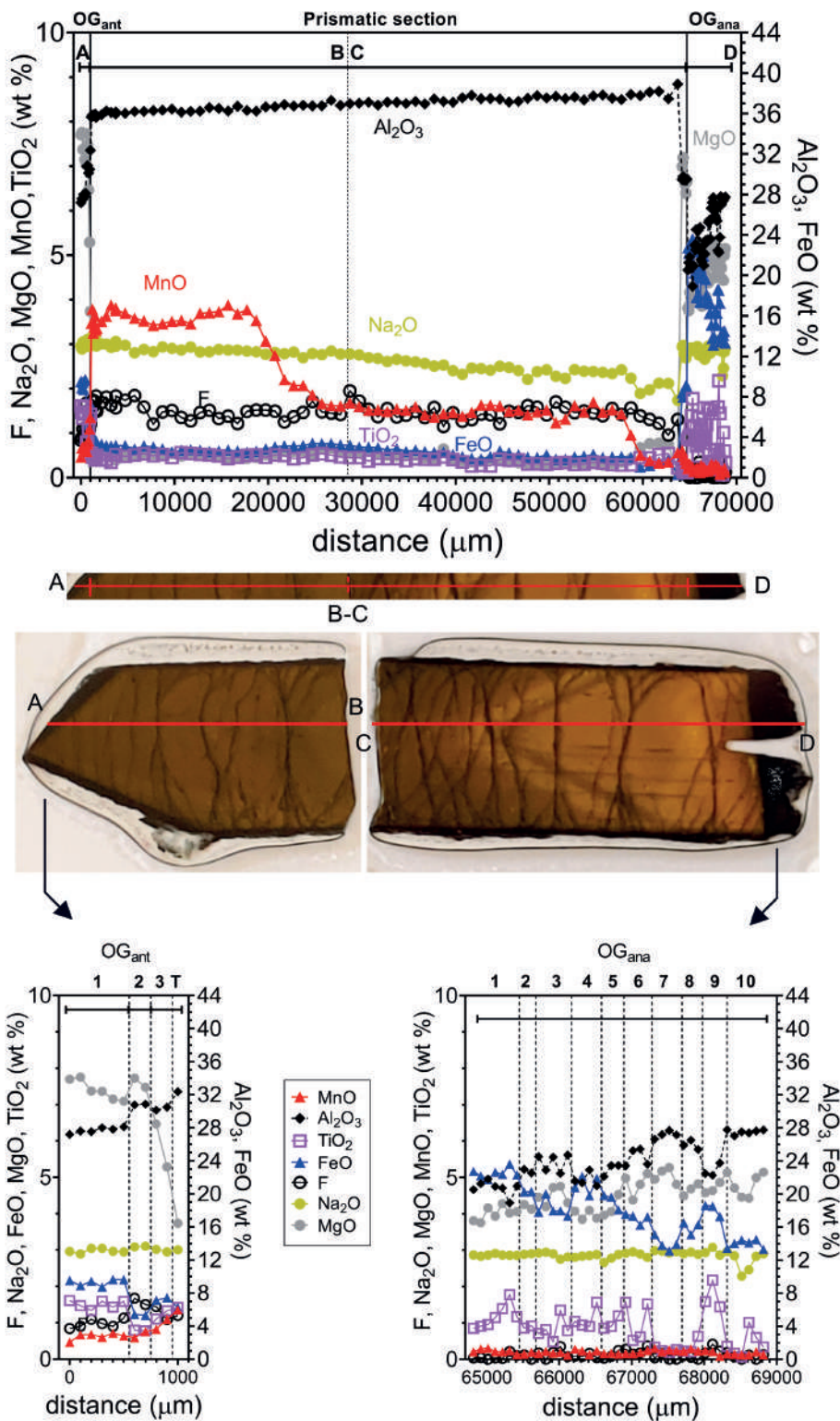


Figure 6 Upper panel: EMP analysis of the MAV 22 sample along a straight traverse parallel to the *c*-axis (only selected oxides are reported). Lower panel: close-up of the chemical composition of antilogs (OG_{ant}) and analogous (OG_{ana}) overgrowths in the MAV 22 sample (only selected oxides are reported).

cavity in which the MAV 22 sample was collected (about 12 m in size), provide evidences that the change in the chemical composition of the crystallization environment was related to an intense and widespread fracturing of the cavity, which culminated with the subsequent collapse of the pocket roof. In this scenario, the propagation of the fracturing phenomenon caused the collapse of the amphibolitic host rock, which reacted with the residual cavity fluids, thus releasing large amounts of Fe and Mg in the system (FeO up to 24 wt% and MgO up to 8 wt%). This condition, associated with a long lasting late-stage tourmaline crystallization ensured by B, which must be still present in the residual fluids of the cavity, allowed

for the development of a thick late-stage black overgrowth covering all over the crystal surfaces, including the prismatic faces and the steep pyramidal faces at the antilogs pole, which characterize the MAV 22 sample. In this case, the pocket collapse was associated to oxidizing conditions as supported by the high Fe³⁺/Fe_{tot} ratio (> 0.50) observed at the analogous termination of MAV 22 sample. Moreover, the great availability of Fe and Mg in the system (FeO up to 24 wt% and MgO up to 8 wt%), allowed for a chemical evolution from an initial F-elbaitite composition to a new Fe³⁺-dominant species at the analogous overgrowth. Infact, chemical, spectroscopic and crystal-structure refinement resulted in a new mine-

ral species of the tourmaline supergroup, ferro-bosiite, ideally $\text{NaFe}^{3+}_3(\text{Al}_4\text{Fe}^{2+}_2)(\text{Si}_6\text{O}_{18})(\text{BO}_3)_3(\text{OH})_3\text{O}$, recently approved by the IMA-CNMNC (proposal n. 2022-069) (Bosi et al., 2022b).

CONCLUSIONS

On the basis of results obtained from the chemical characterization of the detrital tourmalines from the Mavuco area, including those from the MAV 22 sample, as well as structural and paragenetic information of the cavity in which the MAV 22 sample was collected, it has been possible to extend the genetic model defined for Elba tourmalines to the prismatic overgrowths observed in the tourmaline crystals from the Alto Ligonha pegmatite district with some differences.

- 1) The size of the cavities. A larger size of the cavities, combined with extensive fracturing phenomena, may have played a key role in the formation of the prismatic overgrowths in the tourmaline crystals of the Alto Ligonha pegmatite district. In fact, a broader fracturing surface may allow more extensive alteration and corrosion phenomena of the primitive minerals in the enclosing pegmatite by the late-stage fluids of cavity, leading to the formation of dark-colored overgrowths not only at the crystal termination, but also along the prismatic faces;
- 2) Typology of primitive minerals in the enclosing pegmatite. While biotite is the main Fe/Mg supplier in Elba pegmatitic system, biotite and especially ferromagnesian amphiboles are accounted for Fe/Mg supply in the petrogenetic systems of the Alto Ligonha district. In fact, the dramatic destabilizing event that characterizes the cavity in which the MAV 22 sample has been collected, allowed the cavity-fluids to react with the collapsed amphibolitic host rock, with the consequent release of greater amounts of Fe and Mg in the system.

Concerning the Mn availability, in the petrogenetic system of Elba Island, spessartine garnet is responsible for both depletion and release of Mn in the crystallization environment, being the main regulator of Mn levels during the evolution of the pegmatitic system. This is consistent with the low content in Mn recorded in the early-stages of tourmaline crystallization, because of the high degree of Mn incorporation in spessartine garnet. On the other hand, spessartine etching results in high availability of Mn in the pocket environment, with the consequent formation of unusual Mn-rich dark-colored overgrowths. In contrast, in the petrogenetic system of the Alto Ligonha, the scarce presence of spessartine garnet in the secondary deposit of Mavuco suggests that the main regulator of Mn levels during crystallization of tourmaline is apatite. However, apatite is a fairly-competitive mineral for Mn respect to spessartine. This can explain the higher content in Mn recorded in the core

zones of the analyzed detrital tourmalines and the lower increase at the overgrowth right after the pocket rupture event. Also, the presence of apatite in the host rock can explain the release of Ca during the cavity opening, as observed in some overgrowths.

The results obtained in this Ph.D research allowed to define and validate a model for the genesis of the dark-colored overgrowths in pegmatitic gem- tourmaline crystals from Elba Island. This model has been applied to the prismatic overgrowths of the tourmaline crystals from the Alto Ligonha pegmatite district, and can be further extended to explain the late-stage color and composition anomalies of gem-tourmaline crystals in many other gem-pegmatite deposits in the world.

REFERENCES

- Altieri, A., Pezzotta, F., Skogby, H., Hålenius, U. & Bosi, F. (2022): Blue-growth zones caused by Fe^{2+} in tourmaline crystals from the San Piero in Campo gem-bearing pegmatites, Elba Island, Italy. *Mineral. Mag.*, **86**, 910-919.
- Altieri, A., Pezzotta, F., Skogby, H., Hålenius, U. & Bosi, F. (2023): Dark-coloured Mn-rich overgrowths in an elbaitic tourmaline crystal from the Rosina pegmatite, San Piero in Campo, Elba Island, Italy: witness of late-stage opening of the geochemical system. *Mineral. Mag.*, **87**, 130-142.
- Bosi, F., Pezzotta, F., Altieri, A., Andreozzi, G.B., Ballirano, P., Tempesta, G., Cempírek, J., Škoda, R., Filip, J., Čopjaková, R., Novák, M., Kampf, A.R., Scribner, E. D., Groat, L.A. & Evans, R.J. (2022a): Celleriite, $\square(\text{Mn}^{2+}_2\text{Al})\text{Al}_6(\text{Si}_6\text{O}_{18})(\text{BO}_3)_3(\text{OH})_3(\text{OH})$, a new mineral species of the tourmaline supergroup. *Am. Mineral.*, **107**, 31-42.
- Bosi, F., Altieri, A., Skogby, H., Pezzotta, F., Hålenius, U., Tempesta, G., Ballirano, P., Flégr, T. & Cempírek, J. (2022b): Ferro-bosiite, IMA 2022-069. CNMNC Newsletter No. 70, December 2022. *Eur. J. Mineral.*, **34**, 591-601, 2022.
- Henry, D.J. & Dutrow, B.L. (1992): Tourmaline in a low grade clastic metasedimentary rocks: an example of the petrogenetic potential of tourmaline. *Contrib. Mineral.*, **112**, 203-218.
- Lauris, B.M., Zwaan, J.C., Breeding, C.M., Simmons, W.B., Beaton, D., Rijdsdijk, K.F., Befi, R. & Falster, A.U. (2008): Copper-bearing (Paraiba-type) tourmaline from Mozambique. *Gems. Gemol.*, **44**, 4-30.
- Pezzotta, F. (2021): A history of tourmaline from the Island of Elba. *Mineral. Rec.*, **52**, 669-720.
- van Hinsberg, V.J., Schumacher, J.C., Kearns, S., Mason, P.R.D. & Franz, G. (2006): Hourglass sector zoning in metamorphic tourmaline and resultant major and trace-element fractionation. *Am. Mineral.*, **91**, 717-728.

Advanced mineralogical and crystallographical techniques for understanding transformation processes in natural materials and their synthetic analogous

Comparison between natural combustion pyrometamorphism and the synthetic analogous process of cement manufacture

Marco Cantaluppi

Dipartimento di Scienze della Terra "Ardito Desio", Università degli Studi di Milano, Via Botticelli 23, 20133, Milano, Italia

DOI:10.19276/plinius.2023.01.002

INTRODUCTION

Pyrometamorphism is a distinctive type of thermal metamorphism characterized by a wide temperature range and Low-Pressure (LP) conditions, typically occurring at shallower depths compared to regional metamorphism (less than 3-4 km; Bucher & Grapes, 2011).

Combustion Pyrometamorphism (CP) is a complex geological process involving sedimentary sequences and occurs in two stages: (i) 1st stage consists of extreme high-temperature and low-pressure conditions resulting from the self-ignition of coal seams or the rise of methane-rich gases from deep reservoirs along fractures; (ii) 2nd stage involves low-temperature and low-pressure conditions, characterized by the weathering of previously combusted rocks. CP primarily affects lacustrine sequences (clay-rich protoliths, sandstone, and lacustrine sediments) rather than marine sequences (limestone and marls), which can be attributed to the higher weathering resistance of the former CP protoliths (Grapes, 2010). The mineral assemblages in pyrometamorphosed rocks typically fall within the sanidinite and hornfels facies, indicating the high-temperature and low-pressure conditions (Bucher & Grapes, 2011). Additionally, various high-temperature minerals (such as cordierite, mullite, sapphirine, merwinite, and rankinite), including metastable ones (like larnite, hatrurite, brownmillerite, mayenite, and ye'elimite), are found in both pyrometamorphosed rocks and industrial materials (such as metal slags, ceramics, and cements). Therefore, pyrometamorphosed rocks can be considered as natural analogs of certain human-made materials (Sokol et al., 2014; Vapnik et al., 2007).

CP is an understudied geological process within the uncommon field of petrological experiments (i.e., HT and LP involving limestone). The scarcity of geological information and the relative rarity of CP further complicate the understanding of the processes occurring during CP, particularly in the case of limestone protoliths.

This study focuses on the Hatrurim Basin in Israel, which is the most significant and extensive location where

well-preserved CP rocks and their limestone protoliths are exposed, enabling the observation of geological features and collection of rock samples. Investigating CP rocks and the overall pyrometamorphism process is valuable for both geological purposes (providing deeper insights into microstructure development and stability fields of mineral assemblages under HT and LP) and industrial applications (enhancing production processes and properties of final products).

GEOLOGICAL FRAMEWORK AND FIELD TRIP

Hatrurim Basin is located in the northern part of the African Plate inside Sinai Microplate (Freund, 1965), representing the southern shelf of Tethys paleo-ocean before the collision with Eurasian Plate (Novikov et al., 2013). The sedimentary sequence is featured by carbonate sediments interrupted by sedimentation breaks and unconformities, later deformed during Late Cretaceous. Tectonic activity led the deposition of phosphorite beds (Mishash Formation) later covered by limestone and marls (Ghareb and Taqiye Fm.) inside synclines; whereas, mainly chalky rocks were formed in anticlines (Novikov et al., 2013). A sea regression and uplifting produced clastic sediments deposition, mainly conglomerates (Hazeva Formation), from Eocene to Oligocene. An intense faulting occurred from Late Oligocene due to the opening of Levantine Transform Fault (Novikov et al., 2013). Hatrurim Basin is a rectangular shaped area (40 km²) closely located to Dead Sea in which a sedimentary sequence aged from Late Cretaceous to Paleocene undergone in CP ~ 5 Ma forming a CP sequence up to 190 m from the surface. Hatrurim Basin falls inside a syncline with several minor structures related to the Syrian Arc fold system (Burg et al., 1991; Hirsch & Burg, 2008). CP rocks were formed by means of methane-rich gases combustion coming from deep hydrocarbon reservoirs found in several nearest locations (Sokol et al., 2019, 2007): the combustion occurred at foci reaching HT (1100-1450°C) close to the surface; whereas, LT were reached at greater

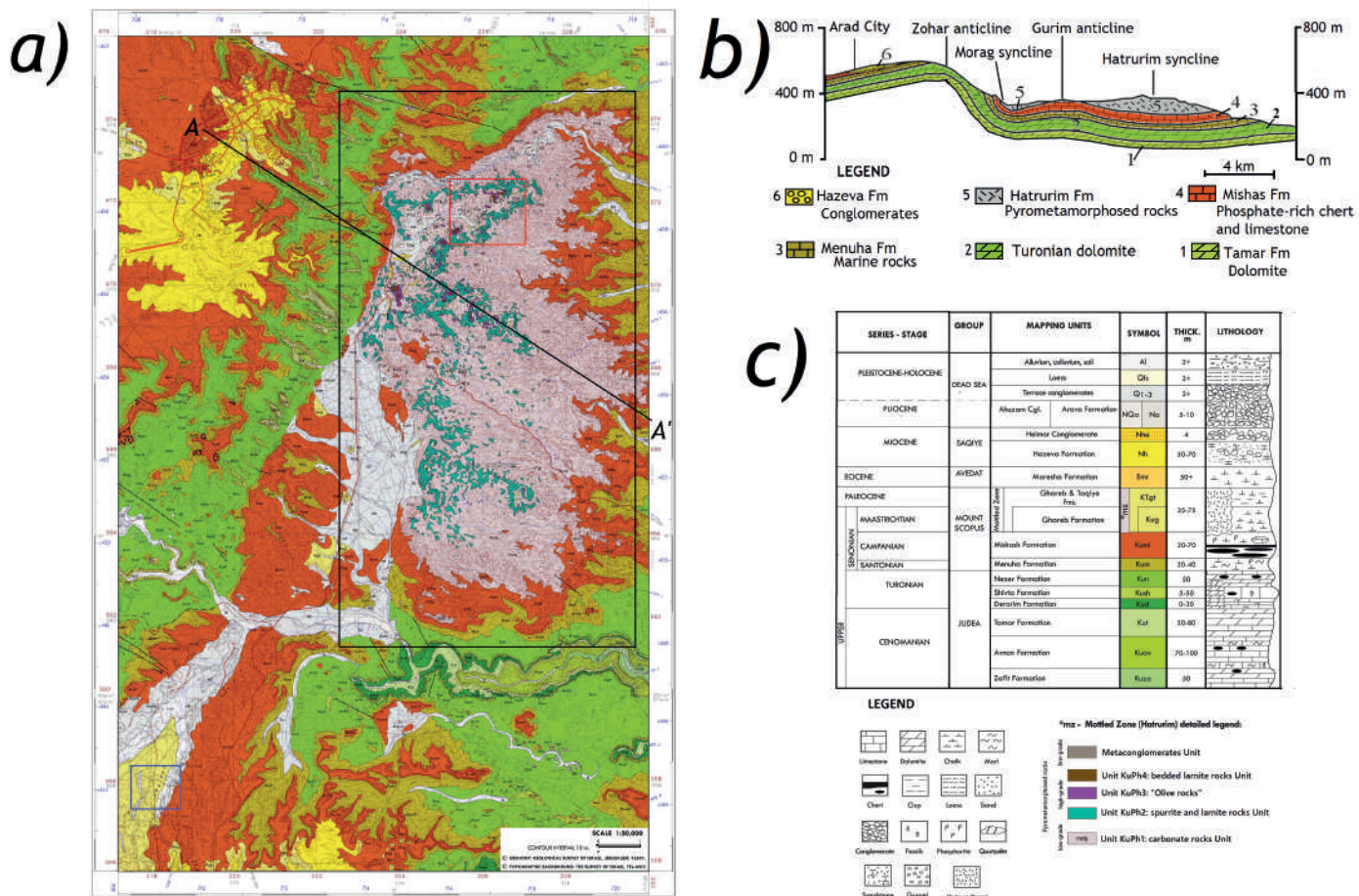


Figure 1 a) Geological map (1:50'000 scale) of Arad, reporting in grey (retrograde CP rocks), cyan, purple and brown (prograde HT CP rocks), black, blue and red squares represent Hatrurim Basin, Rotem Amfort Mine and Larnite-Rocks sampling areas, respectively (Hirsch & Burg, 2008); b) geological section passing through Hatrurim Basin area (Novikov et al., 2013b); c) Legend of geological map (Hirsch & Burg, 2008).

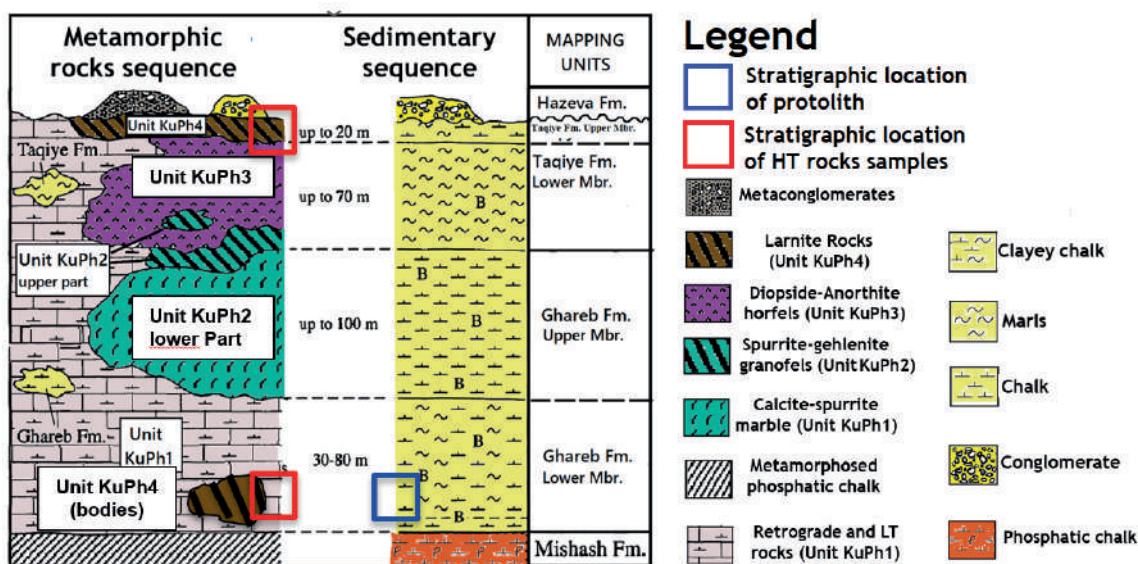


Figure 2 Stratigraphic section of combusted pyrometamorphosed sequence and sedimentary one on left and right respectively (modified from (Burg et al., 1991); red and blue squares highlight the stratigraphic position of sampled HT and sedimentary rocks, respectively).

depths, due to the limited oxygen availability for combustion (Grapes, 2010). The CP sequence is featured by an upward increase of metamorphic grade; however LT and retrograde rocks occur in all parts of the metamorphic sequence. The geological field trip focused on studying CP features and collecting rock samples in the northern part of Hatrurim Basin where the CP sequence is well preserved and exposed along with the sedimentary one (Fig. 1). Highest metamorphic grade rocks were found at top and bottom sequence, representing meta-

morphosed impure limestone (Ghareb and Taqiye Fm.) which are classified as ye'elimite-larnite granofels (also called Larnite Rocks): ye'elimite-larnite granofels rocks are fine and dense rocks always crisscrossed by later hydration veins. Larnite Rocks protolith was sampled from fresh excavation front inside Rotem Amfort Mine close to eastern Hatrurim Basin (Fig. 2): Ghareb Formation rocks were classified as calcimudstone rich in phosphatic pellets and gypsum, very porous and soft.

MATERIALS

Ye'elimite-larnite granofels both anhydrous and hydrated ones collected at the top and bottom of the CP sequence in Hatrurim Basin area were deeply studied by means of conventional and innovative analytical techniques.

Gypsum-apatite-rich calcimudstone (impure limestone) belonging to Ghareb Formation collected inside Rotem Amfort Mine (Israel), close to the western part of Hatrurim Basin, was studied obtaining microstructural, mineralogical and crystallographical features. Furthermore, this impure limestone was used as starting raw meal for preparing new green-cements doped with SO_3 , F and P_2O_5 .

An industrial fine mixture based on limestone, clays, kaolinite, hematite, and quartz was used as starting raw meal for preparing Belite Cement at laboratory scale.

Sample / Oxide (wt%)	Larnite Rocks	Ghareb Fm.	F-BC raw meal
CaO	56 - 53	47.1 [68.4]	38.5 [57.5]
SiO_2	23 - 25	11.8 [17.1]	14.9 [23.2]
Al_2O_3	9 - 10	3.3 [4.9]	5.3 [7.4]
Fe_2O_3	3 - 4	2.5 [3.6]	3.7 [5.5]
MgO	1 - 2	0.2 [0.3]	0.6 [0.9]
SO_3	1 - 4	1.9 [2.7]	2.1 [3.3]
P_2O_5	1 - 3	1.8 [2.5]	0.1 [0.2]
LOI	1 - 3	31.5	34.8
Tot.	99 - 101	100.4	100.6

Table 1 X-ray Fluorescence (XRF) of studied materials; esd is lower than 1 wt%; inside square brackets is reported the wt% value normalized to Tot.-LOI.

METHODS

A multidisciplinary approach based on conventional and innovative techniques was strictly necessary in order to handle the high complexity of studied materials (i.e., low amount of crystal phases, low crystal size, numerous polymorphs and polymorphic transitions during heating), especially for natural ones.

X-Ray Fluorescence (XRF), Reflected and Transmitted Light Microscopy (RLM & TLM), Scanning Electron Microprobe and Electron Microprobe microAnalyser (SEM/EMPA), Laboratory X-Ray Powder Diffraction (LXRPD) and Single Crystal X-Ray Diffraction (SC-XRD) were used as conventional techniques obtaining relevant information for microstructural, crystallographic, mineralogical and chemical information.

Whereas, Synchrotron X-Ray Powder Diffraction with in-situ High Temperature and ex-situ experiments (in-situ HT and ex-situ SXPDP), Neutron Diffraction (NXRD), Single Crystal Synchrotron X-Ray Diffraction (SC-SXRD)

and Computed MicroTomography with in-situ High Temperature and ex-situ experiments (in-situ HT and ex-situ μ -CT) were used to gain relevant microstructural and mineralogical changes occurring during heating and overcoming limitations of ordinary techniques.

HT and LP experiments were performed at laboratory scale to synthesize Belite Cement and S-P-F-doped Cement using industrial raw meal and Ghareb Fm., respectively. A laboratory oven with SiC resistors was used for HT experiments up to 1350°C with an increasing rate of 2°C/min and slow cooling.

Furthermore, Isothermal Calorimetric Analysis (ICA), Thermal Gravimetric Analysis associated with Differential Scanning Calorimetry (TGA-DSC) and Specific Surface Analysis (SSA) were used during hydration study.

RESULTS

Results were presented in four sections considering (i) the study of Larnite Rocks (i.e., natural cement) sampled in Hatrurim Basin (see section 5.1), (ii) investigation and synthesis of S-P-F-doped Cement using Ghareb Fm. rocks (see section 5.2), (iii) synthesis of Belite Cement at laboratory scale (see section 5.3) and (iv) hydration experiments between synthetic Belite Cement and natural Larnite Rocks (see section 5.4).

Ye'elimite-larnite granofels investigations

Ye'elimite-larnite granofels were collected at bottom and top of Hatrurim Basin, highlighting similar features:



Figure 3 Irregular metric outcrops of Larnite Rocks at the bottom of CP sequence in Hatrurim Basin, surrounded by retrograde LT rocks.

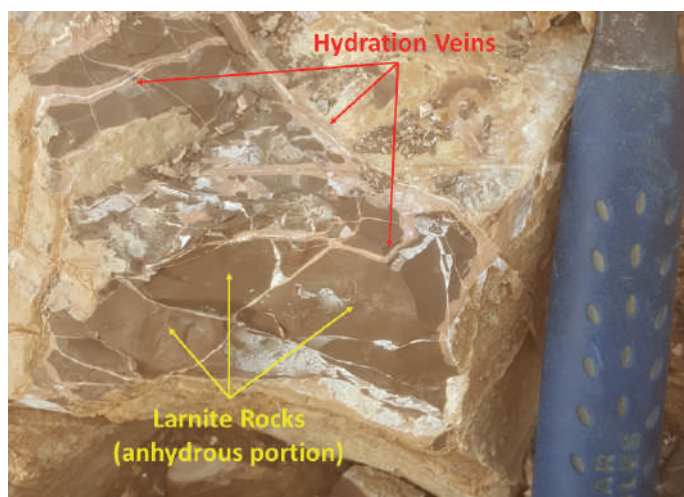


Figure 4 Larnite Rocks outcrop highlighting a fine microtexture and anhydrous dark brown portions crisscrossed by internally structured hydration veins.

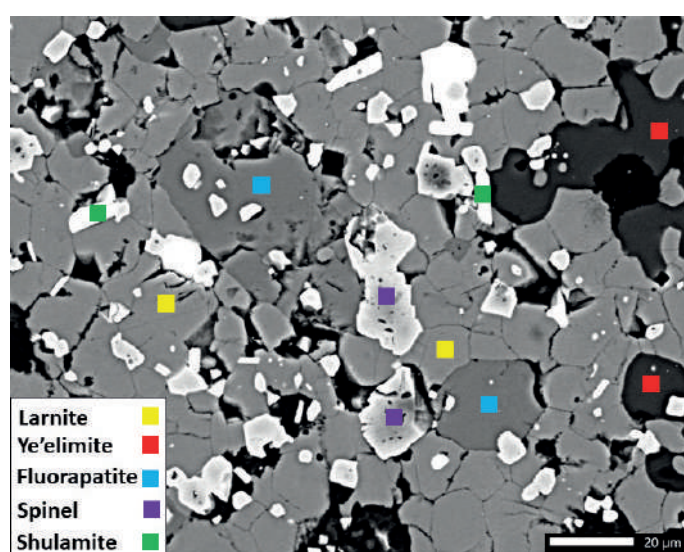


Figure 5 SEM of Larnite Rocks revealing the fine microtexture based on polygonal larnite (medium grey, yellow square), anhedral ye'elimite (dark grey, red square), subhedral spinel (light grey, purple square), prismatic shulamite (white, green square) and euhedral peciloblastic fluorapatite (darker medium grey, light blue square).

dark brown to black rocks with fine microtexture, dense and hard to brake rocks (Figs.3,4). Mineral assemblage is always based on larnite (Larn, β - Ca_2SiO_4) and ye'elimite (Yel, $\text{Ca}_4\text{Al}_6\text{SO}_{16}$) as major phases, and shulamitite (Shul, $\text{Ca}_3\text{Ti}(\text{Al},\text{Fe})_2\text{O}_8$), fluorapatite-ellestadite (Fap-ell, $\text{Ca}_5(\text{P}_{1-x}\text{S}_{x/2}\text{Si}_{x/2})\text{F}$) and spinel (Spin, $\text{Mg}(\text{Al},\text{Fe})_2\text{O}_4$) as minor ones; whereas differences among samples are related on ye'elimite abundance and trace phase occurrence such as brownmillerite (Brw, $\text{Ca}_2(\text{Al},\text{Fe})_2\text{O}_5$), ternesite (Tern, $\text{Ca}_5(\text{SiO}_4)_2(\text{SO}_5)$) and mayenite (May, $\text{Ca}_{12}\text{Al}_{14}\text{O}_{33}$). Microtextural investigations showed high density and low porosity of samples, revealing larnite as main mineral with polygonal shape (i.e., granoblastic texture), anhedral ye'elimite, prismatic shulamitite and peciloblastic euhedral fluorapatite crystals (Fig. 5).

Ye'elimite-larnite granofels are always crisscrossed by later hydration veins that often reveal an internal structural made of a white core and brown rims: white core is mainly composed of calcium carbonate polymorphs

(calcite, aragonite and vaterite) and minor gypsum ($\text{CaSO}_4 \cdot 2\text{H}_2\text{O}$) ettringite (Etrr, $\text{Ca}_5\text{Al}_{12}(\text{OH})_{12}(\text{SO}_4)_3 \cdot 26\text{H}_2\text{O}$) and tobermorite (Tob, $\text{Ca}_5\text{H}_2\text{Si}_5\text{O}_{18} \cdot 4\text{H}_2\text{O}$); whereas, brown rims are composed of low water reactive phases (Shul, Spin and Fap-ell), calcium carbonates, Ca-Si-H phases, hydrogarnet (Hydrg, $\text{Ca}_3\text{Al}_2(\text{OH})_{12}$) and aluminium hydroxides (i.e, gibbsite, nordstrandite and bayerite).

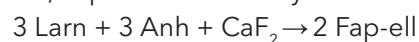
Ghareb Formation HT experiments (S-P-F-doped Cements)

Ghareb Fm. samples were collected at Rotem Amfort Mine (Fig. 2a) and were classified as calcimudstone rich in gypsum and apatite as fish bone fragments and phosphatic pellets (Lewy, 1990; Schneider-Mor et al., 2012). The selection of Ghareb Fm. as starting raw material for synthesizing new green-cements was based on the following reasons: (i) Ghareb Fm. represents a voluminous waste generated from the operations of the Rotem Amfort Mine (Israel), allowing the chance of waste management as alternative raw material promoting Circular Economy; (ii) Ghareb Fm. possesses a high concentration of dopant elements (P, S and F) which are common in several different wastes (phosphogypsum, bottom and fly ashes) that can even boost clinkering reactions (calcium silicate phases formation at HT) if are used as alternative raw materials (Kurdowski, 2014); (iii) Ghareb Fm., along with Taqiye Fm., represents the protolith of ye'elimite-larnite rocks, allowing for the reconstruction of the transformation processes (i.e., metamorphic reactions, microstructural changes, polymorphic transitions and melting) during CP by means of HT laboratory experiments.

Despite Ghareb Fm. samples showed a homogeneous and fine microtexture, three different inhomogeneities locally occurred at larger observation scale: (a) millimetric black, soft and porous nodules composed of calcite, goethite ($\text{FeO}(\text{OH})$), quenstedtite ($\text{Fe}_2(\text{SO}_4)_3 \cdot 11\text{H}_2\text{O}$), bernalite ($\text{Fe}(\text{OH})_3 \cdot 0.25\text{H}_2\text{O}$), titanite (CaTiSiO_5) and minor clays; (b) millimetric gypsum-rich veins (> 90 wt%) with decimetric lateral continuity showing no preferred orientation; (c) submillimetric goethite-rich layers with decimetric later continuity revealing no preferred orientation.

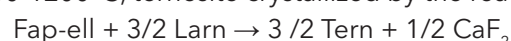
HT experiments and in-situ HT SXRPD on Ghareb Fm. powders highlighted microstructural, metamorphic reactions, polymorphic transition, crystal phase assemblage changes occurring upon heating of impure limestone. Ghareb Fm. powders (i.e., S-P-F-rich impure limestone) were heated up to 1350°C revealing four main features occurring at different temperatures:

(i) 800-1000°C, Fap-ell increased by the reaction



which leads larnite consumption;

(ii) 1000-1200°C, ternesite crystallized by the reaction:



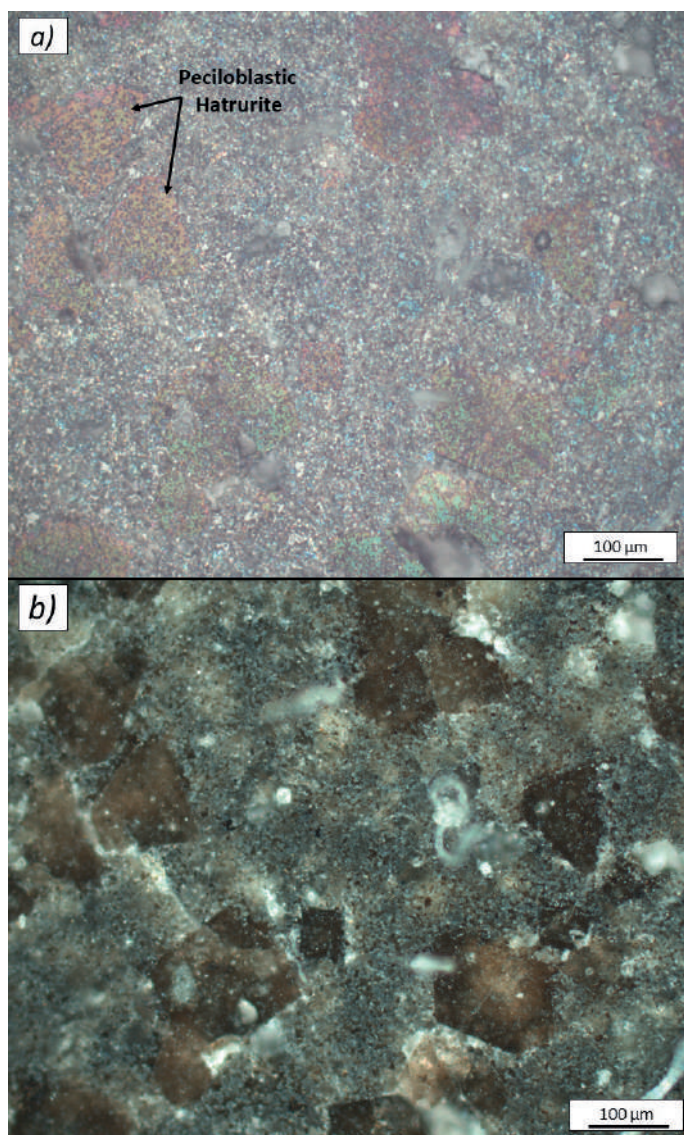


Figure 6 RLM of Ghareb Fm. powders heated at 1250°C after Nital etching at (a) parallel nicols and (b) crossed nicols, revealing peciloblastic pseudo-hexagonal hatrurite.

which released fluorite;

(iii) 1200-1250°C (Fig. 6), 1st melting event (LT melt) due to the incongruent melting of:

$\text{Larn} + \text{Fap-ell} + \text{CaF}_2 \rightarrow \text{Larn} + \text{Fap-ell} + \text{Liquid}$

(iv) 1250-1280°C, 2nd melting event (HT melt) featured by the melting of Ca-Al-Fe-rich phases (i.e., brownmillerite, mayenite and part of ye'elimite) revealed by the change from euhedral to xenomorphic texture.

Furthermore, hatrurite (also called alite, Ca_3SiO_5) crystallized at T of 1200-1250°C forming coarse peciloblastic pseudo-hexagonal crystals (Fig. 6), which later breaks down at $T > 1250^\circ\text{C}$. At $T > 1250^\circ\text{C}$ hatrurite turned from euhedral crystals (100-200 µm) to rounded crystals with lesser inclusions that are made of May+Brw. All these outcomes are relevant for cement manufacture because Ghareb Fm. represents the starting raw material for producing a S-P-F-doped Cement (i.e., new type of green-cement).

Fe-rich Belite Cement (F-BC) synthesis

An industrial raw meal composed of a mixture of li-

mestone, clays, hematite and gypsum was used to prepare F-BC at laboratory scale (Table 1), studying microstructural, mineralogical and crystallographic changes occurring during heating up to 1350°C. Commercial BCs are always composed of mainly larnite, brownmillerite, mayenite and/or celite (Cel , $\text{Ca}_3\text{Al}_2\text{O}_6$) plus a variable amount of ye'elimite depending on the selected SO_3 content (De La Torre et al., 2007). Our F-BC prepared at laboratory scale highlighted Larn-Brw-Yel-May already stable at $T \geq 1200^\circ\text{C}$, despite this final mineral assemblage usually occurs between 1300-1350°C (Ghorab et al., 2014): this result represents an important outcome for improving BCs manufacture. Samples heated at $T \leq 1300^\circ\text{C}$ showed a microtexture based on micrometric crystals of Larn, Yel, May and coarser prismatic Brw with high porosity; whereas samples heated $T > 1300^\circ\text{C}$ figured out lower porosity, coarse rounded Larn, subhedral Yel and xenomorphic matrix of Brw. This dramatic change in microtextural features is accounted to the main melting event of BCs which usually occurs between 1270-1309°C leading the formation of a melt mainly rich in Ca, Al and Fe (Brw and May melt) improving the growth of crystal phases and reactions (Kurdowski, 2014).

Hydration experiments

Hydration properties comparison between ye'elimite-larnite granofels and F-BC prepared at 1350°C was made by means of hydration experiments. Cements were prepared by adding 3 wt% of gypsum to ye'elimite-larnite granofels powder and F-BC. Later, cements were mixed with water (0.5 water/cement ratio) and investigated till 28 hydration days. Results highlighted that natural and synthetic Belite Cement have similar heat release and crystal phase evolution during hydration, excepted for the earlier crystallisation of stratlingite (Strat , $\text{Ca}_2\text{Al}_2\text{SiO}_2(\text{OH})_2 \cdot 3\text{H}_2\text{O}$) after 7 hydration days for natural cement.

Furthermore, the natural hydration of ye'elimite-larnite granofels was reproduced at laboratory scale by hydrating (a) rock powders and (b) rock fragments. (a) Rock powders hydration revealed after 4 months a mineral assemblage composed of unreacted larnite, low reactive phases (i.e., Fap-ell, Shu and spinel), stratlingite, ettringite, calcite, aluminium hydroxides and amorphous Ca-Si-H, which the latter comes from larnite hydration starting after 12 hydration weeks. However, the obtained phase assemblage is similar to brown rims one, excepted for the occurrence of stratlingite and amorphous Ca-Si-H instead of crystalline Ca-Si-H phase and hydrogarnet: stratlingite should later breakdown in hydrogarnet and Ca-Si-H phases when $\text{Ca}(\text{OH})_2$ content increases due to larnite hydration. (b) Rock fragments hydration produced a white precipitate made of calcite, ettringite, gypsum and aluminium hydroxides, which well fits with white core mineral assemblage of natural hydrated veins.

DISCUSSION AND CONCLUSIONS

This study deeply compared the natural process of Combustion Pyrometamorphism (CP) that involved impure limestones occurring in Hatrurim Basin (Israel) and the synthetic analogous process of cement manufacture by means of a multidisciplinary approach.

The geological field trip in Hatrurim Basin area allowed to collect both CP rocks and protolith of Larnite Rocks, and relevant geological features making a direct comparison with available bibliographic data. Chemical composition differences (i.e., changes inside the $\text{CaO-SiO}_2\text{-Al}_2\text{O}_3$) and microstructural changes observed along the metamorphic sequence are well linked to changes occurring inside the pristine sedimentary sequence: (i) metamorphosed Mishash Fm. corresponds to the base of metamorphosed sequence; (ii) gehlenite-wollastonite and anorthite-diopside hornfels represent brown to black layers corresponding to the metamorphism of marls belonging to Taqiye Fm.; (iii) stratified Larnite Rocks and calcite-spurrite well fit with HT metamorphism of well stratified marly limestone of Hafir Member (Upper Taqiye Fm.). Furthermore, HT rocks usually occur at the metamorphic sequence top or areas featured by high oxygen availability. Therefore, all results confirmed the general hypothesis of in-situ HT and LP metamorphism of a sedimentary sequence by methane-rich gases combustion which came from deep hydrocarbon reservoirs.

The study on protolith of Larnite Rocks (Ghareb Fm.) was crucial to reveal detailed mineralogical and crystallographic information and to highlight natural anisotropies which influence mineral assemblage and microtexture of resulting CP rocks. The link between Ghareb Fm. inhomogeneities and ye'elimite-larnite granofels microtexture was confirmed by: (i) millimetric black nodules rich in spinel and Ti-bearing phases in ye'elimite-larnite granofels should be correlated with millimetric dark nodules rich in Fe-phases and minor titanite occurring inside pristine limestone; (ii) coarse fluorapatite crystals occurring inside ye'elimite-larnite granofels should be linked to the occurrence of phosphatic pellets inside protolith rocks.

Detailed crystallographic and microtextural investigations on ye'elimite-larnite granofels and the equivalent green-cement doped in S-P-F, which was laboratory prepared using ye'elimite-larnite granofels protolith, revealed crystal phase evolution upon heating till 1350°C showing two main melting events: (i) low-T melt rich in Anh-Larn- CaF_2 is produced from $T \geq 1054^\circ\text{C}$ when CaF_2 is released during Tern crystallisation and Fap-ell breakdown; (ii) high-T Al-Fe-rich melt occurs at 1250-1270°C, leading microtextural features close to BCs ones. Furthermore, highly doped hatrurite occurred at Room Temperature (RT) after heating Ghareb Fm. at 1244°C even with a slow cooling, representing a relevant outcome for designing new green-cements and advancing cement

manufacture: the simultaneous occurrence of S, P and F in cement raw meal strongly improves hydration properties and reduces combustion T. Therefore, this study figured out the availability of S-P-F-rich wastes reuse (e.g., phosphogypsum, solid urban wastes, F-rich sludges and S-P-F-rich rock wastes) as alternative raw materials in cement manufacture coping with the aim of managing waste-related problems (dangerous elements pollution, reducing land use for landfills and waste treatment costs) and reducing CO_2 emissions (lowering combustion T, fuel and natural raw materials consumption). Furthermore, results could be employed not only for improving cement manufacture but also for advancing oil fields exploration, due to the vicinity of CP rocks to oil and gas reservoirs: CP rocks could be used as a proxy especially for methane-rich reservoirs exploration.

F-BC samples showed a mineral assemblage and hydration properties similar to commercial BCs. Nevertheless, results highlighted that the BCs final mineral assemblage (Larn-Brw-Yel) was already occurring at 1200°C with high porous and fine microtexture representing relevant outcomes for BCs manufacture allowing: (a) lower energy expenditure and CO_2 emission reduction thanks for the lower combustion T compared to common BCs conditions (1250-1350°C); (b) lower grinding costs thanks to the advantageous porous-soft microtexture that represents a main item of expenditure in cement manufacture; (c) the positive reuse of Fe-S-rich wastes as alternative raw material helps in handling bauxite supply and landfill related problems.

Natural ye'elimite-larnite granofels figured out similar hydration reactions of F-BC, excepted for earlier stratlingite occurrence in natural cement due the hydration contribution of minor phases such as mayenite and aluminium hydroxides: $\text{Al}(\text{OH})_3$ that occurs as minor phase in Larnite Rocks and is also produced by mayenite hydration can reacts with Ca-Si-H phases forming stratlingite.

Furthermore, hydration experiments on ye'elimite-larnite granofels clarified the formation of natural hydrated veins better explain their textural features: (i) the weathering of ye'elimite-larnite granofels outcrops caused the water interaction with reactive anhydrous phases (e.g., larnite, ye'elimite, mayenite, brownmillerite and ternsite) leading a circulating pore solution rich in $\text{Ca}(\text{OH})_2$, $(\text{SO}_4)^{2-}$ and $\text{Al}(\text{OH})_3$, and hydration products (i.e., Ca-Si-H phases, Hydr, gibbsite and Ettr); (ii) the resulting pore solution infills cracks and lead the precipitation of calcite, ettringite and gypsum, forming white core of hydration veins; (iii) the hydration products remain in the same position close to anhydrous portions and gradually crystallise as Ca-Si-H phases (tobermorite, jennite and afwillite), hydrogarnet, gibbsite and minor minerals coming from the pore solution (e.g., calcite, ettringite and gypsum), resulting in the brown rims of hydration veins.

REFERENCES

- Bucher, K., & Grapes, R. (2011): Petrogenesis of Metamorphic rocks. Springer, Berlin Heidelberg, pp. 428.
- Burg, A., Starinsky, A., Bartov, Y., & Koldny, Y., (1991): Geology of the Hatrurim Formation (Mottled Zone) in the Hatrurim basin. *Isr. J. Earth-Sciences* **40**, 107-124.
- Cantaluppi, M., (2023): Advanced Mineralogical and Crystallographical Techniques for understanding transformation processes in natural materials and their synthetic analogues. Ph.D. Thesis, Università degli Studi di Milano, Milano.
- De La Torre, Á.G., Morsli, K., Zahir, M., & Aranda, M.A.G. (2007): In situ synchrotron powder diffraction study of active belite clinkers. *J. Appl. Crystallogr.*, **40(6)**, 999-1007.
- Freund, R., (1965): A Model of the Structural Development of Israel and Adjacent Areas Since Upper Cretaceous Times, *Geol. Mag.* **103**, 13-20.
- Ghorab, H.Y., Rizk, M., Ibrahim, B., & Allam, M.M., (2014): High belite cement from alternative raw materials, *Mater. Constr.*, **64(314)**, e012.
- Grapes, R., Pyrometamorphism (2010): Springer, Berlin Heidelberg, pp. 365.
- Hirsch, F., A., & Burg, Y.A. (2008): Geological Map of Israel 1:50'000, Arad, Sheet 15-IV.
- Kurdowski, W. (2014): Cement and concrete chemistry, (2014), Springer, Dordrecht Heidelberg, pp. 700
- Lewy, Z. (1990): Pebbly phosphate and granular phosphorite (Late Cretaceous, southern Israel) and their bearing on phosphatization processes, *Geol. Soc. Spec. Publ.* **52**, 169-178.
- Novikov, I., Vapnik, Y., & Safonova, I., (2013): Mud volcano origin of the Mottled Zone, South Levant, *Geosci. Front.* **4**, 597-619.
- Schneider-Mor, A., Alsenz, H., Ashckenazi-Polivoda, S., Illner, P., Abramovich, S., Feinstein, S., Almogi-Labin, A., Berner, Z., & Püttmann, W., (2012): Paleoceanographic reconstruction of the late Cretaceous oil shale of the Negev, Israel: Integration of geochemical, and stable isotope records of the organic matter, *Palaeogeogr. Palaeoclimatol. Palaeoecol.*, **319**, 46-57.
- Sokol, E. V., Kokh, S.N., Sharygin, V. V., Danilovsky, V.A., Seryotkin, Y. V., Liferovich, R., Deviatiiarova, A.S., Nigmatulina, E.N., & Karmanov, N.S., (2019): Mineralogical diversity of Ca₂SiO₄-bearing combustion metamorphic rocks in the Hatrurim Basin: Implications for storage and partitioning of elements in Oil Shale Clinkering. *Minerals* **9(8)**, 465.
- Sokol, E. V., Kokh, S.N., Vapnik, Y., Thiéry, V., & Korzhova, S.A., (2014): Natural analogs of belite sulfoaluminate cement clinkers from Negev Desert, Israel, *Am. Mineral.* **99**, 1471-1487.
- Sokol, E. V., Novikov, I.S., Vapnik, Y., & Sharygin, V. V., (2007): Gas fire from mud volcanoes as a trigger for the appearance of high-temperature pyrometamorphic rocks of the Hatrurim Formation (Dead Sea area), *Dokl. Earth Sci.* **413**, 474-480.
- Sokol, E. V., & Volkova, N.I., (2007): Combustion metamorphic events resulting from natural coal fires, *GSA Rev. Eng. Geol.* **18**, 97-115.
- Staněk, T., & Sulovský, P., (2013): Active low-energy belite cement. *Cem. Concr. Res.* **68**, 203-210.
- Vapnik, Y., Sharygin, V. V., Sokol, E. V., & Shagam, R., (2017): Paralavas in a combustion metamorphic complex: Hatrurim Basin, Israel, *GSA Rev. Eng. Geol.* **18**, 133-153.

Petrology and geochemistry of Peri-Mediterranean carbonatite magmatism: case studies from Fuerteventura (Canary Islands) and Mt. Vulture Volcano (Southern Italy)

Gabriele Carnevale

Dipartimento di Scienze della Terra e del Mare, Università degli Studi di Palermo, Via Archirafi 22, 90123, Palermo, Italia

DOI:10.19276/plinius.2023.01.003

INTRODUCTION AND AIM OF THE WORK

Carbonatites are rare magmatic rocks but of great importance for several reasons, among which: (i) scientific importance, given their petrogenesis that involves modified carbonated mantle, liquid immiscibility, geodynamic setting (e.g., Yaxley et al., 2022); (ii) economic relevance, given that they are considered the main natural hosts of critical metals for key economic sectors in heavily industrialized countries, due to their great abundance in Rare Earth Elements (REEs) and trace elements (such as Nb, Hf, U, Th, etc), essential in many high-tech applications (e.g., Anenburg et al., 2021); (iii) environmental, due their strict ties with CO₂ uptake and exsolution. Despite their importance, many aspects of carbonatites petrogenesis and evolution processes remain still poorly constrained. One of the principal purposes of the scientific community is to refine the existing models for carbonatite magma petrogenesis, because they provide meaningful information on the deep geochemical cycle of carbon and mantle metasomatism. Then, it is fundamental to understand not only the genesis of carbonatite magmatism investigating its source, but also any possi-

ble post-genetic process during the evolutionary history of carbonatite melt.

This work adopts a multidisciplinary approach to define petrology and isotope geochemistry of carbonatites in different geodynamic settings. The goal is to characterize the source of carbonatite magmatism and identify any post-genetic processes such as crustal contamination, mixing processes, isotopic exchanges, hydrothermal mineralization, that were able to modify the primary signature and the origin composition of carbonatite melts. Fuerteventura (Canary Islands) was taken representative of oceanic carbonatites, while Mt. Vulture (southern Italy) was taken representative of intra-continental carbonatites, within the particular geodynamic context of Apennine subduction zone (Fig. 1). The comparison of oceanic carbonatites with intra-continental ones was aimed to provide information on the mantle source and the relationship of carbonatite magmatism with the various geodynamic settings, trying to understand why oceanic carbonatites are so rare if compared with continental counterpart. Principal inferences regard also the role of the carbonatite melts in metasomatiz-

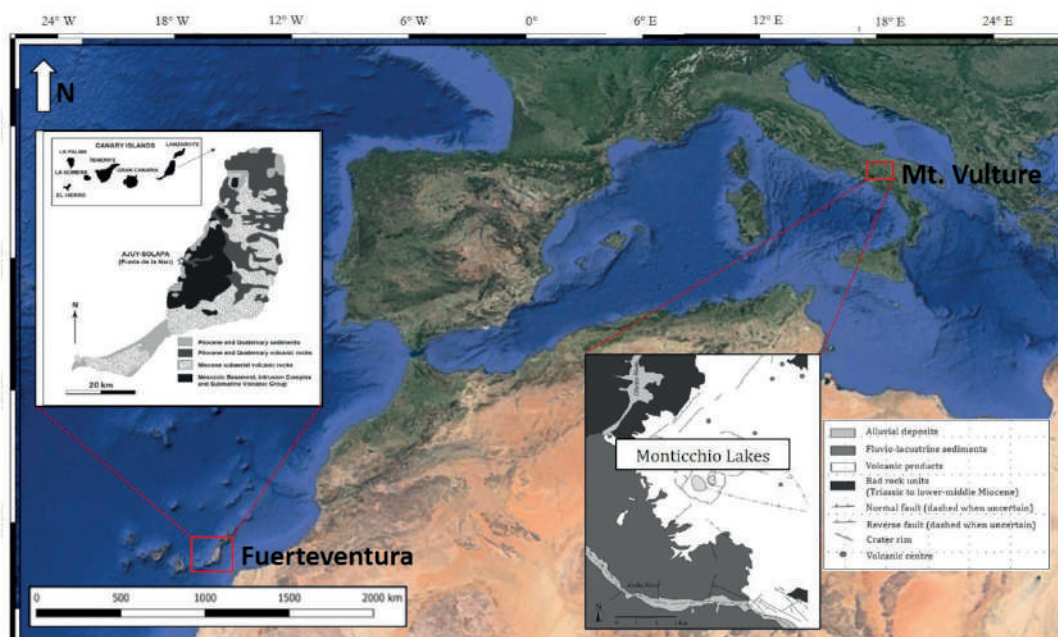


Figure 1 Geographic location of the two studied areas.

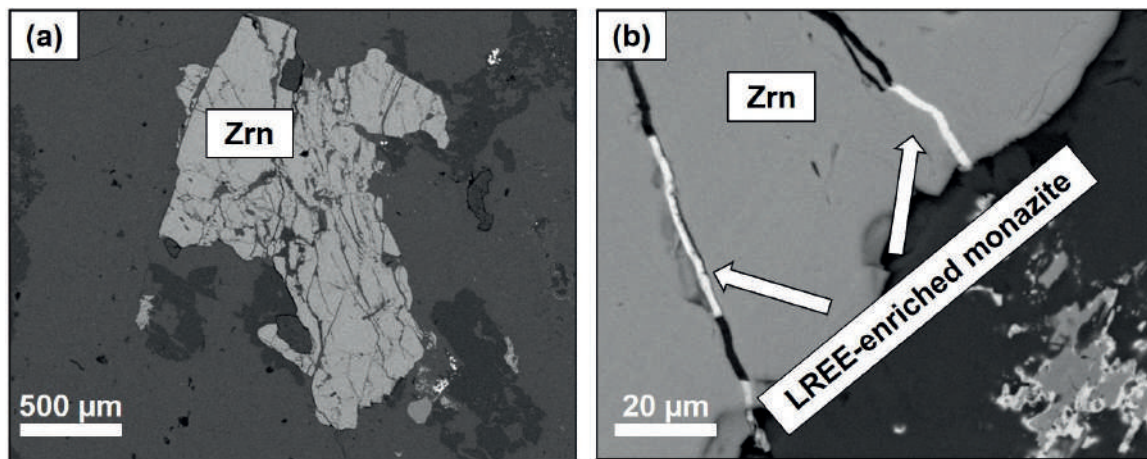


Figure 2 Backscattered electron images (BSE) of (a) zircon (Zrn) crystal and (b) filled microfractures in zircon crystal with monazite enriched in LREE (La, Ce, Nd).

ing the mantle source, and also on the importance of post-magmatic processes in which the infiltrating fluids play an important role in the transport and concentration of REEs.

To achieve these objectives, for each case study, a detailed minero-petrographic and minero-chemical characterization was firstly carried out. In particular, a detailed micro-thermometric study was performed in Fuerteventura carbonatites to understand the processes involved in carbonatite-related hydrothermal mineralization and formation condition (temperature, pressure and composition of fluid inclusions), and in Mt. Vulture products to provide important information about the melilitite-carbonatite magma ascent path and its mantle source, describing the volcano plumbing system and the way in which these very particular magmas are transported to the surface, with considerations about carbonatite mantle metasomatism and possible implications in terms of volcanic hazard. Subsequently, a characterization of noble gases (He, Ne and Ar), together with literature data of stable isotopes ($\delta^{13}\text{C}$ and $\delta^{18}\text{O}$), and Sr-Nd-Pb systematics, applied on studied carbonatite products (or closely related to them), was implemented.

RESULTS AND DISCUSSION

The case study of Fuerteventura (Canary Islands)

Hydrothermal fluids and formation conditions of REE enrichment processes

Carbonatitic dykes that crop out in the central western part of Fuerteventura Basal Complex were affected by the Miocene intrusive event responsible for contact metamorphism and partial melting of part of the alkaline-carbonatitic complex (Casillas et al., 2011). Indeed, the original igneous mineralogy disappeared completely in the anatexis zone, and a metamorphic association composed of wollastonite, monticellite, diopside, vesuvianite, garnet, calcite, perovskite, alabandite, pyrrhotite and Nb-Zr-Ca silicates (cuspidine-niocalite-baghdadite series) was formed (Casillas et al., 2011). The absence of metamorphic minerals typical of the contact zone, together with the presence of primary magmatic mine-

erals such as apatite, biotite, and aegirine-augite, indicate that carbonatite outcrops in Punta de La Nao (Ajuy-Solapa sector) escaped this thermal overprint and preserve their original igneous assemblage and textures (Carnevale et al., 2020). Furthermore, the presence of monazite enriched in LREE (La, Ce, Nd) formation processes in microfractures that affect zircon crystals (Fig. 2), suggests carbonatite interactions with hydrothermal fluids and partial REE remobilization processes. Indeed, at sub-solidus temperatures ($T > 600^\circ\text{C}$) and the brine-melt stage ($600^\circ\text{C} \leq T \leq 400^\circ\text{C}$), where REEs are sufficiently concentrated in the residual brine-melt to form REE-minerals, the infiltrating fluids during the hydrothermal stage play an important role in the transport and concentration of REEs. The identification of chlorite ($d_{001} = 14 \text{ \AA}$), vermiculite ($d_{001} = 16,6 \text{ \AA}$) and interstratified illite-smectite ($d_{001} = 13 \text{ \AA}$) as hydrothermal alteration minerals, allows to frame the hydrothermal event in the metamorphic facies of zeolites, and the formation of these hydrothermal alteration minerals is due to a metasomatism process caused by the exsolution of a hydrothermal fluid phase from the magma that gave rise to carbonatite in the last moments of cooling (i.e. autometasomatism, a common process in carbonatitic intrusive rocks) (Carnevale et al., 2020).

In order to further constrain the formation conditions and characterize the late-stage hydrothermal fluids, the study of fluid inclusions (FIs) in carbonatite rocks is essential, and micro-thermometric studies represent the most straightforward method to obtain information about fluid temperature, pressure and composition (e.g., Carnevale et al., 2022a). Fuerteventura carbonatites show the presence of isolated FIs in host calcite minerals, suggesting a primary origin. The size of the inclusions is $< 10 \mu\text{m}$, and they mostly are in the range of $1\text{-}5 \mu\text{m}$. Their shape is generally irregular, with negative-crystal forms and square shapes, according to the host calcite mineral. Few rounded isolated FIs in apatite are also present. Some FIs show textural characteristics of partial decrepitation, such as haloes of tiny fluid inclusions (diameter $< 0.1 \mu\text{m}$) surrounding the inclusion cavity, revealing that some events of partial density re-equilibration have occurred. Some intragranular trails confined within cal-

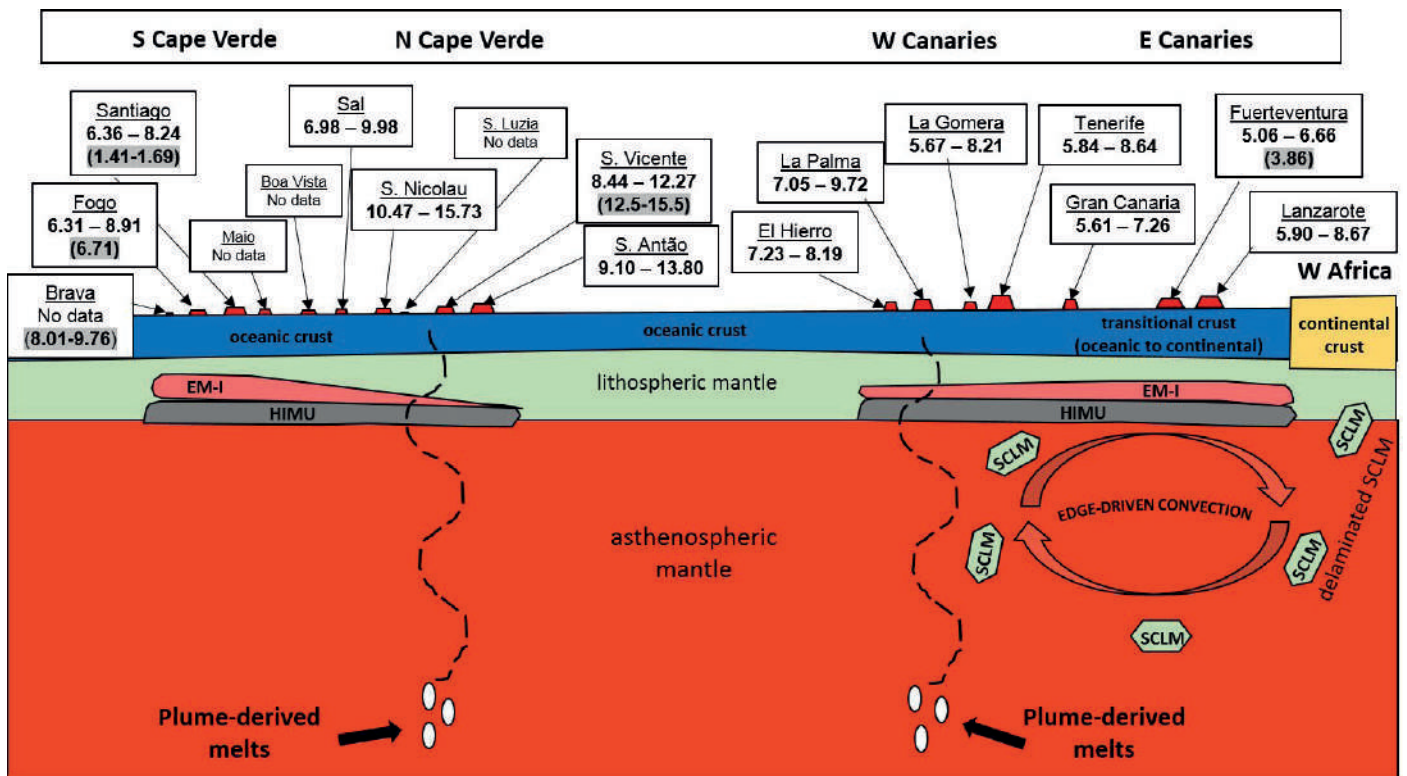


Figure 3 Hypothetical schematic profile view of the upper mantle/crust under Cape Verde and Canary Archipelago (not in scale) with the involvement of the proposed mantle components and the mechanism of physical detachment of the sub-continental lithospheric mantle (SCLM) caused by edge-driven convection during breakup of the Pangea Supercontinent and incorporated into the oceanic lithospheric mantle beneath at least some Canary Islands.

cite grain-boundary and crystal interior are also found. Observing the temperatures of phase changes in FIs during heating/cooling analyses, it is possible to know the composition of the inclusions for the appropriate chemical system, because each chemical system has its own eutectic temperature (T_e). Results show apparent eutectic temperatures ranging from -21.7 to -21.0°C , although the small dimension of FIs did not allow the correct determination of T_e for almost all inclusions. Thus, the eutectic behavior and the narrow range of measured T_e suggest the well known binary $\text{NaCl-H}_2\text{O}$ system ($T_e = -21.2^\circ\text{C}$) as a characterizing chemical system in studied FIs. No CO_2 was detected (the eutectic temperature of pure CO_2 is -56.6°C). With the T_e range and the chemical system, the final ice melting temperatures (T_{im}) during heating was also measured ranging between -3.2 and -2.1°C and corresponding to salinities of 5.3 and 3.6 wt% NaCl_{eq} , respectively. All studied fluid inclusions homogenize to liquid phase (ThL ; $\text{L} + \text{V} = \text{L}$), with homogenization temperature ranging from 142.7 to 208.7°C (corresponding to densities of 0.95 and 0.88 g/cm^3 , respectively) and homogenization pressures ranging from 4.6 to 15.3 bars. To resume, micro-thermometric studies on Fuerteventura carbonatites shows the presence of low salinity ($\cong 5 \text{ wt}\% \text{ NaCl}_{eq}$) and low temperatures ($< 300^\circ\text{C}$) fluids trapped within primary calcite crystals, corroborating that processes of fluid/rock interaction occurred. Thus, REEs can be mobilised and concentrated on the local scale by low-temperature hydrothermal fluids with a process known as autometasomatism, accordingly with the

more recent classification proposed by Mitchell & Gittings (2022) using the term carbo-hydrothermalite, where a carbonatite can precipitate at sub-solidus temperatures from a mixed $\text{CO}_2\text{-H}_2\text{O}$ fluid during late-stage processes.

$^3\text{He}/^4\text{He}$ isotopic ratios

Even though calcite $^3\text{He}/^4\text{He}$ ratios on Fuerteventura carbonatites (up to 3.86Ra) are a little higher than clinopyroxenes ($\approx 2.23\text{Ra}$) and higher than apatites (up to 0.08Ra), they present values significantly lower than typical MORB mantle values ($R/\text{Ra} = 8 \pm 1$), while clinopyroxenes from clinopyroxenite show $^3\text{He}/^4\text{He}$ ratios ($\approx 6.66\text{Ra}$) slightly lower than typical MORB mantle values and in the range of sub-continental lithospheric mantle values (SCLM, $6.1 \text{ Ra} \pm 0.9$). The lower values on mineral separates from Fuerteventura carbonatites might be caused by "magma aging" (i.e. internal production of radiogenic $^4\text{He}^*$ from U and Th content that lower the original R/Ra ratio of the magmatic source). However, considering (i) ^3He and ^4He concentration, (ii) Th and U content measured on calcite and clinopyroxene separates and (iii) contribution of radiogenic $^4\text{He}^*$, using a simple magma aging model, initial R/Ra ratios of calcite and clinopyroxene from carbonatite and clinopyroxene from clinopyroxenite are not significantly modified. Indeed, initial R/Ra ratios continue to present values lower than typical MORB mantle values ($\approx 5.10\text{Ra}$ and $\approx 5.24\text{Ra}$ for calcite and clinopyroxene from carbonatite and $\approx 6.82\text{Ra}$ for clinopyroxene from clinopyroxenite), and they are in the range of SCLM. An age of 53.5 Ma would be required

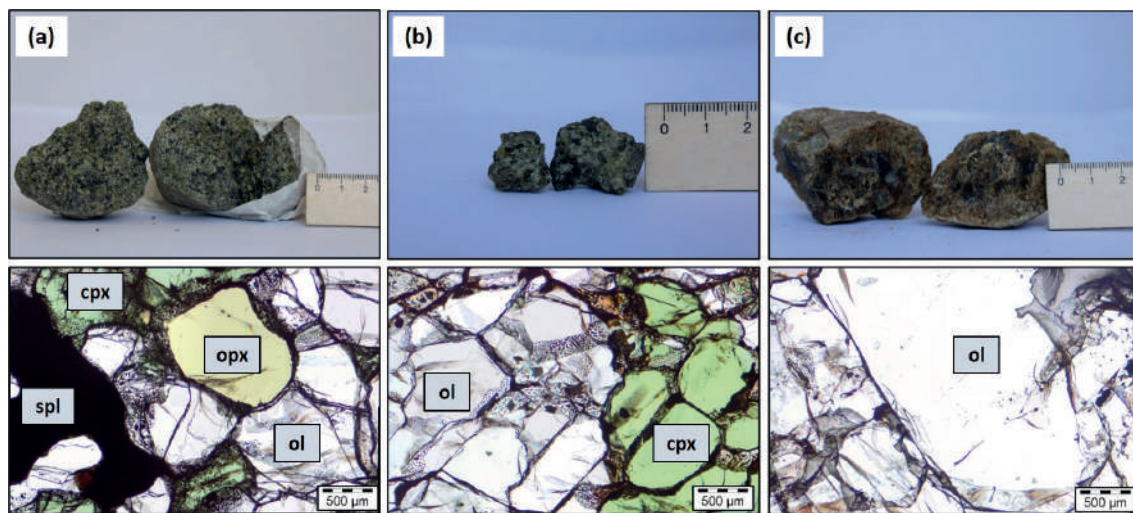


Figure 4 Mantle xenoliths hand specimens and related parallel polars (PPL) photomicrographs of (a) fine-grained lherzolite, (b) medium-grained wehrlite, and (c) coarse-grained dunite, respectively. ol = olivine; opx = orthopyroxene; cpx = clinopyroxene (emerald green Cr-diopside); spl = spinel.

for Fuerteventura carbonatites to bring the initial R/Ra ratio of 8 on calcite, and this is not realistic as have ages close to 25 Ma (Muñoz et al., 2005). We therefore consider the He isotopic ratio from the calcite to be reflective of a sub-continental lithospheric mantle signature.

Figure 3 shows a summary of the proposed mantle components for Canary and Cape Verde primitive magmas and shows also a clear regional distribution and an isotopic dichotomy of $^3\text{He}/^4\text{He}$ ratios in both silicate rocks and Cape Verde carbonatites. This regional distribution appears to be slight on Canary Islands, with an apparent increase of R/Ra from eastern (oldest) to western (youngest) Islands, and all islands except for Fuerteventura, present a MORB-like values. Interestingly, both Fuerteventura carbonatites and silicate rocks, present R/Ra values lower to slightly lower than typical MORB mantle values, and they are in the range of SCLM (Carnevale et al., 2021).

The case study of Mt. Vulture (southern Italy)

Carbonatites and xenoliths: a look into the mantle

The carbonatite magmatism from Mt. Vulture is essentially related to a phreatomagmatic activity of the last melilitite-carbonatite eruption (141 ± 11 ka, Villa & Buetner, 2009). The presence of ash-rich tuff deposits with a melilitite-carbonatite matrix and carbonatite-rich layers within the matrix, reflects the direct evidence of carbonatite magmatism. Furthermore, a robust amount of pelletal lapilli (enclosing mantle xenoliths) and mantle xenoliths from the melilitite-carbonatite matrix, represents a great tool to understand the composition and possible modification of a mantle source influenced by carbonatite metasomatic fluids. Mantle xenoliths are rounded, of an average 4-5 cm in diameter, with some rarely samples up to 10 cm. The grain size of the mantle xenoliths is variable, fine- to medium-grained (0.5-1 mm) in the case of the lherzolite and wehrlite, medium- to coarse-grained (2-5 mm) in the case of the wehrlite, ol-clinopyroxenite and dunite (Fig. 4). The texture is usually equigranular and sub-idioblastic, with the exception of dunite xeno-

lith that show an inequigranular texture. All xenoliths show a granoblastic-decussate structure, where the interlocking and randomly oriented grains are variably elongated. Well-defined triple junctions are common. Olivine usually shows undulose extinction and deformation structures such as kink bands, while orthopyroxene and clinopyroxene (emerald green Cr-diopside) occur as subhedral/anhedral with curvilinear boundaries. Spinel is also present as subhedral/anhedral, with colour varying from brown to dark brown. Noteworthy, is the presence in the xenoliths of phlogopite and reaction rim in orthopyroxene replaced by a very fine-grained assemblage of olivine and clinopyroxene microcrysts, suggesting that metasomatism processes occurred. Among the Mt. Vulture mantle products, the presence of wehrlite xenoliths is widely recognized and is corroborated by our findings where pelletal lapilli cores are largely wehrlitic. (La/Yb)_N ratios ($> 3-4$), the presence of carbonates and apatites in some wehrlites, suggest carbonatite metasomatism and the role of carbonatite melts instead of silicate melts in metasomatizing the wehrlite xenoliths.

The chemical composition of olivine, orthopyroxene, and clinopyroxene minerals from the mantle xenoliths is similar to those from the ultramafic core of pelletal lapilli and from the loose xenocrysts within the melilitite-carbonatite matrix. Olivines show Mg-rich composition (Fo_{87-92}) and relatively high NiO (0.2 to 0.4 wt%), with some exception in dunite xenolith with low NiO content (0.08 wt%). Orthopyroxenes show also high values of Mg ($\text{Mg}\# = 0.89-0.90$), and compositionally, the proportion of En (Wo_{2-3} , En_{86-87} , Fs_{10-11}) shows a positive correlation with the Fo content of the coexisting olivine. Clinopyroxenes are essentially diopside in composition (Wo_{47-51} , En_{44-48} , Fs_{5-7}) with some Na-rich and Ca-poor exceptions, and they generally show high Cr_2O_3 (0.6-1.4 wt%) and high Mg# values (0.87 to 0.91).

Pelletal lapilli are considered the juvenile component of the last Mt. Vulture volcano activity, representing the interface between the erupting silica undersaturated melilititic-carbonatitic magma and the volatile component, this latter considered very important in the evolu-

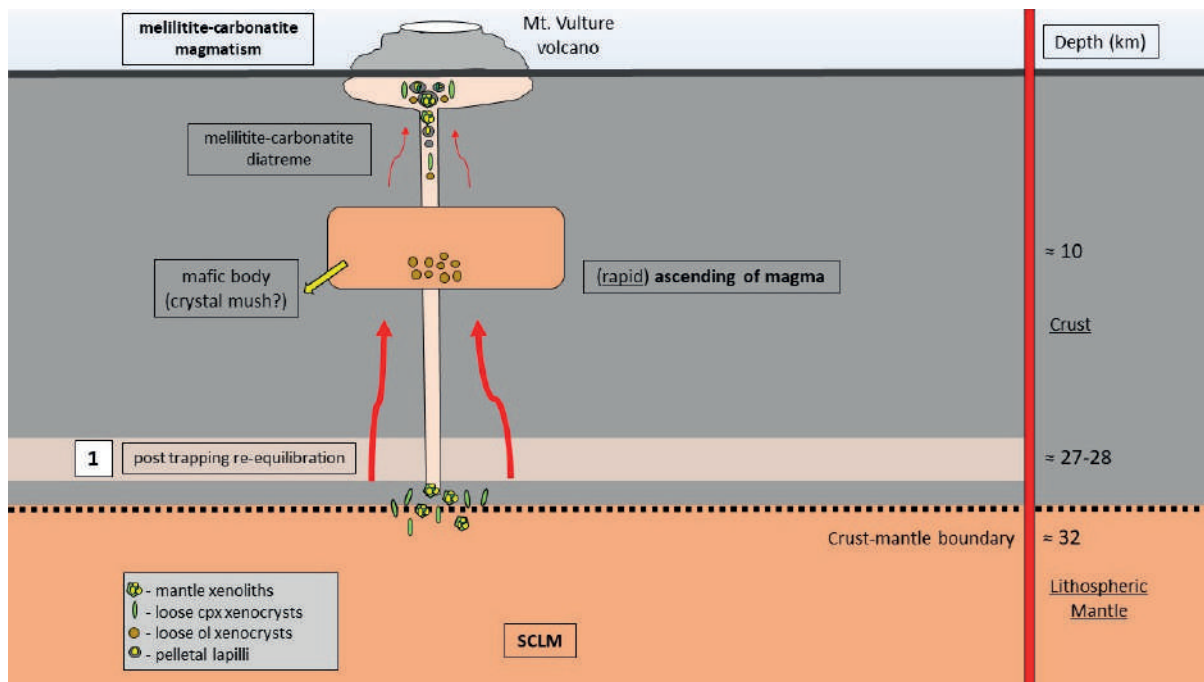


Figure 5 Simplified cross section of Vulture volcano ponding stages.

tionary history of the erupting magma (Lloyd & Stoppa, 2003). Thus, the whole rock chemistry of the external portion of Mt. Vulture pelletal lapilli represents a good tracer to distinguish the literature data of sedimentary calcareo-carbonate portion from the mellilitite-carbonatite one. Indeed, the external portion of pelletal lapilli shows concentrations (e.g., Ba = 2430 ppm; Sr = 1250 ppm; \sum REE = 527 ppm) comparable with those of the average values of Ca-carbonatite and plotting onto the average range of extrusive carbonatites, suggesting a possible contribution of a carbonatite melt in the trace elements enrichment processes.

The study of chemical composition together with trapping temperature and pressure of fluid inclusions trapped in rock-forming minerals of mantle xenoliths provides insights into the PT history of the mantle and the mineral-melt-fluid interaction processes in the mantle and within the volcano magma storage system. Fluid inclusions are present in all studied samples, in both ultramafic cores of pelletal lapilli and in mantle xenoliths. The histograms of densities of FIs in mantle xenoliths show a similar modal distribution if compared with those of mantle xenolith cores of pelletal lapilli (Carnevale et al., 2022b). FIs trapped in lherzolite and wehrlite xenoliths registered magma ponding at different depths within the Mt. Vulture magma system (Fig. 5). The first ponding stage corresponds to the local crust-mantle boundary (at about 32 km depth), while the second corresponds to a shallow ponding stage (at about 12-14 km depth), as corroborated by geophysical evidences of solidified magmatic body at the same depth below the Vulture volcano (Improta et al., 2014). In order to constrain the ascent velocity of the mellilitite-carbonatite magma, we used the equation from Lister & Kerr (1991). Our result of the ascent rate (≈ 20 m/s) of the mellilitite-carbona-

tite magma is in the same order of the ascent rates of kimberlite magmatism. If we consider also recent studies showing how volcanic systems where activity has remained dormant for protracted periods (> 100 ka) still have the potential for reactivation (e.g., Giordano & Caricchi, 2022), and in Mt. Vulture there is a possible link between the development of tear faults, magmatism and related magma ascent along these tectonic pathways (Pecce-rillo, 2017), our study highlight that the volcanological community should pose great attention to volcanic hazard in mellilitite-carbonatite volcanoes, and it should be carefully evaluated even after long time of quiescence.

Oceanic carbonatites: petrogenetic model

Carbonatite magmatism is essentially related to intraplate continental tectonic settings, with only two occurrences in oceanic tectonic setting: Cape Verde and Canary (Fuerteventura) Archipelago. Several studies were proposed trying to explain why oceanic carbonatites are so rare and are not found in all HIMU-OIB-like archipelagos (e.g., Doucelance et al., 2010), but currently there is no petrogenetic model that can constrain the issue in detail. Although it is a simple model, here is presented a carbonatite petrogenetic model in oceanic environment (Fig. 6) based essentially on the most important geochemical and experimental petrology studies and on the main results of this thesis. Since the pioneering studies of experimental petrology about carbonatite petrogenesis it is clear that all petrogenetic processes are related to the formation of a primary carbonate melt derived from a carbonated mantle, with processes of metasomatism with carbonatitic melts, notwithstanding the oceanic or intracontinental context. Hammouda & Keshav (2015) show how the region located in the depth range of 90 to 150 km deep is where carbonatitic melts can most likely

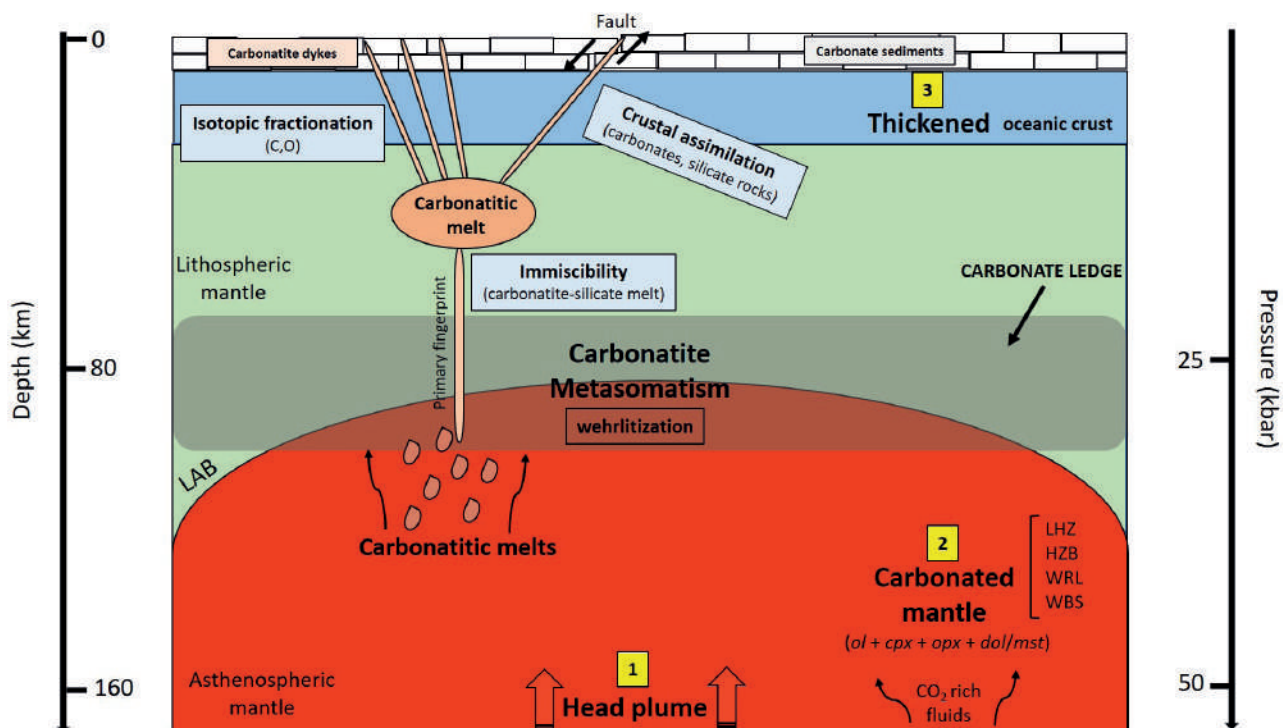


Figure 6 Proposed simple petrogenetic model for oceanic carbonatites with the PluMeTh condition.

be produced and impregnate the surrounding mantle through metasomatism, and the upper bound of this region is called the carbonate ledge. This latter represents the shallowest depth at which carbonate melt is stable before degassing, and in the carbonated peridotite system is located between 20 and 30 kbar (Hammouda & Keshav, 2015). Therefore, the presence of the carbonate ledge prevents carbonatite magmas to reach the surface, and only very fast ascent rates can prevent primary carbonatites from degassing by reaction at the ledge through the ascent to the surface. However, Hammouda et al. (2014) experimentally demonstrated that in hot thermal environments the ledge could be avoided, reacting with an harzburgitic mantle and becoming more calcic upon ascent. Moreover, according to them, Schmidt & Weidendorfer (2018) proposed that oceanic carbonatites develop in hotspots where primitive silicate melts have the lowest SiO_2 and highest total alkalis, characteristics that originate from deep and low-degree melting, and this would be responsible for more abundant carbonatites in continental hotspots, where the lithosphere is a priori thicker than below oceanic crust. Thus, in oceanic tectonic settings it is fundamental the thickness of the lithosphere, and this is perfectly in agreement with the thickness of the lithosphere under Fuerteventura and Cape Verde Archipelago, with an anomalously high transitional oceanic to continental crust. To resume, according also with Doucelance et al. (2010), here it is proposed a petrogenetic model that can be described as the "PluMeTh" condition: 1) there must be a mantle plume to preserve the required hot environment and acting as a trigger for low-degree partial melting at the base of the oceanic lithosphere; 2) processes of mantle Metasomatism by carbonatitic melts in a carbonated mantle with the

involvement of a SCLM are needed; 3) the oceanic lithosphere must be Thick in order to favor plume-induced partial melting at the base, with the production of primitive silicate melts with the lowest SiO_2 and highest total alkalis and the subsequent processes that drive evolving melts into the carbonatite-silicate miscibility gap.

CONCLUSIONS

The multidisciplinary approach of this thesis on petrology and geochemistry of carbonatites permitted characterize the source of carbonatite magmatism in different geodynamic settings, identifying the role of the infiltrating fluids in the transport and concentration of Rare Earth Elements (REEs), and the role of the carbonatite primary melts in metasomatizing the mantle source. To resume,

- (i) regarding the case study of Fuerteventura:
 - (1) isotope geochemistry (noble gases) gives an important contribution to the oceanic carbonatite petrogenesis;
 - (2) combining our results with the most important geochemical and experimental petrology studies a general petrogenetic model for oceanic carbonatites is proposed;
 - (3) petrography, mineral and whole-rock chemistry show how the low temperature fluids play an important role in the transport and REEs concentration processes in carbonatites after the magmatic stage, with direct implications of economic interest.
- (ii) regarding the case study of Mt. Vulture:
 - (1) fluid inclusions micro-thermometry shows the presence of CO_2 -rich fluids in mantle xenoliths, and two

different magma storage at different depth in Mt. Vulture volcanic system;

- (2) modelling magma ascent rate results in quite high velocity (≈ 20 m/s) for melilitite-carbonatite magmas;
- (3) detailed petrographic studies show evidences of wehrlitization processes as a consequence of carbonatite metasomatism in lithospheric mantle;
- (4) the evidences of carbonatite-like metasomatism and mantle degassing, and the presence of mantle xenoliths in volcanic systems related to diatreme explosive eruptions with long quiescence period and high velocity magma ascent rate, are considered important in the evaluation of volcanic hazard.

REFERENCES

- Anenburg, M., Broom-Fendley, S., & Chen, W. (2021): Formation of Rare Earth Deposits in Carbonatites. *Elements*, **17(5)**, 327-332.
- Carnevale, G., Arroyo Rey, X., Correale, A., Rotolo, & S.G. (2020): Procesos hidrotermales con enriquecimiento en REE en las carbonatitas de Fuerteventura: evidencias en minerales accesorios. *Geogaceta*, **69**, 23-26.
- Carnevale, G., Caracausi, A., Correale, A., Italiano, L., & Rotolo, S.G. (2021): An Overview of the Geochemical Characteristics of Oceanic Carbonatites: New Insights from Fuerteventura Carbonatites (Canary Islands). *Minerals*, **11(2)**, 203.
- Carnevale, G., Zanon, V., Ruiz, R.C., & Quintillán, A.A. (2022a): Microthermometry of fluid inclusions in calcite from Fuerteventura carbonatites: composition and formation conditions. *Geogaceta*, **72**, 31-34.
- Carnevale, G., Caracausi, A., Rotolo, S.G., Paternoster, M., & Zanon, V. (2022b): New Inferences on Magma Dynamics in Melilitite-Carbonatite Volcanoes: The Case Study of Mt. Vulture (Southern Italy). *Geophys. Res. Lett.*, **49**, e2022GL099075.
- Casillas, R., Demény, A., Nagy, G., Ahijado, A., & Fernández, C. (2011): Metacarbonatites in the Basal Complex of Fuerteventura (Canary Islands). The role of fluid/rock interactions during contact metamorphism and anatexis. *Lithos*, **125**, 503-520.
- Doucelance, R., Hammouda, T., Moreira, M., & Martins, J.C. (2010): Geochemical constraints on depth of origin of oceanic carbonatites: The Cape Verde case. *Geochim. Cosmochim. Ac.*, **74**, 7261-7282.
- Giordano, G. & Caricchi, L. (2022): Determining the state of activity of Transcrustal magmatic systems and their volcanoes. *Annu. Rev. Earth Pl. Sc.*, **50(1)**, 231-259.
- Hammouda, T. & Keshav, S. (2015): Melting in the mantle in the presence of carbon: Review of experiments and discussion on the origin of carbonatites. *Chem. Geol.*, **418**, 171-188.
- Hammouda, T., Chantel, J., Manthilake, G., Guignard, J., & Crichton, W. (2014): Hot mantle geotherms stabilize calcic carbonatite magmas up to the surface. *Geology*, **42**, 911-914.
- Improta, L., De Gori, P., & Chiarabba, C. (2014): New insights into crustal structure, Cenozoic magmatism, CO₂ degassing, and seismogenesis in the southern Apennines and Irpinia region from local earthquake tomography. *J. Geophys Res-Sol. Ea.*, **119(11)**, 8283-8311.
- Lister, J.R. & Kerr, R.C. (1991): Fluid-mechanical models of crack propagation and their application to magma transport in dykes. *J. Geophys. Res.*, **96(B6)**, 49-77.
- Lloyd, F.E. & Stoppa, F. (2003): Pelletal Lapilli in Diatremes - Some Inspiration from the Old Masters. *GeoLines*, **15**, 65-71.
- Mitchell R.H. & Gittings J. (2022): Carbonatites and carbonatites: A revised classification. *Lithos*, **430-431**, 106861.
- Muñoz, M., Sagredo, J., de Ignacio, C., Fernández-Suárez, J., & Jeffries, T.E. (2005): New data (U-Pb, K-Ar) on the geochronology of the alkaline-carbonatitic association of Fuerteventura, Canary Islands, Spain. *Lithos*, **85**, 140-153.
- Peccerillo, A. (2017): The Apulian Province (Mount Vulture). In: *Cenozoic Volcanism in the Tyrrhenian Sea Region. Advances in Volcanology*. Springer, 203-216.
- Schmidt, M.W. & Weidendorfer, D. (2018): Carbonatites in oceanic hotspots. *Geology*, **46(5)**, 435-438.
- Villa, I. M. & Buettner, A. (2009): Chronostratigraphy of Monte Vulture volcano (southern Italy): Secondary mineral microtextures and ³⁹Ar-⁴⁰Ar systematics. *B. Volcanol.*, **71(10)**, 1195-1208.
- Yaxley, G.M., Anenburg, M., Tappe, S., Decree, S., & Guzmics, T. (2022): Carbonatites: Classification, Sources, Evolution, and Emplacement. *Annu. Rev. Earth Pl. Sc.*, **50(1)**, 261-293.

Tectono-stratigraphic setting and metamorphic evolution of Ligurian-Piedmont Units in the Upper Susa and Chisone Valleys (Western Alps)

Alberto Corno

Dipartimento di Scienze della Terra, Università di Torino, Via Valperga Caluso 35, 10125, Torino, Italia

DOI:10.19276/plinius.2023.01.004

INTRODUCTION

The Alps are a collisional belt, developed after the closure of the Alpine Tethys, opened in Jurassic times between the Adriatic and European continental paleo-margins (see Dal Piaz et al., 2003 for a review). A compelling challenge is to provide new data to constrain the lithostratigraphic setting and metamorphic evolution of various tectonic units from the Ligurian-Piedmont zone. With the intent to constrain the relative pre-collisional position and the Alpine tectono-metamorphic evolution of four tectonic units exposed in the upper Susa and Chisone valleys (Western Alps), the data here presented derive from a Ph.D. project which investigated: the Banchetta-Rognosa unit, the Albergian unit, the Lago Nero unit and the Chenaillet ophiolite.

A multidisciplinary approach was paramount to unravel the tectono-stratigraphic and tectono-metamorphic evolution of these units from the Axial sector of the Alpine belt.

The Ph.D. project was hence based on combined field survey, petrographic observations, and thermodynamic modeling. Field investigations were carried out in order to study the stratigraphic relationships and the present-day juxtaposition among different rock bodies. Petrographic observations (combined with mineral chemistry analyses) were carried out in order to define the blastesis/deformation relationships and constrain tectono-metamorphic events in the different tectonic units, correlating mesoscale and microscale data. Thermodynamic modeling allowed to reconstruct the P-T paths followed by each unit during the Alpine metamorphic evolution.

The overall intent of this work was to propose a reconstruction of the tectono-metamorphic evolution of the axial sector of the Alpine chain in the Cottian Alps, considering the new lithostratigraphic and metamorphic data. The hope is to lead to a better interpretation of the geological features and geometric relationships of four tectonic units, to unravel their syn-rift tectonic history and their following Alpine evolution.

GEOLOGICAL SETTING OF THE STUDIED AREA

Based on geophysical investigations (Roure et al., 1996; Pfiffner et al., 1997), the Western Alps can be subdivided in three sectors: i) the inner part of the chain, the Adriatic paleo-margin representing the upper plate of the collisional system; ii) the outer part of the chain, the European paleo-margin representing the lower plate; iii) the axial sector, where units from the oceanic lithosphere, European and Adriatic crust are tectonically juxtaposed. This sector can be further subdivided (Malusà et al., 2011) in Cretaceous wedge, the Eocene Eclogite belt, and the Frontal Wedge (both made of continental and oceanic-derived Penninic units). The axial sector is characterized by a wide range of peak Alpine metamorphism (from UHP eclogite-facies to greenschist-facies conditions) and is characterized by a double vergence, towards the inner and outer part of the chain.

The studied units belong to the Ligurian-Piedmont Zone (LPZ hereafter) cropping out in the upper Susa Valley and Chisone valleys. In their general traits, the units ascribed to the LPZ are made of widespread calcschists embedding ophiolitic bodies. Locally in the studied area, sectors of crystalline basement rocks with associated carbonate meta-sedimentary covers occur (i.e., the Ambin massif and the here discussed Banchetta-Rognosa tectonic unit).

Well known and studied since the dawn of geological studies (e.g., Barale et al., 2022; Mosca & Barale, 2022), the LPZ cropping out in the considered area can be subdivided into different units taking into account the tectono-stratigraphic records (Servizio Geologico d'Italia, 2002, 2020) an/or the structural setting and metamorphic conditions (Agard et al., 2001; Beyssac et al., 2002; Agard, 2021).

From a general point of view, the studied units fall in the blueschist-facies domain (Bousquet et al., 2008): i) the Albergian and Lago Nero units belong to the blueschist-facies units of the LPZ, mainly made of calcschists and meta-ophiolitic bodies, ii) the Banchetta-Rognosa

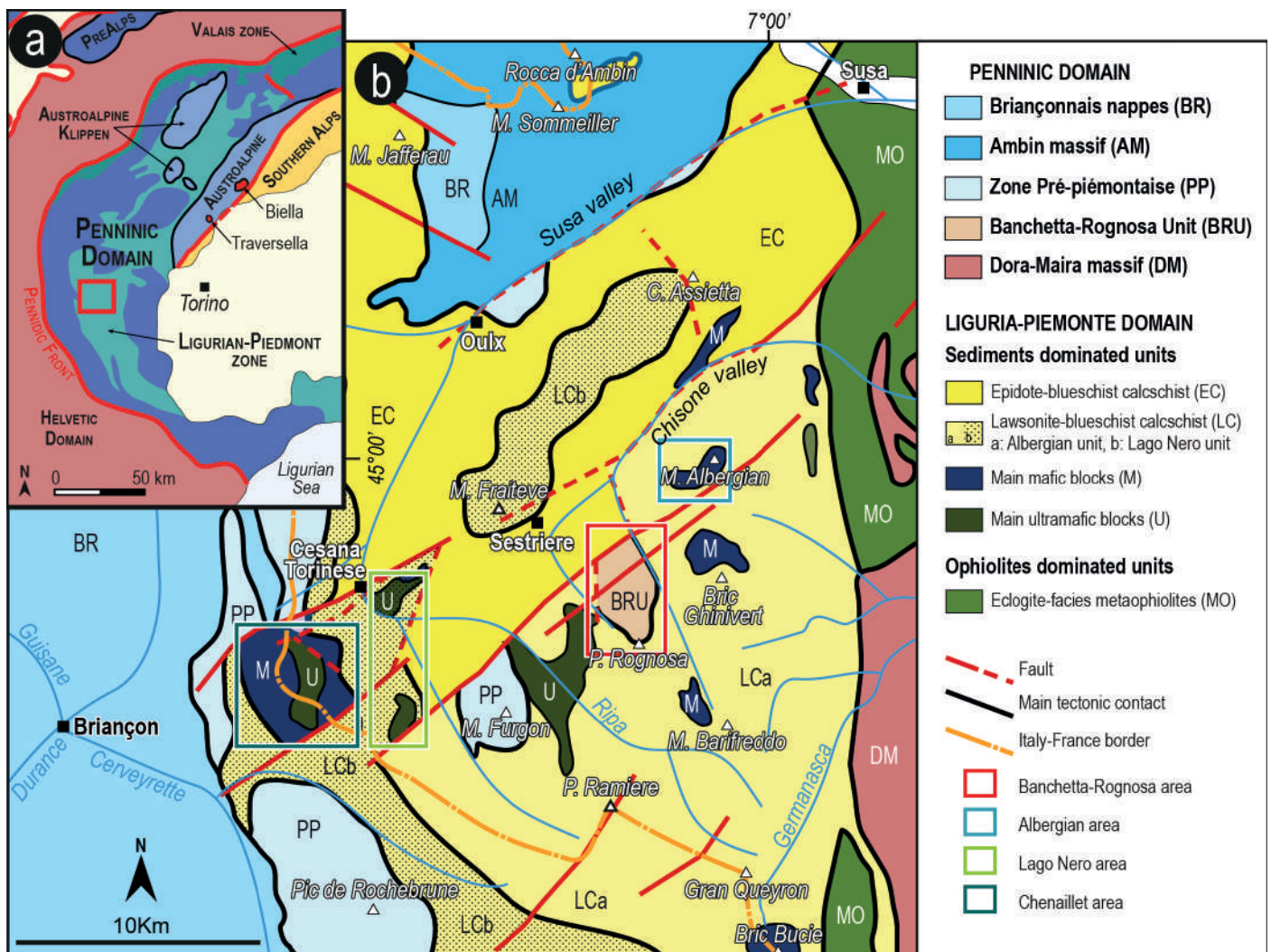


Figure 1 a) Simplified tectonic map of the Western Alps (redrawn and modified from Bigi et al., 1990). b) Schematic geological map of the upper Susa and Chisone valleys (modified from Corno et al., 2021b), the studied units and areas are highlighted with different colored squares.

unit represents a tectonic unit made of both continental- and oceanic-derived rocks, recording eclogite-facies conditions (Corno et al., 2021), iii) the Chenaillet ophiolite has historically been described as a portion of oceanic lithosphere with no sedimentary cover, which escaped Alpine HP metamorphism, although this project found evidence of LT-blueschist metamorphism (Corno et al., 2023).

In last years, several authors focused on the reconstruction of pre-collisional paleo-geographic setting, by comparison with studies on modern tectonic plate boundaries and architecture of ocean floors (Mohn et al., 2012, 2014; Festa et al., 2015; Lagabrielle et al., 2015; Decarlis et al., 2017; Tartarotti et al., 2021). Similar studies are quite difficult for units forming the HP-axial sector of the Alpine belt (e.g. Beltrando et al., 2012, 2014). This study aimed to try to restore the relative positions of the four studied units with respect to the continental margins and the complex framework of the Alpine Tethys.

THE STUDIED UNITS

The Banchetta -Rognosa tectonic unit

The Banchetta-Rognosa tectonic unit (BRU hereafter) consists of two juxtaposed successions respectively re-

cording the Mesozoic tectono-depositional evolution of (i) a continental margin, i.e., Monte Banchetta succession, and (ii) a neighboring oceanic sector, i.e. Punta Rognosa succession, both covered by the same post-rift sediments consisting of Upper Jurassic?-Cretaceous carbonate micaschist. Several papers by the Authors focused on the lithostratigraphy, petrography, and metamorphic evolution of the oceanic succession (Corno et al., 2019) as well as the continental one (Corno et al., 2021a, b). The result of extensive and detailed lithostratigraphic and structural field studies (supported by petrographic analyses) are reported in a 1:6,500 scale geological map (Corno et al., 2021a), which focuses also on the complex relationship between the two successions.

Main lithostratigraphic features of the BRU

The oceanic succession (Corno et al., 2019), is made of serpentinized mantle overlain by syn-rift polymictic meta-breccia (with both oceanic- and continental-derived clasts) and discontinuous meta-sandstone bodies with dolostone clasts and blocks. The thick post-rift sequence is characterized by calcschist, locally embedding ophiolitic bodies.

On the other hand, the continental succession of the BRU, whose main features can be observed in the Tron-

cea valley, is made of a crystalline basement (with minor polymetamorphic bodies), overlain by scarce levels of quartzite and a thick dolomitic sequence, followed by syn-rift carbonate-bearing quartzite, polymictic meta-breccia with quartzite and dolostone clasts within a carbonate matrix with fuchsite (Cr-bearing white mica), and black micaschist. Locally, discontinuous meta-sandstone bodies with dolostone clasts occur, quite similar to those occurring in the oceanic succession. Also, the continental succession is covered by the thick post-rift sequence made of calcschist, occurring on the oceanic succession.

Constrained metamorphic conditions

For thermodynamic modeling purposes, a main focus has been given to the continental succession, better preserving the mineral assemblages useful for the isochemical phase diagram approach. However, thorough petrographic analyses have been carried out on both successions. Since conventional thermobarometry pointed to metamorphic conditions at the doorstep of the eclogite-facies field, the isochemical phase diagram approach proved to be necessary to better constrain the peak P-T conditions. Three samples, were selected on the basis of their mineral assemblages and proved to be the most suitable for this kind of approach. More specifically, the HP tectono-metamorphic evolution of the BRU was constrained based on a Cld+Ph-bearing glaucophanic schist (sample AC44), a Cld-bearing, partially retrogressed, glaucophanite (sample VT8), and a Jd-bearing gneissic micaschist. The isochemical phase diagrams were calculated in the system MnNKFMASOH (MnO-Na₂O-K₂O-FeO-MgO-Al₂O₃-SiO₂-O₂-H₂O) for samples AC44 and AC74 and in the system NKFMASOH (Na₂O-K₂O-FeO-MgO-Al₂O₃-SiO₂-O₂-H₂O) for sample VT8 (see Corno et al., 2021b for more details).

The three modeled peak P-T conditions (based on observed mineral assemblages and compositional isopleths for chloritoid and amphibole) are: i) 21-22 kbar and 450±25°C for the Cld-Ph bearing glaucophanic schist (AC44); ii) 21-22.5 kbar and 450±20°C for the Cld-bearing glaucophanite (VT8); iii) 21-23 kbar and 470±50°C for the Jd-bearing gneissic micaschist.

Hence, based on the intersection of predicted ellipses, common peak P-T conditions can be constrained at 20-23 kbar and 440-500°C (Corno et al., 2021b).

The Albergian unit

In its general features, the Albergian unit (AU hereafter) is made of a thick succession of Cretaceous calcschist wrapping scattered blocks of oceanic lithosphere (i.e., serpentinite, meta-gabbro and metabasite), locally covered by a thin supra-ophiolitic sequence. The AU embeds the Banchetta-Rognosa tectonic unit, while being juxtaposed to the Lago Nero unit by a NE-SW high angle

fault system.

Main lithostratigraphic features of the AU

In order to investigate the pre-collisional evolution of the oceanic sectors sampled by the AU, this study detailed the lithostratigraphic successions exposed along the Albergian-Gran Mioul mountain ridge, located to East with respect to the village of Prigelato (upper Chisone valley).

In this area, a pluri-hm body of meta-mafic rocks (gabbro apophysis and their volcanic and volcano-sedimentary cover) is embedded by heterogeneous calcschist.

In order to show the complex relationships between different lithologies, five lithostratigraphic logs from different localities have been analyzed, consisting of a clast-supported meta-breccia, dominated by metabasite clasts and blocks, with minor doleritic and gabbro clasts. In addition, rare meta-plagiogranitic clasts have been found, wrapped by the same mafic matrix. The whole meta-mafic body is covered by discontinuous levels of quartzitic meta-sandstone and and/or discontinuous levels of black micaschist, followed by a thick sequence of calcschist.

Constrained metamorphic conditions

The isochemical phase diagram approach was carried out on two samples in order to constrain the peak P-T conditions: i) a Grt+Omp Mg-Al metagabbro (sample 5482) and ii) a plagiogranitic meta-breccia (sample 5681). For this latter one, due to the significant difference in bulk compositions related to different mineral assemblages and proportion, two distinct phase diagrams were calculated, one for the plagiogranitic clasts, and one for the mafic matrix. The P-T pseudosection for sample 5482 was calculated in the system MnNCFMASTH (MnO-Na₂O-CaO-FeO-MgO-Al₂O₃-SiO₂-TiO₂-H₂O). For sample 5681, the P-T pseudosection of the plagiogranitic clasts was calculated in the system NCKFMASTOH (Na₂O-CaO-K₂O-FeO-MgO-Al₂O₃-SiO₂-TiO₂-O₂-H₂O), while that for the mafic matrix was calculated in the system NCKFMASTH (Na₂O-CaO-K₂O-FeO-MgO-Al₂O₃-SiO₂-TiO₂-H₂O). For further details and the representative analyses of the mineral phases occurring in these two samples, please refer to Corno et al., 2022. Modeled peak P-T conditions (based on observed mineral assemblages and compositional isopleths for garnet, white mica, and clinopyroxene) are: i) 21±1.5 kbar and 450±30°C for the Mg-Al metagabbro sample 5482; ii) 18 ± 2 kbar and 410±20°C for the matrix and 21-24 kbar and T < 430°C for the meta-plagiogranitic clasts of sample 5681. Hence, based on the partial overlap of predicted ellipses, common peak P-T conditions can be constrained at 18-20 kbar and 380-420 °C (Corno et al., 2022).

The Lago Nero unit

The Lago Nero unit (LNU hereafter) is made of oceanic

lithosphere covered by a meta-sedimentary sequence similar to the ones of the non-metamorphic Ligurian units of the Apennines. The southern portion of the unit is characterized by a pretty continuous oceanic basement, from the serpentinitized exhumed mantle, meta-basalts and syn- and post-rift covers. On the other hand, in the northern portion, only scattered blocks of oceanic lithosphere occur, and the vast majority of the unit is made of post- and minor syn-rift meta-sedimentary rocks.

Main lithostratigraphic features of the LNU

The complex lithostratigraphy of the LNU has been studied mainly in two typical sectors, i.e. the area around the Lago Nero (orographic left, to the South with respect to Cesana T.se) and the M. Cruzore area (orographic right, to the North with respect to Cesana T.se).

In the Lago Nero section the exhumed mantle (i.e. serpentinite) is covered by meta-limestone (i.e. marble), characterized by thick pluri-decimetric bedding. This marble formation displays gradual transition to the Replatte formation (Lemoine, 1971), made of an alternance of calcschist and marble levels attributed to the Palombini shales of Cretaceous age. The Replatte formation at different lithostratigraphic levels envelopes both oceanic- and continental-derived clasts and blocks. Oceanic blocks are made of metabasite s.l. (meta-basalt, greenstone, mafic meta-breccia, meta-gabbro, etc.) and ophi-carbonate rocks. Continental-derived clasts and blocks occur in smaller dimension, from centimetric to pluri-metric, and usually towards the stratigraphic lows of the Replatte formation. They are mainly made of marble and dolostone blocks, and minor clasts of crystalline basement rocks (i.e. micaschist and quartzite). The Gondran flysch follows upwards, made by an alternance of calcschist and meta-sandstone. In the area around the Cima Fournier the transition between Replatte formation and Gondran flysch is marked by grey to black schists (black shales according to Barfety et al., 1996). The Gondran flysch, up to 20 m in thickness, is mainly made of thin calcschist layers alternated with minor coarse-grained meta-sandstone layers. The following Rocher Renard complex is made by scattered blocks, up to decametric in size, embedded by dark schist. Blocks and clasts come from an oceanic lithosphere and its meta-sedimentary cover. Meta-ophiolitic blocks are made of meta-basalt, ophi-carbonate rocks, serpentinite, and meta-gabbro. Blocks from the meta-sedimentary cover are made of marble and calcschist, presumably from the Replatte formation. Locally, smaller blocks and clasts of meta-chert has been observed.

The M. Cruzore section is made of serpentinite, representing a portion of exhumed mantle (Gambino et al., 2022). In addition, the oceanic crust comprises scattered meta-basalt and meta-gabbro bodies, from plurimetric to pluridecametric in size. Within the meta-mafic rocks a partial lithostratigraphic sequence can be provided, with

pillow-like structures observable in the lowermost stratigraphic levels and rimmed by local hyaloclastite and variolite, while brecciated structures with variolite occur in the uppermost levels. Locally, in the upper part of this mafic sequence, where meta-mafic breccias occur, clasts of plagiogranitic compositions have been found. Scarce, decimetric meta-microconglomeratic levels occur in these meta-mafic rocks. These levels broadly represent the transition between the underlying preserved pillow meta-basalts and the overlying mafic meta-breccia (made of reworked pillow basalts). These levels display a brecciated, matrix-supported texture, with mm to pluri-mm clasts dispersed in a fine-grained matrix.

The transition between meta-mafic rocks and the first syn-rift meta-sediments is well observable on the southern slopes of the M. Cruzore. In this sector, reworked fragments of pillow meta-basalt are intercalated with thin layers of meta-chert. This level is then topped by the lower part of the meta-radiolarite formation, showing in turn thin intercalations of mafic debris. This meta-radiolarite sequence is made by two main terms: a lower part of grey and/or green quartzite, gradually fading into an upper red fine-grained meta-shale. Locally, ghosts of the original radiolarians can still be found as small round shapes forming the rocks.

Constrained metamorphic conditions

Metamorphic conditions of the LNU have been constrained with the conventional thermobarometry approach, combined with microstructural observations and chemical analyses. As for the other units, mainly the mafic rocks of the LNU have been used to constrain the Alpine peak conditions. However, also the detrital bodies (meta-microconglomerate, etc.) have provided useful constrains. The peak event is defined by the Na-clinopyroxene + lawsonite \pm Na-amphibole \pm talc \pm white mica + rutile mineral assemblage. The widespread occurrence of fresh lawsonite constrains P-T peak conditions at minimum \sim 17 kbar and maximum of 400-450°C. The occurrence of rare talc + acmite assemblage in metagabbro confirms this estimation (as reported by Corona et al., 2013). These conditions are in agreement with the high Si content of phengite occurring both in basic and detrital rocks (Si up to 3.70 a.p.f.u.), as suggested by the phengite barometry of Massonne & Schreyer (1987). The maximum extension of the stability field of the talc + jadeite association (as reported by Corona et al., 2013) can sensibly be influenced by Fe³⁺ ratio, clinopyroxene composition and the peculiar occurrence of Na-amphibole.

The Chenaillet ophiolite

The Chenaillet Ophiolite represents a very well-preserved portion of Ligurian-Piedmont ocean in the Western Alps. Historically, the Chenaillet Ophiolite has been

known for its very low temperature - low pressure (LT-LP) Alpine metamorphism, ascribed to obduction processes. However, studies aimed at constraining the peak P-T conditions of Alpine metamorphism are virtually lacking, the general focus having been so far on its high temperature (HT) metamorphism and geochemical features.

Main lithostratigraphic features of the LNU

The Chenaillet Ophiolite (CO hereafter) is made of an oceanic lithospheric succession comprising exhumed mantle, various mafic intrusives (i.e. gabbro *sensu lato*) and a world renown sequence of pillow basalts. Apart from scarce breccias closely related to oceanic lithosphere (Bertrand et al., 1980), post-rift Late Jurassic to Cretaceous sedimentary rocks are absent, in contrast with the neighboring oceanic units which comprise a large amount of post-rift meta-sedimentary rocks.

Mantle peridotite consists of strongly serpentinized lherzolite and harzburgite, with minor pyroxenite, dunitite and wehrlite (Bertrand et al., 1980). Within the highly serpentinized mantle rocks, a thin sequence of layered troctolite and olivine-bearing gabbro less than 1 km in diameter occurs, cross-cut by diorite, dolerite, and basalt dykes. Dolerite, diorite, and basalt dykes usually occur within sheared gabbro, close to high-angle normal faults. Albitite/alkali syenite bodies occur as dikes and sills at the serpentinized peridotite-gabbro boundary throughout the massif (Chalot-Prat, 2005). The well-known volcanic sequence of the CO consists of lava flows, pillow basalts, pillow breccias, and hyaloclastites, with strong affinities with MORB (Mid-Oceanic Ridge Basalt) series.

Constrained metamorphic conditions

The isochemical phase diagram approach was carried out on a gabbro sample in order to constrain the peak P-T conditions: This specific gabbro sample was selected for the thermodynamic modeling because it preserves very well the Alpine peak mineral assemblage (e.g. it contains 6% of lawsonite) and it is devoid of white mica and epidote (both <0.5%), thus allowing to simplify the

system by neglecting K_2O and Fe_2O_3 . The P-T pseudosection was calculated in the system MnNCFMASTH (MnO-Na₂O-CaO-FeO-MgO-Al₂O₃-SiO₂-TiO₂-H₂O). For sample 5681, the P-T pseudosection of the plagiogranitic clasts was calculated in the system NCFMASTH (Na₂O-CaO-FeO-MgO-Al₂O₃-SiO₂-TiO₂-H₂O). The fluid saturation assumption and the effects of Fe^{+3} on the stability of the observed peak mineral assemblage were investigated by calculating two P-M(H₂O) (mol%) and two P-X(Fe₂O₃) isochemical phase diagrams at T = 300°C and T = 350°C, available in Corno et al., 2023. For further details and the representative analyses of the mineral phases occurring in these two samples, please refer to Corno et al., 2023. The unfractionated bulk composition (i.e. the measured bulk), was used for modeling, including both the magmatic and HT-related mineral relicts (i.e. clinopyroxene and HT Ca-amphibole respectively). Modeled peak P-T conditions (based on observed mineral assemblages) constrain a minimum of 9 kbar and 350°C to a maximum of 15 kbar and 450°C, which are compatible with a geothermal gradient of 8-10°C/km.

Alpine peak P-T conditions are further constrained by the overlap with the P-T peak conditions estimated for an albitite sample (made of up to 90% of albitite, omphacite, Ca-amphibole and titanite), delimited by the phase-in curves defined for the mafic system according to Harlow et al. (2015). The overlap between the peak P-T conditions inferred for the albitite and the large stability field of the gabbro assemblage predicted by thermodynamic modeling, further constrains peak Alpine metamorphism at 10-11 kbar and 340-360°C (Corno et al., 2023).

FINAL REMARKS

The challenge of this Ph.D. project was to provide new data to constrain the positions of different Ligurian-Piedmont units within the pre-collisional paleogeographic setting as well as their Alpine tectono-metamorphic evolution.

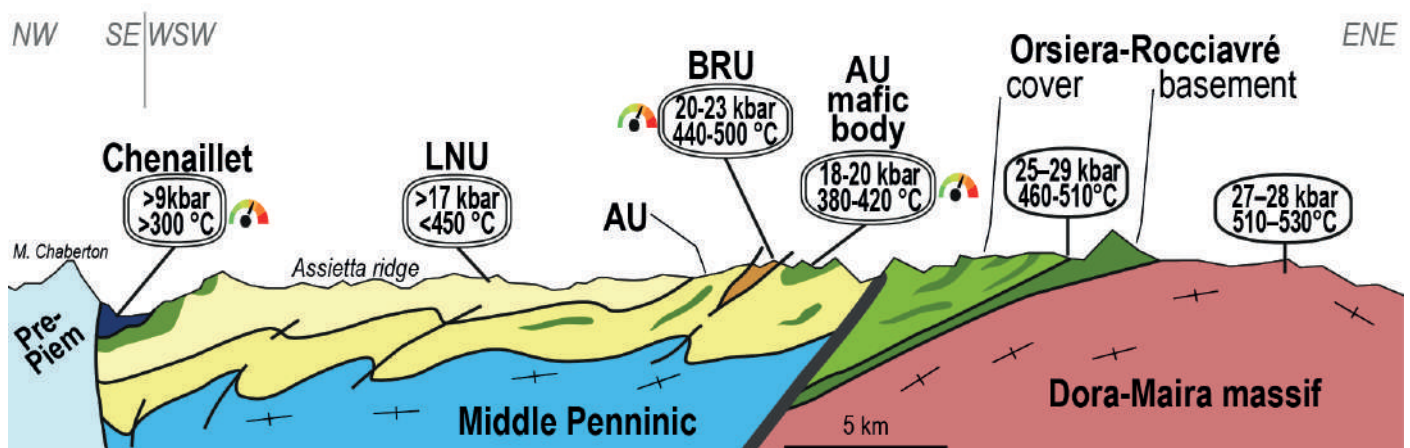


Figure 2 Schematized cross-section along the studied area in the upper Susa and Chisone valleys (exaggerated vertical scale). Peak P-T estimates modeled by the Author are highlighted with small barometer icons (Chenaillet, BRU and AU mafic body). The estimations displayed for the other units are according to the most recent literature available: Manzotti et al., 2022, for Dora-Maira massif; Ghignone et al., 2021, for the Orsiera-Rocciavrè meta-ophiolite (i.e. Internal Piedmont Zone).

Paleogeographic restoration

The Banchetta-Rognosa unit (BRU) sampled a portion of the ocean-continent transition zone, where continental crust and exhumed mantle were adjacent in Mesozoic times (see Corno et al., 2019, 2021a, 2021b). Moreover, the two successions share a common tectono-metamorphic evolution since the earliest event, suggesting that they were already adjacent before (or during) the onset of subduction and Alpine deformation.

In their general features, the Lago Nero unit and the Albergian unit consist of widespread and thick sequences of calcschist, embedding meta-ophiolite bodies. The syn- to lower post-rift deposits of the LNU are characterized by a more abundant continental-derived scree in the detrital levels/bodies (with preserved K-feldspar and zircons) and a coarser grain with larger and angular clasts with respect to the fine-grained quartzitic meta-sandstones of the AU (Corno et al., 2022). These features suggest that the LNU includes continental-derived (meta-) sediments less mature than the AU ones. The meta-sediments of the LNU suffered less transportation than those of the AU and hence an original location of the Lago Nero unit closer to the continental margin can be envisaged.

The Chenaillet ophiolite (CO), as reported by many authors (see Manatschal et al., 2011; Balestro et al., 2019) sampled a portion of oceanic lithosphere, characterized by exhumed mantle, intruded by gabbroic stocks and overlain by basaltic lavas.

Based on these observations, it can be inferred as a major and general conclusion that the LPZ units exposed in the upper Susa and Chisone valleys include different sectors (i.e. units) of the Alpine Tethys, sampled during subduction, and originally occurring in structural highs or in the hanging-wall of detachment faults. These rock bodies were uprooted from the oceanic lithosphere and currently occur embedded in the widespread post-rift meta-sediments within the meta-sedimentary dominated units of the Ligurian-Piedmont zone.

Tectono-metamorphic evolution

The Alpine metamorphic evolution of the units exposed in the investigated area of the Western Alps has been investigated using for the first time the isochemical phase diagram approach.

In particular, the constrained Alpine metamorphic peak conditions are (Fig. 2):

- 20-23 kbar and 440-500°C for the Banchetta-Rognosa unit;
- 18-20 kbar and 380-420°C for the Albergian-Gran Mioul body of the Albergian unit;
- > 9 kbar and >300°C for the Chenaillet ophiolite.

Hence, it is worth stressing that:

- the BRU could represent one of the westernmost eclo-

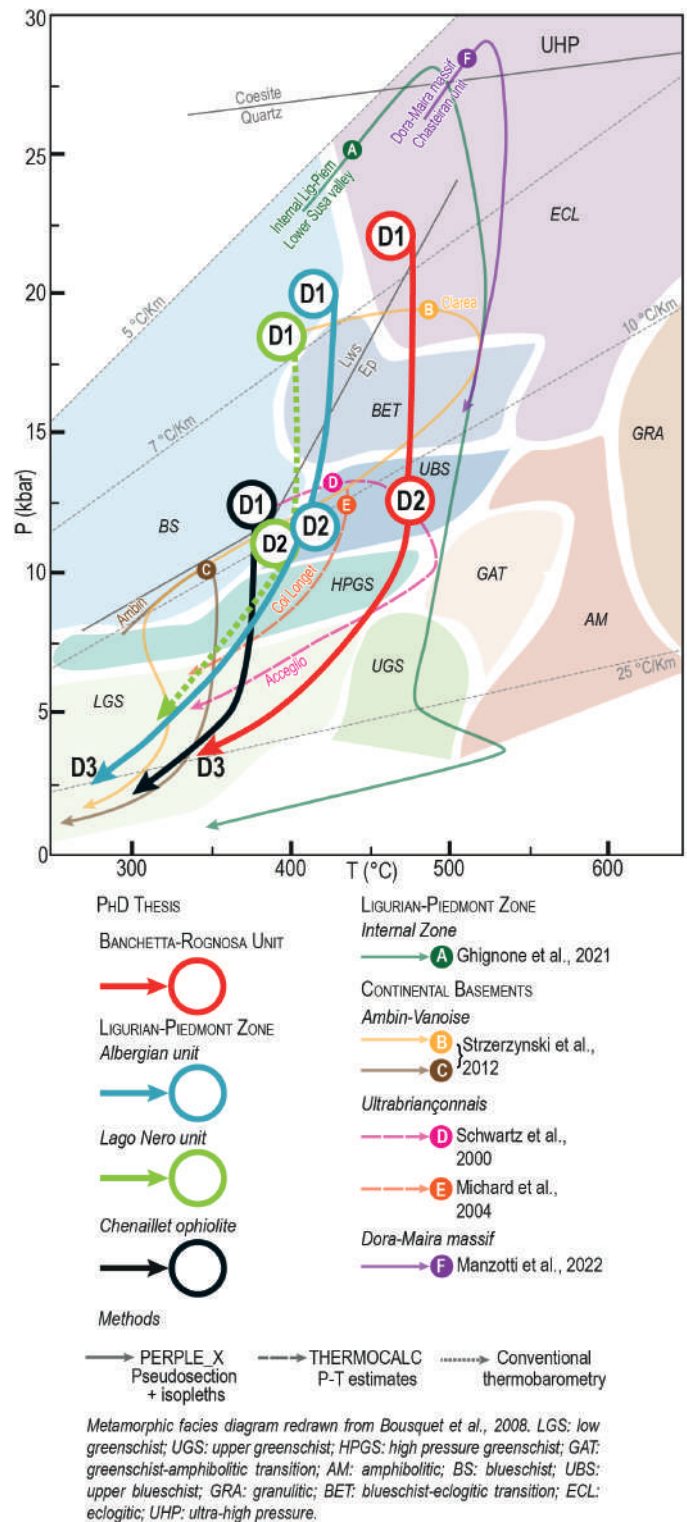


Figure 3 Compilation of P-T paths of different units of the Western Alps, for comparison with the studied units from the upper Susa and Chisone valleys. Studied units (Banchetta-Rognosa unit, Albergian unit, Lago Nero unit, and Chenaillet ophiolite) are reported with thicker lines. Peak conditions were constrained with the isochemical phase diagram approach, while the retrograde exhumation part of the path was qualitatively inferred in the basis of mineral assemblages. Different line patterns indicate different thermobarometric methods, as reported in the legend. Lws-Ep reaction is from Poli & Schmidt (1995), modified below 10 kbar for the modeled bulk compositions.

gitic unit of the Western Alps. This assumption derives from comparison of the peak metamorphic conditions of the BRU with respect to the ones of other eclogitic units on the Middle Penninic known in literature (see Corno et al., 2021b; Fig. 3);

- the general westward decrease in metamorphic peaks is abruptly interrupted by the eclogitic BRU, tectonically embedded within the lawsonite-blueschist AU (Fig. 2). The present emplacement of the BRU within the (slightly) lower grade AU can be tentatively explained taking into account a trans-tensional tectonic regime during exhumation;
- in the blueschist-facies AU and LNU the good and widespread preservation of fresh lawsonite can be related to favorable Ca-rich bulk compositions and fast exhumation processes;
- the new and surprising data on the Alpine metamorphic evolution of the Chenaillet ophiolite (previously considered as anchi- or non-metamorphic) invoke for subduction related processes. Therefore, the Chenaillet ophiolite must be considered in the description of the general westward decreasing of Alpine peak metamorphic conditions (Fig. 2,3).
- this latter assumption brings with it the consequence that the geothermal gradient along the subduction channel, in this sector of the Western Alps (8°C/km according to Agard, 2021), could be revised and lowered to 6-7°C/km (Fig. 3).

REFERENCES

- Agard, P., Jolivet, L., & Goffé, B. (2001): Tectonometamorphic evolution of the Schistes Lustres Complex; implications for the exhumation of HP and UHP rocks in the Western Alps. *B. Soc. Geol. Fr.*, **172(5)**, 617-636.
- Agard, P. (2021): Subduction of oceanic lithosphere in the Alps: Selective and archetypal from (slow-spreading) oceans. *Earth Sci. Rev.*, 103517.
- Balestro, G., Festa, A., & Dilek, Y. (2019): Structural architecture of the Western Alpine Ophiolites, and the Jurassic seafloor spreading tectonics of the Alpine Tethys. *J. Geol. Soc.*, **176(5)**, 913-930.
- Barale, L., Console, F., Corno, A., Frasca, G., Mosca, P., & Pantaloni, M. (2022): The geology of the Western Alps through the field notebooks of Secondo Franchi (1859-1932). *Ital. J. Geosci.*, **141(1)**, 120-143.
- Barfety, J. C., Lemoine, M., Graciansky, P. C. (de), Tricart, P., & Mercier, D. (1996): Notice explicative, carte géologique de la France (1/50 000), feuille Briançon (823). *Bureau de Recherche Géologiques et Minières, Orléans*.
- Beltrando, M., Frasca, G., Compagnoni, R., & Vitale-Brovarone, A. (2012): The Valaisan controversy revisited: Multi-stage folding of a Mesozoic hyper-extended margin in the Petit St. Bernard pass area (Western Alps). *Tectonophysics*, **579**, 17-36.
- Beltrando, M., Manatschal, G., Mohn, G., Dal Piaz, G. V., Vitale Brovarone, A., & Masini, E. (2014): Recognizing remnants of magma-poor rifted margins in high-pressure orogenic belts: The Alpine case study. *Earth Sci. Rev.*, **131**, 88-115.
- Bertrand, J., Steen, D. M., Tinkler, C., & Vuagnat, M. (1980): The melange zone of the col du Chenaillet (Montgenèvre ophiolite, Hautes-Alpes, France). *Arch. Sci.*, **33(2-3)**, 117-138.
- Beyssac, O., Rouzaud, J. N., Goffé, B., Brunet, F., & Chopin, C. (2002): Graphitization in a high-pressure, low-temperature metamorphic gradient: a Raman microspectroscopy and HRTEM study. *Contrib. to Mineral. Petrol.*, **143**, 19-31.
- Bigi, G., Castellarin, A., Coli, M., Dal Piaz, G. V., Sartori, R., Scandone, P., & Vai, G.B. (1990): Structural Model of Italy scale 1:500.000, sheet 1. C.N.R., Progetto Finalizzato Geodinamica, SELCA Firenze.
- Bousquet, R., Oberhänsli, R., Goffé, B., Wiederkehr, M., Koller, F., Schmid, S. M., Schuster, R., Engi, M., Berger, A., & Martinotti, G. (2008): Metamorphism of metasediments at the scale of an orogen: a key to the Tertiary geodynamic evolution of the Alps. *Geol. Soc. London*, **298(1)**, 393-411.
- Chalot-Prat, F. (2005): An undeformed ophiolite in the Alps: Field and geochemical evidence for a link between volcanism and shallow plate tectonic processes. *Geol. Soc. Am. Spec. Pap.*, **388**, 751.
- Corno, A., Mosca, P., Borghi, A., & Gattiglio, M. (2019): Lithostratigraphy and petrography of the Monte Banchetta-Punta Rognosa oceanic succession (Troncea and Chisonetto Valleys, Western Alps). *Ofioliti*, **44(2)**, 83-95.
- Corno, A., Mosca, P., Gattiglio, M., & Borghi, A. (2021a):- Geological map of the Monte Banchetta - Punta Rognosa area (Troncea valley, Western Alps). *J. Maps*, **17(2)**, 150-160.
- Corno, A., Groppo, C., Mosca, P., Borghi, & Gattiglio, M. (2021b): Eclogitic metamorphism in the Alpine far-west: petrological constraints on the Banchetta-Rognosa tectonic unit. *Swiss J. Geosci.*, 114:16.
- Corno, A., Mosca, P., Groppo, C., Borghi, A., & Gattiglio, M. (2022): More widespread than supposed: preserved lawsonite in the blueschist-facies ophiolitic bodies from the Albergian unit (Liguria-Piemonte zone, Western Alps). *Ofioliti*, **47(2)**, 137-154.
- Corno, A., Groppo, C., Borghi, A., Mosca, P., & Gattiglio, M. (2023): To be or not to be Alpine: New petrological constraints on the metamorphism of the Chenaillet Ophiolite (Western Alps). *J. Metamorph. Geol.*, 1-21.
- Corona, J.C., Jenkins, D. M., & Holland, T.J.B. (2013): Constraints on the upper pressure stability of blueschist facies metamorphism along the reaction: glaucophane = talc + 2 jadeite in the Na₂O-MgO-Al₂O₃-SiO₂-H₂O system. *Am. J. Sci.*, **313**, 967-995.
- Dal Piaz, G. V., Bistacchi, A., & Massironi, M. (2003): Geological outline of the Alps. *Episodes J. Int. Geosci.*, **26(3)**, 175-180.
- Decarlis, A., Beltrando, M., Manatschal, G., Ferrando, S., & Carosi, R. (2017): Architecture of the distal Pied-

- mont-Ligurian rifted margin in NW Italy: Hints for a flip of the rift system polarity. *Tectonics*, **36(11)**, 2388-2406.
- Festa, A., Balestro, G., Dilek, Y., & Tartarotti, P. (2015): A Jurassic oceanic core complex in the high-pressure Monviso ophiolite (western Alps, NW Italy). *Lithosphere*, **7(6)**, 646-652.
- Gambino, F., Agostoni, A., Barale, L., Bonetto, S., Borghi, A., Corno, A., & Mosca, P. (2022): Il Verde Cesana: una storica pietra ornamentale delle Alpi Occidentali. In: Bove, A., Masciocco, L., Sassone, P. *Geologia Ambientale in Piemonte e Valle d'Aosta. Monografie di Geologia Ambientale. Edizioni SIGEA*, 124-128.
- Ghignone, S., Borghi, A., Balestro, G., Castelli, D., Gattiglio, M., & Groppo, C. (2021): HP tectono-metamorphic evolution of the Internal Piedmont Zone in Susa Valley (Western Alps): New petrologic insight from garnet+ chloritoid-bearing micaschists and Fe-Ti megacryst. *J. Metamorph. Geol.*, **39(2)**, 391-416.
- Harlow, G. E., Tsujimori, T., Sorensen, S. S. (2015): Jadeitites and Plate Tectonics. *Annu. Rev. Earth Planet Sci.*, **43**, 105-138.
- Lagabrielle, Y., Brovarone, A. V., Ildefonse, B. (2015): Fossil oceanic core complexes recognized in the blueschist metaophiolites of Western Alps and Corsica. *Earth Sci. Rev.*, **141**, 1-26.
- Malusà, M. G., Faccenna, C., Garzanti, E., Polino, R. (2011): Divergence in subduction zones and exhumation of high pressure rocks (Eocene Western Alps). *Earth Planet. Sci. Lett.*, **310(1-2)**, 21-32.
- Manatschal, G., Sauter, D., Karpoff, A. M., Masini, E., Mohn, G., Lagabrielle, Y. (2011): The Chenaillet ophiolite in the French/Italian Alps: An ancient analogue for an oceanic core complex? *Lithos*, **124(3-4)**, 169-184.
- Manzotti, P., Schiavi, F., Nosenzo, F., Pitra, P., & Ballèvre, M. (2022): A journey towards the forbidden zone: a new, cold, UHP unit in the Dora-Maira Massif (Western Alps). *Contrib. to Mineral. Petrol.*, **177(6)**, 59.
- Massonne, H. J. & Schreyer, W. (1987): Phengite geobarometry based on the limiting assemblage with K-feldspar, phlogopite and quartz. *Contrib. to Mineral. Petrol.*, **96**, 212-224.
- Mohn, G., Manatschal, G., Beltrando, M., Masini, E., & Kuzsniir, N. (2012): Necking of continental crust in magma-poor rifted margins: Evidence from the fossil Alpine Tethys margins. *Tectonics*, **31**, TC1012.
- Mohn, G., Manatschal, G., Beltrando, M., & Hauptert, I. (2014): The role of rift-inherited hyper-extension in Alpine-type orogens. *Terra Nova*, **26**, 347-353.
- Mosca P. & Barale L. (2022): Geological explorations in the Italian-French cross-border areas (Western Alps) from 19th to early 20th century. *Rend. Online Soc. Geol. It.*, **57**, 2-16.
- Pfiffner, O.A., Lehner, P., Heitzmann, P., Mueller, St., & Steck, A. (1997): Deep structure of the Swiss Alps. Birkhäuser Verlag, Basel, 380 p.
- Poli, S. & Schmidt, M.W. (1995): H₂O transport and release in subduction zones: Experimental constraints on basaltic and andesitic systems. *J. Geophys. Res.*, **100**, 22299-22314.
- Roure, F., Choukroune, P., & Polino, R. (1996): Deep seismic reflection data and new insights on the bulk geometry of mountain ranges. *C. R. Acad. Sci. Série 2. Sciences de la terre et des planètes*, **322(5)**, 345-359.
- SERVIZIO GEOLOGICO D'ITALIA (2002): Carta Geologica d'Italia alla scala 1:50.0000, F. 132-152-153 Bardonecchia Regione Piemonte, Direzione Regionale dei servizi Tecnici di Prevenzione. Litografia Geda, Nichelino. Torino.
- SERVIZIO GEOLOGICO D'ITALIA (2020): Carta Geologica d'Italia alla scala 1:50.0000, F. 171 Cesana. http://www.isprambiente.gov.it/Media/carg/171_CESANA_TORINESE/Foglio.html.
- Tartarotti, P., Martin, S., Festa, A., & Balestro, G. (2021): Metasediments Covering Ophiolites in the HP Internal Belt of the Western Alps: Review of Tectono-Stratigraphic Successions and Constraints for the Alpine Evolution. *Minerals*, **11(4)**, 411.

New frontiers of mineralogical and structural data analysis in the era of machine learning: tools for modern petrography

Alberto D'Agostino

Dipartimento di Scienze Biologiche, Geologiche ed Ambientali, Università degli Studi di Catania, Corso Italia 57, Catania, 95129, Italia

DOI:10.19276/plinius.2023.01.005

INTRODUCTION

In modern petrography an increasingly significant role is played by automated numerical computations, which determines a higher demand of quantitative analysis. While petrographers' experience still plays a huge role in the recognition of specific features in rocks, it may also lead to misinterpretations driven by subjectiveness. Hence, numerous statistical analyses can be applied on rocks to objectively extract quantitative information through advanced software solutions. However, while machines outperform humans in long and recursive tasks, computer-driven analyses can be misleading and may introduce other kinds of biases if not properly overseen by an expert operator. Therefore, petrologists' experience is still fundamental to validate machine-generated data and identify petrogenetic processes.

Machine learning (ML) algorithms have been widely experimented to support petrography, by processing several types of petrographic data, such as bulk-rock chemistry (e.g., Ren et al. 2019; Itano et al., 2020) and optical thin section images (e.g., Su et al., 2020; Visalli et al. 2021). Optical scans of rocks thin sections, however, can sometimes be a complex type of input to process, and although efforts have been made towards the realization of databases of optical thin section images (e.g., Quinn et al., 2011), an open-access archive of standardized and labeled data is missing. X-ray elemental maps are yet another type of input data that significantly benefits from the application of ML algorithms. Unlike punctual chemical analyses, the information is not scattered and prevents possible biases introduced by the choice of points locations. Therefore, powerful tools have been developed to quantify X-ray maps (e.g., Lanari et al., 2014; Arganda-Carreras et al., 2017; Ortolano et al., 2018). Generally, the acquisition of X-ray elemental maps and BSE maps is an efficient and relatively cheap process; however, an online structured database of labelled X-ray maps or BSE maps is again missing. In this scenario, X-Min Learn is here presented. This stand-alone software allows an interactive and friendly application of ML techniques for

automatically identifying minerals from EDS and WDS X-ray maps and any other type of multi-spectral image data, including, for example, BSE maps. It also allows the development of custom ML models for specific research needs in a friendly way, meeting the needs of users not experienced in computer coding.

Nevertheless, usually fabric plays a central role in the final properties of the lithotypes as well. In this view, ArcStereoNet, which has already been published in Ortolano et al. (2021), is also presented. This ArcGIS® toolbox, useful for the statistical analysis and projection of structural data, allows the comparison of oriented data from the outcrop scale to the thin section scale within the same ArcGIS® project. ArcStereoNet allows the application of statistical analysis on stereographic projections and rose diagrams, while also taking full advantage of default GIS mapping processes, expanding the potential of other pioneering tools (e.g., Kociánová & Melichar, 2016).

X-MIN LEARN

The current free software for the classification of X-ray maps (e.g., Lanari et al., 2014; Arganda-Carreras et al., 2017; Ortolano et al., 2018) implement unsupervised and supervised classifiers. The latter are usually trained on specific user-drawn regions of interest (ROIs) and then employed to classify the full sample. While this approach (referred to as "lazy learning") often yields very accurate results, it may also introduce dangerous user-driven biases (Nickerson, 1998; Mehrabi et al., 2021). Lazy learners just memorize the information and then use it to classify new data by comparison (Hendrickx & Van Den Bosch, 2005). On the other hand, "eager learners" process the training data to extract a function that describes the relationships occurring between the features of the training data, hence producing a generalized enough model that can foresee pixel variance within the same mineral classes.

X-Min Learn (XML) implements both unsupervised and lazy supervised classifiers as well. In addition to that, however, it also includes a collection of interactive

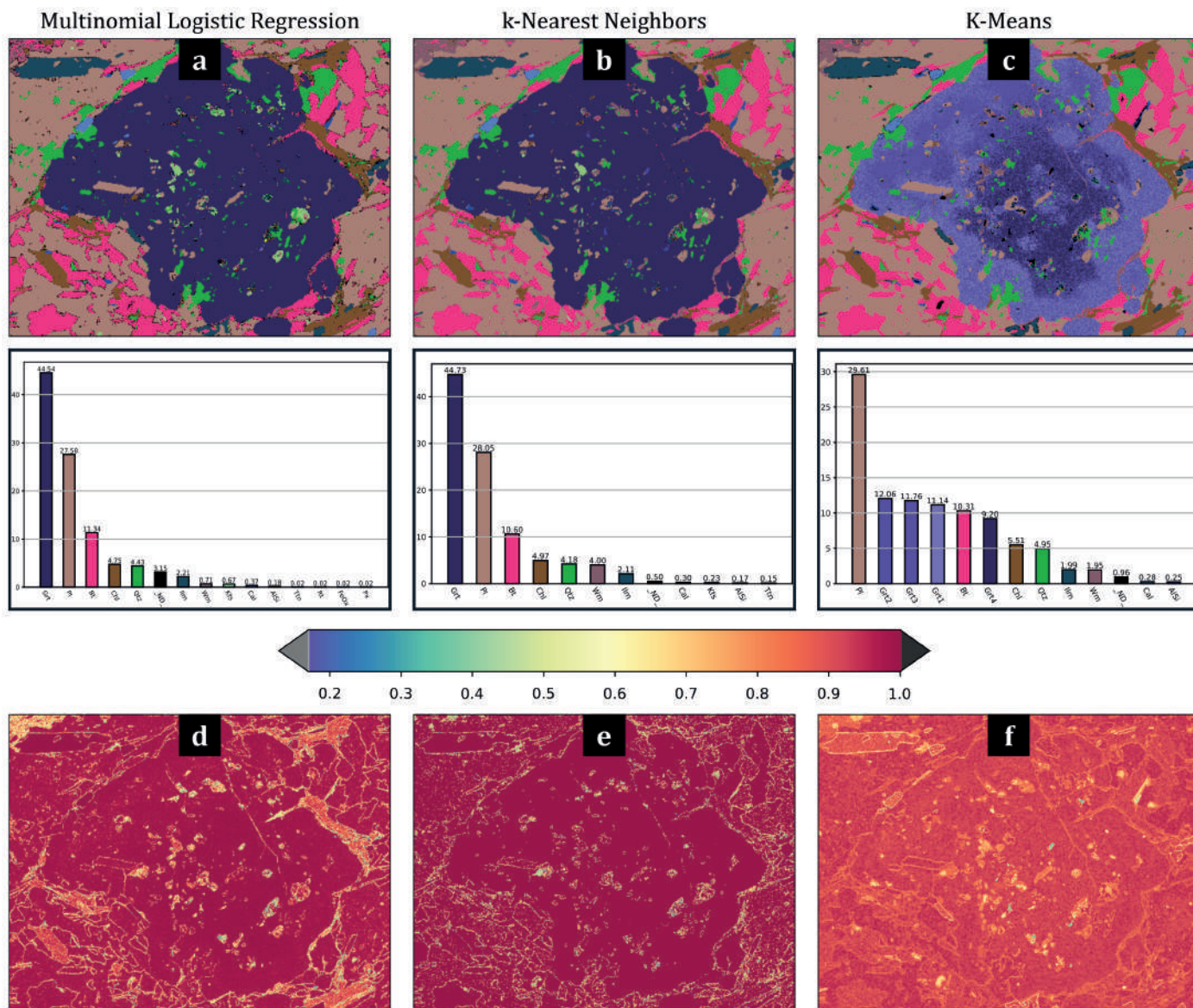


Figure 1 Sample classification using the three classifiers of X-Min Learn: (a) MLR, (b) k-NN, (c) K-Means with (d, e, f) their linked probability maps.

tools for a step-by-step development of custom eager ML models within its “developer’s toolkit”, simplifying the compilation of ground truth datasets and including statistics and graphics useful for the inspection of learning processes. After a custom model is stored, it can be employed to classify new samples automatically, not requiring users to trace additional training ROIs.

Classifiers

X-Min Learn provides three ML algorithms to identify minerals: K-Means (MacQueen, 1967), an unsupervised classifier, K-Nearest Neighbours (k-NN – Cover & Hart, 1967) a lazy supervised classifier and Multinomial Logistic Regression (MLR – Bridle, 1990) a user-trainable eager supervised classifier. They all generate a mineral map and an associated probability map, this latter displaying the classification confidence score of each pixel (Fig. 1d-f). Probability maps are useful for highlighting pixels located at the boundary of two different minerals or near fractures, displaying a mixed chemical composition (i.e., mixed pixels). This score can be used as a rejection factor

to exclude low confidence pixels, providing a stronger user control.

In order to compare the classifiers’ performance, they are here tested on SEM-EDS X-ray maps collected from a thin section of a metamorphic rock. The classification results are displayed in Fig. 1. The time required for the computation was comparable for each classifier (i.e., under 10 seconds). Both k-NN and K-Means, however, required additional time to either draw training ROIs or set the appropriate number of clusters and label them. The MLR model was previously trained using other metamorphic rocks samples collected from different outcrops and lithotypes, and therefore did not require additional training time, achieving a fully automatic mineral classification (Fig. 1a). It assigned some pixels to mineral classes that are not truly occurring in the analyzed sample (i.e., FeOx, Px, and Rt, namely iron oxide, pyroxene, and rutile). These are noisy pixels, that the model assumes as true mineral classes. Although some of them may just be excluded with a confidence threshold, this issue can be fixed with post-processing operations. The overall re-

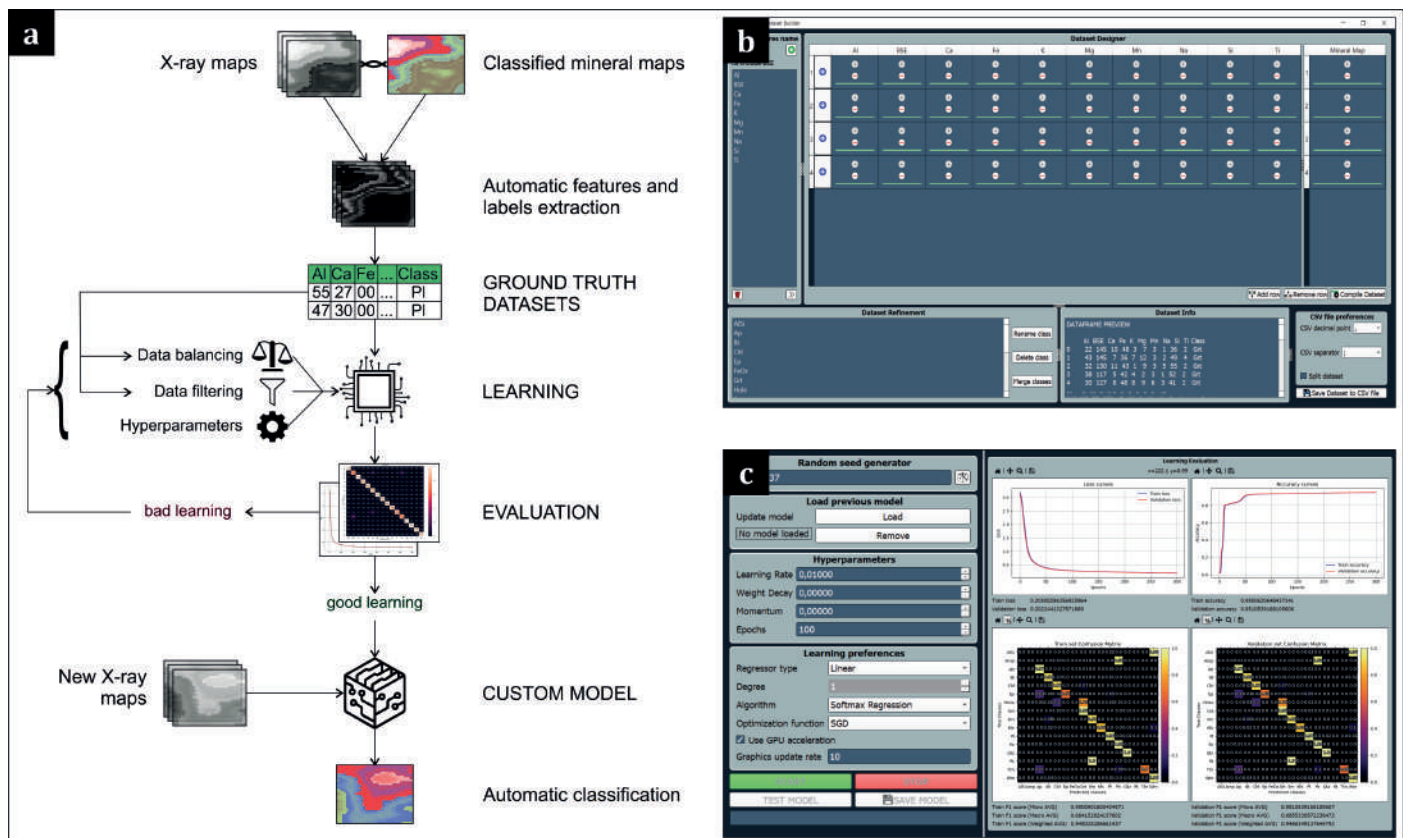


Figure 2 a) Workflow of the developer's toolkit, that allows users to build custom ML models with interactive tools, such as the Dataset Builder (b) and the Model Learner (c)

result is in accordance with that of the other classifiers. The k -NN classifier was steered by the operator, who traced several training ROIs on the occurring mineral phases, and, therefore, the mineral map displays the expected classes (Fig. 1b). While this behaviour is appreciated because provides a stronger user control over the classification, it can also be a dangerous source of sampling and confirmation biases (Nickerson, 1998; Mehrabi et al., 2021). The main drawback is that tracing the training ROIs is time consuming and is required for each analysis. The K -Means differs from the previous classifiers as it employs an unsupervised learning strategy to cluster the data into a K number of classes defined by the user. Although being the most unbiased of the available classifiers, the main drawback of K -Means is that its output classes are not labelled with mineral names, thus the result must be interpreted. Furthermore, it can sometimes struggle with uneven sized clusters, making it not the best choice when analyzing rocks with very imbalanced mineral amounts. Indeed, since garnet displays a high number of pixels (majority class), K -Means separates its zonation patterns in different clusters (i.e., Grt1, Grt2, Grt3, Grt4) at the expenses of minority classes such as titanite (Ttn) and K -feldspar (Kfs) that are not detected (Fig. 1c).

A sub-class analysis can also be achieved with XML (e.g., identification of mineral zonation patterns), by recursively applying the algorithms to already classified mineral maps. The data is automatically masked in order to focus the sub-phase classification only on the selected

class. This process can be repeated an unlimited number of times, also using a sequence of different classifiers.

Phase Refiner

The Phase Refiner allows the removal of noisy pixels (i.e., small classification errors) produced by a classifier, which can negatively affect further analysis on mineral maps (e.g., sub-phase identifications). It provides image processing algorithms in two modalities: basic mode and advanced mode. The basic mode allows the application of a maximum frequency filter to smoothen the entire mineral map, while the advanced mode provides binary morphological operations to refine each mineral class individually. In both modes, users can set the sliding window size and shape to obtain different refinement results. In advanced mode ROIs can be traced to restrict the refinement only to specific areas of the sample and several algorithms can be consecutively applied on different phases, guaranteeing a complete user control over the final result. Six different algorithms are available: Erosion, Dilation, Opening, Closing, Erosion + Reconstruction and Fill Holes. Refined and validated mineral maps could, in turn, be employed as ground truth data to train new ML models.

Developer's toolkit

X-Min Learn is the first mineral-oriented software that allows users to train mineral classifiers by providing a collection of interactive tools for a step-by-step development of custom eager ML models, using fully classi-

fied and validated samples as training data (Fig. 2). A lazy classifier trained with user-drawn ROIs is prone to be affected by confirmation bias (Nickerson, 1998), as operators are led to modify the ROIs multiple times until the model generates a result that aligns with their initial hypothesis. Fully classified samples, on the other hand, provide training data with a larger intraclass variance, since all their pixels are processed rather than just those contained within arbitrary ROIs. The evaluation of XML's custom classifiers, moreover, is not based on the result of a specific classification (i.e., another possible source of confirmation bias), but rather on graphics and statistics during the learning process. Finally, another advantage of providing the instruments to build custom ML classifiers is that users can freely choose how to train their models, potentially developing highly specialized classifiers. The developer's toolkit gathers tools for ground truth datasets management (Dataset Builder - Fig. 2b) and for the actual training of custom machine learning models (Model Learner - Fig. 2c).

Dataset Builder

The Dataset Builder automatizes the compilation of a human readable, machine friendly, standardized dataset from validated examples of already classified data (i.e., ground truth data). Each instance (i.e., row) of such dataset is populated with the features (the numerical values stored in the input maps' pixels) and the corresponding labels (mineral class stored in the classified mineral maps). Users can also operate several dataset refinement operations (e.g., renaming, deleting and merging mineral classes). The dataset is saved as a CSV file; this file format was chosen for both its wide compatibility and its popularity among most users.

Model Learner

The Model Learner allows users to stepwise build new custom ML models after having compiled a ground truth dataset with the Dataset Builder. Custom models can be tailored to solve various tasks, from recognizing the most common mineral classes in different rock types, to identifying intra-class variabilities of individual mineral species. Users may also develop models for classifying specific lithotypes or even samples. Moreover, the Model Learner allows users to update their models with new training data, refining them over time.

The adopted ML algorithm is the Multinomial Logistic Regression (Eq. 1), which is paired with the Cross-Entropy loss function for the quantitative evaluation of the model's errors (Eq. 2) and the gradient descent algorithm for the model's optimization (Eq. 3). Here ϑ are the model's internal parameters, x the input features, K the number of mineral classes, κ the class id (with $\kappa \in [0, K)$), y the true mineral class, N the train set size, ε the learning iteration, η the learning rate, λ the weight decay and μ

the momentum.

$$h_{\vartheta}^{(\kappa)}(x) = \frac{e^{\vartheta^{(\kappa)}T x}}{\sum_{i=0}^{K-1} e^{\vartheta^{(i)}T x}} \quad (1)$$

$$\mathcal{L}(\vartheta) = -\frac{1}{N} \sum_i^N \sum_{\kappa=0}^{K-1} 1\{y_i = \kappa\} \log(h_{\vartheta}^{(\kappa)}(x_i)) \quad (2)$$

$$\vartheta_j^{\varepsilon} = \vartheta_j^{\varepsilon-1} - \eta \cdot \left(\frac{\partial \mathcal{L}_{\vartheta_j}}{\partial \vartheta_j} + \mu \vartheta_j^{\varepsilon-1} \right) - \lambda \eta \vartheta_j^{\varepsilon-1} \quad (3)$$

The learning operations consist of an empirical fine tuning of the model's hyperparameters (i.e., ε , η , λ , μ) performed by users with the aim of optimizing the model's performance. Such operations are reiterated several times with different settings, until a satisfactory performance is achieved. The tool provides interactive instruments for the evaluation of the performance, such as learning scores, loss curves and confusion matrices (Fig. 2c). The automatic pseudo-randomizations that are operated during the learning session are controlled by a random seed, that can be set for reproducibility purposes. Hence, two learning sessions with same input data and hyperparameters settings will always produce the identical result if the same seed is adopted.

Various pre-processing operations can optionally be performed on the train set, such as polynomial features mapping for the identification of non-linear patterns in the data (Theodoridis & Koutroumbas, 2006) and balancing operations. These last consist of over- and under-sampling algorithms as implemented in the open-source Python library imbalanced-learn (Lemaître et al., 2017 and references therein). They are particularly useful to address the problem of imbalanced datasets (Kaur et al., 2019), which occurs when training data contains different amounts of examples per class, that negatively impact the accuracy of supervised ML classifiers. This issue frequently affects mineralogical datasets, as the amount of minerals extremely differs in rocks depending on the mineral species.

Case study

An application of XML for the extraction of quantitative petrographic data from a natural rock is here described. The collected sample (GC29) consists of a late-Variscan amphibolite from the Aspromonte Unit, NE Sicily (Cirrione et al., 2015 and references therein). From a thin section of GC29, three micro-domains were selected, depicting three relict eo-Variscan garnets surrounded by symplectitic micro-structures. WDS X-ray elemental maps and BSE maps were collected and then analyzed with XML.

The first micro-domain was classified with the k-NN classifier (Fig. 3a). The training ROIs were validated with WDS punctual chemical data and optical microscope analysis. A custom ML model was trained with the de-

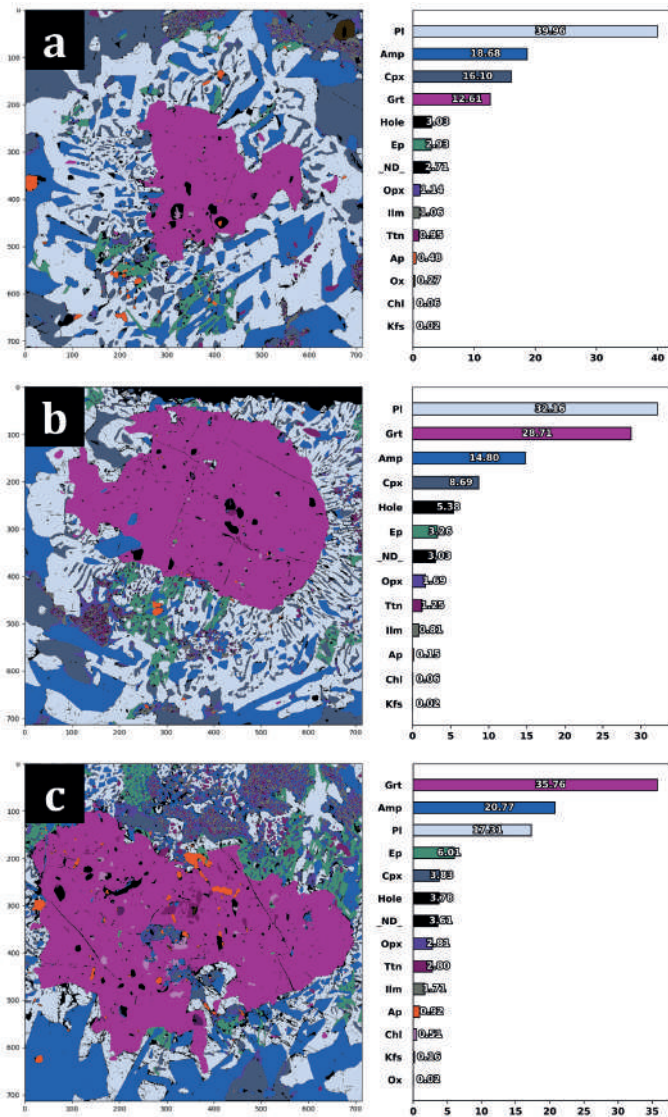


Figure 3 Classification of three micro-domains from GC29 sample. The first micro-domain (a) was classified with k-NN and then processed with the developer's toolkit to generate a custom ML model, which allowed a fully automatic classification of the other two (b, c).

veloper's toolkit using the first micro-domain as ground truth data. Thus, the model was tailored for the classification of the sample GC29, achieving an accuracy of 98.8%. Consequently, the other two micro-domains were automatically classified with such model (Fig. 3b,c). Finally, K-Means classifier was applied on amphibole, clinopyroxene, garnet and plagioclase classes to detect the occurrence of sub-phases in each micro-domain. This allowed the identification of mineral zonation patterns, that were interpreted as the effect of the symplectitic reaction, and the estimation of the reaction rate of garnet porphyroblasts (Fig. 4). This preliminary procedure can be helpful to infer the effective reactant volumes and, in turn, to identify the effective bulk chemistry (Zuluaga et al., 2005) and obtain more reliable pseudo-sections and phase diagrams.

ARCSTEREONET

ArcStereoNet (ASN) is a Python-toolbox that adds geological-oriented tools to ArcGIS®, allowing the projection and the statistical analysis of georeferenced oriented

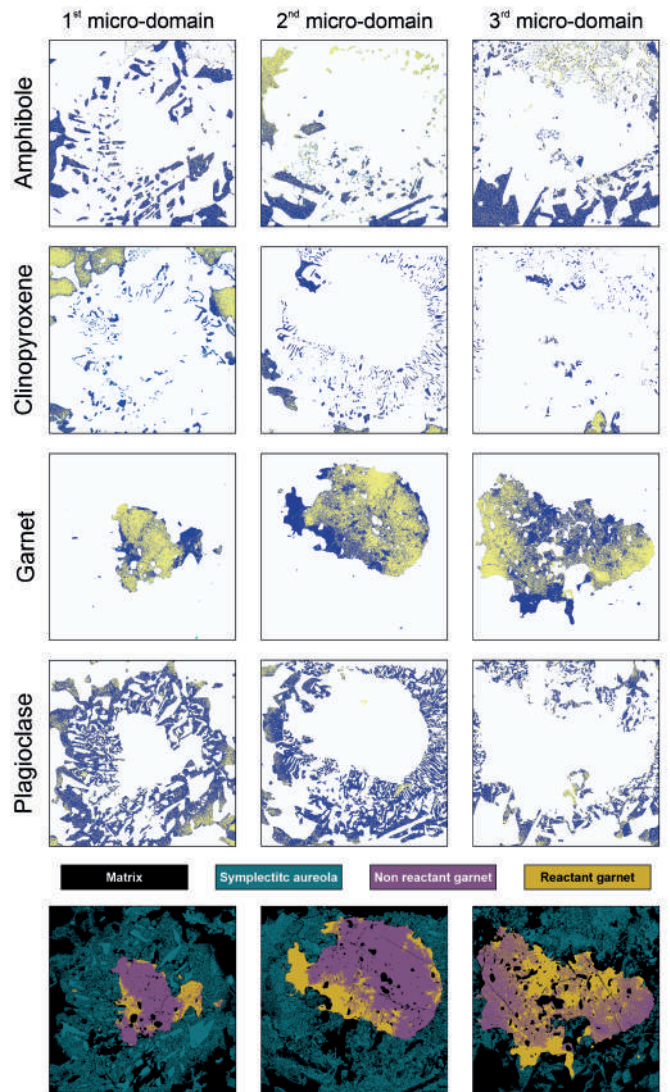


Figure 4 Sub-phase identification achieved with K-Means for amphibole, clinopyroxene, garnet and plagioclase on each micro-domain. The estimated reaction rate of each garnet porphyroblast is, respectively, 0.78, 0.55 and 0.38

data, preserving its coordinates in real space. If paired with ad hoc tools like Micro-Fabric Analyzer (MFA - Visalli et al., 2021), ASN can also process micro-structural data collected from thin sections of rocks. Available statistical functions include contouring, cluster and girdle analysis and mean vectors extraction. A new clustering algorithm (i.e., MEAD - Mean Extractor from Azimuthal Data) is also included in the toolbox. The algorithms can be compared simultaneously, allowing a more reliable interpretation of the data distribution. ASN requires the following information: azimuth angle (dip-direction, strike, trend), dip angle, data format type and data label, which can automatically retrieve by accessing the attribute tables of ESRI® shapefiles. The dataset management operations provided by ArcGIS® can be leveraged to manage and standardize the data.

Tools and algorithms

Three tools are included in ASN: Stereoplots, Rose Diagrams and Graph To Hyperlink, respectively useful to generate stereographic projections and rose diagrams

and to connect them with the geographic position of the data. *Stereoplots* tool generates lower hemisphere equal area or equal angle azimuthal projections, displaying cyclographic traces, and/or poles for planar data, and/or points for linear elements. It allows the overlaying of contours and the comparison of multiple clustering algorithms, as well as the extraction of mean planes or vectors for each cluster. *Rose Diagrams* tool allows the identification of clusters and mean vectors as well. Rose diagrams can also be weighted based on a user-selected parameter included in the input shapefile. *Graph To Hyperlink* tool is useful to link the plots generated by the previous tools to the spatial position of the data in the map. Positions corresponds to the mean latitude and longitude coordinates of plotted data. Users can click on each position to show a popup window displaying the hyperlinked plot.

ASN provides unsupervised algorithms for the recognition of recurring patterns in the data, allowing users to group the data based on orientation similarities (i.e., clustering) and then to extract the average value of each identified group (i.e., mean vector extraction). There are four available algorithms in the *Stereoplots* tool (i.e., MEAD, MEAD + Fisher, K-Means, Bingham) and one in the *Rose Diagrams* tool (MEAD). *MEAD* was created to provide a more user-controlled clustering algorithm. Azimuth and dip tolerance parameters can be fine-tuned to steer the algorithm towards the preferred clustering behaviour, also allowing *MEAD* to discard spurious (i.e., noisy) data. A slightly modified version of *MEAD* is implemented in the *Rose Diagrams* tool to address some specific requirements of such types of projections. *MEAD + Fisher* is an alternative version of *MEAD*, where the mean vector extraction process is carried out by the Fisher function (Fisher et al., 1993). It yields three statistics: R value (mean vector magnitude), confidence radius (mean vector confidence) and K value (dispersion factor). *K-Means* (MacQueen, 1967) strategy differs from *MEAD* mainly for the selection of the starting cluster centroid and for the absence of user-controlled tolerance parameters. *Bingham* (Bingham, 1974) does not perform a clustering process, but rather finds the best fit plane of a girdle-like distribution pattern. A full description and comparison of the algorithms is provided in Ortolano et al. (2021).

Case study

ArcStereoNet was tested by extracting, analyzing and comparing meso-structural (outcrop scale) and micro-structural (thin section scale) oriented data collected at Palmi (SW Calabria) within the Palmi Shear Zone (Fazio et al., 2017; Ortolano et al., 2020; Ortolano et al., 2021), integrated with meso-structural data virtually collected after an aerial photogrammetry survey. The *Stereoplots* tool was employed to analyze both the manually and the virtually collected meso-structural data (Fig. 5),

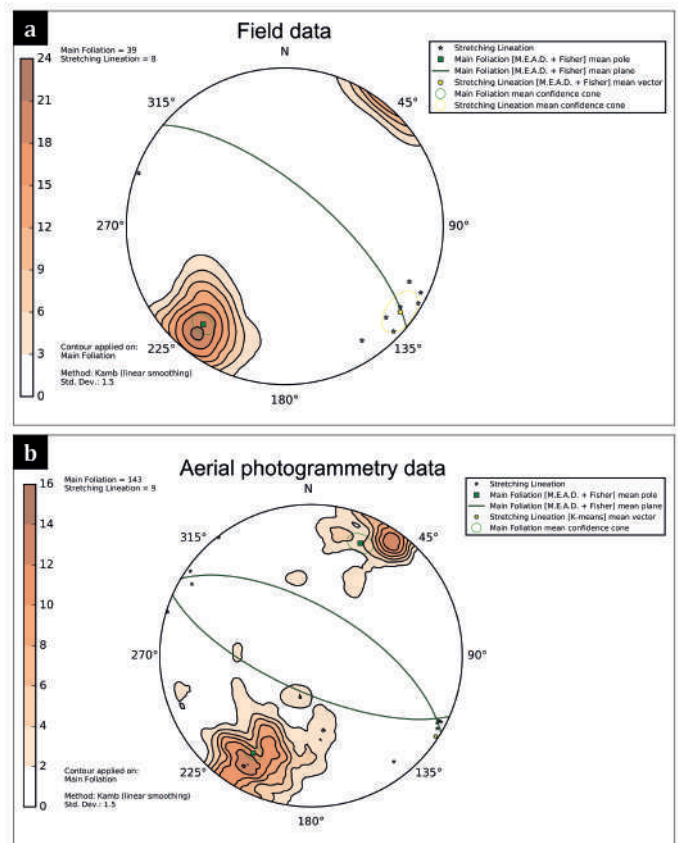


Figure 5 Modified after Ortolano et al. (2021). Meso-structural data (main foliations and stretching lineations) collected (a) manually and (b) after aerial photogrammetry survey

while the *Rose Diagrams* tool allowed the analysis of micro-structural data (Fig. 6), which was extracted with the *Micro Fabric Analyzer* tool (Visalli et al., 2021) from thin sections of samples collected at the same outcrops. The analysis was performed on the minerals belonging to porphyroclastic domains, highlighting their preferred orientations. Here, pre-kinematic clasts behave as rigid phases during sub-simple shearing plastic deformation events (see Ortolano et al., 2020 for further details).

A correlation between the orientation of micro-structural and meso-structural data can be observed; the mean main foliation planes (outcrop scale) and the porphyroclasts (thin section scale) are oriented WNW – ESE. The porphyroclasts, which are surrounded by quartz-rich weak layers, determine a relatively small rheology contrast, facilitate wing formation, producing greater resistance to the mylonitic flow and, in turn, clearer evidence of formation of sub-simple shear kinematic indicators. Aerial photogrammetry data is in accordance with field collected data, enlarging the amount of available meso-structural data, previously scarce because of the impervious terrain. This further confirms the versatility of ASN in processing data collected from different sources and at different scales.

CONCLUSIONS

In the era of digitalization and big data collection, petrography can benefit from the application of data science techniques such as machine learning algorithms. In

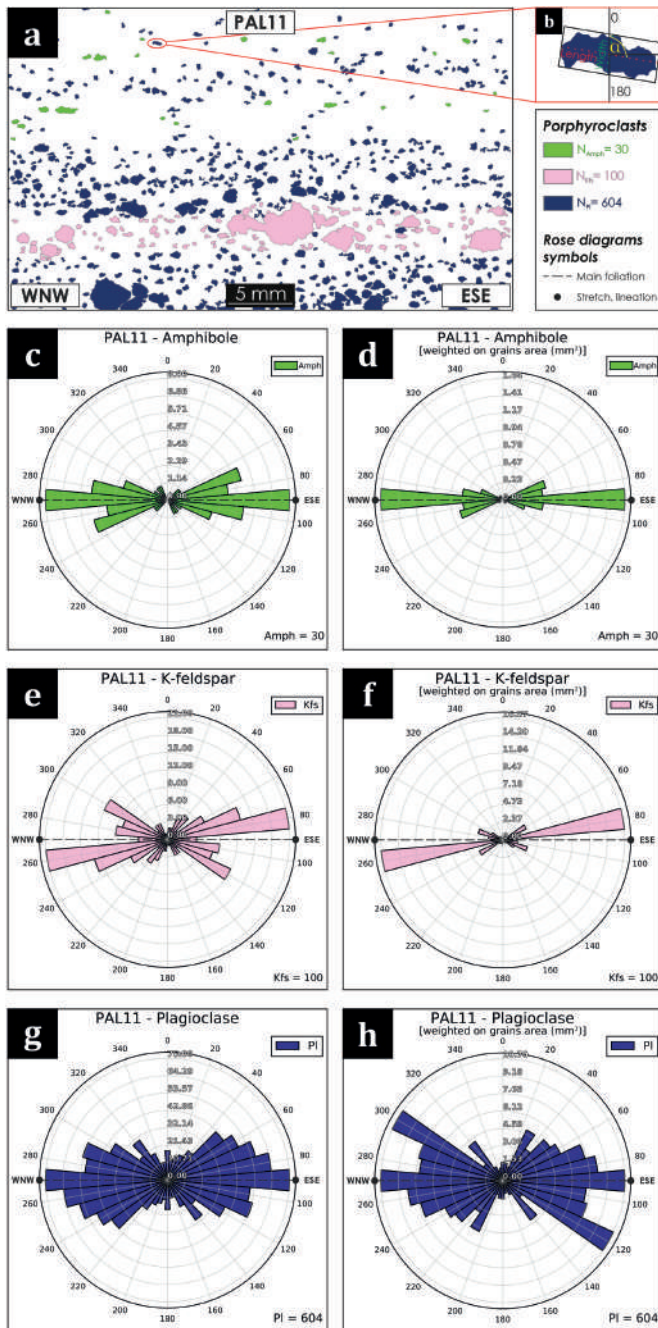


Figure 6 From Ortolano et al. (2021). Micro-structural data extracted with MFA (Visalli et al., 2021) after (a) thin sections digitalization (sample "PAL11"), using the (b) minimum bounding geometry of each single grain. The displayed rose diagrams of amphibole, K-feldspar and plagioclase porphyroclasts are both unweighted (c, e, g) and weighted (d, f, h) on grains' cumulative area (in mm²).

this view, two new computer software, useful for the quantitative investigation of the mineralogy and the fabric of rock samples, were introduced: a) X-Min Learn, that provides customizable machine learning algorithms to identify rocks minerals from thin section multi-spectral data and b) ArcStereoNet, that allows the statistical analysis of structural oriented data within the ArcGIS® environment. By encouraging users towards an aware application of the provided algorithms, both software allow the derivation of reliable interpretations and constraints, representing an important contribution towards the increasingly pressing demand of achieving quantitative results in petrography. This is at the service of the most diverse facets of geosciences, from the resolution

of petrological problems to micro-structural ones, passing through the field of geomaterial analysis.

REFERENCES

Arganda-Carreras, I., Kaynig, V., Rueden, C., Eliceiri, K.W., Schindelin, J., Cardona, A. & Sebastian Seung, H. (2017): Trainable Weka Segmentation: a machine learning tool for microscopy pixel classification. *Bioinform.*, **33**, 2424-2426.

Bingham, C. (1974): An antipodally symmetric distribution on the sphere. *Ann. Stat.*, **2**, 1201-1225.

Bridle, J.S. (1990): Probabilistic interpretation of feed-forward classification network outputs, with relationships to statistical pattern recognition. *Neurocomputing*, **68**, 227-236.

Cirincione, R., Fazio, E., Fiannacca, P., Ortolano, G., Pezzino, A. & Punturo, R. (2015): The Calabria-Peloritani Orogen, a composite terrane in Central Mediterranean; its overall architecture and geodynamic significance for a pre-Alpine scenario around the Tethyan basin. *Period. Mineral.*, **84**, 701-749.

Cover, T.M. & Hart, P.E. (1967): Nearest neighbor pattern classification. *IEEE T. Inform. Theory*, **13**, 21-27.

Fazio, E., Ortolano, G. & Cirincione, R. (2017): Eye-type folds at the Palmi shear zone (Calabria, Italy). *Int. J. Earth Sci.*, **106**, 2039-2040.

Fisher, N.I., Lewis, T. & Embleton, B.J. (1993): Statistical analysis of spherical data. *Cambridge university press*, 344.

Hendrickx, I. & Van Den Bosch, A. (2005): Hybrid algorithms with instance-based classification. *Lect. Notes Comput. Sc.*, **16**, 158-169.

Itano, K., Ueki, K., Iizuka, T. & Kuwatani, T. (2020): Geochemical discrimination of monazite source rock based on machine learning techniques and multinomial logistic regression analysis. *Geosciences*, **10**, 63.

Kaur, H., Pannu, H.S. & Malhi, A.K. (2019): A systematic review on imbalanced data challenges in machine learning: Applications and solutions. *ACM Comput. Surv.*, **52**, 1-36.

Kociánová, L. & Melichar, R. (2016): OATools: An ArcMap add-in for the orientation analysis of geological structures. *Comput. Geosci.*, **87**, 67-75.

Lanari, P., Vidal, O., De Andrade, V., Dubacq, B., Lewin, E., Grosch, E.G. & Schwartz, S. (2014): XMapTools: A MATLAB®-based program for electron microprobe X-ray image processing and geothermobarometry. *Comput. Geosci.*, **62**, 227-240.

Lemaître, G., Nogueira, F. & Aridas, C.K. (2017): Imbalanced-learn: A python toolbox to tackle the curse of imbalanced datasets in machine learning. *J. Mach. Learn. Res.*, **18**, 559-563.

MacQueen, J. (1967): Some methods for classification and analysis of multivariate observations. *Proceedings of the Fifth Berkeley Symposium on Mathematical*

- Statistics and Probability*, **1**, 281-297.
- Mehrabi, N., Morstatter, F., Saxena, N., Lerman, K. & Galstyan, A. (2021): A survey on bias and fairness in machine learning. *ACM Comput. Surv.*, **54**, 1-35.
- Nickerson, R.S. (1998): Confirmation bias: A ubiquitous phenomenon in many guises. *Rev. Gen. Psychol.*, **2**, 175-220.
- Ortolano, G., Visalli, R., Godard, G. & Cirrincione, R. (2018): Quantitative X-ray Map Analyser (Q-XRMA): A new GIS-based statistical approach to Mineral Image Analysis. *Comput. Geosci.*, **115**, 56-65.
- Ortolano, G., Fazio, E., Visalli, R., Alsop, I., Pagano, M. & Cirrincione, R. (2020): Quantitative microstructural analysis of mylonites formed during Alpine tectonics in the western Mediterranean realm. *J Struct. Geol.*, **131**, 103956.
- Ortolano, G., D'Agostino, A., Pagano, M., Visalli, R., Zucali, M., Fazio, E., Alsop, I. & Cirrincione, R. (2021): ArcStereoNet: a new ArcGIS® toolbox for projection and analysis of meso-and micro-structural data. *ISPRS Int. J. Geo-Inf.*, **10**, 50.
- Quinn, P., Rout, D., Stringer, L., Alexander, T., Armstrong, A. & Olmstead, S. (2011): Petrodatabase: an on-line database for thin section ceramic petrography. *J. Archaeol. Sci.*, **38**, 2491-2496.
- Ren, Q., Li, M., Han, S., Zhang, Y., Zhang, Q. & Shi, J. (2019): Basalt tectonic discrimination using combined machine learning approach. *Minerals*, **9**, 376.
- Su, C., Xu, S.J., Zhu, K.Y. & Zhang, X.C. (2020): Rock classification in petrographic thin section images based on concatenated convolutional neural networks. *Earth Sci. Inform.*, **13**, 1477-1484.
- Theodoridis, S. & Koutroumbas, K. (2006): Pattern recognition. *Elsevier*, 856.
- Visalli, R., Ortolano, G., Godard, G. & Cirrincione, R. (2021): Micro-Fabric Analyzer (MFA): A new semiautomated ArcGIS-based edge detector for quantitative microstructural analysis of rock thin-sections. *ISPRS Int. J. Geo-Inf.*, **10**, 51.
- Zuluaga, C.A., Stowell, H.H. & Tinkham, D.K. (2005): The effect of zoned garnet on metapelite pseudosection topology and calculated metamorphic PT paths. *Am. Mineral.*, **90**, 1619-1628.

Mineralogical and chemical characterization of Bottom Ashes from Municipal Solid Waste Incinerator

A multi-techniques approach for an extremely complex and heterogeneous material

Chiara De Matteis

Dipartimento di Scienze Chimiche, della Vita e della Sostenibilità Ambientale, Università di Parma, Parco Area delle Scienze 157/A, 43124, Parma, Italia

DOI:10.19276/plinius.2023.01.006

INTRODUCTION

Humanity is now a dominant geological actor, as human activities induce great, multiple and irreversible changes on Earth. The study of these human-associated changes led to the suggestion that we should not refer to the present time as pertaining to the Holocene epoch but to a new geological epoch called the “*Anthropocene*” (Crutzen, 2002; Steffen, 2021; Trischler, 2016; Zalasiewicz et al., 2011). This new epoch is characterized by the appearance of “*new materials*”: a set of anthropogenic materials, which do not exist in nature, designed by man through the development of research and technology and born to satisfy the needs of our society. An important input of anthropic material in environmental matrices is given by the production of waste.

The EU policy strategy for waste reduction and management is based on the following principles, in order of preference: prevention, reuse, recycling, recovery and disposal. A *recovery* strategy is to send Municipal Solid Waste (MSW) to Waste-to-Energy (WtE) plants, that reduce mass and volume of input waste up to 25% and recover energy from waste in the form of heat and electricity (Brunner & Rechberger, 2015). From the combustion of waste not only energy is obtained but also residual ashes.

BA are one of the major by-products obtained during MSW incineration in WtE plants; their mass is about 20% of the incinerated waste. Once the incineration process is complete, the BA are thrown into a tank full of water for rapid cooling. The BA are classified as non-hazardous waste (EWC code 19.01.12: bottom ash and slag other than those in 19.01.11 *).

The BA are very heterogeneous materials made up of different fractions (glass, synthetic ceramic, mineral, metals and unburning organic matter) which, thanks to the non-hazardousness nature of the unburned material, can be recycled becoming a resource. The mineralogical and chemical composition of BA varies due to the different waste input, combustion temperature, plant type, quenching, aging and weathering.

The most common mineralogical phases are (i) silicates (quartz, melilites, feldspars), (ii) carbonates (calcite, vaterite), (iii) oxides (magnetite, hematite, corundum), and (iiii) hydrated phases typical of cementitious materials (hydrocalumite, portlandite, ettringite, stratlingite). In addition to these main phases, a high content of amorphous material, is also present (Alam et al., 2019; Bayuseno and Schmahl, 2010; Bertolini et al., 2004; Caviglia et al., 2019; Mantovani et al., 2023).

Chemically, most abundant elements in BA such as Al, Fe, Si, Ti, K and Na are very close to those of the continental crust. Among the minor and trace elements, Co, Zr, Li, Hf, Ti, Rb, F, V, Mn, Sr, Ga, U, Th show an average composition in BA similar to the earth continental crust content, whereas a significant enrichment in BA is found for Cl, Zn, Cu, S, Pb, Br, Mo and Sn. The presence of these *Potential Toxic Elements* (PTE) poses an issue about the potential toxicity of the BA. The toxicity of an element depends on its oxidation state and/or its concentration in a given environment, which depends on its leachability. On its turn, the leachability of an element in environmental matrices depends on the mineralogical phase in which it is hosted. Investigate the chemical form of PTE and know the crystalline and amorphous phases that host them is a key point in assessing the potential toxicity of BA and to implement safer and viable material recycling strategies.

This complex chemical and mineralogical composition and the presence of PTE gives rise to numerous scientific questions regarding their reuse and non-hazardousness. In this work a multi-techniques approach was used to characterise BA and understand the distribution and behaviour of PTE.

MATERIALS AND METHODS

Sampling and sample preparation

The BA studied in this work were sampled from 5 WtE plants in different cities of northern Italy: Parma (PR), Piacenza (PC), Torino (TO) (plants owned by the company *Iren Ambiente*), Ferrara (FE) and Forlì-Cesena (FC) (plan-

ts owned by the company *Hera Ambiente*). Forlì-Censena WtE plant burns only MSW while the others burn special non-hazardous waste. The BA investigated were taken randomly from a 2-3 m high stock, representative of more than one month of accumulation. Approximately 5 kg of BA samples were collected from each plant.

Grain size analysis

The samples from the 5 WtE plants were first dried in an oven at 50°C for 24h and then sieved into ten grain size classes (Φ : 16, 8, 4, 2, 1, 0.5, 0.3, 0.2 e 0.063mm) according to the prescriptions of the European standards for aggregates EN 933-2 (Ente Nazionale di Unificazione, 2020).

Each particle size class was weighed and, by calculating the percentage of material that passed through the sieves, cumulative particle size curves were made in order to evaluate their distribution and mechanical qualities.

Thermo Gravimetric Analysis (TGA)

TGA were conducted on samples taken from each particle size class by a Perkin Elmer 8000 instrument equipped with a Pt-crucible at a heating rate of 10 °C/min in the temperature range 35°C - 800 °C. All the measurements were run under a constant flux of dry air atmosphere (30 mL/min).

SEM - EDS observations and analysis

As a preliminary step, several grains (8 - 16 μ m) were observed with a Scanning Electron Microscope coupled with Energy Dispersive System (SEM-EDS) JSM IT300LV Jeol 6400 equipped with an Oxford EDX microprobe. Microprobe analysis was performed with operating conditions 20 or 25 kV and 1.2 mA current, \sim 1 μ m beam diameter and 75 s counting time.

Subsequently, a great quantity of granules (0.5 - 1 mm), were embedded in epoxy resin stabs, cut longitudinally and analysed by a JEOL JSM-IT 300LV Scanning Electron Microscope, equipped with Oxford INCA Energy 200 EDS SATW detector (WD 10, KV 15), at 15 kV, 1.2 mA current and 1 μ m beam diameter.

X - Ray Powder Diffraction (XRPD) Analysis

For each grain size, XRPD was used for the identification and quantification of the phases in the samples using a Bragg-Brentano Bruker 2D Phaser Diffractometer, with θ - θ geometry, Cu K α radiation, 30 kV and 10mA and a solid-state detector.

Quantitative analysis was done by means of the Rietveld method.

X - Ray Fluorescence (XRF) Analysis

XRF spectroscopy: conventional source

Chemical composition was analysed for each grain size with a WDXRF Axios PanAlytical spectrometer, equipped with a Rh tube working at 4 kW. The analyses were performed on both major elements (expressed g/100g) and trace elements (expressed in g/Kg).

μ - XRF spectroscopy: synchrotron radiation

μ - XRF maps were done at the XRF beamline at Elettra Sincrotrone Trieste (ETS). The experiment has been conducted using both HE multilayer for the collection of μ -XRF maps, with standard 45°/45° geometry for fluorescence mode measurements, using an XFlash 5030 SDD detector (Bruker, Berlin, Germany). μ -XRF maps were collected with an incident beam energy of 14 keV and a beam size at the exit slits of 50x50 μ m² (H*V).

X-ray Absorption Near Edge Structure (XANES)

Some PTE (Cu, Cr, Zn, Pb, Ni, and Co) were analysed by XANES in order to investigate their oxidation state and the mineralogical environment in which they were hosted. XANES measurements were conducted at the XRF beamline at Elettra Sincrotrone Trieste (EST). The experiment has been conducted using Si111 monochromators, with standard 45°/45° geometry for fluorescence mode measurements, using an X-Flash 5030 SDD detector (Bruker, Berlin, Germany). All spectra were collected using 5 seconds per step and a variable energy step as a function of the energy: Large step (5 eV) in the first 200 eV of the spectrum, smaller step (0.2 eV) in the near-edge region and a k-constant step of 0.05 Å⁻¹ further above the absorption edge. The oxidation state will be determined using least-squares Linear Combination Fitting (LCF) based on reference spectra collected on compounds of known oxidation state.

Leaching Test

Leaching tests and analysis of the leachates were performed following the *UNI EN 12457-2:2004 "Waste Characterization - Leaching - Compliance test for granular waste and sludge leaching - Part 2: Single-stage test with a liquid/solid ratio of 10 l/kg for materials with particle sizes less than 4 mm (with or without size reduction)"*. The test was carried out on the particle size classes below 4 mm from all the five WtE plants examined.

Eluates collected were analysed by: *Atomic Absorption Spectroscopy (AAS)* (Thermo S Series AA Spectrometer) for cations (Ca, Mg, Na, K); *Ion Chromatography (IC)* (Metrohm Compact IC pro 881) for anions (Cl⁻, SO₄²⁻, F⁻, Br⁻, PO₄³⁻); *Inductively Coupled Plasma - Mass Spectrometry (ICP - MS)* (Perkin Elmer ICP-MS ELAN DRC-e) for the investigation of trace elements (Al, Ba, B, Cr, Co, Fe, Pb, Li, Mn, Mo, Ni, Se, Sr, Tl, Ti, V, Zn).

Sequential Extraction Procedure (SEP)

A new 5 - step SEP was set in this work. SEP was performed on BA (0.063 - 0.2 mm, 0.3 - 0.5 mm, 2 - 4mm and < 4 mm) sampling from Parma WtE plant.

Solid residues obtained from each step were analysed by XRPD and XRF.

Eluates collected were analysed by Agilent 7500 ICP-MS for the investigation of critical raw elements.

Statistical analysis

The results obtained were investigated by statistical analysis using: *Pearson's r index (r-index)*, *correlation index R (or p) by Spearman ranks* and *Principal Component Analysis*.

RESULTS AND DISCUSSION

Bottom Ashes morphology and composition

Optical observation was done on several grains, chosen for different colour and lustre, from the portion larger than 4 mm. The grain colour varies with the crystalline and amorphous phase content, as revealed subsequently by XRPD. The rounded reddish-grey grains, which are most abundant, are mainly made by a heterogeneous aggregation of residual refractory material and metals coexisting with crystals and amorphous (Fig. 1d). The amorphous acts as a matrix that binds the crystalline and metallic fractions (Fig. 1b) of the original waste and the new-formed minerals. The original waste grains show rounded edges, indicating partial reabsorption (Fig. 1c), whereas new formed crystals are often present as sharp needles within the glass. Vesicles and bubbles appear indicating that some degassing occurred (Fig. 1a).

The bulk mineralogical composition for each WtE plant was obtained from each grain size. The main mineralogical phases are reported in Table 1 whose abundance has been refined by Rietveld analysis. A number of minor phases is also present, which either showed very faint peaks in XRPD. During Rietveld analysis it was shown

that the inclusion of a higher number of phases leads to refinement instability, so that a compromise was necessary between the number of phases to be included and the number that could be refined. Most evident is the amorphous content, which is higher in the BA of the three plants (TO, PR, PC) so as that it overtakes the entire quantitative of crystalline component. In these plants, the amorphous is over 75% on average, and ranges in different grain size between 67 and 88 wt%. In the plants of FE and FC, instead, bulk amorphous is, on average, less than 35% (depending on grain size between 7 and 55 wt%). The lower quantity of amorphous material in FE and FC occurs together with higher calcite, quartz and feldspar. Also, ettringite content is higher in FE and FC than the other 3 plants sampled, indicating a probable greater reactivity of these ashes in the aging process.

Among minerals, quartz, calcite, melilites, iron oxides and some alteration products such as sulphates, chlorides, and hydrated minerals are ubiquitous. Strätlingite is found only in the PR samples. This mineral is typical of cementitious materials and can be formed either from the degradation of gehlenite or from the reaction between calcium silicates (Ca_2SiO_4 - belite) with $\text{Al}(\text{OH})_3$ in hydration processes involve the degradation of gehlenite, as some evidence found in SEM analyses showing that gehlenite has been formed in the combustion chamber (crystals with typical neof ormation and rapid cooling shape). Iron-containing minerals as hematite and magnetite are revealed by X-ray diffraction, although likely other metal phases are present like Cu or Ni-Ti alloys. Last, a number of silicate phases, like pyroxene, gehlenite-akermanite, and anorthite, are found without significant difference with grain size, and are likely formed at high temperature in the combustion chamber.

According with XRPD data, the bulk chemical composition of BA is represented by the major oxides of Si, Ca, Fe and Al. In fact, the sum of these elements (in oxides) represents from 60 to 77 g/100 g. S and Cl are found in

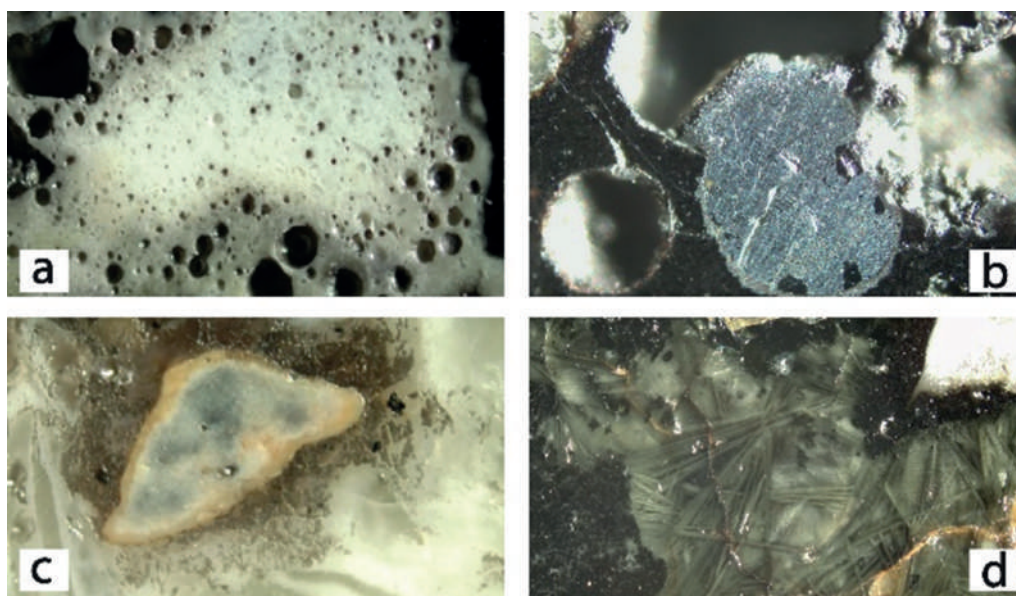


Figure 1 Photomicrograph showing the inner part of the clasts cut longitudinally. Each of them appears different from the other in terms of morphology but we can observe frequently a part of a dark matrix (b,d) and within it areas of different color, sometimes white (c) or transparent (d). Many samples present little vesicles and bubble structures, indicating degassing processing (a), metallic, alloy or refractory inclusions (b) sometime with reaction rims (c).

Table 1 XRPD identification of bottom ash. The minerals are arranged in the following sequence: (x) major minerals (*) minor or trace minerals, (/) not found or very doubtful presence.

Mineral phase	PR	TO	PC	FE	FC
calcite	X	X	X	X	X
vaterite	X	X	X	X	X
quartz	X	X	X	X	X
crystalite	/	/	*	/	/
plagioclase	X	X	X	X	X
pyroxene	*	*	*	/	/
melilite	X	X	X	X	X
ettringite	X	X	X	X	X
hydrocalumite	X	X	X	X	X
portlandite	X	X	X	X	X
strätlingite	X	*	*	*	*
apatite	*	*	*	*	*
larnite	*	*	*	x	x
tobermorite	*	*	*	/	/
sjogrenite	/	/	/	*	*
magnetite	X	X	X	X	X
hematite	X	X	X	X	X

a range from 0.3 to 2 g/100g. Among minor elements, Zn, Cu, Pb and Ba content is higher than 1000 mg/kg. The oxides show a rather similar pattern in the different plants, albeit with some slight difference: the BA from TO show higher Fe_2O_3 and lower CaO, and those from PC shows lower SiO_2 and higher LOI than the others. Also, for minor and trace elements our data show that the compositional variability related to grain size. In PC higher value are found for Cl, and Cu, and overall, a higher compositional spread in S, Cl and Zn content. The smaller fraction is richer in Ca due to the faster carbonation occurring in smaller particles with larger surface area. Si is positively correlating with grain size probably due to the glass shards in larger grain size. Na as well correlates with Si, possibly for the addition of Na as a fining agent in glass production technology and for the presence of plagioclase solid solution. Ca, Ti, S, LOI (in all the plants) and Cl (in PR, PC, FE) correlate negatively with grain size. The higher Ca in smaller particles goes together with the higher Ca-carbonate content. Higher decarbonation means also higher weight loss in LOI, which is greater in smaller particle sizes having higher active surfaces. We suppose that S follows the same trend due to the sulfa-

tion process and the formation of the ettringite phase, which, as shown in XRPD analysis, is more present in finer sized grains. Most of the PTE like Cu, Pb and Cr are negatively related with grain size. To note, the differences in the minor elements concentration between plants could be related to the different waste input. Other elements, like Al, Fe, Mg, P and Cr show little change between samples of different grain size. An exception in TO is MgO and Al_2O_3 , which show a significant increase in the smaller sized grains. S and Cl are contained in the BA in considerable quantities, causing metal erosion if they are used as supplementary cementitious material in reinforced concrete. In BA examined in this work, S and Cl range between 2000 to 21000 mg/kg. These two elements are positive correlated in all incinerators and show an inverse correlation with the grain size, suggesting that they are mostly present as weathering of the products.

TGA shows a continuously weight decreases with temperature for any grain size. The weight loss is higher in the smaller grain size, where the mass loss at 800°C is about 25%. For the larger grain size, the loss is about 5-10% and for intermediate ones about 15%. An exception is PC, where the weight loss is similar for every grain size. The analysis of the first derivative shows few temperature ranges where higher weight loss is present. A moderate (3-4%) weight loss occurs in the interval 50-100°C, likely ascribable to two reactions: one at 50-60°, likely due to surface water, and another just above 100°C, related to the first dehydration of ettringite with further dehydration possibly revealed by the faint peaks at 250 and 350°C. The second loss is 1-2 wt% and appeared over the range 250-450°C and a 4-7 wt% in the interval 620-760°C. The 250-450°C reaction is likely due to plastic combustion residue (molecular decomposition), while the 620-760°C loss is ascribable to the transformations involving carbonate (decarbonation) phases. In FE and FC the de-carbonation loss is greater than in the other plants, accordingly with XRPD and XRF data that show a higher carbonate content. Despite the general shape of the TGA curves appear similar, some difference with particle size dimension and between plants is found. A peak at 450°C has been found only in FE and FC BA. The peak is more apparent in the finer portion, and it is likely due to the de-hydration of portlandite which occurs between 450 and 500°C. Portlandite is present only in the two incinerators of FE and FC, between 5-10 wt% in the finer portion, and between 1 and 2% in the larger grains.

Potential Toxic Elements speciation and behaviour

Prediction of leaching behaviour in a complex system like BA involves the phases within the ashes, their proportion, and their thermodynamic properties in multiple equilibria. For these reasons, PTE behaviour must be studied by a multi-technical approach.

XANES analyses together with a μ -XRF mapping by synchrotron radiation and SEM - EDS allowed to investi-

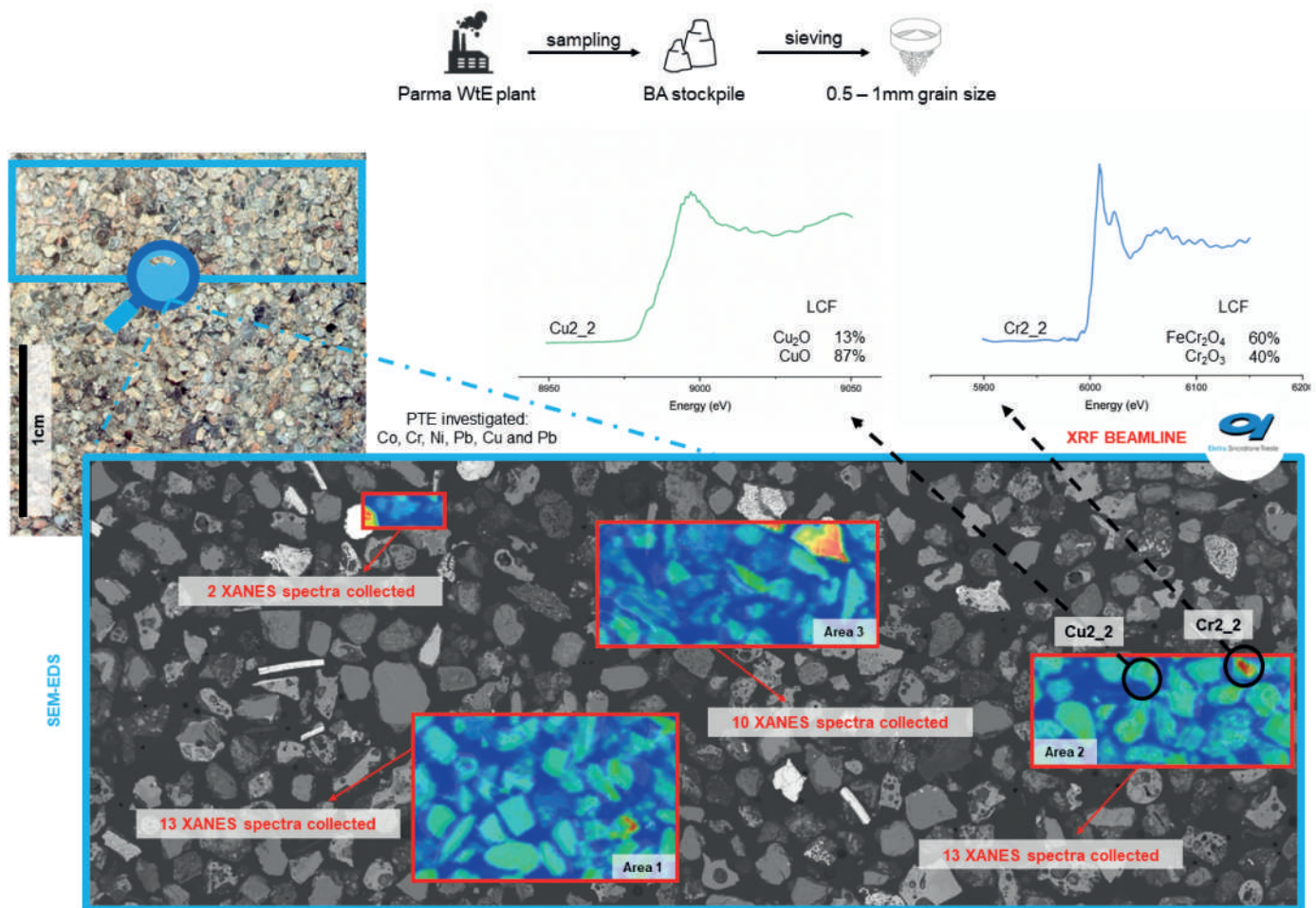


Figure 2 Graphical abstract of the experiment conducted at the Elettra XRF beamline, Sincrotrone Trieste.

gate distribution and speciation of PTE (Fig. 2). XANES spectra collected at the Cu K-edge in different clasts suggests that Cu chemical environment and oxidation state are heterogeneous even in the same area (0, +I and +II); this is interpreted as an effect of zones in the fuel bed with different access to the oxygen. Pb is present in +II and +III chemical forms. In all XANES spectra Cr was present in the Cr 0 and Cr III+ oxidation state. No evidence of Cr VI+. Zn was found in BA in a number of different phases, some of them well visible also in SEM-EDS. Various XANES spectra were collected on different clasts. Zn is not present as a metal but mainly occurred in oxidation state +II. In all the spectra, a great fit is obtained with Zn-carbonate, in the form of smithsonite ($ZnCO_3$) or hydrozincite ($Zn_5(CO_3)_2(OH)_6$). Zincite (ZnO) was found in few grains, confirming SEM-EDS results. Also, spinel phases like gahnite and Zn-ferrite ($ZnFe_2O_4$) are present, as well as the silicate hemimorphite [$Zn_4Si_2O_7(OH)_2 \cdot H_2O$]. Ni is found in SEM-EDS only in the above described grain together with Co. Ni is present in metal and oxidized form, but hydration is also possible.

Leaching tests were done on particle sizes below 2 mm, as XRF analyses showed that they are richer in PTE. Marked differences in leaching behaviour have been found between the two different owner corporation that is IREN for PR, PC and TO and HERA for FC and FE. With respect to a given particle size, the leaching of an element has

been compared to the total content in the bulk sample (from XRF analysis) and calculated in percentage (all referred to mg/kg of material). The most released element is Cl with a release percentage of about 70/90%, higher in the finer fraction. We suggest that Cl is present in very soluble salts, like NaCl and KCl, dispersed on the surface of the grains. This suggestion is confirmed by the linear relation found in leached Na+K with Cl, whereas such relation does not exist in the sample composition determined by XRF as most Na and K are likely caged within the amorphous and silicates structures. Therefore, no diffraction peaks attributable to Na, KCl are found in XRPD analysis, suggesting that not all the Cl is bound to Na and K in salts, and that a significant release of Cl may be originate by the dissolution of ettringite. SEM -EDS analyses of the ashes showed that Cl is often associated with silicate glassy phases. We suggest therefore that chloride is most released by dissolution of weakly bonded Cl at the surface of the amorphous phases. All tests exceeded the legal limits for Cl (Legislative Decree 152/06) suggesting that washing and selection of larger grains may be combined technique to reduce Cl for a correct reuse. S shows a release, about 30% for PR, PC and TO and 3% for FE and FC, with no dependence on the particle size. S is present in the ettringite structure which is observed in XRPD in all the plants, especially in FE and FC. However, the release in SO_4^{2-} is lower in the

two HERA WtE plants, whereas the Ca is higher. Moreover, Al is released by at least two order of magnitude less in HERA than in IREN plants. Another relevant difference is that the measured pH in the leached IREN plants is between 10 and 11, whereas in the HERA plants it varies between 12 and 12.5. We suggest that in the HERA plants, the dissolution of portlandite, which is absent in the IREN plants, gives rise to a basic environment, where ettringite is less prone to dissolution. In the IREN plants, ettringite dissolves, with sulphate and Al hydroxide solubilization. Therefore, probably the contribution of ettringite dissolution is minor, due to the very similar ratio in Na+K/Cl in the 5 plants, in spite of the different amount and solubilization of ettringite. The different mineralogy in IREN and HERA plants, and the consequent different leaching in major elements has an effect also on minor elements. Minor elements are often present in solid solution within phases more or less prone to dissolution at different pH, and the dissolution of the host phases releases also the exsolved element. Therefore, the release in minor elements is different in the different WtE plants, often by two order of magnitude. For instance, sulphate and Cr are above regulatory limits only in IREN BA, but Ba and Ni (with the exception of TO) only in the HERA plants. A likely interpretation is that Cr could have a significant concentration in ettringite, which is dissolved in IREN plants, whereas Ba and Ni could exchange with Ca in significant amount in portlandite, which is dissolved in HERA plants. In TO the leaching of SO_4^{2-} , Co, Cu and Zn is higher than in other plants. Cu, Cr and Ni are, among the PTE, the most released in all plants with values below 0.5%, except for TO where the Cu stands at 3%. On the other hand, the release of Ti, Pb and Zn is relatively low (<0.01%), never exceeds law limits (Legislative Decree 152/06) suggesting their presence in a non-soluble structure, like glass or silicate minerals.

The SEP has been specifically adapted for BA. Some steps have been added and/or modified compared to the BCR standard method up to obtain a five-step extraction procedure to remove i) water-soluble phases, ii) carbonate phases, iii) reducible fraction, iiiii) oxidable fraction and iiiiii) residues. The leaching of a few elements (Pb, Cu, Zn, Mn, Ni, Fe, Cr and Ti) was investigated by ICP-MS analysis after each step. As expectable they have different behaviour, for they are hosted in different mineralogical and/or amorphous environments. Due to the heterogeneity of BA, it is difficult to create a link between the element and the hosting phase: The element may be present as an impurity or as a major constituent of a given phase. In the latter case such phases are present in a concentration below 1% and are not detected by XRPD. This could explain the high release of some elements, such as Pb and Zn, even if no mineralogical phase having these elements was identified by XRPD. Yet, some speculation can be done by the results of the ICP-MS analyses

of the leachates. In the first step, some release was recorded for Fe and Cu, although in a small proportion. Cu could possibly be hosted in chloride, and Fe in larnite, both as impurities. The almost negligible extraction suggests that these elements are not present in salts or water-soluble phases. In second step, Pb and Zn are most leached, showing both a weight loss between 50 to 70% of their original budget. Almost all of the leached Zn was extracted in this step, recording a release of about 70% in both grain size. XANES analysis found Zn typically associated to carbonates, like smithsonite (ZnCO_3) or hydrozincite ($\text{Zn}_5(\text{CO}_3)_2(\text{OH})_6$), or to hydroxides like $\text{Zn}(\text{OH})_2$, which are leached by acid attack. For Pb, the leached fraction ranges between 47 and 64% in larger and smaller grains, respectively. XANES analysis showed that Pb could be present as a carbonate and as Pb_3O_4 , both phases unstable in a highly acid environment. Also, other oxide phases found in SEM-EDS analysis of the BA, like Ca_2PbO_4 , are soluble in acid environment. Cu present a moderate release at this step, about 35% for < 4 mm and 22% for 0.3 - 0.5 mm grain size. Its presence can be inferred as a carbonate phase and within amorphous phases that are removed in this step. In the third step, the most released elements are Ni, with a percentage in leachates of about 22% in the < 4mm grain size and 14% in the 0.3 - 0.5 mm grain size, Ba and Pb, both with a release of about 10%. At this stage Fe/Mn oxyhydroxides dissolution was rather small, testified by the small weight loss in Fe and Mn. In fourth step, Ni and Cu are the elements most leached. For Cu it is about 50% of the bulk composition. SEM-EDS and XANES showed for both elements that they are commonly found as metal droplets within a silicate matrix, which are oxidized in a soluble ionic species. Other elements are most concentrated in the residuals: Cr, Fe, Mn and Ti may be present in silicate glass or in spinel oxides; Ba could likely occur as an impurity in feldspars.

CONCLUSION

The mineralogy, chemical composition and properties of the BA in five WtE plants in Northern Italy were examined. The average composition, and the changes of the composition with grain size follow quite similar trends in all the incinerators. The major and minor elements compositions are very similar, and are well grouped in the compositional variation of the incinerators worldwide. This may indicate that, in spite of the different type of input waste, the chemical output is comparable, at least in the residual fraction. On the other side, there are orders of magnitude in the leached fraction between the different WtE plants, with higher differences between the plants of FE and FC, and the others. The difference is related to the mineralogical composition i.e where a given element occurs in a more soluble phase, and affects also whether the ashes are beyond legislation limits.

The quantitative mineralogical differences (amorphous, carbonates) found between the WtE plants of IREN and HERA groups could be related to some different local burning temperatures, operating procedures or weathering conditions, and make an example on how the mineralogy may affect the properties of the ashes. The combined SEM-EDS, XRF-XANES, XRPD analyses on different grain size and different grains enabled to find a number of new mineral hosts of the PTE (Co, Zn, Ni, Cu, Pb, Cr), found in metallic inclusions, oxides, carbonates, and amorphous matrices. As a combined investigation was not yet previously done, we may assume that the mineralogical variety which has since now been determined in BA, already represented by a considerable number of phases, is just a fraction of the actual one. As long as SEM-EDS is used on single grains, we observe that each grain shows chemically different bulk composition, and mineralogical assemblages. Just for an example Zn was found in BA in 27 mineral phases, of which 15 were confirmed or discovered in this work. Also, what is generally and simply described as an amorphous or glassy phase, is in fact a number of different phases, each of them in local equilibrium with the embedded crystals. This makes the prediction of the leaching behaviour of the ashes a risky task: the leached fraction for PTE is just a very small fraction, between 10⁻³ and 10⁻⁶ of the global content of the element, and a slight change in mineralogy, hardly or not detectable by XRD, may have a profound effect on the leaching of the samples. The precipitation of a small amount of a highly soluble phase containing PTE may increase dramatically the leached fraction.

There are however some regular features in the compositional relations between the elements, which could be outlined by the analysis of different portions of the same sample, sorted by grain size. Two opposite trends are observed: one shown by Si and grain size, the other, opposite correlated to the first, is shown by Ca, Cl, S and the residual loss on ignition. The first trend is followed also by some more lithophile elements, like Zr and Rb, the latter likely present in feldspar or silicate glass. The second trend is followed by PTE elements like Cu and Zn, but with some exceptions: in the BA from PC Zn does not follow a specific trend, and in the FC plant, Cu follows the Si trend. Pb, Ni and Cr do not follow neither trend, with the exception of the FE plant, where Pb goes with S. It appears that Cu and Zn are hosted in carbonate, sulphate or chlorides in the different grain size, whereas Pb, Ni, Co and Cr may have different host minerals in the different compositions. As for the leaching behaviour it is generally observed that leaching increases as the grain size decreases, for Cl, Na (and K) and Cu, but other elements, like Cr and Ni follow a different trend in the WtE plants of TO, PC and PR, where they follow the trend of Cl and Na, respect to FE and FC, where they seem unrelated to the grain size. This again, highlights the differ-

ence between the different plants.

For a possible recycle of the BA, the results in leaching tests indicate that all the grain size below 2 mm, from any WtE plants are beyond legal limits for some element. Cl and Cu are always beyond legal limits, and again we find a difference between WtE plants: Ba, Ni, F are above limits in the FE and FC plants, SO₄²⁻ and Cr for the other incinerators. Ni and other elements, like Pb and Zn were always leached below limits, although in FE the Pb leaching is close to the critical value. Therefore, to make any use other than as insulator fillers, some kind of treatment is needed. The observation that PTE decrease with increasing grain size, is not always correct, and for Cu and Cl, in the examined grain size the leaching is so high that it is not expectable that simply sieving the larger portion will solve the issue. However, the larger grain size could be easier to wash, and the reactivity in the grains could be slower: our SEP showed that the leached fraction, no matter its toxicity, is higher in finer grains. The highly reactive nature of the ashes can be used as an aggregate in cement, most for highly matured material where cement minerals are present. Concrete obtained using BA as aggregate could fix the PTE in a structure where leaching occurs less. By this respect an investigation on the performance and on the leaching of concrete, obtained using ashes of different grain size as aggregates in concrete, before and after washing could be promising. Also, in light of the observed differences in the mineralogy of the different incinerators, we may expect different performances in concrete using ashes from different plants. Preliminary washing at some pH value should be useful, as our observation showed that most of the coarser grains do show a rim, made by smaller grains, and likely the more reactive part. The washing should be made as to disaggregate the rim portion, whose sewage could be subject of further recovery of metals.

REFERENCES

- Alam, Q., Schollbach, K., van Hoek, C., van der Laan, S., de Wolf, & T., & Brouwers, H.J.H. (2019): In-depth mineralogical quantification of MSWI bottom ash phases and their association with potentially toxic elements, *Waste Manag*, **87**, 1-12.
- Bayuseno, A.P., & Schmahl, W.W. (2010): Understanding the chemical and mineralogical properties of the inorganic portion of MSWI bottom ash, *Waste Manag*, **30**, 1509-1520.
- Bertolini, L., Carsana, M., Cassago, D., Curzio, A.Q., & Collepardi, M. (2004): MSWI ashes as mineral additions in concrete. *Cem. Concr. Res*, **34**, 1899-1906.
- Brunner, P.H., & Rechberger, H. (2015): Waste to energy - key element for sustainable waste management, *Waste Manag*, **37**, 3-12.
- Caviglia, C., Confalonieri, G., Corazzari, I., Destefanis, E., Mandrone, G., Pastero, L., Boero, R., & Pavese, A.

- (2019): Effects of particle size on properties and thermal inertization of bottom ashes (MSW of Turin's incinerator), *Waste Manag*, **84**, 340-354.
- Crutzen, P.J. (2002): The "anthropocene", *J. Phys. Arch. IV Fr*, **12**, 1-5.
- Ente Nazionale di Unificazione, E.N.I. (2020): Tests to Determine the Geometric Characteristics of Aggregates – Part 2: Determination of the Particle Size Distribution – Control Sieves, Nominal Dimensions of the Openings, UNI EN 933-2: 2020. Milan.
- Mantovani, L., De Matteis, C., Tribaudino, M., Boschetti, T., Funari, V., Dinelli, E., Toller, S., & Pelagatti, P. (2023): Grain size and mineralogical constraints on leaching in the bottom ashes from municipal solid waste incineration: a comparison of five plants in northern Italy, *Front. Environ. Sci*, **11**, 1-15.
- Steffen, W. (2021): Introducing the Anthropocene: The human epoch. *Ambio*, **50**, 1784-1787.
- Trischler, H. (2016): The Anthropocene: A Challenge for the History of Science, Technology, and the Environment. *NTM Int. J. Hist. Ethics Nat. Sci. Technol. Med*, **24**, 309-335.
- UNI EN 12457-4 (2004): Waste characterization-leaching-compliance test for leaching of granular and sludge waste—Part 2: Single stage test, with a liquid/solid ratio of 10 L/kg, for materials with particles smaller than 4 mm (with or without size reduction). Available at: <https://store.uni.com/en/uni-en-12457-4-2004> (Accessed October, 2021).
- Zalasiewicz, J., Williams, M., Fortey, R., Smith, A., Barry, T.L., Coe, A.L., Bown, P.R., Rawson, P.F., Gale, A., Gibbard, P., Gregory, F.J., Hounslow, M.W., Kerr, A.C., Pearson, P., Knox, R., Powel, J., Waters, C., Marshall, J., Oates, M., & Stone, P. (2011): Stratigraphy of the anthropocene. *Philos. Trans. R. Soc. A Math. Phys. Eng. Sci*, **369**, 1036-1055.

Geochemical modeling of solid waste-binder systems in stabilization/solidification applications

Yikai Liu

Dipartimento di Geoscienze e Centro CIRCe, Università degli Studi di Padova, via G. Gradenigo 6, 35129, Padova, Italia

DOI:10.19276/plinius.2023.01.007

INTRODUCTION

Sustainable soil stewardship provides the basis for terrestrial ecosystems and geochemical cycles. However, the unprecedented urbanization in the last decades brought massive solid waste stockpiles worldwide, detrimental to soil health and the neighborhood flora and fauna.

Herein, in-situ solidification/stabilization (S/S) has been proposed as a remediation strategy to prevent further pollution in the contaminated sites. But the challenges of substantial CO₂ emission and the sensitive durability attributed to ordinary Portland cement (OPC), which is the most widely used binder in the S/S technique, place this strategy under scrutiny. Herein, developing alternative low-carbon and cost-effective binders is important for facilitating these traditional remediation technologies.

In this work, we examined the feasibility of mitigating or negating the use of OPC in the S/S process of pyrite ash and phosphogypsum, the primary hazardous solid wastes generated in the phosphate industry. One traditional binder (OPC) and four alternative low-carbon footprint binders (calcium aluminate cement (CAC), white-steel-slag activated blast furnace slag (GGBFS), alkaline-GGBFS, and OPC-GGBFS) were applied in the remediation process. After the physicochemical and mineralogical characterization of the stabilized products, we constructed the geochemical modeling to reveal the potential mechanisms of contaminant retention and ensure long-term environmental availability. Finally, we evaluated how integrating these innovative technologies could shed light on reducing greenhouse gas emissions and offer technical benefits in future field trials.

The overall findings underscore the immobilization mechanisms of pollutants using different binder strategies and highlight the urgent need to bridge the zero-emission insights to sustainable S/S technologies. The constructed geochemical modeling, in tandem with the inclusion of more solid waste types and properties in the following models, will be pivotal in predicting the availability and efficiency of green and sustainable remedia-

tion strategies.

WASTE CHARACTERIZATION

The waste used in this work was excavated from an abandoned fertilizer production facility in Italy, which is now used as a storage site for the solid waste generated by pyrite roasting, sulfuric acid production, and phosphorus fertilizer production. The contaminated soil was collected following a systematic sampling grid from the surface to 2.5 m depth covering the whole area of around 0.11 km². In this work, the soil was mainly composed of black pyrite ashes. The soil sample was placed in a polyethylene bag and then transported to the laboratory. Then the sample was air-dried, ground, and passed through a 2 mm mesh sieve prior to the following characterization experiments.

Characterization of pyrite ash

The SEM images (Fig. 1a, b, and c), as well as the XRD investigations, evidence the presence of hematite, jarosite, gypsum, quartz, and anglesite (Liu et al., 2023b). Besides forming sparingly soluble anglesite at acidic conditions, Pb was found in complex exsolution/intergrowth textures in amorphous Fe oxide phases (Fig. 1d and e) and incorporated in the Fe-K-S-Pb oxide rims in a compact form along the edges of the structures (Fig. 1f and g). The presence of Fe-K-S-Pb oxide rims could imply Pb incorporation within the jarosite crystal structure. In addition, the fate of Zn was related to the formation of sulfur minerals, as a Zn-Fe-S assemblage was observed in Fig. 1i. But as a minor component, it is hard to assess the exact origins of this assemblage, which may represent a residue of the primary ore or a precipitated secondary phase.

To analyze the Pb distribution mechanisms in the contaminated soil, Raman spectroscopy was further used to examine the area with high Pb concentration presented in Fig. 1d and g. The results imply the presence of kintoreite and Pb incorporation into jarosite.

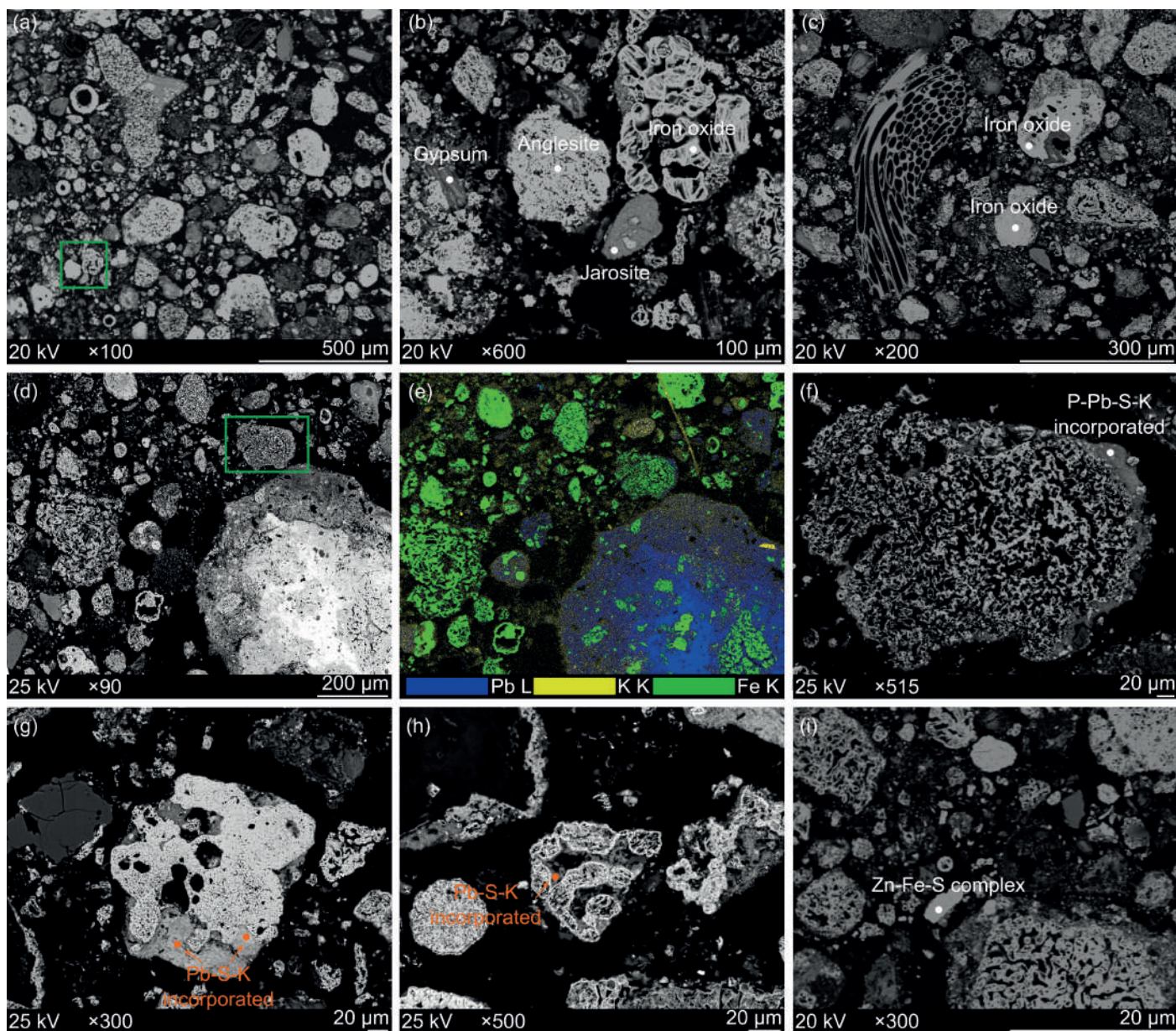


Figure 1 SEM micrographs of the sample. **a)** backscattered scanning electron (BSE) microscopy image of contaminated soil. **b)** BSE image showing the presence of anglesite. **c)** BSE image implies the iron oxide; **d)** BSE image demonstrates the distribution of Pb. **e)** elemental mapping of lead, potassium, and iron attributing to image **d**. **f)** the magnified BSE image corrected to the green rectangle marked area in image **d**, indicating a Pb-incorporated structure. **g)** and **h)** the compacted Pb-bearing assemblages. and **i)** BSE image shows the Zn-Fe-sulfate assemblage.

Leachability of potentially toxic elements

When using deionized water as the leachate (at pH 4.6), the leachability of the tested elements showed that the contaminated soil should be classified as hazardous waste, with all the concentrations being significantly higher than the limits established by Italian laws. The leaching of the studied trace metals (Pb, Zn, and Fe) showed a strong dependence on the pH values, indicating that the contaminated soil is susceptible to changing conditions of the stockpile.

At the pH value of 1.98, the highest concentrations of Pb, Zn, and Fe in the leachate were reached at 1.59×10^1 , 7.49×10^1 , and 2.69×10^2 $\mu\text{mol/L}$. The minimum release of Pb (0.38 $\mu\text{mol/L}$) and Zn (0.30×10^{-1} $\mu\text{mol/L}$) was found at the pH value of 9.04. However, with the increase in pH values, Pb and Zn showed an upward tendency in the release under alkaline conditions. The enhanced element release at basic conditions was due to the occur-

rence of specific dissolution of minerals (e.g., the transformation of Pb/Zn bearing carbonates to hydroxides) and desorption reactions of elements from reactive surfaces (e.g., Pb/Zn may desorb from Fe-oxides surfaces and favor the formation of hydroxyl-complexes). By contrast, the release of Fe at the neutral/alkaline conditions fluctuated approximately from 0.32 to 3.40 $\mu\text{mol/L}$, which was probably related to the formation of iron hydroxide. Besides, the increasing leachability of SO_4^{2-} was only observed under alkaline conditions, with the concentrations being constant at around 104 $\mu\text{mol/L}$ in the acidic and neutral regions.

HIGH-PERFORMANCE S/S (HPSS) TO WASTE

Solidification/stabilization (S/S) is a mature industrial process for the remediation of solid waste containing hazardous substances (Calgaro et al., 2021; Contessi et al.,



Figure 2 HPSS® process framework.

2020). Typically, as one of the most widely used artificial materials in industries (Habert et al., 2020; Bui Viet et al., 2020), ordinary Portland cement (OPC) is extensively applied in the S/S process due to its unique properties and simplicity of use (Hou et al., 2023; Ouhadi et al., 2021). However, the substantial carbon dioxide emission during OPC production and the concerns about its undesirable retention capacity for potentially toxic elements strain this strategy.

To tackle this objective, we herein tailored four alternative binders (CAC, OPC-activated GGBFS, white-steel-slag activated GGBFS, and alkaline-activated GGBFS) for facilitating immobilization of high Pb content pyrite ash, with the perspectives of enhancing Pb retention and mitigating anthropogenic carbon dioxide emissions.

Given in Fig. 2 is the framework of the high-performance S/S (HPSS®) process proposed by our co-workers (Bonomo et al., 2009; Contessi et al., 2020). After removing the large aggregates of the collected contaminants, the sieved sample and binder, primarily cementitious materials, are blended in a mechanical disc pelletizer with a predetermined amount of aqueous solution (water or alkaline solution). Then the pellets are cured in air or atmosphere-isolated conditions for subsequent real-world use.

This management is deemed to effectively convert the solid waste to a physiochemically stable solid assemblage that can long-term or permanently store contaminants in a relatively less mobile form (Chen et al., 2009).

HPSS of natural resource-derived binders

In OPC-based pellets (OP), typical crystalline hydration products of OPC (ettringite, 5.5 wt%) and unhydrated clinker phases (Alite and Belite, 1.6 wt% in total) were clearly detected in its XRD pattern (Fig. 3a). Hematite (54.0 wt%), jarosite (2.1 wt%), and gypsum (6.7 wt%), originating from the raw pyrite ash, were also present. The amorphous content, primarily composed of C-S-H gel, was quantified as 24.2 wt%. The absence of portlandite is possibly related to the carbonation with the atmospheric CO₂ because approximately 4.4 wt% of calcite was observed (Du et al., 2019).

XRD mineralogical analyses of the CAC-based samples (CA) show that the amount of precipitated ettringite (15.1 wt%) is approximately triple of the CP samples. This is because the CAC binder is mainly composed of CaO·Al₂O₃ (CA), CaO·2Al₂O₃ (CA2), and 12CaO·7Al₂O₃ (C12A7), thus producing considerable aluminum-containing hydration products, as ettringite and gibbsite (4.3 wt%) present in CA samples. In turn, the amorphous content (10.7 wt%) is only half of the CP samples, possibly assigned to amorphous aluminum hydrates, instead of the C-S-H gel precipitation as in the CP system (Hidalgo et al., 2009; Li et al., 2017).

SEM/EDS analysis of OP samples shows that the dark rims around the unhydrated OPC particles are C-S-H gel, which is the typical amorphous hydration product of the OPC system, as high Ca and Si weight fractions detected. The presence of Pb is observed in the mixtures of pyrite ash phases and cementitious matrices adjacent to the iron oxide particles and is preserved in the C-S-H. In CA samples, more cracks are observed throughout the analyzed areas, which could be attributed to ettringite dehydration due to the oven drying process during the sample preparation (Bizzozero et al., 2014) and the high vacuum condition reached in the SEM experiments (Contessi et al., 2020). SEM/EDS analysis of OP samples shows that the dark rims around the unhydrated OPC particles are C-S-H gel, which is the typical amorphous hydration product of the OPC system, as high Ca and Si weight fractions detected. The presence of Pb is observed in the mixtures of pyrite ash phases and cementitious matrices adjacent to the iron oxide particles and is preserved in the C-S-H.

In CA samples, more cracks are observed throughout the analyzed areas, which could be attributed to ettringite dehydration due to the oven drying process during the sample preparation (Bizzozero et al., 2014) and the high vacuum condition reached in the SEM experiments (Contessi et al., 2020). The presence of Pb in CA pellets has a high correlation with the spatial distribution of Ca, Al, Fe, and S, inferring that Pb-bearing species are well-intermixed with ettringite through the adsorption

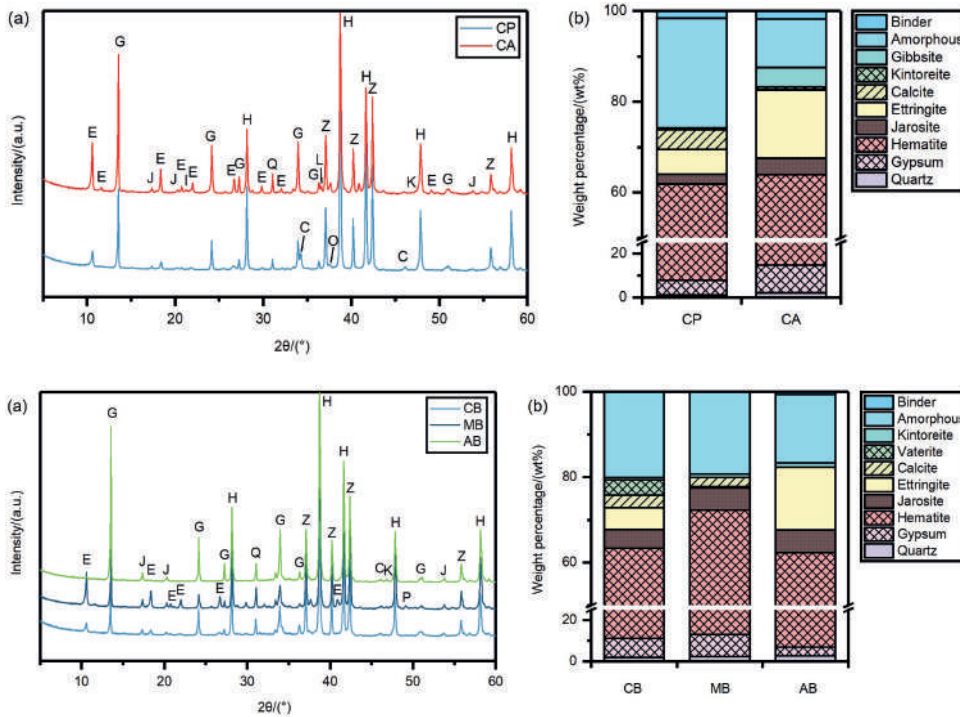


Figure 3 XRD characterization of CP and CA samples. (a) The detected XRD spectra and (b) The correlated quantification results. C: calcite, E: ettringite, G: gypsum, H: hematite, I: Gibbsite, J: jarosite, K: kintoreite, L: gehlenite, O: alite and/or belite, Q: quartz, and Z: zincite. Binder in Fig. 3b indicates the sum fraction of alite and belite in CP samples and the gehlenite fraction in CA samples.

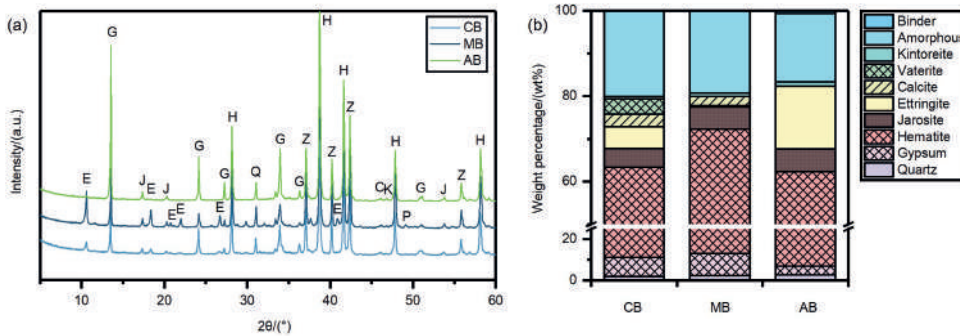


Figure 4 XRD characterization of CB, MB, and AB samples. (a) The detected XRD spectra and (b) The correlated quantification results. C: calcite, E: ettringite, G: gypsum, H: hematite, J: jarosite, K: kintoreite, Q: quartz, and Z: zincite. Binder in Fig. 4b indicates the sum fraction of alite, belite, and gehlenite fraction.

and/or incorporation.

HPSS of by-products-derived binders

The XRD results of CB pellets (Fig. 4a and b) illustrate that hematite is the main crystalline phase detected (52.0 wt%). Meanwhile, jarosite and gypsum, also originating from the pyrite ash, are observed at 4.4 and 9.2 wt%, respectively. The binder hydration products are ettringite (5.1 wt%) and amorphous phases (20.1 wt%) that mainly consist of C-(A)-S-H gel and unreacted slags (Berthomier et al., 2021). Carbonates (vaterite and calcite) deriving from the carbonation of calcium species (e.g., portlandite and gypsum) at alkaline conditions are quantified as 6.6 wt%. A minor proportion (0.5 wt%) of the crystalline Pb-bearing phase kintoreite is found, with the most pronounced diffraction peak being observed at $46.8^\circ 2\theta$.

MB samples present similar hydration products as the CB scenario, however, with more crystalline ettringite (14.7 wt%) and fewer amorphous contents (16 wt%). Accordingly, the sulfate contents (gypsum 4.2 wt% and jarosite 5.3 wt%) are decreased. The carbonate species detected in CP and CB pellets are not present in the MB samples, indicating the low concentration of calcium in the pore solutions, which is not conducive to the formation of portlandite and its subsequent carbonation. Further, although high aluminum content steel slag and GGBFS are aluminate-rich materials like the CAC binder, the crystalline gibbsite is not observed in the XRD spectra of MB samples.

XRD mineralogical analyses of the AB pellets show that the ettringite formation is inhibited in this system (0.3 wt%). Likewise, the phases originate from pyrite ash (hematite (59.0 wt%), gypsum (10.9 wt%), jarosite (5.2 wt%), quartz (2.3 wt%), and kintoreite (0.9 wt%)) account for

over 75 wt% of the quantified pellets fraction, implying a relatively low hydration degree in AB samples. Note, the amorphous fraction in CB, MB, and AB samples can also be partially attributed to unhydrated GGBFS, which are amorphous (Gardner et al., 2015; Kirca et al., 2013).

Leachability of Pb and carbon emissions estimation of each binder scenario

The results of ultrapure water leaching (Fig. 5) confirmed the immobilization efficiency of Pb in the collected pyrite ash and applied binder scenarios, as well as the detected leachability of Al, Fe, and sulfates. Without the HPSS process, the release of Pb (1900 $\mu\text{g/L}$) from the pyrite ash is two orders of magnitude higher than the limits (10 $\mu\text{g/L}$ based on D.Lgs. n. 152/2006 and 50 $\mu\text{g/L}$ based on D.M. n. 186). In the CP pellets, the Pb leachability (180 $\mu\text{g/L}$) far exceeded the concentration limit for on-site reuse (10 $\mu\text{g/L}$), which confirms previous results showing that the OPC binder is insufficient when the Pb concentration is in a relatively high range (Contessi et al., 2020). The Pb leachability of CB, CA, and MB decreased to 30, 20, and 57 $\mu\text{g/L}$, respectively.

In addition, Fig. 5 summarizes the carbon emissions and the preparation cost associated with each binder scenario. CP pellets show the largest carbon footprint, as recycling 1 tonne of pyrite ash will release 215 kg of CO_2 . Considering the CO_2 saving in view of the samples in its use stage by reacting with atmospheric CO_2 (Habert et al., 2020), CP carbonation can eliminate 29.7 kg CO_2/t of the carbon footprint, which is approximately 14% of the precursor pelletizing process. Herein the overall cost for the CP pellets preparation could reach 30.8 €/t (17.8 from the binder and water supply and 13.0 from the estimated CO_2 tax in E.U.). With regard to CA pellets, the overall cost related to the pelletization process could

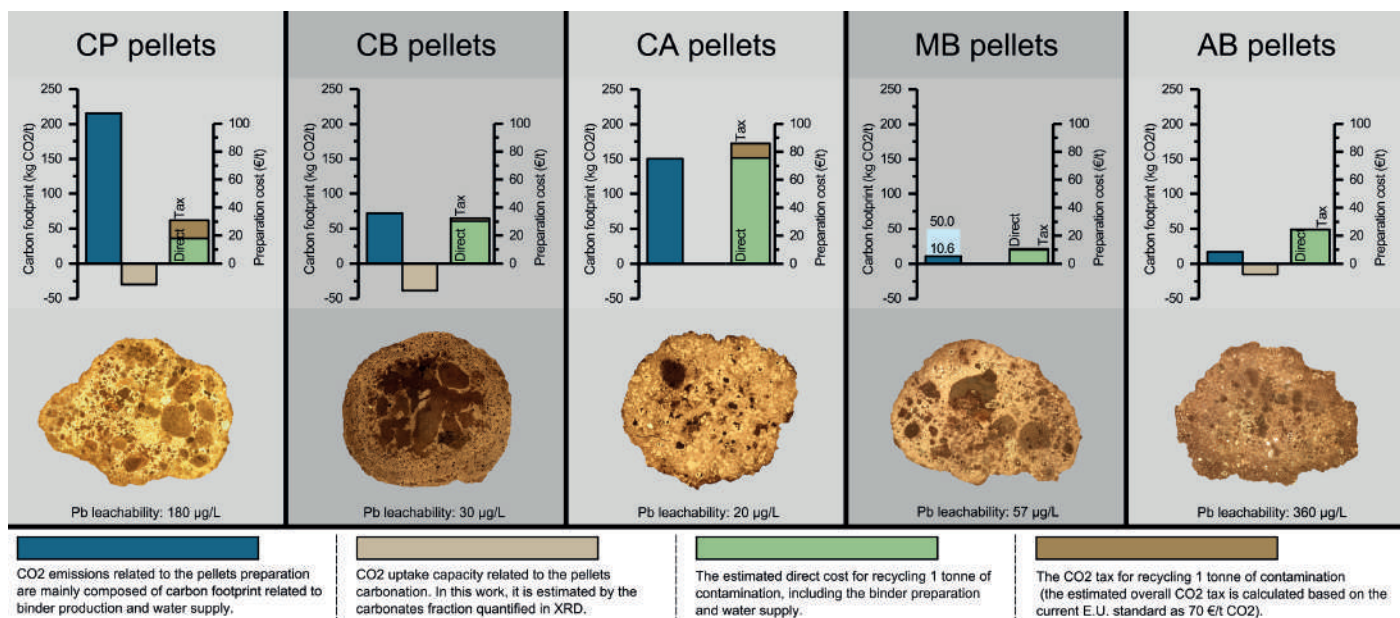


Figure 5 The optical microscope images and the related carbon footprint of the pellets preparation. The carbon uptake of CA and MB pellets is estimated to be 0 because the carbonates are not found in their XRD patterns. The "Direct" represents the direct cost related to the pellets preparation and the "Tax" indicates the indirect cost of CO₂ tax. Note that the carbon footprint and CO₂ tax of MB pellets are estimated based on recycled steel slag (10.6 CO₂/t CO₂ emission, 10.0 €/t direct cost, and 0.7 €/t CO₂ tax), while the bright blue column marked indicates the estimation is from synthetic mayenite, which is the primary component of recycled steel slag (50.0 CO₂/t CO₂ emission, 12.8 €/t direct cost, and 3.5 €/t CO₂ tax).

make this strategy unprofitable (75.5 €/t) because of the high price of CAC binder and its production is less carbon-negative, which may emit 150.5 kg CO₂/t. Further, the inhibited carbonation in CA pellets may bring less CO₂ tax benefit to this strategy.

With the substitution of industrial by-products, the CO₂ benefits under CB, MB, and AB options are optimized accordingly. The calculated CO₂ release and uptake of CB samples are 71.9 and 38.7 kg CO₂/t, indicating that more than half of the CO₂ emission related to binder production can be mitigated as a consequence of the sponge effect. Although the CB binder preparation cost (30.2 €/t) is higher than the CP pellets, the CO₂ tax (2.3 €/t) is much less than the traditional pathway. For the MB pellet, despite the carbonates (calcite and vaterite) are also not found in this sample, its associated carbon footprint is only a quarter of the CP preparation at 50.0 kg CO₂/t. Meanwhile, because of the broad quantities and economics of GGBFS, the overall cost of the MB scenario is only 10.0 €/t. The lowest carbon footprint corresponds to the cases of AB pellets, with the emission estimated as 16.9 kg CO₂/t. The following carbonation takes up 15 kg of CO₂ emissions.

GEOCHEMICAL MODELING SUMMARY

Characterizing the PTEs leaching behaviors and the associated mechanisms over a broad pH range is fundamental in tailoring the field application. However, relevant empirical analysis to reveal the underlying mechanisms responsible for the leaching behavior of constituents remains poorly understood.

Based on recent studies, the geochemical modeling approach could disentangle how this coupling operates,

where insights can be gained through the use of pH-dependent leaching tests in association with geochemical speciation modeling (Chen et al., 2021; Du et al., 2019; Jarošíková et al., 2018; Sun et al., 2019). The dissolution/precipitation equilibrium of the PTEs-containing phases and the cementitious assemblages is assumed to be the primary mechanism for the leaching behavior of the PTEs. However, there is strong evidence that the ion exchange and adsorption also play a critical role in controlling the PTEs release, for instance, the Pb could be incorporated into the ettringite structure (Contessi et al., 2021) and adsorbed onto the surface of C-S-H/C-A-S-H gel (Chen et al., 2022; Liu et al., 2021). The reconstruction of these processes in geochemical modeling is still fragmented and poorly constrained (Vega-Garcia et al., 2021; Zavarin et al., 2022). This is because the representativeness of the modeling is limited by the amount of available data from the thermodynamic database (Holmes et al., 2022; Lu et al., 2022). These knowledge gaps hinder the development of a fundamental understanding of the controls on PTEs release and migration.

To contribute to filling in these gaps, we elucidated the roles of traditional (OPC) and alternative (CAC) binders in Pb retention, thus addressing the relatively low Pb immobilization efficiency associated with conventional OPC and (2) integrating the insights into the adsorption and ion exchange mechanisms controlling Pb mobilization. With the thorough characterization of the partitioning of chemical species, we constructed geochemical modeling coupled with the Parameter Estimation software (PEST). By comparing the identified PTEs' leaching behavior from experiment and simulation, we investigated and quantitatively classified the impacts from dissolution/precipitation, adsorption, and physical encapsula-

tion on Pb capture. The results of this paper demonstrate the feasibility of using the Portland-free pathway to immobilize the PA. Further, it provides a reliable methodology to guide and test the plausibility of conceptual and numerical models of Pb mobilization and transport, even with a limited dataset, which may contribute to a more complete picture of PTEs release mechanisms in the stabilized products and improve the trial application of S/S technologies.

Quantification of Pb and sulfates retention in OPC- and CAC-based pellets.

Fig. 6 gives the quantitative results of the Pb and sulfates-bearing species of OP and CA modelings under the studied pH ranges. At alkaline pH conditions (pH > 8), the immobilization of Pb in the OP samples mainly relies on the adsorption and ion exchange capabilities of C-S-H and ettringite. With the decrease in pH values, the neutral pH conditions are no more suitable for the equilibrium of C-S-H and ettringite (Liu et al., 2023a).

Therefore, the adsorbed Pb is gradually released as a consequence of the dissolution of hydration products. Then the soluble Pb precipitates as cerussite or is partially immobilized by the ferrihydrite ($\text{Fe}(\text{OH})_3$) and hematite. At acidic conditions (pH < 5), the Pb immobilization is attributed to the anglesite precipitation and hematite adsorption. However, non-negligible amounts of Pb remain soluble in pore solutions, as the leaching tests ascertained that the Pb leachability at pH 3.3 is a thou-

sand times higher than the specified limit.

In Fig. 6b, the Pb retention of CA samples at alkaline conditions is primarily assigned to the adsorption and ion exchange with ettringite and hematite or precipitation as $\text{Pb}(\text{OH})_2$. At neutral pH conditions (pH 7 to 8), Pb leachability is dominated by hematite and ferrihydrite adsorption. Then Pb partially redissolves and reprecipitates as cerussite and anglesite, and a portion of soluble Pb remains in the pore solution in the forms of Pb^{2+} , PbNO_3^- , and $\text{PbSO}_{4(\text{aq})}$ when the pH shifts to acid conditions. From Fig. 6c and d, the sulfates variation of OP and CA samples demonstrate a similar trend in acidic conditions (pH from 3 to 7). In these conditions, sulfate mainly precipitates as jarosite, anglesite, and gypsum. Whereas gypsum is the principal sulfate-bearing phase at pH values ranging from 7 to 9. The ettringite fraction increases at basic conditions, which are suitable for the stability of hydration products.

In general, our developed method enables a better understanding of the PTEs immobilization roles of the main hydration products and inherent phases in solid waste, which is hardly revealed by the experimental techniques. In turn, understanding the extent of this role variation will allow a more accurate and reliable mixture design for the in-situ remediation industry. The implications of these results underscore the importance of not only predicting and clarifying the PTEs immobilization amounts as a function of pH values but also highlighting the essential question of how the stabilized products would

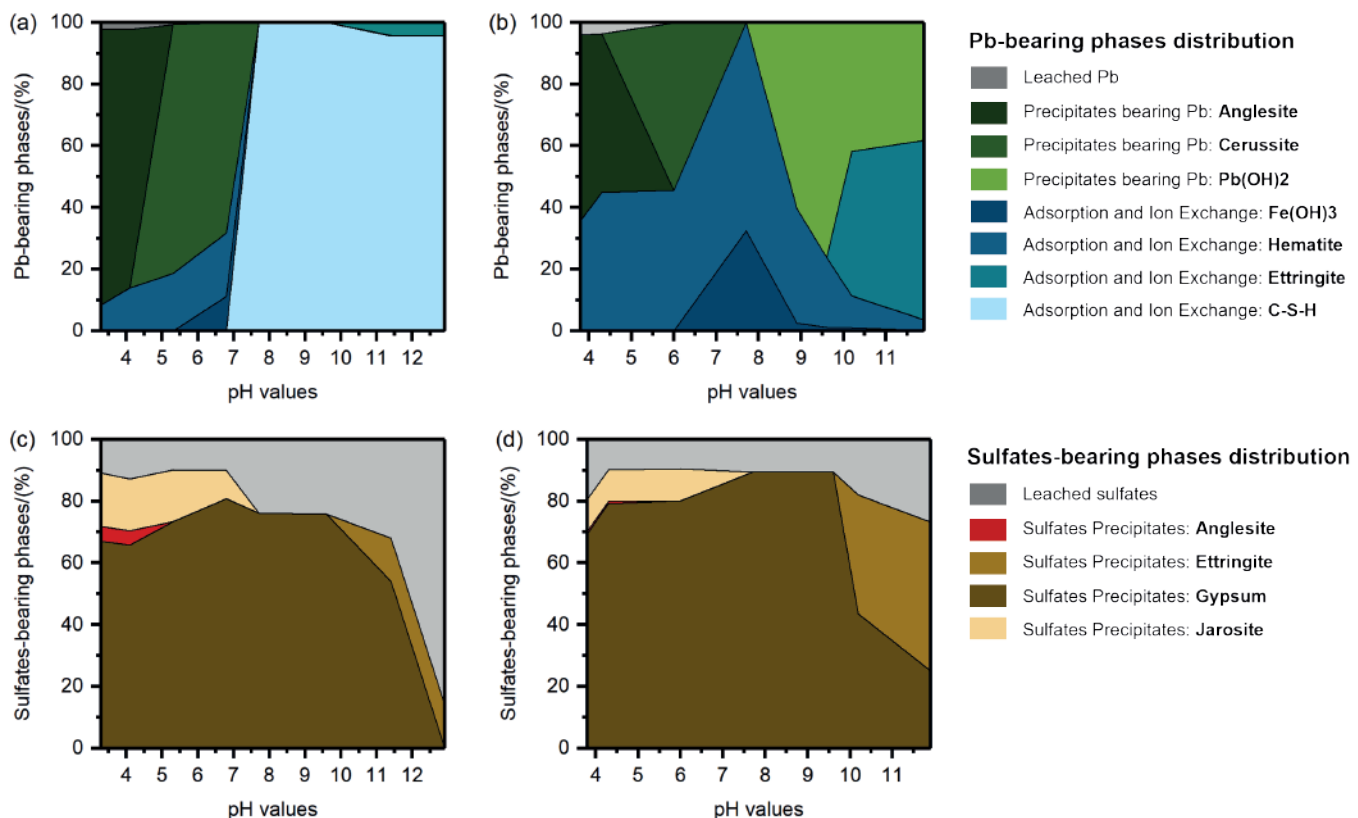


Figure 6 The simulated PTEs-bearing phases variation as a function of pH values. **a)** The variation of the Pb-bearing species in OP. **b)** The variation of the Pb-bearing species in CA. **c)** The variation of the sulfates-bearing species in OP. **d)** The variation of the sulfates-bearing species in CA samples.

contribute to PTEs retention when the field conditions are under harsh or unsuitable conditions. For example, when the pH of the rainfall and groundwater changes with the season or anthropogenic activities, the predicted concentrations of dissolved PTEs could be used to forecast whether secondary pollution will occur.

CONCLUSIONS

In this work, in-situ S/S has been proven a promising technology that can treat the PTEs contaminated soil profitably and scalably. Using the low-carbon binders to partially or entirely replace the use of ordinary Portland cement (OPC) has been proven a high-hope strategy that promotes the PTEs' remediation efficiency and bridges the gap between carbon-neutral world rhetoric and the reality of solid waste remediation applications. The developed geochemical modeling has prompted the possibility of an in-depth investigation for in-situ remediation in industrial sites by evaluating the PTEs leachability and the sponge effect of S/S products. The overall findings shed light on the understanding of PTEs immobilization mechanisms in multiple alternative sustainable binders, highlighting the significance of the perspectives of carbon neutrality in the emission-intensive S/S applications and providing new insights into the highly efficient S/S of contaminated wastes. The main conclusions are as follows:

- (1) The characterization results demonstrate that Pb and Zn are the most abundant heavy metal pollutants within the collected pyrite ash samples. With the XRD, SEM/EDS, and Raman investigation, anglesite and kintoreite have been confirmed as the primary Pb-bearing crystalline phases, which may be generated from the oxidation of remaining pyrite particles. In addition, the jarosite could be a heavy metal host, as the Pb or Zn-incorporated jarosite was characterized along the edge of the hematite particles. The pH-dependent leaching tests and geochemical modeling reveal that the Pb and Zn leachability strongly depends on the pH values of the leachates, with a downward trend towards the near-neutral pH region from 6 to 10. At acid conditions, the increased solubility of Pb is dominated by the dissolution of anglesite and the formation of Pb nitrate complexes, while Zn is controlled by Zn ions and Zn-sulfate complexes in the solution. In contrast, when the pH values move to strong alkaline conditions, the upward trend could be associated with the complexation of aqueous metal hydrates. Noteworthy, the results indicate that even under normal conditions (for instance, normal rainfall), the stockpile of pyrite ash poses a great environmental risk and strongly threatens human health, which only worsens under acidic or alkaline conditions. Herein, integrating profitable and sustainable remediation technologies in the contaminated site is
- critically essential to prevent further pollution.
- (2) In the S/S applications, the use of OPC is insufficient for efficient Pb immobilization due to the high alkaline conditions of the soil-binder system resulting from the dissolution of clinker phases, which may interfere with Pb precipitation. Meanwhile, the substantial carbon footprint attributed to OPC production also places critical scrutiny on this scenario. Although the CAC binder incorporation provides a promising Pb immobilization efficiency, the less satisfactory ecological benefits and the relatively high carbon footprint diminish the trial application of CAC. The GGBFS-incorporated binder tends to be a comprehensively sustainable and profitable strategy due to its excellent compatibility with Pb and relatively low-carbon nature. The experimental results indicate that aside from the Pb incorporation in the binding matrix similar to the OPC-waste system, the formation of low Ca/Si ratio C-(A)-S-H gel promoted the Pb retention, fulfilling the Pb leachability requirements for reuse as S/S material. Furthermore, the quantified sponge effect of industrial by-products incorporated pellets (MB and/or CB) suggests that it would promote the achievement of carbon neutrality. Overall, it provided useful guidance for improving the design and application of cement-free pathways for sustainable solid waste amendment, which bridged the gap between carbon-neutral world rhetoric and the reality of solid waste remediation applications.
- (3) The pH-dependent leaching tests of CP and CA samples indicate both scenarios demonstrate high retention of Pb at neutral and alkaline pH conditions (approximately from 7 to 11). The use of CAC binder effectively enhanced the Pb retention capacity of the stabilized product, especially in harsh acid conditions, with only a quarter of Pb concentration detected in CA samples (11000 µg/L) compared to CP samples (43000 µg/L). Experiments reveal that Pb incorporation in OPP samples is mainly associated with the presence of C-S-H, with an observed enrichment in Ca and Si-rich areas along the cement particles (where C-S-H precipitation occurs), whereas the Pb is homogeneously distributed in the CA samples. Geochemical modeling reveals that C-S-H adsorption is the primary Pb immobilization mechanism of CP samples under alkaline conditions, with a 0.1 mol/mol Pb retention capacity that can be reached. When the pH is unsuitable for C-S-H precipitation, cerussite and anglesite precipitation are the main controls of Pb leachability, with small amounts of soluble Pb being adsorbed by hematite and ferrihydrite. Regarding the CA samples, precipitation of Pb(OH) and incorporation in ettringite are the primary control mechanisms for Pb equilibrium in alkaline environments. The Pb host capacity of ettringite is estimated

to be approximately 0.1 mol/mol, which is equivalent to C-S-H. However, the contribution of hematite and ferrihydrite adsorption to Pb equilibrium is observed in a broader pH range compared to OPP samples. Likewise, the cerussite and anglesite precipitation shows stronger affinities for Pb immobilization in acid conditions.

- (4) The following works on revealing the physical profile would allow a more consistent description of the solid waste-binder systems. In addition, we recognize that the reliability and accuracy of our present model can be improved by further efforts of data collection in PTEs pH-dependent leachability with different PTEs concentrations and different mixtures proportions. Should the changes be significant, the model will need to be re-assessed and re-calibrated.

REFERENCES

- Berthomier, M., Lors, C., Damidot, D., De Larrard, T., Guérandel, C., & Bertron, A. (2021): Leaching of CEM III paste by demineralised or mineralised water at pH 7 in relation with aluminium release in drinking water network. *Cem. Concr. Res.*, **143**, 106399.
- Bizzozero, J., Gosselin, C., & Scrivener, K.L. (2014): Expansion mechanisms in calcium aluminate and sulfoaluminate systems with calcium sulfate. *Cem. Concr. Res.*, **56**, 190-202.
- Bonomo, L., Careghini, A., Dastoli, S., De Propris, L., Ferrari, G., Gabellini, M., & Saponaro, S. (2009): Feasibility studies for the treatment and reuse of contaminated marine sediments. *Environ. Technol.*, **30**, 817-823.
- Calgaro, L., Contessi, S., Bonetto, A., Badetti, E., Ferrari, G., Artioli, G., & Marcomini, A. (2021): Calcium aluminate cement as an alternative to ordinary Portland cement for the remediation of heavy metals contaminated soil: mechanisms and performance. *J. Soils Sediments.* **21**, 1755-1768
- Chen, Q.Y., Tyrer, M., Hills, C.D., Yang, X.M., & Carey, P., (2009): Immobilisation of heavy metal in cement-based solidification/stabilisation: A review. *Waste Manag.*, **29**, 390-403.
- Contessi, S., Calgaro, L., Dalconi, M.C., Bonetto, A., Bellotto, M. Pietro, Ferrari, G., Marcomini, A., & Artioli, G. (2020): Stabilization of lead contaminated soil with traditional and alternative binders. *J. Hazard. Mater.*, **382**, 120990.
- Du, B., Li, J., Fang, W., & Liu, J., (2019): Comparison of long-term stability under natural ageing between cement solidified and chelator-stabilised MSWI fly ash. *Environ. Pollut.*, **250**, 68-78.
- Gardner, L.J., Bernal, S.A., Walling, S.A., Corkhill, C.L., Provis, J.L., & Hyatt, N.C. (2015): Characterisation of magnesium potassium phosphate cements blended with fly ash and ground granulated blast furnace slag. *Cem. Concr. Res.*, **74**, 78-87.
- Habert, G., Miller, S.A., John, V.M., Provis, J.L., Favier, A., Horvath, A., & Scrivener, K.L. (2020): Environmental impacts and decarbonization strategies in the cement and concrete industries. *Nat. Rev. Earth Environ.*, **111**, 559-573.
- Hidalgo, A., García Calvo, J.L., Alonso, M.C., Fernández, L., & Andrade, C. (2009): Microstructure development in mixes of calcium aluminate cement with silica fume or fly ash. *J. Therm. Anal. Calorim.*, **96**, 335-345.
- Hou, D., Al-Tabbaa, A., O'Connor, D., Hu, Q., Zhu, Y.G., Wang, L., Kirkwood, N., Ok, Y.S., Tsang, D.C.W., Bolan, N.S., & Rinklebe, J. (2023): Sustainable remediation and redevelopment of brownfield sites. *Nat. Rev. Earth Environ.*, **44**, 271-286.
- Kirca, Ö., Özgür Yaman, I., & Tokyay, M. (2013): Compressive strength development of calcium aluminate cement-GGBFS blends. *Cem. Concr. Compos.*, **35**, 163-170.
- Li, G., Zhang, A., Song, Z., Shi, C., Wang, Y., & Zhang, J. (2017): Study on the resistance to seawater corrosion of the cementitious systems containing ordinary Portland cement or/and calcium aluminate cement. *Constr. Build. Mater.*, **157**, 852-859.
- Liu, Y., Molinari, S., Dalconi, M.C., Valentini, L., Ricci, G., Carrer, C., Ferrari, G., & Artioli, G. (2023): The leaching behaviors of lead, zinc, and sulfate in pyrite ash contaminated soil: mineralogical assessments and environmental implications. *J. Environ. Chem. Eng.*, **11**, 109687.
- Liu, Y., Molinari, S., Dalconi, M.C., Valentini, L., Bellotto, M.P., Ferrari, G., Pellay, R., Rilievo, G., Vianello, F., Salviulo, G., Chen, Q., & Artioli, G. (2023): Mechanistic insights into Pb and sulfates retention in ordinary Portland cement and aluminous cement: accessing the contributions from binders and solid waste. *J. Hazard. Mater.*, **458**, 131849.
- Ouhadi, V.R., Yong, R.N., & Deiranlou, M. (2021): Enhancement of cement-based solidification/stabilization of a lead-contaminated smectite clay. *J. Hazard. Mater.*, **403**, 123969.

Lithium enrichment in anatectic pegmatites: new insights from the thermometamorphic aureole of the Adamello batholith

Lorenzo Magnani

Dipartimento di Scienze della Terra "Ardito Desio", Università degli Studi di Milano, Via Mangiagalli 34, 20133, Milano, Italia

DOI:10.19276/plinius.2023.01.008

INTRODUCTION

Lithium is the least dense alkali metal, it is electrochemically active, featuring the highest redox potential value of all metals, and has the highest specific heat capacity of any solid element. These characteristics make it one of the most important commodity for modern life and a key element for modern electric vehicle revolution (e.g. Swain et al., 2017). Newly mined lithium to supply the estimated demand will come largely from pegmatite and related magmatic deposits, evaporative brines, and a growing group of unusual deposits including both rocks and brines (Kesler et al., 2012). Pegmatites are of interest due to their wider geographic distribution, lesser susceptibility to supply disruptions and environmental impact and they are the types of Li deposits on which the research effort has mostly focused on in the last years. Although several works addressing the genesis of Li-enriched pegmatites have been published (e.g. Černý, 1991; Černý & Ercit, 2005; Simmons et al., 1995, 1996, 2008, 2016, 2018), the processes that lead to the formation of these rocks are still not well understood. New research on these economically strategic resources is needed to expand our knowledge on the geological constraints that determine their formation and produce the metal endowment of pegmatites-hosted Li resources. The presented Ph.D. project, in particular, tries to provide tighter constraints on the evolution of Li-pegmatites by studying small Li-enriched bodies emplaced in the thermometamorphic aureole of the Adamello pluton (Northern Italy).

MATERIALS AND METHODS

This study is based on a set of forty samples from low-grade metamorphosed to migmatitic rocks of the Verrucano Lombardo formation as well as barren and Li-rich pegmatites collected in the Forcel Rosso area. In addition, five unmetamorphosed samples of Verrucano Lombardo pelites were also collected. Extensive and detailed field mapping was carried out to identify small-scale lithological variations and map the distribu-

tion of pegmatitic dykes. The mineralogy and texture of the collected samples were characterized in fifty-five thin sections by optical microscopy while mineral chemical data were obtained by electron microprobe. The whole rock major elements composition of the samples was determined at the department of Earth Sciences of the University of Milan (Italy) using an iCAP ICP-MS quadrupole coupled with a 193 nm Ar-F excimer laser on pressed powder pellets following the procedure of Peters and Pettke (2016). Data treatment was performed on SIL-LS (Guillong et al., 2008). The whole rock composition of the zoned LCT pegmatites has not been determined directly due to its extreme textural heterogeneity and large crystal dimensions which have hindered the collection of a single representative sample. To overcome this limitation the average composition of the pegmatites was calculated as the weighted average of the composition of each zone multiplied for their volumetric abundance. Radiogenic Sr and Nd isotopic analyses of 10 selected samples were performed using a Thermo Fisher Neptune Plus MC-ICP-MS at the Istituto di Geoscienze e Georisorse - CNR in Pisa (Italy) in 2% HNO₃ solution containing 20-200 ng*g⁻¹ of analyte. The in-situ B isotope composition of tourmaline crystals was measured by LA-MC-ICP-MS technique at the Geochemistry, Geochronology and Isotope Geology Laboratory at the Earth Science Department "A. Desio", University of Milan (Italy) by coupling the laser system used for the trace element determination to a Neptune XT MC-ICP-MS (Thermo Fisher Scientific).

GEOLOGICAL SETTING

The Adamello batholith is the largest of the Tertiary Periadriatic plutons and was emplaced at 6-10 km depth (Broderick et al., 2015) in the central Southern Alps during the Eocene-Oligocene. The rocks of the Adamello massif show a distinct compositional similarity to volcanic rocks of equivalent SiO₂ content from calc-alkaline suites of continental margins (Dupuy et al., 1982). Variation trends of major and trace elements generally resemble trends generated by fractional crystallization

dominated by plagioclase and to a smaller degree by amphibole and pyroxene. Overall, the Adamello plutons show a sequential emplacement from the oldest units in the south (Re di Castello pluton, RdC, ~43 Ma) to the youngest in the north (Avio pluton, ~30 Ma; Del Moro et al., 1985; Schaltegger et al., 2019). Strontium isotope ratios ($^{87}\text{Sr}/^{86}\text{Sr}$) indicate a mantle origin and tend increase from 0.7036 in the south to 0.7120 in the north (Del Moro et al, 1983; Blundy, 1989) indicating that contamination by radiogenic upper-crustal strontium increased with time, becoming most significant in the youngest, northernmost plutons. Most of the country rocks (ca. 90%) surrounding the Adamello batholith exhibit evidence of contact metamorphism within the ca. 1 km to 4 km thick thermal aureole (Callegari & Brack, 2002), inside which the studied LCT pegmatites are intruded. Two families of pegmatites are present: one Li-enriched related to the migmatites and one Li-poor intruded into the Adamello pluton magmatic mass.

RESULTS

P-T conditions and Role of fluids in partial melting

In the contact aureole of the collisional metaluminous Adamello pluton (Italy), pelites reached hornfels facies conditions locally undergoing partial melting, forming Crd-bearing and Crd-absent migmatites. This small-scale migmatitic field is spatially associated with barren and Lithium-Cesium-Tantalum (LCT) pegmatitic dykes of granitic composition, suggesting a direct link between low-pressure partial melting and generation of Li-enriched felsic melts. Phase equilibria modelling reveals that the Crd-bearing metapelitic migmatites produced around 20 vol.% melt fraction through fluid-assisted melting reactions, while the Crd-absent stromatic metatexites produced ca. 35 vol.% of melt during fluid-rich partial melting. No melting was expected in strictly fluid-absent conditions. Peak P-T metamorphic conditions were calculated at 690-700°C and 300 MPa for both rock types. Because of the steep contact thermal gradient, the underlying and older conglomerates of the Verrucano Formation, of which the pelitic succession is part of, as well as rocks of the Collio Formation experienced comparably lower temperature metamorphism. Their mica-poor mineral compositions prevented them from melting and influencing the local anatectic processes. Crd-bearing migmatites leucosomes are compositionally similar to anatectic melts obtained by phase equilibria modelling, connected to fluid-assisted melting and defined as unfractionated. The leucosomes dominated by Kfs-Bt cumulus mineral composition and extremely enriched in K_2O , Sr and Ba are connected to fluid-rich melting and Crd-absent migmatites.

The first documented case of anatectic LCT pegmatites in Italy

Major and trace element modelling suggests that part of the melt formed during fluid-present melting was extracted from the source. The composition of this evolved anatectic magma is compatible with the chemical composition of the migmatites-hosted LCT pegmatites. Whole rock Sr-Nd isotopic data confirm that the Li-rich pegmatites of the Forcel Rosso area are indeed crustally derived (ca. 0.74 $^{87}\text{Sr}/^{86}\text{Sr}_i$ and ca. -10 ϵNd) marks them as produced by direct anatexis of metapelites. The isotopic data characterizing the pluton-hosted pegmatites (0.705 $^{87}\text{Sr}/^{86}\text{Sr}_i$, -3 ϵNd) marks them as mantle-derived and directly linked to the Adamello batholith, clearly marking the lack of direct relationship existing between this magmatic intrusion and pegmatites featuring Li enrichment in its contact aureole. The data from this study shows that cordierite, or the absence of it, plays a key role in regulating the lithium transfer during partial melting in low pressure migmatites. Zircon U-Pb ages for all pegmatites in the area point to the same age of the Adamello pluton intrusion, from 37.5 to 38.5 Ma, and trace elements compositions outline important differences in the geochemical signature between pluton-derived and metapelite-derived pegmatites. LCT pegmatites zircons are rich in Y while pluton-related pegmatites zircons are enriched in Th. The Ti-in-zircon geothermometer confirms that anatectic pegmatites crystallized at the peak metamorphic temperature calculated through phase equilibria modelling.

Tourmaline as petrogenetic indicator: confirming the hypothesis

Once defined that Li-enriched pegmatites are anatectic, tourmaline was used to study the continuous evolution of the metapelitic system from unmetamorphosed up to the conditions of pegmatite crystallization. This mineral is the main boron carrier among the rock forming minerals and it's ubiquitous in the studied rocks. Studying the major element composition and boron isotopic signature several changes and trends are identified highlighting how this mineral evolves through the metamorphic history of metapelites, revealing a seemingly more complex picture compared to what is reported in the published literature data. Also, the data show how this mineral records variations during pegmatites crystallization processes making it valuable in the interpretation of their complex internal evolution processes.

IMPLICATIONS AND CONCLUSIONS

This Ph.D. project proved that Li-enriched pegmatites may be anatectic and originate through fluid-present melting of metapelites, even in the thermometamorphic aureole of plutons. This work identifies the mineral cor-

dierite as the main regulator of lithium liberation during low-pressure anatexis of suitably Al-rich pelitic rocks. The results highlight that in-source and en-route melt fractionation play an extremely important role each time magma is extracted from its source and that this process is the one ultimately responsible for the formation of Li-enriched melts. Pegmatitic zircons, although complex, can be used as tracers in order to help define the origin of pegmatitic dykes, particularly in cases in which these bodies are too old for Sr isotopic determination. The studied area shows that small scale variations in the pre-anatectic abundance and presence of aqueous fluids influences melt production and melt composition of different migmatitic areas. Finally, the metamorphic and magmatic history of the studied tourmaline crystals highlights how this mineral may record almost every boron-involving reaction and help unravel the complex history of migmatites, pegmatites and Tur-bearing plutons.

REFERENCES

- Broderick, C., Wotzlaw, J. F., Frick, D. A., Gerdes, A., Ulianov, A., Günther, D., & Schaltegger, U. (2015): Linking the thermal evolution and emplacement history of an upper-crustal pluton to its lower-crustal roots using zircon geochronology and geochemistry (southern Adamello batholith, N. Italy). *Contrib. Mineral. Petrol.* **170(3)**, 1-17.
- Callegari, E., & Brack, P. (2002): Geological map of the tertiary Adamello batholith (northern Italy). Explanatory notes and legend. *Mem. Soc. Geol. It.*, **54**, 19-49.
- Černý, P. (1991): Rare-element granitic pegmatites. Part I: Anatomy and internal evolution of pegmatite deposits. *Geosci. Can.*, 18(2), 49-67.
- Cerný, P. & Ercit, T.S. (2005): Classification of granitic pegmatites revisited. *Can. Mineral.*, **43**, 2005-2026.
- Del Moro, A., Pardini, G. C., Quercioli, C., Villa, I. M., & Callegari, E. (1983): Rb/Sr and K/Ar chronology of Adamello granitoids, southern Alps. *Mem. Soc. Geol. It.*, **26(1)**, 285-299.
- Del Moro A., Ferrara G., Pesca A., & Callegari E. (1985): A geochemical study on the acid and basic rocks of the Adamello batholith. *Mem. Soc. Geol. It.* **26**, 223-259
- Dupuy, C., Dostal, J., Marcelot, G., Bougault, H., Joron, J. L., & Treuil, M. (1982): Geochemistry of basalts from central and southern New Hebrides arc: implication for their source rock composition. *Earth Planet. Sci. Lett.*, **60(2)**, 207-225.
- Kesler, S. E., Gruber, P. W., Medina, P. A., Keoleian, G. A., Everson, M. P., & Wallington, T. J. (2012): Global lithium resources: Relative importance of pegmatite, brine and other deposits. *Ore Geol. Rev.*, **48**, 55-69.
- Schaltegger, U., Nowak, A., Ulianov, A., Fisher, C. M., Gerdes, A., Spikings, R., & Müntener, O. (2019): Zircon petrochronology and $40\text{Ar}/39\text{Ar}$ thermochronology of the Adamello Intrusive Suite, N. Italy: monitoring the growth and decay of an incrementally assembled magmatic system. *J Petrol*, **60(4)**, 701-722.
- Simmons, Wm.B., Foord, E.E., Falster, A.U., & King, V.T. (1995): Evidence for an anatectic origin of granitic pegmatites, western Maine, USA. *Geol. Soc. Amer. Ann. Mtng.*, New Orleans, LA, Abstr. Prog., 27, A411.
- Simmons, Wm.B., Foord, E.E., & Falster, A.U. (1996): Anatectic origin of granitic pegmatites, western Maine, USA. *GAC-MAC Ann. Mtng.*, Winnipeg, Abstr. Prog., A87.
- Simmons, W. B. S., & Webber, K. L. (2008): Pegmatite genesis: state of the art. *Eur. J. Mineral.*, **20(4)**, 421-438.
- Simmons, W. B., Pezzotta, F., Shigley, J. E., & Beurlen, H. (2012). Granitic pegmatites as sources of colored gemstones. *Elements*, **8(4)**, 281-287.
- Simmons, W., Falster, A., Webber, K., Roda-Robles, E., Boudreaux, A. P., Grassi, L. R., & Freeman, G. (2016): Bulk composition of Mt. Mica pegmatite, Maine, USA: Implications for the origin of an LCT type pegmatite by anatexis. *Can. Mineral.*, **54(4)**, 1053-1070.
- Simmons, W. B., Webber, K. L., Falster, A. U., & Roda-Robles, E. (2018): Post-orogenic, prerifting anatectic origin of the Oxford Co., Maine, USA pegmatite field. In *XXII International Mineralogical Association meeting at: Melbourne, Australia. Book of Abstracts (Vol. 288)*.
- Swain, B. (2017): Recovery and recycling of lithium: A review. *Sep. Purif. Technol.*, **172**, 388-403.

Crystal chemistry and physical-chemical behaviour of RE-E-bearing phosphates and arsenates

The case study of Mt. Cervandone

Francesco Pagliaro

Dipartimento di Scienze della Terra "A. Desio", Università degli Studi di Milano, via Botticelli 26, Milano, Italia

DOI:10.19276/plinius.2023.01.009

INTRODUCTION

Rare Earth Elements

Rare Earth Elements (REE) correspond to the lanthanoid group, Sc and Y, which are recognized as indisputably fundamental materials for several economic sectors, mostly connected with high-tech industry and the so-called "green" energy. Within the last few decades, their market has experienced a strong increase. The applications of REE are bound to several modern technologies, like, but not limited to, permanent magnets, battery alloys, catalysts for petroleum and automotive sectors, glass additives, polishing and phosphors in monitors (e.g., Blengini et al., 2020).

Rare Earth Elements are conventionally split into two major groups, the Light REE (LREE) and Heavy REE (HREE), based on their atomic radii and electronic configuration of the 4f electron shell: LREE comprising the Ce-Gd group, while the HREE includes the Tb-Lu series; in addition, Y was included as one of the HREE, being its atomic radius intermediate between those of Ho and Er, while Sc is not included in any of the two groups, although it is worth to mention that the smaller ionic radius of Sc makes it to behave as one of the HREE.

Mt. Cervandone

The present study focuses on several mineral samples from hydrothermal quartz fissures outcropping at the Mt Cervandone (Leontine Alps), in Piemonte, Italy. From the geographical point of view, the area of interest is in the Verbano-Cusio-Ossola province, within the natural park "Parco dell'Alpe Veglia e dell'Alpe Devero. From the geological perspective, the Cervandone area is located within the Penninic domain of the Central Alps and, more specifically, within the Lower Penninic units.

The Mt. Cervandone is one of the most renowned REE deposits of the Alps, known among both collectors and scientists for its unusual and changing nature of the REE- and As-bearing mineralogical species. Unfortunately, despite the huge number of studies focused on the Mt. Cervandone area, most of them relate to the mineralogy

of unusual specimens and very little efforts have been dedicated to unveil its geological features. Indeed, there are only few studies (Guastoni et al., 2006; Guastoni et al., 2013) concerning the REE-source in Mt. Cervandone. It is known that the origin of REE-minerals is connected to the NYF pegmatites: within the pegmatites, the REE-bearing minerals are rather abundant, and the pegmatites likely represent the pristine REE source (Graeser & Roggiani 1976) with allanite-(Ce) representing the most likely source mineral (Alessandro Guastoni, personal communication). On the other side, within the quartz fissures, the occurrence of REE-bearing minerals is rather sporadic (Guastoni et al., 2006).

Allanites can undergo a complete dissolution, leaving centimetric allanite-shaped voids, often filled by monazite-(Ce) and synchyste-(Ce) (Alessandro Guastoni, personal communication). The decomposition of allanites leads to a REE enrichment in the hydrothermal fluids, which determined the crystallization of REE-minerals within the quartz fissures.

ATO₄ minerals

Among the several REE-minerals belonging to the alpine-fissures of the Cervandone complex, in the context of the present project, two arsenates [chernovite-(Y) and gasparite-(Ce)] and two phosphates [xenotime-(Y) and monazite-(Ce)] have been selected. All of them belong to the so-called ATO₄ group. The expression ATO₄ is a general term used in the literature to define ternary, inorganic compounds, usually oxides. Within ATO₄, A and T represent two cations, not necessarily different, that can combine with oxygen (and seldom with other anions) in several structural topologies, including, but not limited to, scheelite, zircon, monazite, fergusonite, barite, quartz, cristobalite, wolframite and rutile topologies (Fukunga & Yamaoka, 1979).

In the current project, the charge and rather large size assumed by the A-cation (i.e., REE³⁺, in this particular case) also restrict the chemical composition (and charge) of the possible T-site, which is limited to As, P, V, Cr and

Si. Thus, within the ATO_4 minerals object of the present study, *A* stands for REE, Ca, U and Th, whereas *T* stands for tetrahedrally-coordinated cations (As, P, V, as well as minor Si and Cr). Concerning the structural topologies, almost exclusive attention is dedicated to the zircon and monazite structures, shown by the four minerals object of this work: chernovite-(Y) [nominally $YAsO_4$], xenotime-(Y) [nominally YPO_4], gasparite-(Ce) [nominally $CeAsO_4$] and monazite-(Ce) [nominally $CePO_4$]. Chernovite-(Y) and xenotime-(Y) are characterized by a zircon-type structure; monazite-(Ce) and gasparite-(Ce) share the same monazite-type topology. The crystal structure of these minerals has been the object of a large number of studies and reviews (e.g., Clavier et al., 2011; Finch & Hanchar, 2003).

The zircon-type topology is characterized by a highly symmetric tetragonal *I*-centered lattice (space group $I4_1/amd$). The tetragonal zircon-type is made by the infinite chains, developed along [001]. These chain units are the result of the connection along the polyhedral edges, between the eightfold coordinated *A*-site dodecahedron (AO_8 or $REEO_8$) and the TO_4 tetrahedra (Fig. 1). The AO_8 polyhedron displays two independent *A*-O atomic distances, whereas the TO_4 is an undistorted polyhedron defined by a single *T*-O bond distance. Each chain is in contact with 4 others in the (001) plane, by means of the connecting edges along a AO_8 units and the four surroundings. Due to the high symmetry space group ($I4_1/amd$) the zircon structure shows only three independent atomic coordinates.

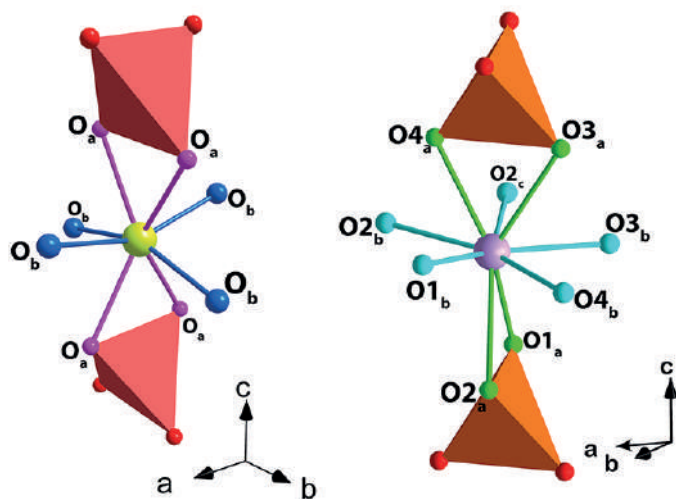


Figure 1 Crystal structure of a) zircon- and b) monazite-type minerals, showing the architecture of the chain-unit and REE-coordination polyhedron

The so-called monazite-type crystal structure crystallizes in the $P2_1/n$ space group. The monazite-type structure is characterized by the REE site in ninefold coordination. As the zircon-type, the monazite-type structure is characterized by infinite chains running along the [001] direction (*c*-axis), composed by the alternation of the REE-coordination polyhedra and the *T*-hosting tetrahedra

(Fig. 1). The REE-polyhedron coordination environment is made by nine symmetrical independent oxygen atoms ($REEO_9$) and it can be described as an equatorial pentagon (sharing vertices with five TO_4 tetrahedra of five adjacent chains in correspondence of the $O1_b$, $O2_b$, $O2_c$, $O3_b$ and $O4_b$ oxygen atoms), interpenetrated by a tetrahedron (made by the $O1_a$, $O2_a$, $O3_a$ and $O4_a$ oxygen atoms, see Fig. 2, which is in contact, along the [001] direction, with two subsequent TO_4 tetrahedra, leading to the formation of the infinite chain units. According to the notation reported in Fig. 2, the REE- $O2_a$ bond length is sharply longer than the other REE-O bonds, contributing to a significant distortion of the $REEO_9$ polyhedron (Clavier et al. 2011).

MATERIALS AND METHODS

Fourteen rock specimens, pertaining to different Alpine quartz-bearing fissures, have been selected from the personal collection of the Italian collector Enzo Sartori, all sampled from the Mt. Cervandone area between 2000 and 2020. They were first observed under a stereomicroscope, with the aim to identify their mineralogical assemblage, which was later confirmed by single-crystal X-ray diffraction and spectroscopic analysis. Fifteen REE-bearing phosphate and arsenate crystals have been selected and extracted from the fourteen rock specimens under study (see Pagliaro et al., 2022a for the details), and then characterized by means of electron probe microanalysis in wavelength dispersion mode (EPMA-WDS), single-crystal X-ray diffraction, Raman spectroscopy and non-ambient X-ray diffraction studies.

Non-ambient characterization

In situ high-pressure single-crystal synchrotron X-ray diffraction experiments have been conducted at two different synchrotron beamlines: the P02.2 extreme condition beamline at Desy Petra III facilities (Hamburg, Germany) and the ID15b beamline at the European Synchrotron Radiation Facility, ESRF (Grenoble, France). The single crystal XRD experiments under pressure interested all the four minerals under investigation and they have been performed using a diamond anvil cell (DAC), as a device to increase the pressure applied on the samples.

The high-temperature single-crystal XRD experiments have been performed at the Institute of Mineralogy and Petrology of the University of Innsbruck. The data collection has been conducted using a Stoe IPDS II diffractometer system with a Heatstream HT device, which provides a continuous hot N_2 flux and the diffraction pattern has been collected using an image plate detector.

Two combined, isothermal *HP-HT* single-crystal X-ray diffraction ramps have been collected on both chernovite-(Y) and monazite-(Ce). Resistive heated DAC has been

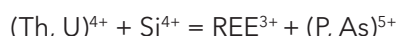
used as devices to increase both temperature and pressure.

RESULTS AND DISCUSSION

Crystal chemistry characterization

Chemical composition

Thorium is the most variable element among all the points of analysis for both zircon- and monazite-type minerals. The enrichment of Th within the $REETO_4$ compounds is controlled by two potential substitution mechanisms:



respectively known as cheralite and thorite substitution mechanisms. In Fig. 2, all the data are reported in a P/(P+As+Si) vs. Y diagram, which clearly allows to distinguish between the four minerals under investigation, arranged in four distinct quadrants. The Y-poor side of the diagram contains the chemical data from the monazite-(Ce) and gasparite-(Ce) crystals, respectively enriched in P and As. Data from chernovite-(Y) and xenotime-(Y) lie on the Y-enriched side of the diagram and are characterized by a highly variable P and As fraction, resulting in an almost complete solid solution along the join chernovite-(Y)–xenotime-(Y). On the other side, the composition of gasparite-(Ce) and monazite-(Ce) cry-

stals is closer to the ideal endmembers, and only a partial solution is observed.

The A-site of the chernovite-(Y)–xenotime-(Y) series is characterized by a relatively constant composition, where Y is always the dominant cation (ranging from a maximum of 0.78 a.p.f.u. to a minimum of 0.46 a.p.f.u.), followed, on average, by Dy, Er, Gd, Yb and Ho. When the Y content is lower than ~ 0.6 a.p.f.u., Th or LREE become relevant A-site occupying cations.

The REE pattern for all the samples under investigation is reported in Fig. 3, normalized to the REE concentration of the Carbonaceous Chondrite C1. As mentioned above, the tetragonal structure of chernovite-(Y) and xenotime-(Y) has a strong preference for Y and, in general, the smaller HREE: this pattern is reflected by the positive slope reported in Fig. 3. Conversely, in the gasparite-(Ce)–monazite-(Ce) series, the LREE enrichment is responsible for the negative slope in Fig. 3. It is worthwhile to point out that the relatively high Gd content, shown by the three monazites under investigation, has been already described in alpine-fissures minerals related to the circulation of hydrothermal fluids, as in the case of Mt. Cervandone.

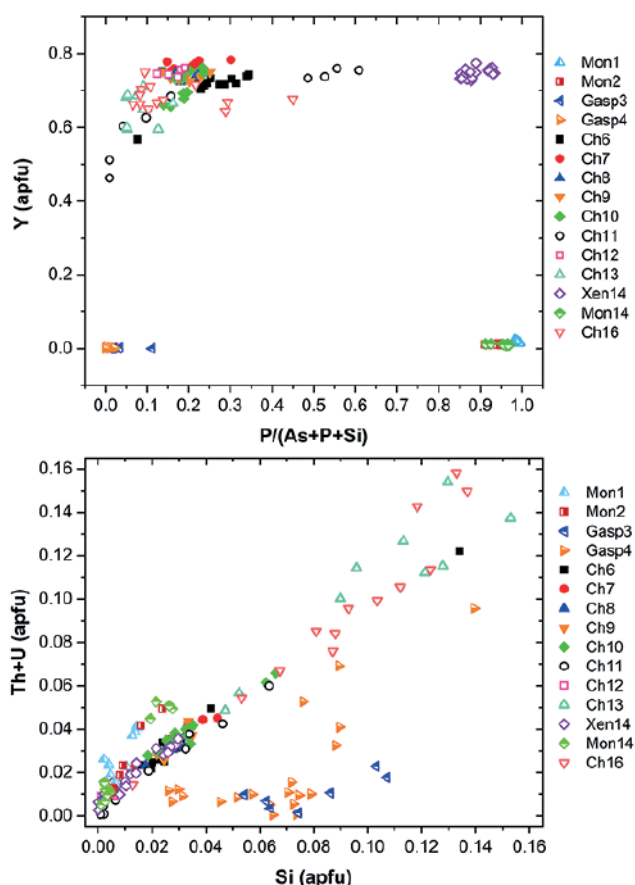


Figure 2 a) P/(P+As+Si) vs. Y diagram and b) Si vs. Th+U (in apfu) for all the samples under investigation

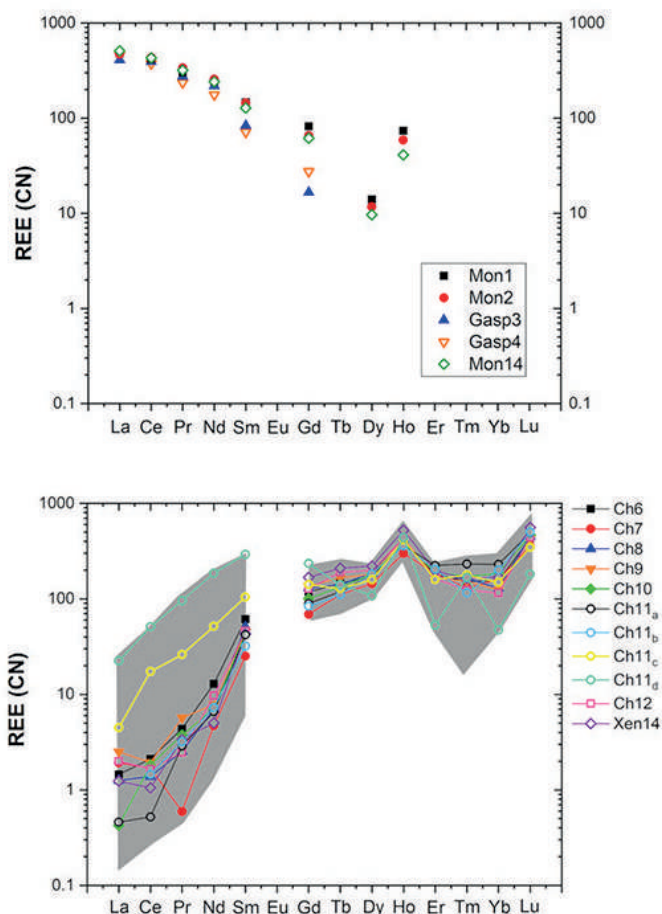
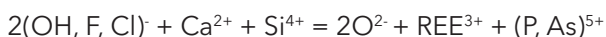


Figure 3 Average composition of REE (normalized to the CN-1 chondrite, after Wasson and Kallemeyn (1988)) of all the samples of the gasparite-(Ce)–monazite-(Ce) series a) and of the chernovite-(Y)–xenotime-(Y) series b). The grey belt in b) represents the range of the lanthanides composition for all the points of analysis of the chernovite-(Y)–xenotime-(Y) series. For sample Ch11 in b) are reported four distinct chemical compositions, due to its strong chemical zonation (see Pagliaro et al. 2022a for further details)

Although the trivalent cations are always dominant within the A-site of the tetragonal series, some data points from the samples Ch6, Ch10, Ch11, Ch13 and Ch16 show a relatively large amount of Th. The thorite substitution mechanism likely occurs in the chernovite-(Y)-xenotime-(Y) series under investigation, as suggested by the strong positive linear correlation between Si and the Th+U fraction (Fig. 2). For a better representation of the

crystal-chemistry of the mineral samples of this study, the (tetragonal) 2-component system chernovite-(Y)-xenotime-(Y) could be replaced by a 3-component solid solution between the endmembers chernovite-(Y), xenotime-(Y) and ThSiO_4 . The most Th-enriched analyses on the chernovite-(Y)-xenotime-(Y) edge belong to Ch13 and Ch16, which are also characterized by a highly altered, likely metamict texture and variable composition. In these cases, the major chemical variations concern a strong Th-enrichment, reflected by a ThSiO_4 up to 15 mol%. Moreover, these samples are also characterized by a larger fraction of CaO (up to 1.93 wt%, in Ch16, vs. an average 0.1(3) wt% for the other chernovite-(Y) samples), suggesting the occurrence of the cheralite substitution mechanism as well.

All the gasparite-(Ce) and monazite-(Ce) samples show a rather similar composition of the ninefold-coordinated A-site and the main differences concern in particular the abundance of Y and Ca. A relatively high amount of Y (Y_2O_3 on average, 0.7(2) wt%) is shown by the three monazite-(Ce) samples investigated, whereas this element is almost absent in the two gasparite-(Ce) samples ($\text{Y}_2\text{O}_3 < 0.13$ wt%). Unlike monazite-(Ce), gasparite-(Ce) shows a higher content and more uniform distribution of Ca (CaO 1.8(2) wt%, vs 1.1(4) wt% for monazite-(Ce)). Also, in the gasparite-(Ce)-monazite-(Ce) series, Th has been found as the most variable element and, in addition, gasparite-(Ce) incorporates the highest fraction of Si among the investigated REE minerals. In this case, a further charge-compensating mechanism should be involved, to fully explain the anomalous amount of Ca and Si, not compensated by Th+U. The presence of monovalent anions, such as OH^- , F^- or Cl^- , in place of O^{2-} , may compensate for the presence of Si and Ca, according to the following equation:



According to this equation, if just OH^- is taken into account, the corresponding amount of H_2O necessary to compensate the charge defect is, on average, ~ 0.45 wt% for both Gasp3 and Gasp4. The occurrence of some hydroxyl is corroborated by the Raman spectra, showing some peaks in the so-called hydroxyl region (Pagliaro *et al.* 2022b).

Instead, for all the samples of monazite-(Ce), the combination of cheralite and thorite substitution fully satisfies the pattern shown in Fig. 2.

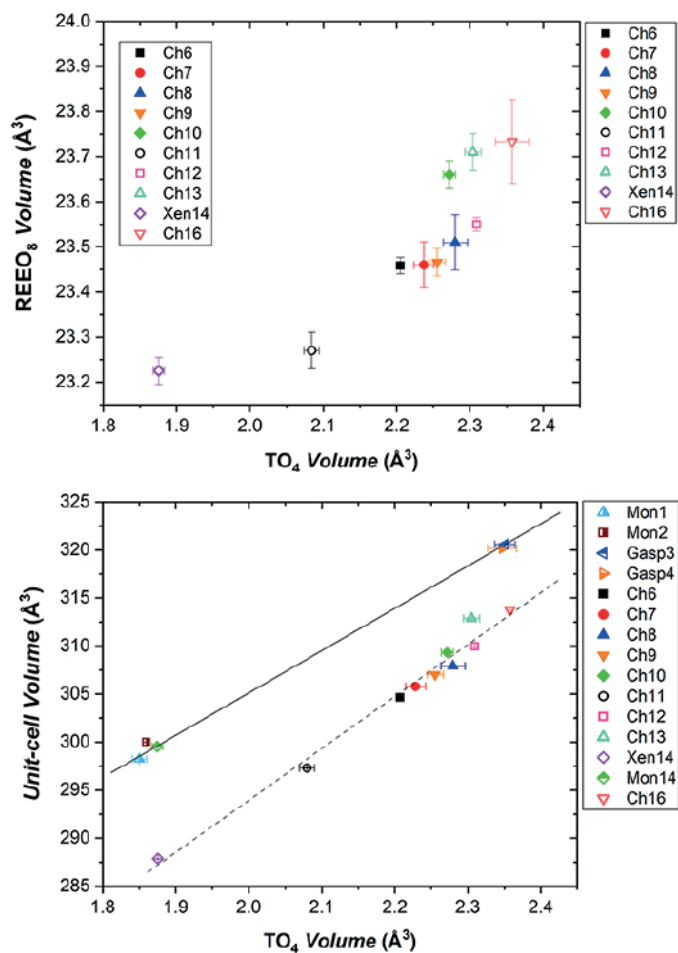


Figure 4 a) Volume of the TO_4 tetrahedron vs. volume of the (REE)-bearing A-polyhedron for the samples pertaining to the chernovite-(Y)-xenotime-(Y) series. b) Volume of the TO_4 tetrahedron vs. unit-cell volume for all the samples investigated

Crystal structural characterization

The atomic structural models refined for all the samples under study are reported in Fig. 4. It has been demonstrated that the chemical composition of the T-site exerts strong control over all the other structural features in zircon-type minerals. Indeed, a correlation between the P (and As) content and the unit-cell volume has been clearly determined. In addition, a correlation among the volumes of (P, As)-tetrahedra (directly related to the chemical composition of the T-site) and the A-site polyhedra is also shown by the synthetic REETO_4 compounds, which structural models are reported in the International Crystal Structure Database. A comparative analysis of the structural parameters of synthetic REE-bearing phosphates has been carried out. Given the same elemental composition of the REE-bearing A-site, the volume of its coordination polyhedron is different in phosphates and arsenates, being always lower in phosphates, pointing out the dominant role played by the TO_4 structural units ($V_{\text{TO}_4} \sim 2.4 \text{ \AA}^3$ for AsO_4 and $\sim 1.8 \text{ \AA}^3$ for PO_4) in controlling most of the structural parameters of the REETO_4 compounds. Therefore, the REE-bearing A-site of the zircon-type structure behaves somehow passively, while the T-site exerts a strong active control over the crystal structure interatomic interactions.

Similar behaviour to that described above for the (tetragonal) chernovite-(Y)-xenotime-(Y) series is also shown by the (monoclinic) gasparite-(Ce) and monazite-(Ce). However, in this case, the distribution of the chemical compositions in two clusters close to the ideal end members prevents a robust extrapolation along the whole series (Fig. 4).

High-pressure behaviour

From the *in situ* XRD data the unit cell volumes through pressure have been determined and the bulk moduli calculated for the four minerals under investigation (see Table 1). The bulk moduli have been modelled by Birch Murnaghan equations of state.

Table 1 Refined bulk moduli, compressibilities, first derivative bulk modulus ($K'=4$ fixed for the BM2-EoS) and unit-cell volumes for all the ATO_4 minerals.

Sample	K_{P_0,T_0} (GPa)	β_V (GPa ⁻¹)	K'	V_0 (Å ³)
Ch10	136(2)	0.0074(1)	3.9(4)	309.96(3)
Xen14	148(4)	0.0068(2)	3.9(5)	289.5(2)
Gasp3	108.3(1.0)	0.00923(8)	4.2(2)	320.59(3)
Mon14	121(3)	0.0083(2)	-	299.3(4)

Zircon-type minerals under compression

Both chernovite-(Y) and xenotime-(Y) undergo a phase transition. In detail, chernovite-(Y) undergoes an irreversible phase transition at about 11 GPa, to a scheelite-type structure, while xenotime-(Y) undergoes a reversible zircon-to-monazite phase transition at about 17 GPa. In the case of the xenotime-(Y), for the high-pressure polymorph (hereafter xenotime-II) it was possible to refine the unit cell volume and crystal structure model through pressure. Conversely, to previous studies, the bulk modulus of xenotime-II refined in the present study is significantly lower and substantially of the same order of magnitude of that of the ambient-pressure xenotime-(Y). Such a result is in disagreement with the literature data available on the high-pressure polymorph of YPO_4 , which was reported to be significantly more compressible compared to its ambient-conditions polymorph (Lacomba-Perales et al. 2010; Zhang et al. 2009). On the other hand, it is worth mentioning that the current project relies on a larger amount of experimental data and, therefore, the modelled bulk modulus obtained in this study is believed to be more accurate.

As shown in Table 1, chernovite-(Y) is more compressible compared to xenotime-(Y), without any significant difference in the A-site composition (since the investigated samples are the Ch10 and Xen14, see Fig. 3). In addition, as already discussed above, the chemical composition of the T-site exerts a strong control on the structural features of ATO_4 minerals, especially on the A-site polyhedral volume and bond distances, whereas the crystal chemistry of the the A-site apparently has a milder role.

Whether the T-site is mostly occupied by As or P affects the size of the A-site polyhedron: larger when the larger As prevails in the T-site, smaller when the smaller P is the prevailing tetrahedral cation. Consequently, the Y-O bond distances in chernovite-(Y) are longer, compared to the same structural parameters in xenotime-(Y). The experimental data of this study suggest that the larger A-site of arsenates is more compressible with respect to the smaller REE-hosting polyhedron of phosphates, at a similar chemical composition in terms of Y and HREE. Therefore, the observed different compressibility among chernovite-(Y) and xenotime-(Y) can be mainly ascribed to the different chemical composition of the T-site cations and its influence on the overall crystal structure.

The A-site coordination environment absorbs most of the compression, while the T-site behaves as a rather rigid unit ($K_{TO_4} > 300$ GPa). The AsO_4 tetrahedron, indeed, is more compressible than the PO_4 one and this concurs with the higher compressibility of arsenates with respect to phosphates.

Monazite-type minerals under compression

First of all, the compressional behaviour of the investigated minerals suggests that, in general, the studied monazite-type compounds are more compressible compared to the zircon-type ones. On the other side, as pointed out by Li et al. (2009), this conclusion may be biased by the role played by the ionic radius of the A-site. If, on one side, the bulk modulus decreases across the Ln series from the smaller Lu to the larger La for any group of compounds (*i.e.*, phosphates or arsenates), a discontinuity associated with a stiffening (*i.e.*, an increase in the bulk modulus value) occurs when the structure topology changes from the zircon- to monazite-type. Therefore, the lower bulk moduli shown by gasparite-(Ce) and monazite-(Ce), when compared to chernovite-(Y) and xenotime-(Y) respectively, can be mainly ascribed to the significant difference in the ionic radius of their A-sites, rather than to the structure topology.

Most of the conclusions already discussed for the zircon-type topology can be extended to the monazite-type. Indeed, the dominant role played by the chemical composition of the T-site over all the other structural features can explain the different compressibilities shown by monazite-(Ce) and gasparite-(Ce). Moreover, due to the low symmetry of the structure, monazite-type compounds show a strong angular deformation, which significantly concurs to the overall compression of the crystal structure. The details are discussed in Pagliaro et al. (2022b).

In addition, for both monazite-(Ce) and gasparite-(Ce) a significant change in compressional behaviour has been observed at about 18 GPa and 15 GPa, respectively. Such a behaviour has been described previously by Huang et al. (2010) and Errandonea et al. (2018), although it was considered biased by non-hydrostatic condi-

tion of the *P*-transmitting fluid during the high-pressure experiments. In the current work, a detailed structural analysis enlightened a correlation between such a change in compressional behaviour and the shortening of a "tenth" REE-O interatomic distance out from the "classical" ninefold coordinational sphere of the REE atom at ambient conditions. Therefore, such a change in compressional behaviour is likely to be influenced by a rearrangement of the crystal structure due to the increase in the coordination number of the REE_x polyhedron from nine to ten. For monazite-type compounds, such a behaviour has never been described in literature before and it could represent a link between the monazite-type structure, characterized by a ninefold coordination of the A atom and the post-barite-type (*P*2₁2₁2₁ space group, Ruiz-Fuertes et al. 2016), one of the high-pressure polymorph of monazite, which is characterized by an elevenfold A-site.

High-temperature behaviour

The thermal behaviour of chernovite-(Y), xenotime-(Y) and monazite-(Ce) has been modelled using a Holland-Powell equation of a state, a polynomial and a linear fits. For gasparite-(Ce), due to the small size of the crystals available, no high-temperature experiment has been carried out. The corresponding results are reported in Table 2.

Table 1 Refined bulk moduli, compressibilities, first derivative bulk modulus ($K'=4$ fixed for the BM2-EoS) and unit-cell volumes for all the ATO_4 minerals.

sample	$\alpha_V (\times 10^{-6} K^{-1})$	$V_0 (\text{\AA}^3)$	LTEC ($\times 10^{-6} K^{-1}$)	$V_0 (\text{\AA}^3)$
Ch10	9.7(1)	307.02(3)	4.81	306.74
Xen14	9.6(1.2)	288.07(4)	6.00	287.73
Mon14	19.9(1.3)	297.97(5)	9.73	297.50

In the first place, in all the cases, similar behaviour of the A-site polyhedron and of the *T*-site tetrahedron can be observed: in all three minerals, the thermal expansion of the REE-polyhedron is larger compared to the bulk unit-cell, while the *T*-site tetrahedron is largely less expandable. Secondly, the behaviour under heating of the monazite- and zircon-type structures is significantly different. Monazite-(Ce) is significantly more expansible compared to the zircon-type minerals studied in the present study.

It is also reasonable to state that the phosphates are more expansible than the zircon-type arsenates studied in the present work. On the other hand, the lack of the HT ramp on gasparite-(Ce) does not allow a complete comparison among the zircon- and monazite-type phosphates and arsenates, although Li et al. (2009) corroborate that monazite-type REEAsO₄ are less expansible compared to REEPO₄. Following the discussion carried out in the previous section, the expansive behaviour of

arsenates and phosphates may be correlated *indirectly* with the role played by the TO₄ units.

The structure is affected by a chemical deformation, driven by the composition of the *T*-site atom: indeed, in the ATO₄ arsenates, the volume of the REE coordination polyhedron is larger compared to that of the isostructural phosphates. As reported by Zhang et al. (2008) and Li et al. (2009), the calculated bond distances thermal expansion of ATO₄ compounds is larger with decreasing bond length. In this light, the different behaviour of phosphates and arsenates is bound to the different A-O bond lengths, in turn, controlled by the chemical composition of the *T*-site, following the model previously described.

Combined high-temperature and high-pressure behaviour

Eventually, for chernovite-(Y) and monazite-(Ce), the *P-V-T* equation of state has been fitted to the HP (at ambient-*T*), HT (at ambient-*P*) and combined HT-HP data, by using a 2nd order Birch-Murnaghan EoS and a modified Holland-Powell EoS and refining a constant $(dK/dT)_P$. The corresponding refined room-*T* α_V and *K* are rather close to the thermos-elastic parameters based on individual HP- and HT-ramps of monazite-(Ce) and chernovite-(Y).

REFERENCES

- Blengini, G.A., Mathieux, F., Mancini, L., Nyberg, M., & Viegas, H.M. (2020): Study on the EU's list of Critical Raw Materials. Executive Summary. Publication Office of the European Commission, Luxembourg.
- Clavier, N., Podor, R., & Dacheux, N. (2011): Crystal chemistry of the monazite structure. *J. Eur. Ceram. Soc.*, **31**, 941-976.
- Errandonea, D., Gomis, O., Rodríguez-Hernández, P., Muñoz, A., Ruiz-Fuertes, J., Gupta, M., Achary, S. N., Hirsch, A., Manjon, F.J., Peters, L., Roth, G., Tyagi, A.K., & Bettinelli, M. (2018): High-pressure structural and vibrational properties of monazite-type BiPO₄, LaPO₄, CePO₄, and PrPO₄. *J. Condens. Matter Phys.*, **30**, 065401.
- Finch, R.J., & Hanchar, J.M. (2003): Structure and chemistry of zircon and zircon-group minerals. *Rev. Mineral. Geochem.*, **53**, 1-25.
- Graeser, S., & Roggiani, A.G. (1976): Occurrence and genesis of rare arsenate and phosphate minerals around Pizzo Cervandone, Italy/Switzerland. *Rendiconti della Società Italiana di Mineralogia e Petrologia*, **32**, 279-288.
- Guastoni, A., Nestola, F., Gentile, P., Zorzi, F., Alvaro, M., Lanza, A., Peruzzo, L., Schiazza, M., & Casati, N. M. (2013): Deveroite-(Ce): a new REE-oxalate from Mount Cervandone, Devero Valley, Western-Central Alps, Italy. *Mineral. Mag.*, **77**, 3019-3026.

- Guastoni, A., Pezzotta, F., & Vignola, P. (2006): Characterization and genetic inferences of arsenates, sulfates and vanadates of Fe, Cu, Pb, Zn from Mt. Cervandone (Western Alps, Italy). *Period. Mineral.*, **75**, 141-150.
- Huang, T., Lee, J.S., Kung, J., & Lin, C.M. (2010): Study of monazite under high pressure. *Solid State Commun.*, **150**, 1845-1850.
- Lacomba-Perales, R., Errandonea, D., Meng, Y., & Bettinelli, M. (2010): High-pressure stability and compressibility of APo_4 (A= La, Nd, Eu, Gd, Er, and Y) orthophosphates: An x-ray diffraction study using synchrotron radiation. *Phys. Rev. B*, **81**, 064113.
- Li, H., Zhang, S., Zhou, S., & Cao, X. (2009): Bonding characteristics, thermal expansibility, and compressibility of RXO_4 (R= Rare Earths, X= P, As) within monazite and zircon structures. *Inorg. Chem.*, **48**, 4542-4548.
- Pagliaro, F., Lotti, P., Guastoni, A., Rotiroti, N., Battiston, T., & Gatta, G.D. (2022a): Crystal chemistry and miscibility of chernovite-(Y), xenotime-(Y), gasparite-(Ce) and monazite-(Ce) from Mt. Cervandone (Western Alps, Italy). *Mineral. Mag.*, **86**, 1-18.
- Pagliaro, F., Lotti, P., Comboni, D., Battiston, T., Guastoni, A., Fumagalli, P., Rotiroti, N., & Gatta, G.D. (2022b): High-pressure behavior of gasparite-(Ce) (nominally $CeAsO_4$), a monazite-type arsenate. *Phys. Chem. Miner.*, **49**, 1-11.
- Ruiz-Fuertes, J., Hirsch, A., Friedrich, A., Winkler, B., Bayarjargal, L., Morgenroth, W., Peters, L., Roth, G., & Milman, V. (2016) High-pressure phase of $LaPO_4$ studied by x-ray diffraction and second harmonic generation. *Phys. Rev. B*, **94**, 134109.
- Wasson, J.T., & Kallemeyn, G.W. (1988): Compositions of chondrites. Philosophical Transactions of the Royal Society of London. Series A, *Math. Phys. Sci.*, **325**, 535-544.
- Zhang, F.X., Wang, J.W., Lang, M., Zhang, J.M., Ewing, R.C., & Boatner, L.A. (2009): High-pressure phase transitions of $ScPO_4$ and YPO_4 . *Phys. Rev. B*, **80**, 18411.

Unveiling the thermo-structural setting of collisional orogens

Example from the Variscan chain in Sardinia

Alessandro Petroccia

Dipartimento di Scienze della Terra, Università di Torino, Via Valperga Caluso 35, 10125, Torino, Italia

DOI:10.19276/plinius.2023.01.010

INTRODUCTION

The geodynamic evolution of collisional orogens has been classically described using an orogenic wedge model, in which different rock packages experience different finite tectono-metamorphic histories (e.g., Jaquet et al., 2018). The hinterland-foreland transition zone is characterized by the progressive transition from tectonic units occurring in the metamorphic core of the belt to the ones deformed at shallower crustal levels and steadily included in the orogenic wedge (Thigpen et al., 2010, 2017).

Different features control the thermo-structural architecture and variation across orogenic wedges, such as the efficiency of erosion, the temperature/deformation ratio within nappes and the presence of ductile tectonic contacts (Jamieson et al., 2002).

Despite the relevance of this topic and the widespread distribution within orogenic wedges, relatively few methods are available for low-grade metapelites (Frey, 1987; Frey & Robinson, 1999). Thus, the unravelling of the thermo-structural architecture of this sector of the belt is hampered by the presence of strongly deformed large-scale nappes made by apparently homogeneous low-grade metasedimentary rocks lacking index minerals useful for pressure and temperature (*P-T*) estimations. In addition, the presence of strong overprinting belonging to the post-nappe stacking deformation that modifies the original attitude of pre- and syn-nappe stacking elements complicates the untangling of this area.

The Variscan belt in Sardinia represents a continental crustal section, exposing a quite continuous metamorphic field gradient from greenschist- to granulite-facies rocks (Carmignani et al., 1994; Cruciani et al., 2015 for a review). This work aimed to reconstruct the thermo-structural architecture of the low-grade Internal and External Nappe Zone exposed in the hinterland-foreland transition zone in Sardinia and of the ductile boundary in between (i.e., the Barbagia Thrust). In order to explore these topics, an approach with a broad perspective was chosen, combining fieldwork with different scales

of structural analysis, and quantitative temperature constraints by RSCM, coupled with kinematics of the flow and finite strain estimations.

GEOLOGICAL SETTING

The Sardinian Variscan belt comprises: (i) the External Zone, (ii) the Axial Zone, and (iii) the Nappe Zone (Fig. 1a; Carmignani et al., 1994). The latter has been divided into External (central to southern Sardinia) and Internal (northern to central Sardinia) Nappe Zone. The boundary between them is marked by a regional-scale, top-to-the S-SW thrust-sense ductile to brittle shear zone, the Barbagia Thrust (BT; Fig. 1a,b,c; Carosi & Malfatti, 1995; Montomoli et al., 2018; Petroccia et al., 2022a,b). The Internal Nappe Zone (Fig. 1a) includes the Low-Grade Metamorphic Complex (LGMC), which reached low- to upper-greenschist-facies metamorphic conditions, and the Medium-Grade Metamorphic Complex (MGMC), which reached amphibolite-facies conditions (Franceschelli et al., 1989; Carosi et al., 2020, 2022; see Cruciani et al., 2015 for a review). In the External Nappe Zone, all units are characterized by syn-tectonic regional greenschist-facies metamorphism (Carosi et al., 1991, 2004, 2010; Franceschelli et al., 1992; Petroccia et al., 2022a,b,c), except for the deepest Monte Grighini Unit, which reached amphibolite-facies conditions (Musumeci, 1992; Cruciani et al., 2016). The investigated area comprehends both the Barbagia Unit (BU) and the Meana Sardo Unit (MSU), belonging to the Internal and External nappes, and the northernmost sector of the Low-Grade Metamorphic Complex, belonging to the Internal Nappe Zone, close to Lula and Bitti towns (Fig. 1b,c).

METHODOLOGY

Vorticity and finite strain analysis

The non-coaxiality of the flow in shear zones is defined by the W_k number (Xypolias, 2010), which several vorticity analysis techniques can estimate. Pure and simple shear components may be described through the di-

In the present work, the C' shear band method (Kurz & Northrup, 2008; Gillam et al., 2013) and two different porphyroclasts-based methods, the porphyroclast aspect ratio method (PAR; Passchier, 1987; Wallis et al., 1993) and the rigid grain net method (RGN; Jessup et al., 2007), have been applied to evaluate the percentage of pure and simple shear of the BT. The nominal error for vorticity analysis is ± 0.1 (Tikoff & Fossen, 1995). A comparison of different possible systematic error sources indicates that for medium to low vorticity numbers ($W_m < 0.8$), the vorticity data minimum systematic error is ± 0.2 (Iacopini et al., 2011).

Finite strain analyses were performed using the centre-to-centre method (Fry, 1979) by the EllipseFit 3.8.0 software (Vollmer, 2015). Samples were cut and polished perpendicular to the foliation and both parallel and perpendicular to the mineral lineation (XZ and YZ sections of finite strain ellipsoid). This method is based on the redistribution of the centres of the strain markers caused by deformation and is independent from their shape. Data have been plotted on the Flinn diagram.

Raman Spectroscopy on Carbonaceous Material (RSCM) geothermometer

The peak temperature was derived using Raman Spectroscopy on Carbonaceous Material (RSCM) geothermometer. This method is based on the progressive transformation of Carbonaceous Material (CM) during the temperature increase, and it is not affected by the retrograde history (i.e., the T_{max} ; Beyssac et al., 2002). The Raman spectrum of perfect graphite is made by a single G band and other two bands D1 and D2. The intensity of the D1 band is used to evaluate the degree of disorder in the CM. Beyssac et al. (2002) established a correlation between the temperature and Raman parameters of the CM called R2. The RSCM geothermometer has an absolute precision of $\pm 50^\circ\text{C}$ due to uncertainties of the petrological data used for the calibration. The relative uncertainties on temperature are $\pm 10\text{-}15^\circ\text{C}$ if the guidelines and recommendations of Beyssac et al. (2002, 2004) and Lündorf et al. (2014, 2017) are followed. Raman microspectroscopy has been performed with the Horiba Jobin Yvon LabRam HRVIS Raman System at the Centro "G. Scansetti", Dipartimento di Scienze della Terra, Università degli Studi di Torino. Before each measurement session, the spectrometer was calibrated using the 520.5 cm^{-1} peak (r band) of a silicon standard. Spectra were acquired by a beam spot of approximately one μm diameter with a green Nd 532.06 nm laser source at 80 mW, corresponding to 2-4 mW at the sample surface, with a 100x magnification. For each sample, a minimum of 10 spectra was recorded, except for samples containing very little CM amount. The peak position, band area, and bandwidth (FWHM) were determined using the computer program PeakFit 4.0, fol-

lowing the fitting procedure described by Beyssac et al. (2002). The fitting itself followed the Voigt area, and the algorithm combined Gaussian and Lorentzian profiles. Because obtained spectra were acquired using a green Nd 532.06 nm laser, the RSCM temperature estimates discussed in the following sections were derived from the Aoya et al. (2010) calibration, which was established based on the same laser wavelength.

STRUCTURAL AND RSCM RESULTS

Internal and External nappes

Detailed mapping, coupled with multi-scale structural observations, allowed the definition of a polyphase evolution (see Petroccia et al., 2022a,b for further explanation and the mapped area), consisting of three ductile deformation phases developed under a contractional tectonic regime (D_1 - D_2 - D_3) and the fourth one under extensional conditions (D_4). The prominent deformation phase (D_2) is responsible for the development of the main foliation (S_2). It becomes more mylonitic moving toward the BT and displays several kinematic indicators with a main top-to-the S-SW sense of shear. The S_2 foliation is marked by greenschist-facies mineral assemblage. D_1 and D_2 structural elements are widely deformed by weakly asymmetric to upright F_3 folds. Folds with sub-horizontal axial planes (F_4), developed during the orogenic extensional phase (D_4), are recognizable.

In the northernmost investigated sector of the Internal Nappe Zone (Fig. 2), the derived T_{max} within the Lula and Bitti villages agree with those obtained with thermodynamic modelling estimations ($\sim 450\text{-}470^\circ\text{C}$) on nearby samples by Costamagna et al. (2012), highlighting the reliability of the obtained RSCM results. The presence of garnet, plagioclase, biotite and white mica in the northernmost rocks is in agreement with the obtained T_{max} of $\sim 500\text{-}520^\circ\text{C}$ and P - T data from Franceschelli et al. (1989).

The central Nappe Zone, where the BU juxtaposed onto the MSU crops out, is characterized by a more complex thermal architecture driven by regional scale antiform and synform (see Fig. 1a and Fig. 2). The BU displays a general T_{max} of $\sim 470\text{-}440^\circ\text{C}$ whereas the MSU has T_{max} of $\sim 440\text{-}380^\circ\text{C}$ (Fig. 2). Previous investigations do not document a thermal difference between the BU and MSU (Franceschelli et al., 1992; Carosi et al., 2010; Montomoli et al., 2018). However, the T_{max} coverage highlights a systematic difference of $\sim 10\text{-}20^\circ\text{C}$ between them within the Gennargentu Antiform and $\sim 30\text{-}70^\circ\text{C}$ in the southernmost sector (Fig. 1b, c and Fig. 2). The T_{max} shifting between the MSU and the BU is higher in the southernmost sector ($\sim 30\text{-}70^\circ\text{C}$) than within the Gennargentu Antiform ($\sim 10\text{-}20^\circ\text{C}$). The post-nappe stacking folded structure is also highlighted by the presence of the BT with the same structural and kinematic features and high T_{max} in the two limbs of the Barbagia Synform

(see Petroccia et al., 2022a).

Barbagia Thrust

Detailed meso- and microstructural analyses have been performed in two different sectors of the BT in the Sardinian Variscan belt (Fig. 1b). This region has undergone a polyphase evolution consisting of four ductile deformation phases (see the previous chapter and Petroccia et al., 2022a,b). The main structures of the study area are caused by the D_2 deformation phase. This phase is linked to the syn-nappe stacking and exhumation of the BU (Carosi et al., 2004; Montomoli et al., 2018). An increase in shear deformation along with the progressive transposition of previous D_1 structures approaching the BT has been highlighted, as shown in Fig. 3a,b. The S_2 foliation, parallel to the boundaries of the shear zone, and the F_2 fold axes, perpendicular to the L_2 object lineation, are coeval with the overthrust of the Internal Nappe Zone onto the External Nappe Zone (Carosi et al., 2004). The syn-kinematic mineral assemblage (chlorite + white mica) along the S_2 mylonitic foliation is indicative of greenschist-facies metamorphic conditions. This is, in agreement with the main dynamic recrystallization mechanism of quartz, indicative of temperature between 400 and 450°C (BLG II and local SGR; Stipp et al., 2002). Kinematic indicators, both at the meso- and microscale, reveal a top-to-the-S-SW sense of shear. This also agrees with the S-SW F_2 fold vergence detailed by previous authors (Carosi, 2004; Carosi et al., 2004; Montomoli et al., 2018). The whole architecture of the Nappe Zone is affected by regional-scale F_3 folds (D_3). The D_3 phase is characterized by pressure solution, indicating an upper structural level deformation. Also, the presence of the BT mylonitic zone in the different sectors of the Barbagia Synform, with the same structural and kinematic features, indicates that F_3 folding deformed this tectonic contact. Similar structural results and the same shear sense were obtained from both zones, confirming the post-nappe stacked folded structure (i.e., Barbagia Synform; Fig. 1b,c). Subsequent post-collision extensional tectonics was characterized by the development of open folds (F_4).

Montomoli et al. (2018) performed both illite and chlorite crystallinity measurements on samples transecting the BT but found no systematic changes in those parameters across the structural profile. T_{max} across the BT on both strongly and weakly deformed samples have been measured from two different structural sectors of the same shear zone (Fig. 1b). An increase in temperature moving from the structurally higher parts of the BU, or from the structurally lower parts of the MSU, toward the BT core has been highlighted. The detected T_{max} shift between non-mylonitic and mylonitic rocks is in the range of ~50-70°C (Fig. 3c). T_{max} for non-mylonitic rocks range from ~420 to ~450°C, in agreement with the documented metamorphic mineral assemblage and recrystallization

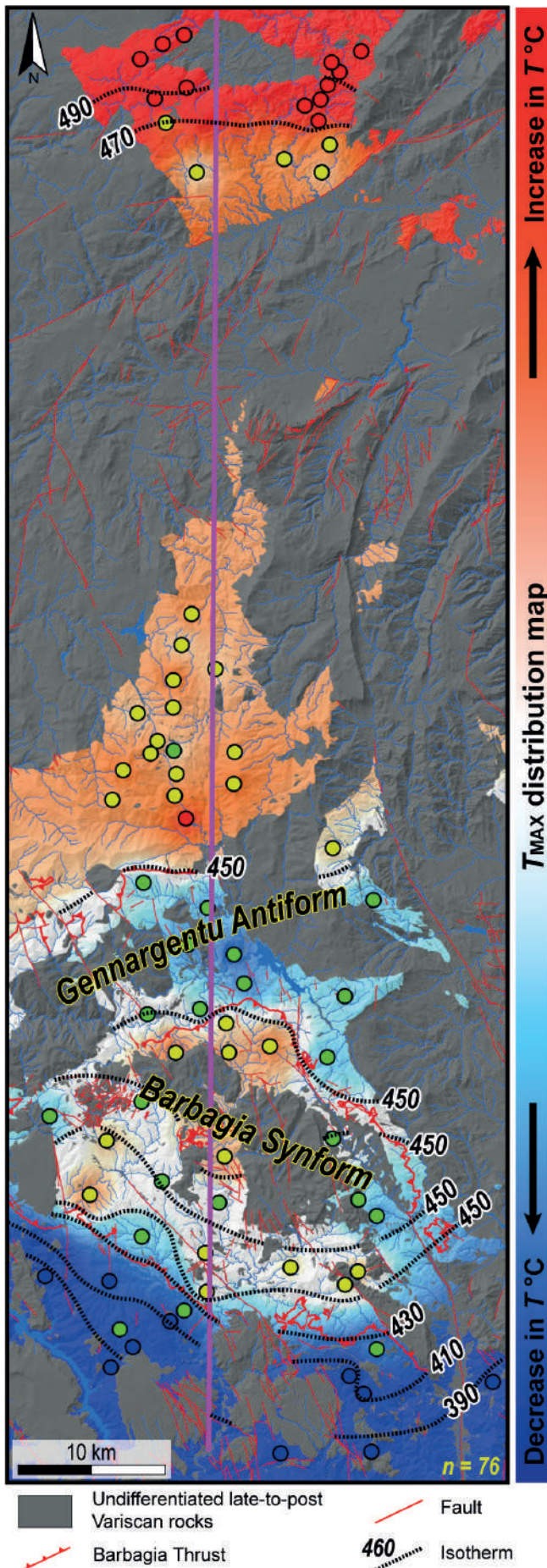


Figure 2 T_{max} contour map and isotherms of the investigated area from Petroccia et al., 2022c. See Figure 1c for the symbology of RSCM data. The trace of the simplified tectonic cross-section shown in Figure 5a has been displayed in purple.

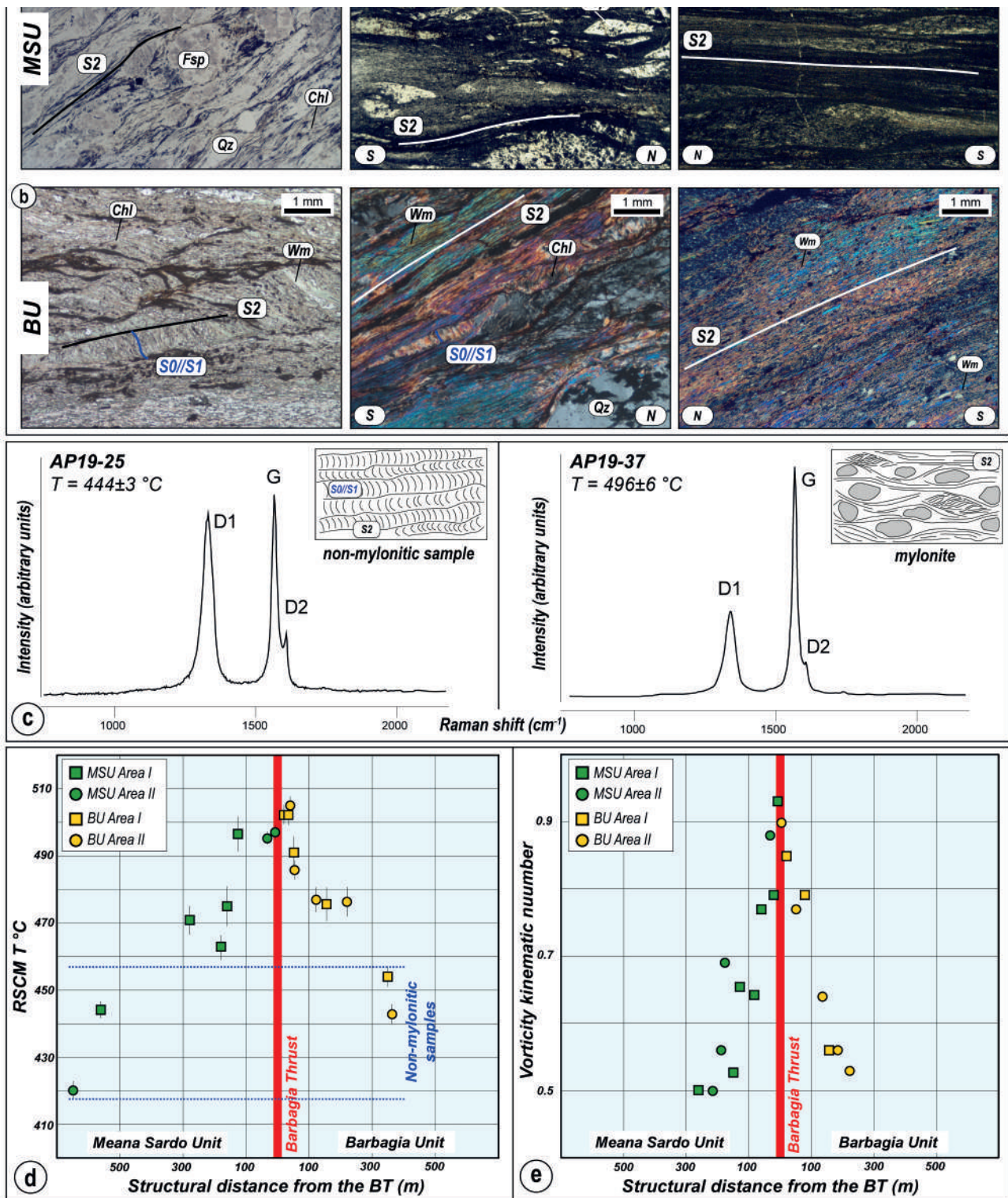


Figure 3 a, b) Structural variation going toward the Barbagia Thrust in both units: a) variation from mylonites (on the left) to ultramylonites (on the right) in metavolcanic rocks belonging to the MSU; b) progressive variation of the foliation from spaced cleavage to a continuous cleavage moving toward the BT in metasedimentary rocks; c) Representative Raman spectra for CM from MSU samples AP19-25 and AP19-37, respectively outside and inside the mylonitic zone. Note that the T_{max} is higher in the mylonite; d) Distribution of T_{max} compared with the sample structural distance with respect to the BT; e) Distribution of estimated vorticity kinematic number against the structural distance from the BT

stallization mechanism of quartz. In comparison, mylonites return higher T_{max} , ranging from ~ 470 to $\sim 500 \text{ } ^\circ\text{C}$ (Fig. 3c, d).

Several factors could cause this rise in temperature towards the core of shear zones: (i) graphite precipitation from a hydrothermal fluid; (ii) detrital graphite; (iii) strain reorganization of graphite; and (iv) shear heating. The T_{max} reported here shows a persistent and systematic increase in T_{max} with increasing strain intensity pro-

gressively moving into the BT high strain shear zone. All characteristics point to shear heating phenomena (see Petrocchia et al., 2022a for a complete discussion).

The kinematic vorticity data obtained through the C' shear bands method (Kurz & Northrup, 2008), PAR, and the RGN method (Jessup et al., 2007) have allowed quantification of the flow regime as a non-coaxial flow. The obtained data highlight that the simple shear component increases progressively towards the centre of the

BT, from both MSU and BU rocks (Fig. 3e). A variation of simple shear from ~33% up to ~77% has been recognized. Mylonites and less deformed rocks record a flow regime dominated by pure shear, whereas ultramylonites in the center of the shear zone record an increasing amount of simple shear (Fig. 3e). This is associated with a change in the finite strain ellipsoid from close to the plane strain up to prolate conditions. A higher R_{xz} value is inferred from ultramylonitic samples only within the core of the shear zone. This implies that the core of the BT accommodated a higher amount of strain compared to the shear zone peripheries (Fossen & Cavalcante, 2017). Higher W_k values within the centre of the BT, and a prolate strain ellipsoid are associated with higher T_{max} , whereas lower W_k values, far from the BT core, and plane strain conditions are associated with samples showing lower T_{max} (Fig. 3d, e).

The progressive increase in temperature towards the BT, coupled with the increase of simple shear, could indicate a syn-shearing temperature imprint (Petroccia et al., 2022a). This broad correlation between T_{max} and the deformation gradient could imply that the flow path was combined with by a progressive localization of deformation in the core of the shear zone, due to thermal weakening, during the ductile deformation.

DISCUSSION AND CONCLUSION

A polyphase deformation history regarded as the result of pre-, syn- to post-nappe stacking evolution developed under contractional (D_1 to D_3) and extensional conditions (D_4), has been recognized. Also, RSCM data provide quantitative T_{max} constraints at the belt scale with a relative uncertainty of less than 10-15°C. This highlights a complex thermal orogenic wedge architecture previously unrecognized (Petroccia et al., 2022a,c). Deforming the primary bedding S_0 , far from the main tectonic contacts, the D_1 event is well-recognizable, both at micro- and mesoscale, in the hinge of the D_2 folds and in S_2 microlithons (Fig. 4). This event has been associated with the burial and the pre-nappe stacking during the early collisional stage and the orogenic wedge growth (Carmignani et al., 1994; Carosi et al., 2004; Conti et al., 1999, 2001; Montomoli et al., 2018). The D_2 deformation phase at the belt scale is linked to the syn-collisional exhumation associated with the Barbagia Thrust (BT) shear activity (Montomoli et al., 2018 and references therein). The D_2 is associated with both folding and shearing with a top-to-S-SW vergence and sense of shear, respectively (Fig. 4). The presence of the BT mylonitic zone in the different sectors of the Barbagia Synform, with the same structural and kinematic features and the same T_{max} distribution, emphasizes the presence of regional-scale antiforms and synforms, driving the present-day thermo-structural architecture of the belt (Fig. 5a,b). All these results are in agreement with the model

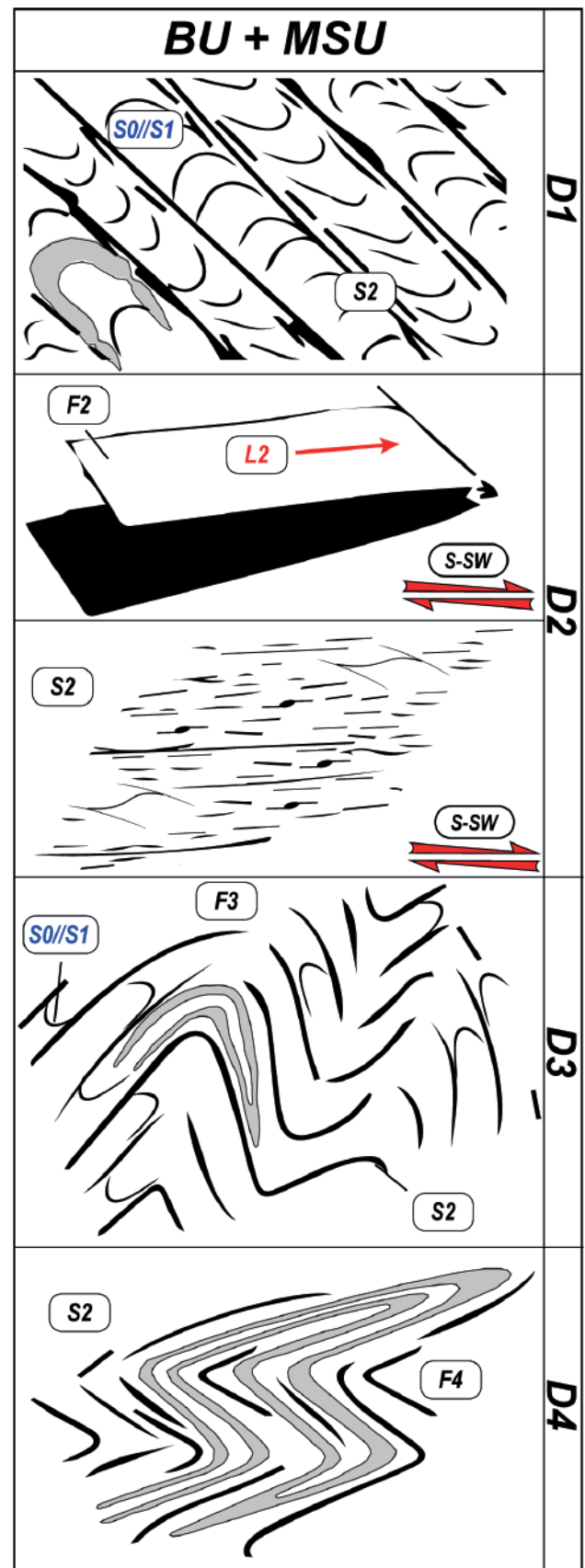


Figure 4 Synoptic reconstruction of the field and microstructural investigations of the deformation history of the BU and MSU.

of Carmignani et al. (1994) and Conti et al. (1999), which highlighted the presence of large-scale structures acquired in a contractional setting during the late deformation stage of crustal thickening and not during the late orogenic extension. Subsequent post-collision and post-nappe-stacking or transpression were characterized by

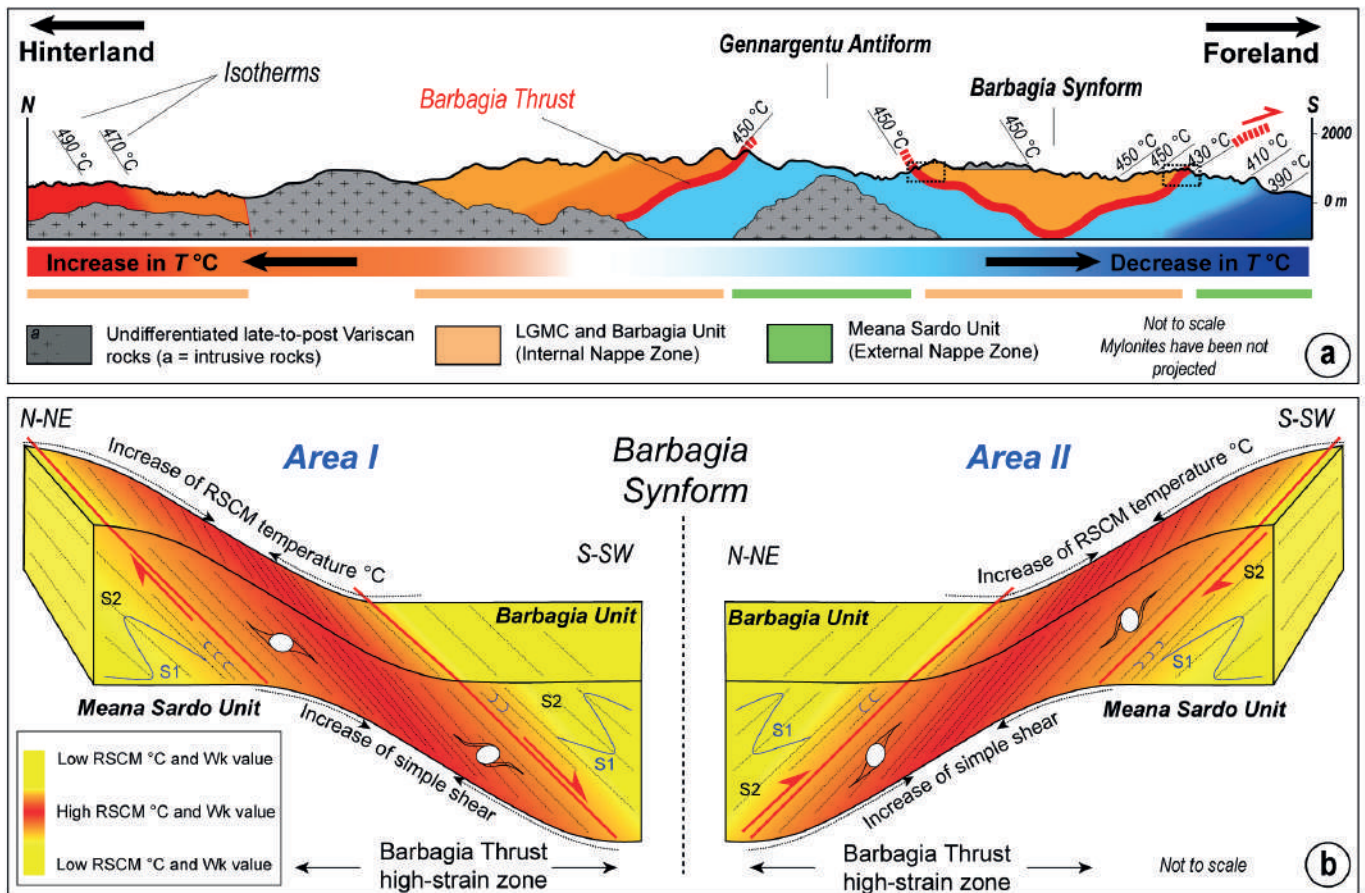


Figure 5 a) Thermal architecture of the study area in a cross-section view (see Fig. 2 for the trace of the cross-section). Orange and green bars refer to the spatial extension of the Internal and External nappes respectively. The thick red line, that marks the BT, suggests the role of shear heating along the shear zone. The spatial distribution of the isotherms occurrence is displayed. The position of both Area I and Area II has been provided; b) Not to scale representations of the BT, along which the northern and southern limb of the Barbagia Synform, have been displayed. The progressive strain partitioning and gradient, from fold structures to a mylonitic foliation (approaching the Barbagia Thrust high-strain zone), have been highlighted, mirrored by the increase of both simple shear and the T_{max} .

the development of open folds with sub-horizontal axial plane and axes (D_4 ; Fig. 4).

Obtained results support a scenario of (Fig. 5a,b): (i) early collision and T_{max} acquisition, different between Internal and External nappes (D_1 ; Fig. 5a); (ii) syn-collisional exhumation of the Internal Nappe Zone associated with shear heating along thrust-sense structures (i.e., the BT; Fig. 5b) (D_2); (iii) subsequent regional-scale folding during the latest stage of collision, that drove the present-day T_{max} architecture (D_3 ; Fig. 5a). A late extensional stage (D_4), with the development of collapse folds with associated brittle/ductile to brittle structures, marks the end of the orogenic cycle.

REFERENCES

Aoya, M., Kouketsu, Y., Endo, S., Shimizu, H., Mizukami, T., Nakamura, D., & Wallis, S. (2010): Extending the applicability of the Raman carbonaceous-material geothermometer using data from contact metamorphic rocks. *J. Metamorph. Geol.*, **28**(9), 895-914.

Beysac, O., Bollinger, L., Avouac, J.P., & Goffé, B. (2004): Thermal metamorphism in the lesser Himalaya of Nepal determined from Raman spectroscopy of carbonaceous material. *EPSL*, **225**(1-2), 233-241.

Beysac, O., Goffé, B., Chopin, C., & Rouzaud, J.N. (2002):

Raman spectra of carbonaceous material in meta-sediments: a new geothermometer. *J. Metamorph. Geol.*, **20**(9), 859-871.

Carmignani, L., Carosi, R., Di Pisa, A., Gattiglio, M., Musement, G., Oggiano, G., & Pertusati, P.C. (1994): The hercynian chain in Sardinia (Italy). *Geodin. Acta*, **7**(1), 31-47.

Carosi, R. (2004): Carta geologico-strutturale del Monte S. Vittoria (Sarcidano-Barbagia di Belvì, Sardegna centrale, Italia). Carosi R., Elter F.M. Gattiglio M. (1997). Scala 1:25.000, Centro Offset, Siena, 1997. *Atti Soc. Toscana Sci. Nat. Mem. A*, **108**.

Carosi, R., & Malfatti, G. (1995): Analisi Strutturale dell'Unità di Meana Sardo e caratteri della deformazione duttile nel Sarcidano-Barbagia di Seulo (Sardegna centrale, Italia). *Atti Soc. Toscana Sci. Nat. Mem. A*, **102**, 121-136.

Carosi, R., Iacopini, D., & Montomoli, C. (2004): Asymmetric folds development in the Variscan Nappe of central Sardinia (Italy). *CR. GEOSCI.*, **336**(10), 939-949.

Carosi, R., Leoni, L., Paolucci, F., Pertusati, P.C., & Trumpy, E. (2010): Deformation and illite crystallinity in metapelitic rocks from the Mandas area, in the Nappe Zone of the Variscan belt of Sardinia. *Rend. Online Soc. Geol.*, **11**, 393-394.

- Carosi, R., Montomoli, C., Iaccarino, S., Benetti, B., Petroccia, A., & Simonetti, M. (2022): Constraining the timing of evolution of shear zones in two collisional orogens: fusing structural geology and geochronology. *Geosc.*, **12**, 231.
- Carosi, R., Musumeci, G., & Pertusati, P.C. (1991): Differences in the structural evolution of tectonic units in central-southern Sardinia. *Boll. Soc. Geol. Ital.*, **110(3-4)**, 543-551.
- Carosi, R., Petroccia, A., Iaccarino, S., Simonetti, M., Langone, A., & Montomoli, C. (2020): Kinematics and timing constraints in a transpressive tectonic regime: the example of the Posada-Asinara shear zone (NE Sardinia, Italy). *Geosc.*, **10**, 288.
- Conti, P., Carmignani, L., Cerbai, N., Eltrudis, A., Funedda, A., & Oggiano, G. (1999): From thickening to extension in the Variscan belt - kinematic evidence from Sardinia (Italy). *Terra Nova*, **11(2/3)**, 93-99.
- Conti, P., Carmignani, L., & Funedda, A. (2001): Change of nappe transport direction during the Variscan collisional evolution of central-southern Sardinia (Italy). *Tectonophysics*, **332(1-2)**, 255-273.
- Costamagna, L.G., Cruciani, G., Franceschelli, M., & Puxeddu, M. (2012): A volcano-sedimentary sequence with albitite layers in the Variscan basement of NE Sardinia: a petrographical and geochemical study. *Period. di Mineral.*, **81(2)**, 179-204.
- Cruciani, G., Franceschelli, M., Massonne, H.-J., Musumeci, G., & Spano, M.E. (2016): Thermomechanical evolution of the highgrade core in the nappe zone of Variscan Sardinia, Italy: the role of shear deformation and granite emplacement. *J. Metamorph. Geol.*, **34**, 321-342.
- Cruciani, G., Montomoli, C., Carosi, R., Franceschelli, M., & Puxeddu, M. (2015): Continental collision from two perspectives: a review of Variscan metamorphism and deformation in northern Sardinia. *Period. di Mineral.*, **84**, 657-699.
- Fossen, H., & Cavalcante, G.C.G. (2017): Shear zones—A review. *Earth. Sci. Rev.*, **171**, 434-455.
- Franceschelli, M., Gattiglio, M., Pannuti, F., & Fadda, S. (1992): Illite crystallinity in pelitic rocks from the external and nappe zones of the Hercynian chain of Sardinia. In L., Carmignani, F.P., Sassi (Ed.). *Contributions to the Geology of Italy with special regard to the Paleozoic Basements*. (pp. 127-135) IGCP Project No. **276**, Newsletter.
- Franceschelli, M., Memmi, I., Pannuti, F., & Ricci, C.A. (1989): Diachronous metamorphic equilibria in the Hercynian basement of northern Sardinia, Italy. *Geol. Soc. Spec. Publ.*, **43(1)**, 371-375.
- Frey, M. (1987): Very low grade metamorphism of clastic sedimentary rock. In M., Frey (Ed.). *Low temperature metamorphism*. Chapman and Hall, New York, pp 9-57
- Frey, M., & Robinson, D. (1999): Low-grade metamorphism. Blackwell Science, Oxford. pp. 312
- Fry, N. (1979): Random point distribution and strain measurement in rocks. *Tectonophysics*, **60**, 89-105.
- Gillam, B.G., Little, T.A., Smith, E., & Toy, V.G. (2013): Extensional shear band development on the outer margin of the Alpine mylonite zone, Tatara Stream, Southern Alps, New Zealand. *J. Struct. Geol.*, **54**, 1-20.
- Iacopini, D., Frassi, C., Carosi, R., & Montomoli, C. (2011): Biases in three-dimensional vorticity analysis using porphyroclast system: limits and application to natural examples. *Geol. Soc. Spec. Publ.*, **360(1)**, 301-318.
- Jamieson, R.A., Beaumont, C., Nguyen, M.H., Lee, B. (2002): Interaction of metamorphism, deformation and exhumation in large convergent orogens. *J. Metamorph. Geol.*, **20(1)**, 9-24.
- Jaquet, Y., Duretz, T., Grujic, D., Masson, H., & Schmalholz, S.M. (2018): Formation of orogenic wedges and crustal shear zones by thermal softening, associated topographic evolution and application to natural orogens. *Tectonophysics*, **746**, 512-529.
- Jessup, M.J., Law, R.J., & Frassi, C. (2007): The Rigid Grain Net (RGN): An alternative method for estimating mean kinematic vorticity number (W_m). *J. Struct. Geol.*, **29**, 411-421.
- Kurz, G.A., & Northrup, C.J. (2008): Structural analysis of mylonitic rocks in the Cougar Creek Complex, Oregon-Idaho using the porphyroclast hyperbolic distribution method, and potential use of SC'-type extensional shear bands as quantitative vorticity indicators. *J. Struct. Geol.*, **30(8)**, 1005-1012.
- Lünsdorf, N.K., Dunkl, I., Schmidt, B.C., Rantitsch, G., & Von Eynatten, H. (2014): Towards a higher comparability of geothermometric data obtained by Raman spectroscopy of carbonaceous material. Part I: evaluation of biasing factors. *Geostand. Geoanal. Res.*, **38**, 73-94.
- Lünsdorf, N.K., Dunkl, I., Schmidt, B.C., Rantitsch, G., & Von Eynatten, H. (2017): Towards a higher comparability of geothermometric data obtained by Raman spectroscopy of carbonaceous material. Part 2: A revised geothermometer. *Geostand. Geoanal. Res.*, **41(4)**, 593-612.
- Montomoli, C., Iaccarino, S., Simonetti, M., Lezzerini, M., & Carosi, R. (2018): Structural setting, kinematics and metamorphism in a km-scale shear zone in the inner nappes of Sardinia (Italy). *Ital. J. Geosci.*, **137**, 294-310.
- Musumeci, G. (1992): Ductile wrench tectonics and exhumation of hercynian metamorphic basement in Sardinia: Monte Grighini Complex. *Geodin. Acta*, **5(1-2)**, 119-133.
- Passchier, C. W. (1987): Stable positions of rigid objects in non-coaxial flow—a study in vorticity analysis. *J. Struct. Geol.*, **9(5-6)**, 679-690.

- Petroccia, A., Carosi, R., Montomoli, C., Iaccarino, S., & Vitale Brovarone, A. (2022a): Deformation and temperature variation along thrust-sense shear zones in the hinterland-foreland transition zone of collisional settings: a case study from the Barbagia Thrust (Sardinia, Italy). *J. Struct. Geol.*, **161**, 104640.
- Petroccia, A., Montomoli, C., Iaccarino, S., & Carosi, R. (2022b): Geology of the contact area between the Internal and External Nappe Zone of the Sardinian Variscan Belt (Italy): new insights on the complex polyphase deformation occurring in the hinterland-foreland transition zone of collisional belts. *J. Maps*, **18(2)**, 472-483.
- Petroccia, A., Carosi, R., Montomoli, C., Iaccarino, S., & Vitale Brovarone, A. (2022c): Thermal variation across collisional orogens: insights from the hinterland-foreland transition zone of the Sardinian Variscan belt. *Terra Nova*, **35(2)**, 113-123.
- Stipp, M., Stünitz, H., Heilbron, M., & Schmid, D.W. (2002): The eastern tonale fault zone: A natural laboratory for crystal plastic deformation of quartz over a temperature range from 250 to 700°C. *J. Struct. Geol.*, **24**, 1861-1884.
- Thigpen, J.R., Ashley, K.T., & Law, R.D. (2017): Evaluating kinematic displacement rate effects on transient thermal processes in thrust belts using coupled thermo-mechanical finite-element models. In R.D., Law, J.R., Thigpen, A.J., Merschat, & H.H. Stowell, (Ed.). *Linkage and Feedbacks in Orogenic Systems*. (213, pp. 1-23). *Mem. Geol. Soc. Am.*
- Thigpen, J.R., Law, R.D., Lloyd, G.E., Brown, S.J., & Cook, B. (2010): Deformation Temperatures, Vorticity of Flow and Strain Symmetry in the Loch Eriboll Mylonites, NW Scotland: Implications for the Kinematic and Structural Evolution of the Northernmost Moine Thrust Zone. *Geol. Soc. Spec. Publ.*, **335**, 623-662.
- Tikoff, B., & Fossen, H., (1995): The limitations of three-dimensional kinematic vorticity analysis. *J. Struct. Geol.*, **17**, 1771-1784.
- Vollmer, F.W. (2015): EllipseFit 3.2.
- Wallis, S.R., Platt, J.P., & Knott, S.D. (1993): Recognition of synconvergence extension in accretionary wedges with examples from the Caledonian Arc and the Eastern Alps. *Am. J. Sci.*, **293**, 463-495.
- Xypolias, P. (2010): Vorticity analysis in shear zones: A review of methods and applications. *J. Struct. Geol.*, **32**, 2072-2092.

Biogeochemical processes affecting Volatile Organic Compounds (VOCs) in interstitial soil gases from geogenic sources and municipal waste landfills

Antonio Randazzo

Dipartimento di Scienze della Terra, Università degli Studi di Firenze, Via La Pira 4, 50121, Firenze, Italia

DOI:10.19276/plinius.2023.01.011

INTRODUCTION

Non-methane volatile organic compounds (hereafter VOCs) are synthetically and naturally sourced organic compounds, having an initial boiling point less than or equal to 250°C measured at a standard pressure of 101.3 kPa, as defined by the Directive 2004/42/CE. Owing to their high volatility, VOCs are inevitably emitted into the atmosphere. Atmospheric VOCs are generated mostly by (i) biogenic and, secondarily, by (ii) geogenic, and (iii) anthropogenic processes. The contribution of geogenic VOCs is mostly related to volcanic/hydrothermal degassing and surficial seepages from deep oil and natural gas deposits. Among the anthropogenic sources, municipal waste (MW) landfills represent a major concern given the projected increase of MW generation in the next future (Chen et al., 2020). Geogenic and landfill gases comprise different cocktails of VOCs including alkane, alkene, aromatic, cyclic, terpene, halogenated and O-, Cl-, N- and S-substituted compounds (Tassi et al., 2009, 2015a). Most of these VOCs have severe impacts on the environment, air quality and human health (Gallego et al., 2012; Nair et al., 2019).

Emerging evidence has shown that soils may be powerful drivers for the global VOC cycle by acting as a sink or source (Insam and Seewald, 2010; Peñuelas et al., 2014). Soil VOC uptake occurs through mutual interactions between (i) abiotic factors, depending on physicochemical soil characteristics, and (ii) biological processes driven by microbes that use VOCs as a carbon source (Tang et al., 2019). Whilst the rapid uprising of hypogenic gases (i.e., geogenic and landfill gas) is presumed to best preserve their chemical composition up to the surface (Tassi et al., 2015b), the slow-moving through the soil is expected to exacerbate VOC compositional changes due to the long-lasting stay of the hypogenic gases at physicochemical conditions markedly different from those of their genetic environments. However, how these hypogenic VOCs respond to biogeochemical soil processes and whether soil acts as a sink for these VOCs is poorly understood so far.

According to these considerations, this study, based on fieldwork and laboratory experiments, aims to investigate biodegradation mechanisms regulating the fates of VOCs in soils affected by inputs of extra-atmospheric gases from natural and anthropic systems. Fieldwork was carried out to find out whether soil processes affecting VOCs depend on (i) the hypogenic gas composition and soil chemical-physical conditions, (ii) the residence time of uprising gases within the soil, and (iii) O₂ availability. Laboratory experiments were devoted to deeply investigating VOCs in MW landfill systems.

FIELDWORK

Study areas

The effects of the biogeochemical processes affecting hypogenic gas composition within the soil were examined by selecting six different study areas in Italy, encompassing different geological settings and a representative MW landfill, as follows: (i) an active volcanic system i.e., La Fossa Crater (LFC) associated with a high enthalpy hydrothermal system i.e., Baia di Levante (BdL) in Vulcano Island (the Aeolian Archipelago, southern Italy), which is affected by large CO₂-dominated degassing; (ii) two medium-to-high enthalpy hydrothermal systems i.e., Solfatara di Nepi (SdN) and Caldara di Manziana (CdM) belonging to the Sabatini Volcanic District (central Italy), which is characterised by CO₂-dominated diffuse emissions; (iii) a CH₄-seepage at Terre Calde di Medolla (TCM), pertaining to the CH₄-rich sedimentary basin of Po plain (northern Italy); an MW landfill, i.e., Belvedere Inc. landfill (LL) sited in Peccioli (Central Italy), characterised by landfill gas (dominated by CO₂ and CH₄) leakages.

Materials and methods

Fieldwork was based on the measurement of different geochemical parameters from a total of about 200 sampling sites properly selected to cover, as much as possible, the spatial variabilities of the study areas, as follows: (i) $\Phi(\text{CO}_2 + \text{CH}_4)$ i.e., soil CO₂ and CH₄ fluxes that were

conveniently used as a proxy for the residence time of gases within the soil; (ii) isotope ($^{13}\text{C}/^{12}\text{C}$ in CO_2 and CH_4 i.e., $\delta^{13}\text{C}\text{-CO}_2$ and $\delta^{13}\text{C}\text{-CH}_4$, respectively) and chemical compositions of inorganic volatiles and VOCs from (1) interstitial soil gases collected at two selected depths (overall in the interval depth from 60 cm depth to the effective emission into the atmosphere) along vertical soil profiles in which shallow depths were expected to be more oxidising than the deeper depths, and (2) gas vents (e.g., fumaroles, bubbling pools, dry vents) and landfill gas from a recovery well as representatives of the source gas composition of the study areas. About 500 soil gas samples were analysed and more than 20,000 data were produced. Gas analyses were conducted at the Laboratory of Fluid Geochemistry of the Department of Earth Sciences of Florence (University of Florence).

Results and discussion

Source gas composition

The different sources of gases from the investigated systems were clearly distinguished by correlating the total concentration of VOCs (ΣVOCs) with the $\text{CH}_4/(\text{C}_2\text{H}_6+\text{C}_3\text{H}_8)$ ratio (Fig. 1), which is commonly used for discerning the genetic pathways of light hydrocarbons, since biogenic gases have typically ratios $>1,000$, whilst values <100 are generally ascribed to thermogenesis (Whiticar, 1999). The ΣVOCs values decreased at increasing temperatures of the associated system, confirming that temperature favours the reactivity of VOCs (Capacioni *et al.*, 1995). On the other hand, the generation of hydrocarbons at LL and TCM is exacerbated by the large abundance of organic matter expected in their genetic environments (Randazzo *et al.*, 2020; Sherwood Lollar *et al.*, 2002). The $\text{CH}_4/(\text{C}_2\text{H}_6+\text{C}_3\text{H}_8)$ ratios were consistent with the biogenic origin, with the sole exception of CdM that falls in an intermediate interval between biogenesis

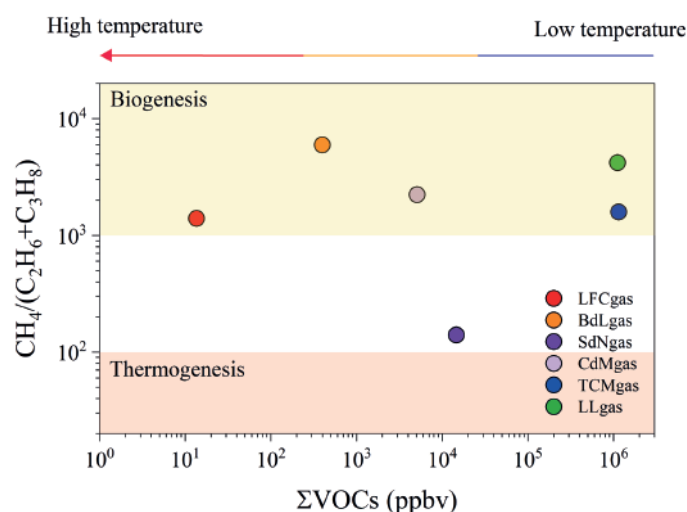


Figure 1 $\text{CH}_4/(\text{C}_2\text{H}_6+\text{C}_3\text{H}_8)$ ratio vs total concentration of VOCs (ΣVOCs , expressed as ppbv) of gas vents from La Fossa Crater (LFCgas), Baia di Levante (BdLgas), Solfatara di Nepi (SdNgas), Caldara di Manziana (CdMgas), Terre Calde di Medolla (TCMgas), and landfill gas from Legoli landfill (LLgas).

and thermogenesis (Fig. 1). Actually, a biogenic origin is plausible only for the cold LL and TCM systems. In fact, the relatively high temperature characterising the terrains of volcanic/hydrothermal systems hinders microbial activities (Colwell *et al.*, 1997). Accordingly, the apparent biogenic signature of volcanic and hydrothermal gases is to be ascribed to secondary processes, such as the dehydrogenation of light alkanes that is favoured under hydrothermal and volcanic conditions (Fiebig *et al.*, 2013).

The chemical VOC composition of source gases significantly differed among the investigated systems (Fig. 2), reflecting differences in the environmental conditions of the pertaining reservoir, mostly the quality and quantity of degrading organic matter, temperature, and redox state.

Controls on hypogenic CO_2 and CH_4 in soil

Overall, most soil gases, except for those of LFC, got depleted in CH_4 with respect to CO_2 compared to the expected theoretical mixing line between air and the corresponding source gases. This clearly reflects the CH_4 -to- CO_2 oxidation by methanotrophic bacteria mostly occurring within the soil, where O_2 is available (Le Mer & Roger, 2001). Differently, LFC gas samples got relatively enriched in CH_4 compared to their source gas, suggesting that the feeding gas at LFC soil was a mixture between gases from the volcanic source and a low-temperature CH_4 -enriched endmember.

It is commonly accepted that high $\Phi(\text{CO}_2+\text{CH}_4)$ values limit soil processes, decreasing their residence time within the soil, whilst low $\Phi(\text{CO}_2+\text{CH}_4)$ values favour chemical changes in the hypogenic gas composition (Randazzo *et al.*, 2020). Actually, the CO_2/CH_4 ratios of interstitial gases were not (or only roughly) related to $\Phi(\text{CO}_2+\text{CH}_4)$ values, suggesting a weak dependence of CH_4 -to- CO_2 oxidation processes on the $\Phi(\text{CO}_2+\text{CH}_4)$ values. This may have been related to spatial soil inhomogeneities, including physicochemical-biological characteristics, local permeability barriers, and waterlogging.

Neither $\delta^{13}\text{C}\text{-CO}_2$ nor $\delta^{13}\text{C}\text{-CH}_4$ trends were observed in the soil. This is to be ascribed to multiple, interdependent, local, isotope fractionation processes occurring in soil, including: (i) the CH_4 -to- CO_2 oxidation; (ii) autotrophic and heterotrophic respiration; (iii) rate, extent, and pattern of organic matter degradation processes; (iv) mixing with air or shallow-sourced gases; (v) carbon isotope exchanges at high temperature.

Soil biogeochemical mechanisms affecting hypogenic-sourced VOCs

Biogeochemical processes occurring within the soil affected to different extents the various types of hypogenic VOCs whose composition significantly changed during their transfer through the soil (Fig. 2). Biochemical degradation pathways within the soils from different stu-

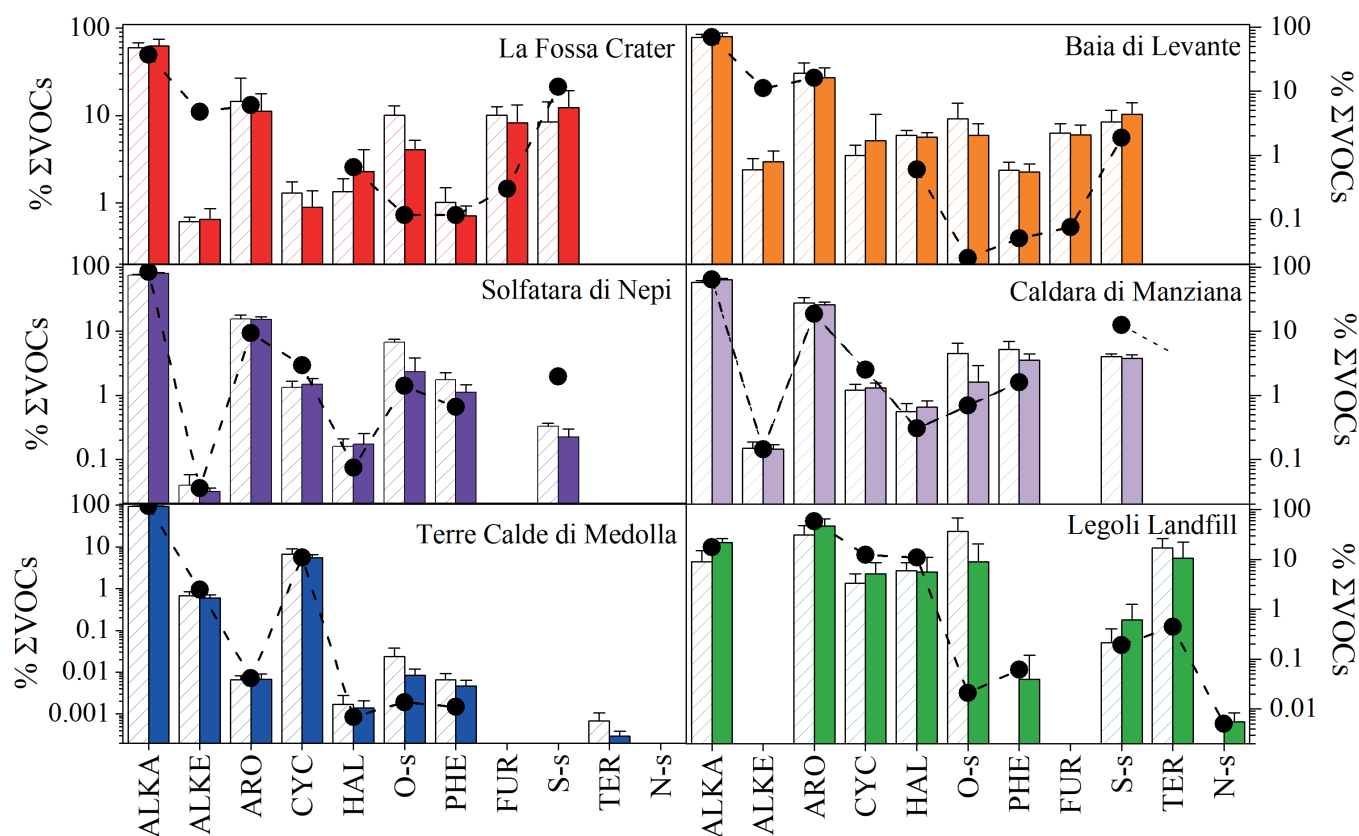


Figure 2 Bar charts representing the mean and standard deviation of the organic group concentrations (expressed as % Σ VOCs) detected in shallow (diagonal line texture) and deep (filled column) soil gas samples. Circle symbols indicate the relative abundance of the organic groups in the source gases. Legend: ALKA = alkanes; ALKE = alkenes; ARO = aromatics; CYC = cyclics; HAL = halogenated compounds; O-s = O-substituted compounds; PHE = phenol; FUR = furans; S-s = S-substituted compounds; TER = terpenes; N-s = N-substituted compound i.e., benzothiazole

dy areas showed important similarities and interesting differences.

The aerobic biodegradation of alkanes is well documented to proceed through the production of O-substituted compounds (Rojo, 2009). Consistently, most soil gases were enriched in O-substituted compounds (Σ OXY, including aldehydes, esters, ketones, and alcohols) and depleted in alkanes (Σ ALKA) respect to the corresponding gas source (Fig. 3). The excess in alkanes exhibited by some SdN and CdM soil gases was interpreted as due to mixing with low-temperature shallow gases. Also, lines of evidence have reported that branched alkanes are harder to degrade than n-alkanes (Brzeszcz & Kaszycki, 2018). The depletion of long-chain alkanes (Σ ALK-AC₅-C₇-C₈) on the short-chain ones (Σ ALK-AC₂-C₃-C₄) in soil with respect to the source gas was clearly observed for SdN and CdM soil gases, with no noticeable difference from deep to shallow soil gases, and LL soil gases, which showed a strong depletion of long-chain alkanes only at the shallowest depth (Fig. 4). This suggests that at SdN and CdM the large depth of the gas source (located at about 3,000 km depth) implied the most long-chain alkane depletion occurred before they reached the soil, whereas at LL, the proximity of the gas source (few meters) preserved long-chain alkanes almost up to the surface. The occurrence of long-chain alkanes in soil gases from LFC and BdL and not in their source gases (Fig. 4)

suggests that they were effectively cracked at relatively high temperature (Capaccioni et al., 1995), implying mixing with low-temperature shallow gases. A further source of long-chain alkanes has to be also invoked for TCM (Fig. 4). The relatively low reactivity of hexane compared to the long-chain alkanes provided by the C₆-structure was confirmed (Randazzo et al., 2020).

Our data also showed strong correlations between the total contents of alkanes and those of both cyclics and alkenes in soil gases that may support a similar reactivity of aliphatic hydrocarbons (Watkinson & Morgan, 1990). Nevertheless, a relative enrichment of alkanes on alkenes in soil gases from BdL and LFC compared to their source gases was seen, presumably caused by the hydrogenation of alkenes during the gas uprising triggered by temperature drop (Seewald, 2001). Similarly, we also observed a relative enrichment of alkanes on cyclics in soil gases from SdN, CdM, and LL that may suggest that cyclics are generally less stable than alkanes.

Cogent evidence has stated that aromatics can undergo biogeochemical degradation in soil (Díaz et al., 2013; Weelink et al., 2010). In particular, alkylated benzenes are considered relatively more reactive than benzene (Weelink et al., 2010). Consistently, soil gases from LFC, SdN, CdM, and LL were relatively enriched in benzene with respect to the source gases and the Benzene/ Σ Alkyl-benzenes ratios rose upwards along the ver-

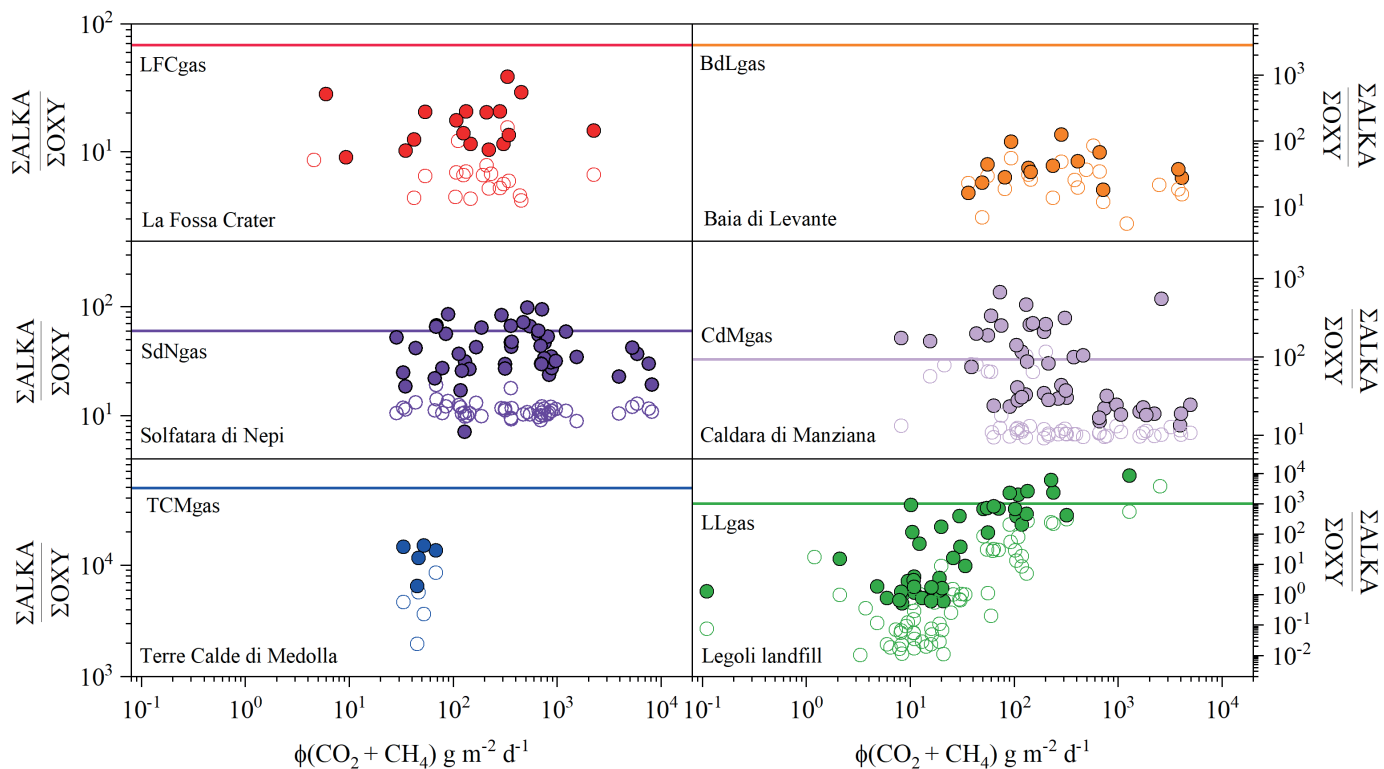


Figure 3 Binary diagrams of the ratios of alkanes (Σ ALK) on O-substituted compounds (Σ OXY) in soil gases. The Σ ALK/ Σ OXY ratios of the source gases are also reported (bold lines). Solid and open symbols represent deep and shallow soil gas samples, respectively.

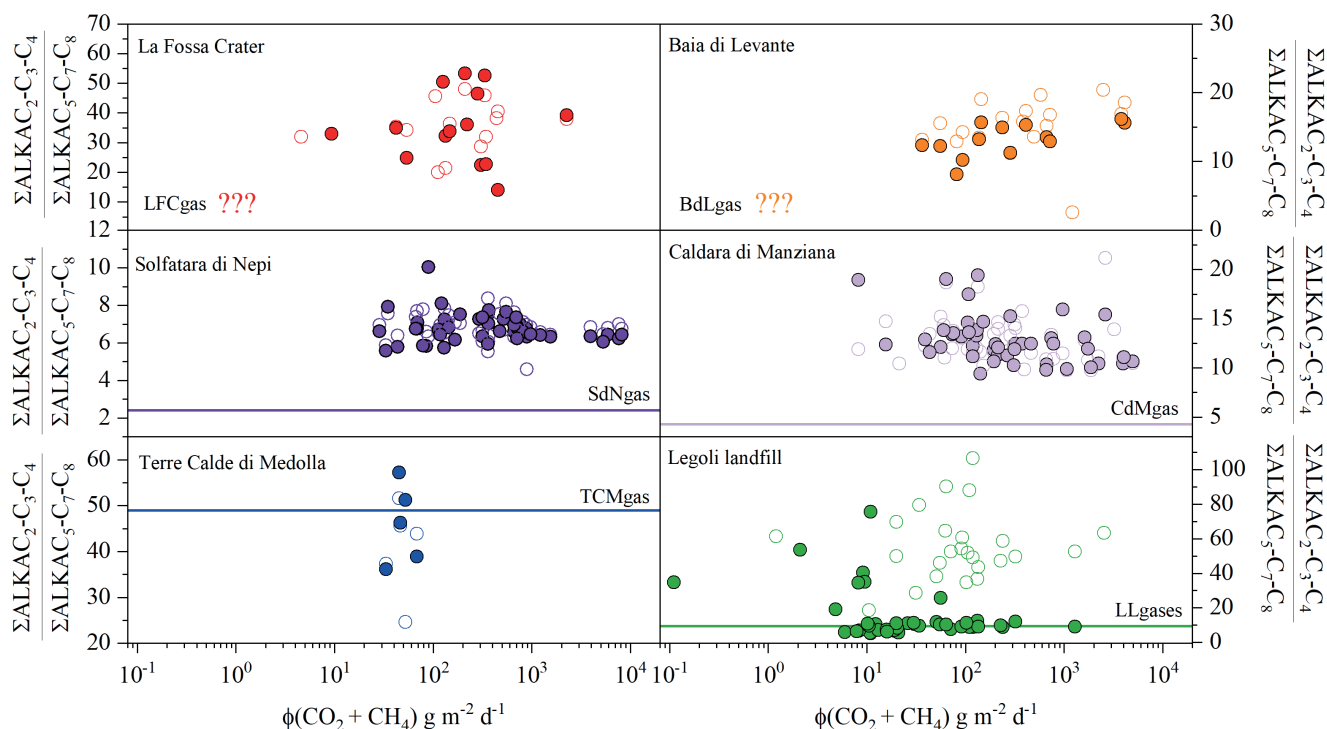


Figure 4 Binary diagrams of the ratios of short-chain alkanes (Σ ALKAC₂-C₃-C₄) on long-chain alkanes (Σ ALKAC₅-C₇-C₈) in soil gases. The Σ ALKAC₂-C₃-C₄/ Σ ALKAC₅-C₇-C₈ ratios of the source gases are also reported (bold lines). Solid and open symbols represent deep and shallow soil gas samples, respectively. The Σ ALKAC₂-C₃-C₄/ Σ ALKAC₅-C₇-C₈ ratios of the source gases from La Fossa Crater and Baia di Levante were not computed due to the lack of long-chain alkanes

tical profiles in LL and CdM (Fig. 5). The opposite trend observed for BdL (Fig. 5) supports mixing with low-temperature shallow gases. Differently, no variation in the composition of aromatics was found in TCM (Fig. 5): presumably the low temperature characterising the overall geogenic system and the lack of aromatic degrader microbes caused by the low amounts of aromatics (Fig. 2)

preserved alkylated-benzenes. Despite the relatively low reactivity of benzene, its degradation has been reported under both anaerobic and, to a higher extent, aerobic conditions, proceeding through the formation of phenol as an intermediate metabolite (Jindrová et al., 2002). We observed a relative enrichment of phenol on benzene only at SdN and CdM (from deep to shallow soil gases)

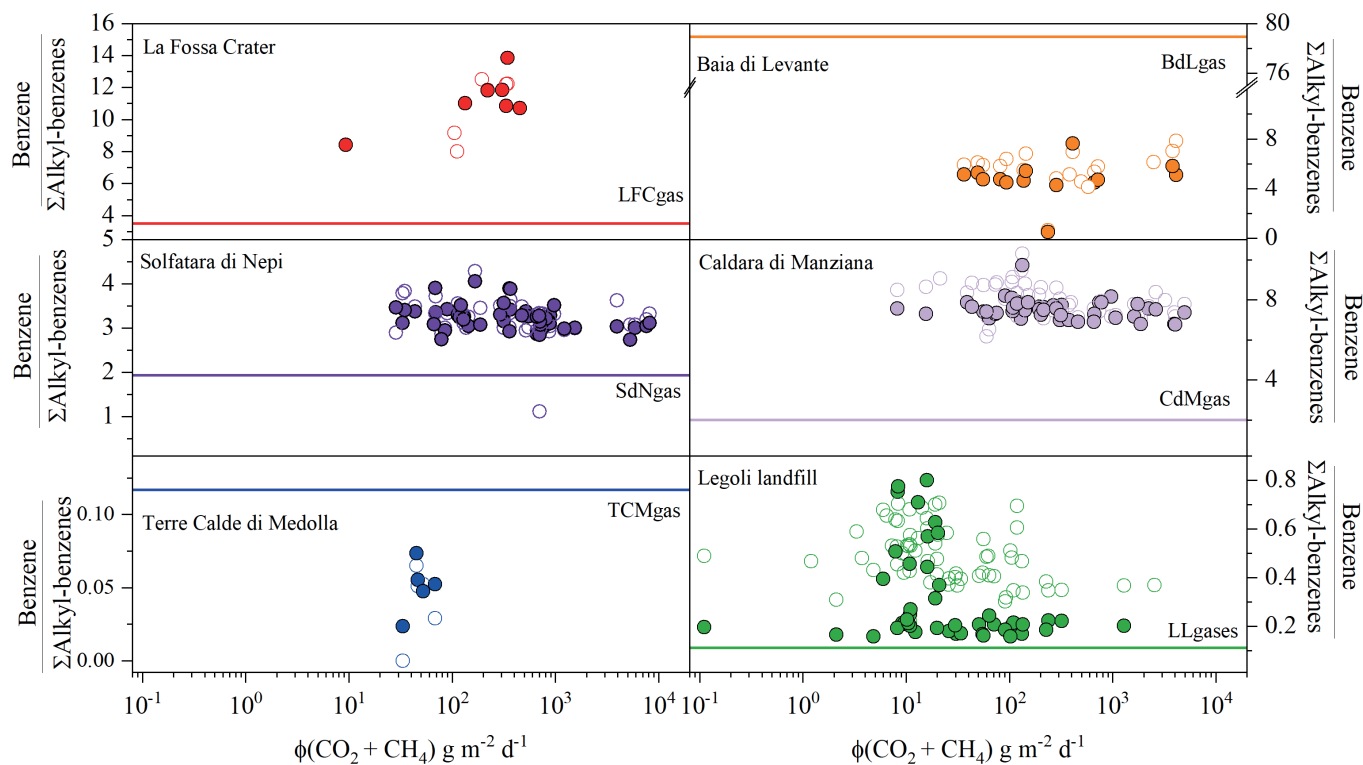


Figure 5 Binary diagrams of the ratios of benzene on alkylated benzenes (Σ Alkyl-benzenes) in soil gases. The Benzene/ Σ Alkyl-benzenes ratios of the source gases are also reported (bold lines). Solid and open symbols represent deep and shallow soil gas samples, respectively

and at BdL, LFC, and TCM where most soil gases were enriched in phenol with respect to benzene compared to the source gases. It likely reflected the development of phenol-degrading bacteria at variable depth.

Among S-substituted compounds, dimethylsulfoxide and dimethylsulfide were found in every investigated system except at TCM (Fig. 2), being their origin related either to high S fugacity (as occurred in volcanic/hydrothermal systems) or to degrading organic matter enriched in S (as occurred in MW landfill). The relative enrichment of dimethylsulfoxide on dimethylsulfide observed in the shallow soil gases with respect to deep soil gases and source gases confirmed the high reactivity of dimethylsulfide under oxidising conditions (Schäfer et al., 2010). Thiophenes were instead found only in volcanic/hydrothermal systems since their genetic environment is strictly related to reducing conditions, relatively high fS , and high temperature (Tassi et al., 2010). Given their strong similarity with the chemical structure of aromatics, cometabolic degradation of thiophenes with aromatics as a primary substrate has been reported (Joule, 2014). Actually, our data showed a relative depletion of thiophenes on alkylated aromatic compounds, suggesting that thiophenes were relatively more reactive.

Furans are typical high-temperature O-bearing organic compounds (Tassi et al., 2010) and were only detected at LFC and BdL (Fig. 2). Our data showed that furan is relatively less reactive than its methylated counterparts, which may support the lower stability of alkylated compounds with respect to the non-alkylated ones.

Terpenes occurred in relatively high amounts in LL soil

gases (Fig. 2) where they originate from the degradation of organic waste or direct volatilisation from detergents and air fresheners (Randazzo et al., 2020). Among these terpenes, we observed a relative increase of the concentration of α -pinene with respect to that, as a sum, of limonene and camphene upwards from the landfill gas to the shallowest gas samples, indicating a certain recalcitrance of α -pinene under oxidising conditions compared to its homologies.

No insight was observed into the degradation of neither halogenated nor N-substituted (benzothiazole) compounds.

Concluding remarks

Soil processes caused strong modifications to the compositional features of hypogenic gases affecting preferentially selected VOCs. The rates and types of these processes were different among the investigated systems, indicating a certain control of the soil conditions (e.g., microbial populations, organic matter and moisture contents, texture, structure, pH) and hypogenic gas composition.

The $\Phi(CO_2 + CH_4)$ values measured at the surface were not a reliable proxy for the residence time of the gas within the soil due to soil inhomogeneities.

O_2 availability appears to be a major control for the biogeochemical processes of selected VOCs, such as alkanes and dimethylsulfide.

LABORATORY EXPERIMENTS

Generation of VOCs from the anaerobic degradation of green waste

This experiment was focused on characterising the composition of VOCs originating from the anaerobic digestion (AD) of green waste (GW), as a representative category of the organic fraction of MW, with the scopes of (i) identifying the source processes and (ii) assessing its potential impacts if released into the atmosphere.

The experiment consisted of an AD reaction line, lasting about 50 days, at mesophilic conditions. The digester was filled with a mixture of GW with inoculum. GW consisted of municipal and domestic vegetal wastes, whilst the inoculum was an anaerobic sludge originating from municipal wastewater treatments. A total of 8 gases were periodically collected from the digester headspace. Semiquantitative VOC (C₄₊) analyses distinguished up to 29 different species in the GW biogases that were largely dominated by the high odorous terpenes in concentration, followed by alkanes and alkenes. These compounds are commonly synthesized by plants (Randazzo et al., 2022). Aromatic, halogenated, and S- and O-substituted compounds were found in lower amounts. Aromatics are also contained in vegetal tissues, such as lignin but they, together with halogenated compounds may be also assimilated by plants from contaminated air and soils (Randazzo et al., 2022). Finally, S- and O-substituted compounds are normally released by the degradation of fresh waste and decomposition of organic waste containing sulfur (Randazzo et al., 2022).

These results showed that GW, if disposed of in MW landfill, may potentially contribute to the overall odorous charge of MW biogas, releasing large quantities of terpenes.

Lab-scale prototype for simulating landfill cover soil

The second experiment was devoted to investigating the biochemical mechanisms by which landfill cover soils mitigate the complex variety of VOCs commonly pertaining to the landfill gas under controlled conditions. An experimental apparatus was properly designed and constructed to reliably simulate MW landfill systems. The apparatus consisted of a 20 L tank (digester), where the anaerobic digestion of selected waste categories (food

waste was selected as a representative category of the organic fraction of MW) occurred, connected to a vertical pipe (H = 60 cm, d = 15 cm) packed with vegetal soil (soil column). The generated biogas naturally flew from the digester into the soil column through pressure and concentration gradients. The experiment lasted for 23 days. Gases from the digester headspace and at regular intervals along the soil column were periodically collected and analysed in terms of: (i) main components i.e., CH₄, CO₂, H₂, N₂, O₂, and Ar; (ii) VOCs; (iii) δ¹³C-CO₂ and δ¹³C-CH₄. Overall, the concentration of biogas-related components (CH₄, CO₂, H₂, and VOCs) in the digester headspace and the soil column, sharply increasing in the first part of the AD, was relatively high until day 17 and then decreased. This decrease was associated with a drop in the N₂/O₂ ratios, indicating that air entered the digester i.e., biogas pressure was no longer capable of effectively counteracting air permeation along the cover soil. Along the soil column, the concentration of the biogas-related components relatively decreased upwards, mainly due to the air dilution effect. In the soil column, CO₂ and CH₄ always showed a ¹³C-enrichment compared to the corresponding source gases, according to the preference of microorganisms to metabolise the lightest isotope (Randazzo et al., 2020). We observed an increase of both O-substituted compounds and short-chain alkanes (C₂-C₃) on alkanes and long-chain alkanes (C₃₊), respectively, towards the top of the soil column, confirming the relative degradation of alkanes under aerobic conditions and the preferential degradation of long-chain alkanes compared to the short-chain ones. Consistently with the relative recalcitrance of benzene, a relative enrichment of benzene compared to alkylated-benzenes upwards the soil column was observed.

These results, consistent with the fieldwork observations, indicates that degradation processes occurring in landfill cover soils are highly selective for VOC compounds.

CONCLUSIONS

Soil processes caused strong modifications to the VOC compositional features of hypogenic gases during their uprising towards the atmosphere, especially pas-

VOCs relatively MORE affected by soil processes	VOCs relatively LESS affected by soil processes	VOCs as BY-PRODUCTS of VOC degradation pathways
Long-chain alkanes	Short-chain alkanes	O-Substituted compounds (aldehydes, esters, ketones, and alcohols)
Alkenes	Hexane	
Cyclics	Benzene	Phenol
Alkylated-benzenes	Phenol	
Dimethylsulfide	Dimethylsulfoxide	Phenol
Thiophenes	Furan	
Methylated-furans	α-pinene	
Limonene, Camphene		

Table 1 VOC species and groups classified on the basis of their behaviour in soil

sing within the soil where the physical-chemical conditions strongly differ respect to those dominating at the gas source. As shown in Table 1, the most reactive VOC species and organic groups in soil were recognised. Generally, long-chain and high-molecular weight molecules of alkane, alkene, cyclic, aromatic, and furan compounds were found to be relatively more affected by soil degradation processes. On the other hand, short-chain, low-molecular weight, and O-containing molecules were found to be recalcitrant to degradation processes with respect to their respective homologues (Table 1). Molecules characterised by six carbon atoms were among the less reactive compounds, confirming the relatively high chemical stability of the C₆ molecular structure. O-substituted organic compounds (i.e., aldehydes, esters, ketones, alcohols, and phenol), may be considered as tracers of the ongoing degradation of the VOCs, being them metabolites of hydrocarbon biodegradation pathways (Table 1).

Further investigation based on multidisciplinary approaches, involving microbiological, ecological, and pedological analysis, could provide new insights into the dependence of VOC degradation processes on soil microbial communities and micro-heterogeneities.

ACKNOWLEDGMENTS

Franco Tassi, Stefania Venturi, Fabio Tatàno, and Orlando Vaselli are acknowledged for their valuable technical and practical support. The author thanks also the colleagues of the Department of Earth Science of the University of Florence, the Institute of Geosciences and Earth Resources of the National Research Council of Italy, and the National Institute of Geophysics and Volcanology of Italy who kindly attended the sampling campaigns and helped with the preparation of the laboratory experiments. The author is also grateful to Belvedere Inc. and ASET for the logistic support during the fieldwork and the running of the AD experiment, respectively.

REFERENCES

- Brzeszcz, J., & Kaszycki, P. (2018): Aerobic bacteria degrading both n-alkanes and aromatic hydrocarbons: an undervalued strategy for metabolic diversity and flexibility. *Biodegradation*, **29**, 359–407.
- Capaccioni, B., Martini, M., & Mangani, F. (1995): Light hydrocarbons in hydrothermal and magmatic fumaroles: hints of catalytic and thermal reactions. *Bull. Volcanol.*, **56**, 593–600.
- Chen, D.M.C., Bodirsky, B.L., Krueger, T., Mishra, A., & Popp, A. (2020): The world's growing municipal solid waste: trends and impacts. *Environ. Res. Lett.*, **15**, 074021.
- Colwell, F.S., Onstott, T.C., Delwiche, M.E., Chandler, D., Fredrickson, J.K., Yao, Q.J., McKinley, J.P., Boone, D.R., Griffiths, R., Phelps, T.J., Ringelberg, D., White, D.C., LaFreniere, L., Balkwill, D., Lehman, R.M., Konisky, J., & Long, P.E. (1997): Microorganisms from deep, high temperature sandstones: Constraints on microbial colonization. *FEMS Microbiol. Rev.*, **20**, 425–435.
- Díaz, E., Jiménez, J.I., & Nogales, J. (2013): Aerobic degradation of aromatic compounds. *Curr. Opin. Biotechnol.*, **24**, 431–442.
- Fiebig, J., Tassi, F., D'Alessandro, W., Vaselli, O., & Woodland, A.B. (2013): Carbon-bearing gas geothermometers for volcanic-hydrothermal systems. *Chem. Geol.*, **351**, 66–75.
- Gallego, E., Roca, F.J., Perales, J.F., Sánchez, G., & Esplugas, P. (2012): Characterization and determination of the odorous charge in the indoor air of a waste treatment facility through the evaluation of volatile organic compounds (VOCs) using TD-GC/MS. *Waste Manag.*, **32**, 2469–2481.
- Insam, H., & Seewald, M.S.A. (2010): Volatile organic compounds (VOCs) in soils. *Biol. Fertil. Soils*, **46**, 199–213.
- Jindrová, E., Chocová, M., Demnerová, K., & Brenner, V. (2002): Bacterial Aerobic Degradation of Benzene, Toluene, Ethylbenzene, and Xylene. *Folia Microbiol.*, **47**, 83–93.
- Joule, J.A. (2014): Thiophenes. In: Joule, J. (eds) *Thiophenes. Topics in Heterocyclic Chemistry*, vol 39. Springer, pp. 305
- Le Mer, J., & Roger, P. (2001): Production, oxidation, emission, and consumption of methane by soils: A review. *Eur. J. Soil Biol.*, **37**, 25–50.
- Nair, A.T., Senthilnathan, J., & Nagendra, S.M.S. (2019): Emerging perspectives on VOC emissions from landfill sites: Impact on tropospheric chemistry and local air quality. *Process Saf. Environ. Prot.*, **121**, 143–154.
- Peñuelas, J., Asensio, D., Tholl, D., Wenke, K., Rosenkranz, M., Piechulla, B., & Schnitzler, J.P. (2014): Biogenic volatile emissions from the soil. *Plant, Cell Environ.*, **37**, 1866–1891.
- Randazzo, A., Asensio-Ramos, M., Melián, G.V., Venturi, S., Padrón, E., Hernández, P.A., Pérez, N.M., & Tassi, F. (2020): Volatile organic compounds (VOCs) in solid waste landfill cover soil: Chemical and isotopic composition vs. degradation processes. *Sci. Total Environ.*, **726**, 138326.
- Randazzo, A., Folino, A., Tassi, F., Tatàno, F., De Rosa, S., & Gambioli, A. (2022): Volatile organic compounds from green waste anaerobic degradation at lab-scale: evolution and comparison with landfill gas. *Detritus*, **19**, 63–74.
- Rojo, F. (2009): Degradation of alkanes by bacteria: Mini-review. *Environ. Microbiol.*, **11**, 2477–2490.
- Schäfer, H., Myronova, N., & Boden, R. (2010): Microbial degradation of dimethylsulphide and related C₁-sulphur compounds: Organisms and pathways con-

- trolling fluxes of sulphur in the biosphere. *J. Exp. Bot.*, **61**, 315-334.
- Seewald, J.S. (2001): Aqueous geochemistry of low molecular weight hydrocarbons at elevated temperatures and pressures: Constraints from mineral buffered laboratory experiments. *Geochim. Cosmochim. Acta*, **65**, 1641-1664.
- Sherwood Lollar, B., Westgate, T.D., Ward, J.A., Slater, & G.F., Lacrampe-Couloume, G. (2002): Abiogenic formation of alkanes in the earth's crust as a minor source for global hydrocarbon reservoirs. *Nature*, **416**, 522-524.
- Tang, J., Schurgers, G., & Rinnan, R. (2019): Process Understanding of Soil BVOC Fluxes in Natural Ecosystems: A Review. *Rev. Geophys.*, **57**, 966-986.
- Tassi, F., Montegrossi, G., Vaselli, O., Liccioli, C., Moretti, S., & Nisi, B. (2009): Degradation of C₂-C₁₅ volatile organic compounds in a landfill cover soil. *Sci. Total Environ.*, **407**, 4513-4525.
- Tassi, F., Montegrossi, G., Capecchiacci, F., & Vaselli, O. (2010): Origin and distribution of thiophenes and furans in gas discharges from active volcanoes and geothermal systems. *Int. J. Mol. Sci.*, **11**, 1434-1457.
- Tassi, F., Venturi, S., Cabassi, J., Capecchiacci, F., Nisi, B., & Vaselli, O. (2015a): Volatile organic compounds (VOCs) in soil gases from Solfatara crater (Campi Flegrei, southern Italy): Geogenic source(s) vs. biogeochemical processes. *Appl. Geochemistry*, **56**, 37-49.
- Tassi, F., Venturi, S., Cabassi, J., Vaselli, O., Gelli, I., Cinti, D., & Capecchiacci, F. (2015b): Biodegradation of CO₂, CH₄ and volatile organic compounds (VOCs) in soil gas from the Vicano-Cimino hydrothermal system (central Italy). *Org. Geochem.*, **86**, 81-93.
- Watkinson, R.J. & Morgan, P. (1990): Physiology of aliphatic hydrocarbon-degrading microorganisms. *Biodegradation*, **1**, 79-92.
- Weelink, S.A.B., van Eekert, M.H.A., & Stams, A.J.M. (2010): Degradation of BTEX by anaerobic bacteria: Physiology and application. *Rev. Environ. Sci. Biotechnol.*, **9**, 359-385.
- Whiticar, M.J. (1999): Carbon and hydrogen isotope systematics of bacterial formation and oxidation of methane. *Chem. Geol.*, **161**, 291-314.

Ceramic production in the *Ager Calenus* from the 3rd century BCE to early Imperial period

Maria Verde

Dipartimento di Scienze della Terra, dell'Ambiente e delle Risorse, Università di Napoli Federico II, Via Cintia 21, 80126, Napoli, Italia

DOI:10.19276/plinius.2023.01.012

INTRODUCTION AND AIM

The ancient city of Cales (modern Calvi Risorta) is located in the northern sector of the Campania region of Italy. Thanks to its geographical position Cales had an important strategic function for the Roman control of the *Ager Falernus*, the *Campus Stellatis* and the *Ager Campanus* (Pedroni, 1993; Ruffo, 2010), also known as Campania Felix thanks to the fertile soil of the *Volturnum* river that runs through the plain.

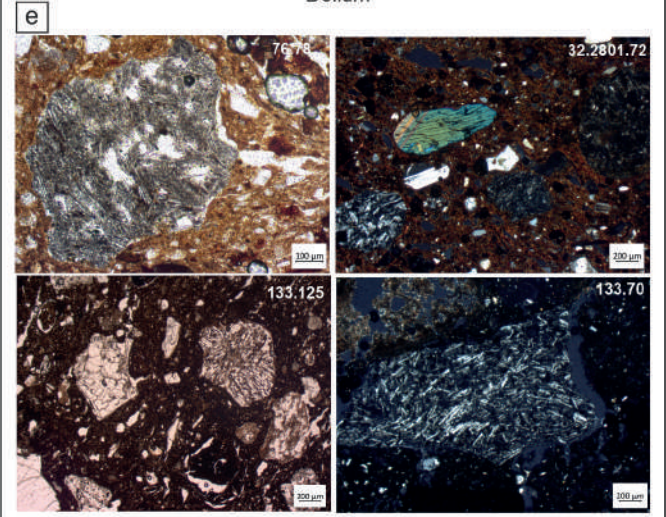
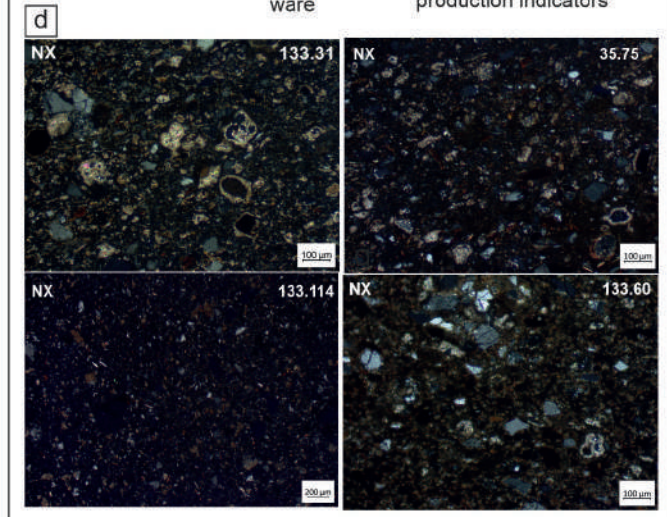
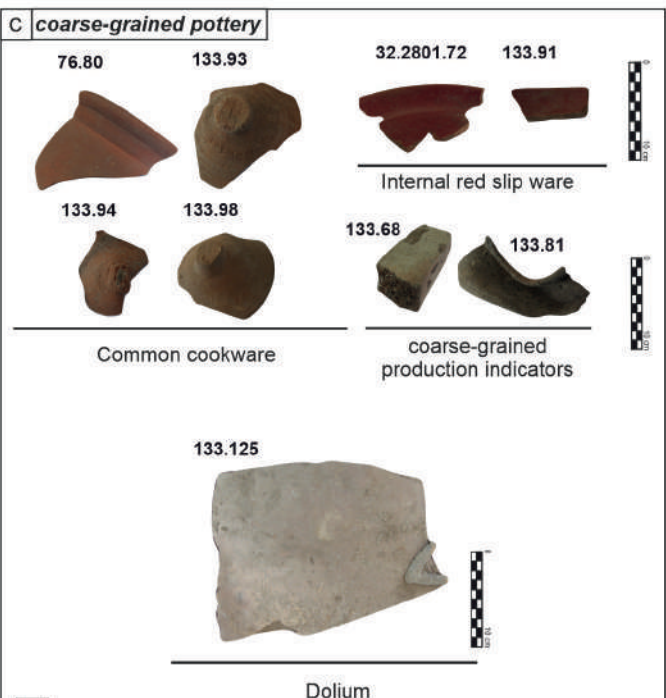
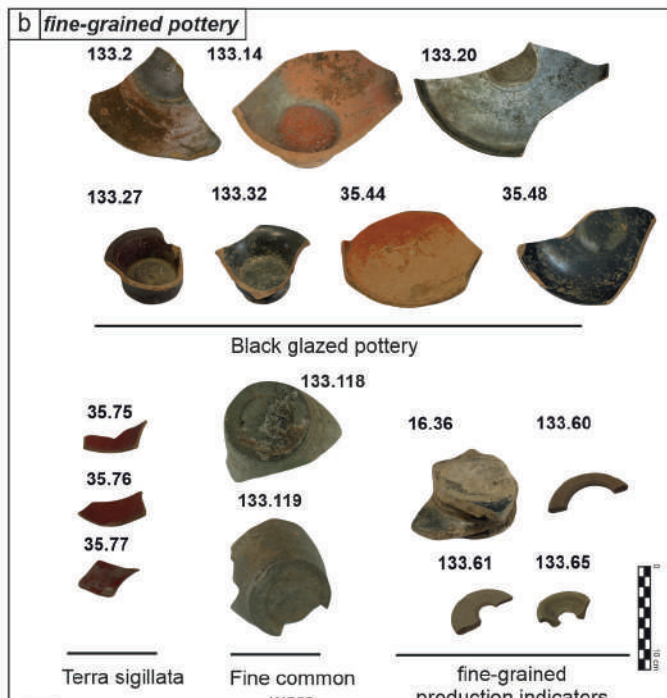
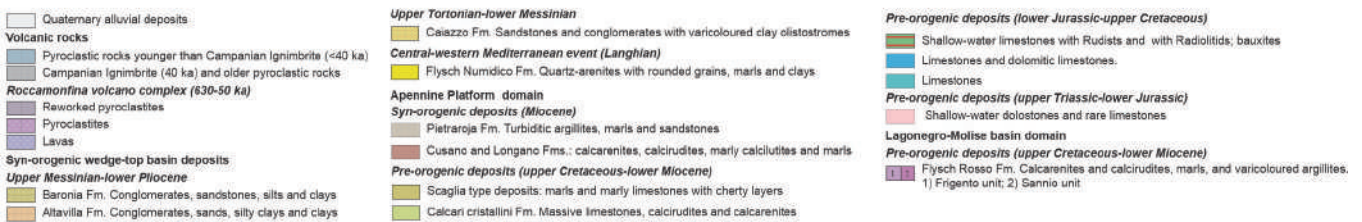
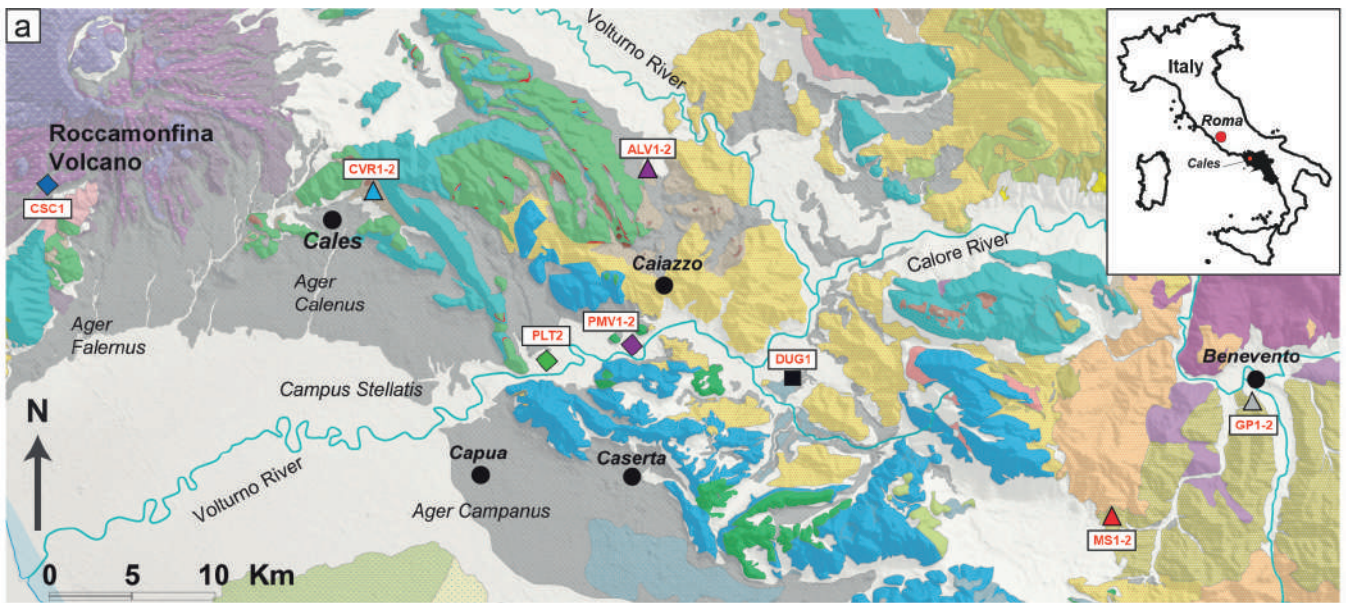
The territory of Cales is considered one of the most important production centers of fine-grained pottery, oriented towards the export of tableware. Cales was particularly renowned for its production and distribution of black glazed ware, a type of fine pottery first made in Greece in the 5th century BCE (Pedroni & Soricelli, 1996), and later in the western Mediterranean from the end of the 4th century BCE to the middle of the 1st century BCE. Following the foundation of the Roman colony in the port of *Volturnum* in 194 BCE (Pedroni, 2001), it is presumed to be connected with the long-distance export of Calenian ceramics. For centuries the black glazed pottery has been considered the hallmark of Calenian production, in particular thanks to the availability of raw materials close to the city (De Bonis et al., 2013). As a matter of fact, in such an important manufacturing center of ceramics, it is not surprising that the workshops also produced common ware, documented over a wide time span from the 3rd century BCE to the 2nd-3rd century CE. The collected data allow us to shed new light on the production activities of the Calenian workshops and document their remarkable continuity over time. The end of the production of black glazed pottery in the early imperial period does not determine the end of production activities. On the contrary, there is an adjustment to new market demands with the manufacture of Sigillata pottery and a vast production of common ware. The continuity and liveliness of production testify to the role of an important craft center that Cales continued to play in the height of the imperial period, when the different senatorial families, linked to the imperial court, continued to boost the

local economy, fitting into a market logic that managed to survive the strong economic changes that occurred during this period. The production of most of these important ceramic classes, fine-grained pottery in particular, took advantage of the presence of large outcrops of clay next to the city of Cales (De Bonis et al., 2013), which represented important sources of raw materials.

The study aims to define the local production of fine and coarse-grained pottery from the 3rd century BCE to the 2nd century CE through a minero-petrographic characterization of 125 samples. The samples include black glazed pottery, Terra sigillata, fine common ware, common cookware, internal red slip ware, thin-walled pottery imitation, and objects related to the production process. The study benefits from the comparison of important production indicators, such as wastes of black glazed pottery and common cookware, along with spacers and supports, these represent significant materials for defining with certainty the compositional features of local potteries. The study also aims to expand previous knowledge on these important ceramic classes, through comparison with other fine ceramics found in the same context. Indeed, for the first time, three isotopic systematics were used to perform provenance studies, Sr-Nd and Pb respectively. This pioneering approach allowed us to understand the existing relationships between raw material and finished products. In the light of this, some Campanian clay raw materials Ca-rich and Ca-poor, well known in the literature, were selected and compared to the ceramics under study. This approach highlights the importance of combining geochemical data to identify sources of raw materials and gave us back encouraging results that strengthening the previously experimental study, providing further confirmation of the validity of the method.

GEOLOGICAL SETTING

Cales is located on the northern edge of the Campanian plain, right between the Roccamonfina volcano and the Trebulani mountains belonging to the carbonate pla-



(◀ previous page) **Figure 1 a)** geological sketch map of the investigated area; **b)** macroscopic fragments of fine-grained pottery; **c)** macroscopic fragments of coarse-grained pottery; **d)** Thin-sections of fine-grained pottery; **e)** thin-sections of coarse-grained pottery. crossed polars; Nil=parallel polars

tform succession that forms the Matese, Maggiore, and Camposauro mountain ridges (Fig. 1a; Bonardi et al., 2009). Just north of Cales, extensive clay deposits crop out on the Trebulani mountains slopes. These clay sediments belong to the Pietraraja foredeep succession of the Middle-Upper Tortonian (Fig. 1a) and were utilized until recently to make bricks (Guarino et al., 2011).

Just west of Cales there is the Roccamonfina volcano, which is a stratovolcano characterized by pyroclastic rocks and lavas erupted during three periods of activity that led to the formation of an apical central caldera and sector collapses (Rouchon et al., 2008). The pre-caldera stage is characterized by ultrapotassic leucite-bearing rocks with geochemical characteristics akin to those of the Roman volcanic province (Peccerillo, 2017). Products following the major sector collapse (ca. 400 ka) are mostly shoshonitic rocks erupted from cinder cones and domes located within the caldera and on the pre-caldera outer flanks of the volcano (Conticelli et al., 2009).

In a vast territory around Cales, volcanic deposits also belong to the two high-magnitude eruptions of the Phlegraean fields, which mostly produced trachytes ascribed to the potassium series (KS) of shoshonitic affinity (Conticelli et al., 2004). The most intense and older eruption is that of the Campanian Ignimbrite, which occurred ca. 40 ka before the present (Giaccio et al., 2017). This eruption emplaced huge pyroclastic flows that reached the territory of Cales and a large part of the inner Campania region. The second eruption is that of the Neapolitan Yellow Tuff (ca. 15 ka; Galli et al., 2017) which is represented in the area of Cales only by incoherent deposits.

MATERIAL AND METHODS

The study has focused on 125 samples of different ceramic classes (Fig. 1b,c) discovered during the excavations carried out at the so-called Arx of Cales by the Soprintendenza in 2007. The wide variety of selected material can be divided into two major groups based on inclusions grain size: fine (Fig. 1b) and coarse-grained pottery (Fig. 1c).

On all samples a mineralogical-petrographic characterization via a multi-analytical approach was carried out.

The color of the ceramic bodies was evaluated visually using the Munsell Soil Colour Chart. Hardness was assessed using the Williams hardness test (Williams, 1990).

Polarized light microscopy (PLM) in thin section was used to investigate the textural and petrographic features of ceramic pastes with an OPTIKA V-600 POL microscope and a ZEISS AxioCam 105 color camera (ZEN 2.3 Lite software) for capturing the images.

The mineralogical composition was determined via X-ray powder diffraction (XRPD) on random powder

samples with a PANalytical X'Pert PRO 3040/60 PW diffractometer (CuK α generator operating at 40 kV, 40 mA, at a scanning interval from 4 to 50° 2 θ , step interval of 0.017°2 θ , a step counting time 66 s).

Microstructural observations of fresh fracture surfaces were conducted using a Zeiss Merlin VP Compact FE-SEM (Field Emission Scanning Electron Microscopy).

Quantitative Microchemical Analyses were performed on Polished thin sections of the ceramic bodies, coated with carbon, using FESEM equipped with an energy-dispersive X-ray spectrometer (EDS) and Oxford Instruments Microanalysis Unit (X Max 50 EDS detector). Data were processed with the INCA Xstream pulse processor. Mineral standards and the precision/accuracy of the EDS analyses were described in previous publications (Rispoli et al., 2019).

The chemical composition of the samples was analyzed using XRF (X-ray fluorescence) on pressed powder pellets. An AXIOS PANalytical Instrument was used for this analysis. The concentration of 10 major oxides (SiO₂, TiO₂, Al₂O₃, Fe₂O₃, MnO, MgO, CaO, Na₂O, K₂O, P₂O₅ in wt%) and 10 trace elements (Rb, Sr, Y, Zr, Nb, Ba, Cr, Ni, Sc, V in ppm) were determined. The analytical uncertainty for major elements was 1–2%, and for trace elements was 5–10% (Cucciniello et al., 2017).

The routine analytical techniques described above were completed implementing a new geochemical approach using TIMS (Thermal Ionization Mass Spectrometry) and MC-ICP-MS (Multi Collector - Inductively Coupled Plasma - Mass Spectrometer), which includes for the first time three isotopic systematics: Sr, Nd and Pb. This method provided stronger feedback both in terms of provenance and clay-temper processing.

RESULTS AND DISCUSSION

Fine-grained pottery

Thin section analyses showed that almost all the samples had an optically inactive matrix; in some cases a diffuse birefringence was visible in the matrix due to secondary calcite.

From a textural point of view, the 79 ceramic samples analyzed are extremely fine. The size of the inclusions is generally less than 200 μ m and the type of phases present is consistent in all samples. The presence of feldspars, extremely abundant calcite, very small quartz crystals, sporadic mica, lithic fragments of both sedimentary (carbonatic fragments) and volcanic nature (fragments of trachyte >200 μ m, and sometimes even fossil fragments) were recognized (Fig. 1d).

Mineralogical analysis shows that quartz is the most abundant phase in all the samples analyzed, along with

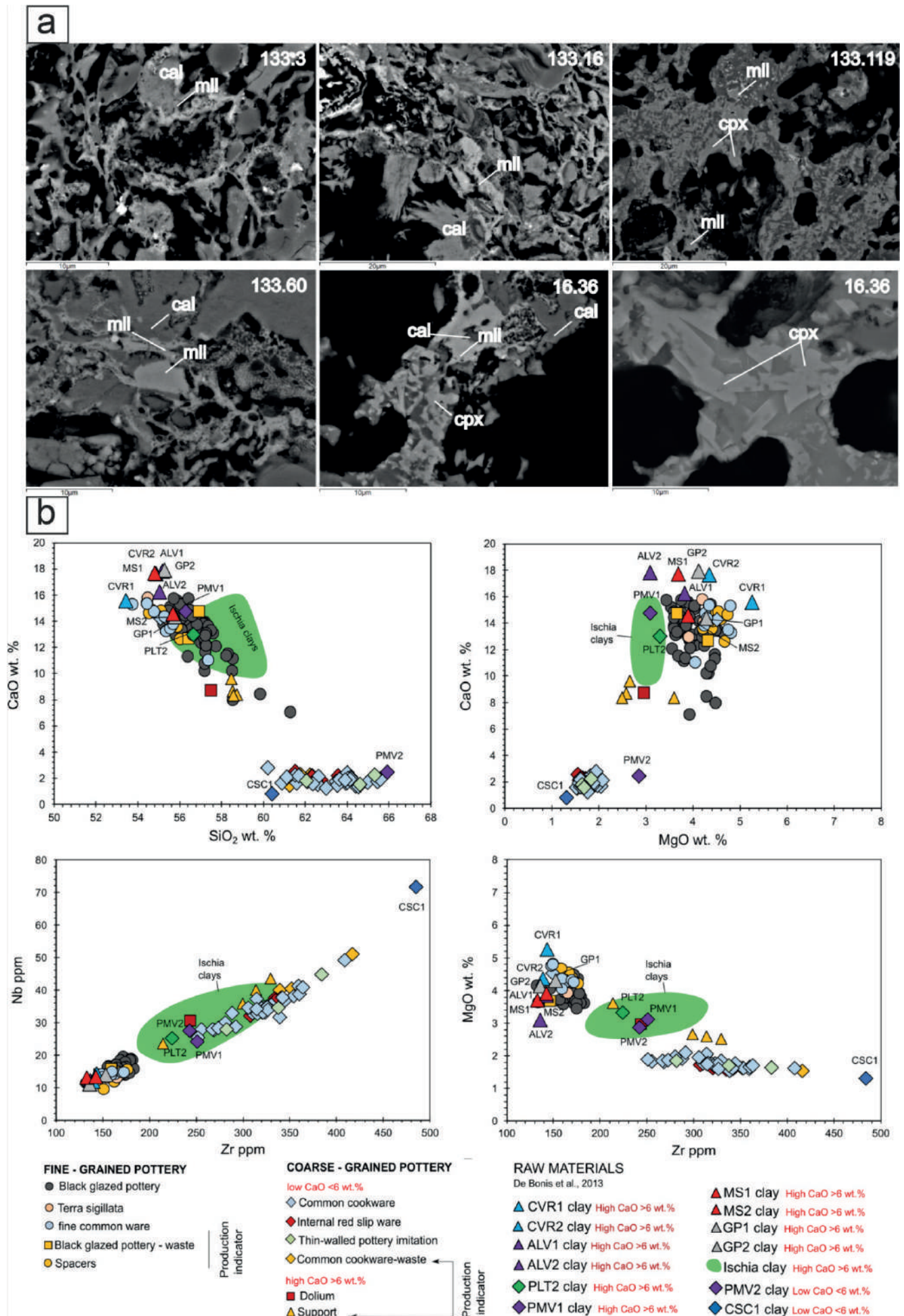


Figure 2 a) Backscattered electron images of polished surfaces. Abbreviation according to Whitney & Evans, 2010: cal = calcite; mll = melilite; cpx = clinopyroxene. b) XRF binary diagrams with major oxides (wt%) and trace elements (ppm) for fine- and coarse-grained pottery, compared with Ca-rich and Ca-poor clay raw material from the Campania region

frequent feldspar, calcite, and traces of mica. Neofromed pyroxene and gehlenite (Fig. 2a) were detected in all samples. These Ca-silicates formed over firing at specific temperatures are used to estimate the EFTs (Equivalent Firing Temperatures). These ranges from 850 and 1050°C, with some exceptions. In particular, sample 35.44 has lower firing temperatures (< 850) due to the presence of phyllosilicates and the absence of newly formed Ca-silicates.

The chemical analysis shows that all the samples are characterized by a calcareous composition of the ceramic body along with a very homogeneous chemical composition (Fig. 2b). The production indicator (16.36) is in line with the chemical composition of the other samples analyzed. In the chemical binary diagrams the ceramic samples were also compared to some Ca-rich clay raw materials from the deposits most likely exploited in the past in the surroundings of Cales (data from De Bonis et al., 2013). From this comparison, the 79 samples of fine-grained pottery show a greater affinity with the Mio-Pliocene marine clay sediments of the Apennine chain sector, among which the local clay samples (CVR) also fall.

The efficiency of Pb isotopes for determining different sources of raw materials was already tested by several authors (e.g., Carter et al., 2011; Makarona et al., 2014; Renson et al., 2013), by comparing different geological materials (from bedrocks to their weathered products) to pottery sherds. The results show a good geochemical affinity with the Mio-Pliocene basin clays of the Apennine chain sector.

For Sr and Nd isotope ratios the local clay (CVR) and a volcanic temper from the area were considered for comparison. All the ceramic samples of glazed pottery, Terra sigillata, fine common ware and the production indicators (wasters of black glazed pottery and spacers) are very close to the local clay raw material. This is an interesting point, in fact the considered ceramic classes are fine-grained and the use of sporadic volcanic temper does not induce any meaningful changes in the isotopic signature as already demonstrated in experimental study by De Bonis et al. (2018). In the same way, the isotopes ratio of the production indicators follow the same behavior of the ceramics. The isotopic fingerprint allows us to define with great approximation the validity of the method as a support of the usual analytical routine used for the archaeometric characterization and the definition of the origin of the possible sources of supply of raw material used for these artifacts.

Coarse-grained pottery

Samples belonging to the investigated classes show very homogeneous macroscopic and petrographic features. The arrangement of aplastic inclusions is characterized by a bimodal distribution, where a fine (generally < 50 µm) and a coarse (generally > 200 µm) fraction are

recognizable (Fig. 1e). The coarse fraction is mainly formed of feldspar, clinopyroxene, prevailing volcanic lithics, juvenile fragments represented by pumices and glass shards, with a composition consistent with products of the Roccamonfina volcano and other Plio-Quaternary volcanic complexes (i.e., Phlegraean fields) of the Tyrrhenian border. The fine fraction mainly contains quartz and mica. This led us to hypothesize that a coarse volcanic-bearing temper was added to a clay body containing a tiny siliciclastic natural skeleton to improve the physical properties of the ceramic body, especially for cookwares that had to stand thermal shocks during their use (De Bonis et al., 2014 and reference therein)

The chemical composition of the investigated samples shows a narrow variability among samples of common cookware, internal red slip ware, thin-walled pottery imitation, and wasters of common cookware, thus reasonably suggesting that the same raw material was employed for their manufacture. On the contrary, the high concentration of calcium oxides in the supports and the dolium suggests that a different clay raw material was employed.

To establish their local origin, the pottery samples were compared with raw materials Ca-poor and Ca-rich (Fig. 2b; data from De Bonis et al., 2013). Taking into account all the results of this comparison, the Ca-poor wares represented by common cookware, internal red slip ware, thin-walled pottery imitation show a greater affinity with the alluvial clays from the Volturnum river plain in the locality of Piana di Monte Verna (PMV2). This confirms the use of alluvial raw materials from the Volturnum river plain, as already verified in the production of Alife (Grifa et al., 2015), an ancient town not so far from Cales. On the other hand, samples of supports and the dolium have a Ca-rich character and show a greater affinity with the alluvial clays from the Volturnum river plain from Piana di Monte Verna (PMV1) and Pontelatone (PLT2). This result highlights that alluvial clays from the surrounding area (i.e., Volturnum river plain) could represent the raw material used for coarse-grained ceramic objects.

These sources also differ from those used for the fine ware production at Cales (3rd and the 1st century BCE), for which the local marine clay from the Calvi Risorta outcrop was preferred (Guarino et al., 2011), likely for its better technological performances (natural refined material and sintering attitude) for manufacturing fine pottery (De Bonis et al., 2013). The difference between the considered alluvial and marine clays is provided by the presence of planktonic foraminifers in marine clays, which also occur in fine ware (Verde et al., 2023).

As already shown for the fine-grained pottery, in order to define the origin of ancient ceramics, the determination of Sr, Nd and Pb isotopes ratio was applied.

As far as the Pb isotope ratios are concerned, they confirm the geochemical affinity with the alluvial clays from

the Volturnum river plain from Piana di Monte Verna (PMV1-2) and Pontelatone (PLT2).

For Sr-Nd isotopes we taken into account as comparison materials the Alluvial clays from the Volturnum river plain in the locality of Piana di Monte Verna (PMV1-2) and a local volcanic temper (DUG1). The results are very encouraging because, as already observed for fine-grained pottery, valuable information on the origin of the raw material was obtained. In fact, the analyzed pottery have a composition that indicates the use of Ca-rich PMV1, PLT2) and Ca-poor (PMV2) from the Voltorno floodplain. In addition, the influence of the volcanic inclusions on the isotopic fingerprint is well detectable and can be used to predict the temper-clay ratio.

CONCLUSION

The archaeometric characterization of the fine-grained pottery revealed a remarkable homogeneity within the different ceramic classes, including black glazed pottery, Terra sigillata, fine common wares, and production indicators. The production indicators, such as spacers and welded pieces of black glazed pottery, played a significant role in identifying local ceramic production due to their historical importance.

The petrographic analysis showed an extreme compositional homogeneity of all the finds belonging to the different ceramic classes along with same mineralogical assemblage.

The chemical analysis indicates that all samples are characterized by high concentrations of CaO which is compatible with the use of a local clay raw material from the Apennine chain sector. This conclusion was further supported by geochemical analysis using three different isotopic systems: Sr, Nd, and Pb. These isotopic analyses helped distinguish different ceramic productions and identify the specific sources of the raw materials. The isotopic "fingerprint" of the fine-grained pottery aligned closely with the clay raw material used, indicating a negligible manipulation of the starting clay.

From a technological point of view, the samples exhibit an extreme variability of the EFTs (from 750 to 1050°C). The presence of hematite suggested that an oxidizing atmosphere predominated during firing, with a brief reducing phase potentially employed for blackening the coating of the black glazed pottery.

As far as the coarse-grained pottery is concerned, the set of techniques used for the archaeometric characterization showed the compositional homogeneity between the common cookware, internal red slip ware, thin-walled pottery imitation, including the production indicators. The latter are represented by wastes of common cookware that provided a great contribution to the definition of a local production of coarse pottery.

The chemical analysis highlights that common cookwares, internal red slip ware, thin-walled pottery imitation

and wastes of common cookware are characterized by Ca-poor character, compatible with the use of an Alluvial clay raw material from the Volturnum river plain with similar features with the alluvial clay of Piana di Monte Verna (PMV2). On the other hand, the supports and the dolium are characterized by Ca-rich character, compatible with the use of an Alluvial clay raw material from the Volturnum river plain with similar features with the alluvial clay of Piana di Monte Verna but collected in a level with higher CaO values (PMV1) and Pontelatone (PLT2). These affinities were closely confirmed by isotopic analysis of Sr, Nd and Pb isotopes.

As observed for fine-grained pottery, the use of three different isotope systems is a valuable tool for investigating the provenance of ceramics, even when considering and expecting the addition of temper to reduce plasticity, in particular for the coarse-grained pottery production. In this regard, the method allowed us not only to discriminate the origin of the raw material, but also to be able to define its mix design (temper-clay ratio).

This pioneering approach is not intended to replace traditional methods for characterizing archaeological ceramics, but rather to provide more support to the normal analytical routine used for provenance studies.

From a technological point of view, the samples of coarse-grained pottery fired at temperatures varying from 750 to 950°C in a prevailing oxidizing atmosphere. Production indicators clearly show higher temperatures than those of other investigated ceramic classes, occasionally exceeding 1000°C.

REFERENCES

- Bonardi, G., Ciarcia, S., Di Nocera, S., Matano, F., Sgrosso, I., & Torre, M. (2009): Carta delle principali Unità Cinematiche dell'Appennino meridionale. Nota illustrativa. *Ital. J. Geosci.*, 128, 47-60, Scale 1:250,000, 1 sheet.
- Carter, S.W., Wiegand, B., Mahood, G.A., Dudas, F.O., Wooden, J.L., Sullivan, A.P., & Bowering, S.A., (2011): Strontium isotopic evidence for prehistoric transport of grayware ceramic materials in the eastern Grand Canyon region, USA. *Geoarchaeology* **26**, 189-218
- Corticelli, S., Marchionni, S., Rosa, D., Giordano, G., Boari, E., & Avanzinelli, R. (2009): Shoshonite and sub-alkaline magmas from an ultrapotassic volcano: Sr-Nd-Pb isotope data on the roccamonfina volcanic rocks, Roman Magmatic Province, southern Italy. *Contrib. Mineral. Petr.*, **157**, 41- 63.
- Corticelli, S., Melluso, L., Perini, G., Avanzinelli, R., & Boari, E., (2004): Petrologic, geochemical and isotopic characteristics of shoshonitic to potassic and ultrapotassic alkalic magmatism in central-southern Italy: inferences on its genesis and on the nature of its mantle source. *Period. Mineral.* **73**, 135-164.
- Cucciniello, C., Melluso, L., le Roex, A.P., Jourdan, F., Mor-

- ra, V., de Gennaro, R., & Grifa, C. (2017): From nepheline, basanite and basalt to peralkaline trachyphonolite and comendite in the Ankaratra volcanic complex, Madagascar: $^{40}\text{Ar}/^{39}\text{Ar}$ ages, phase compositions and bulk-rock geochemical and isotopic evolution. *Lithos*, **274-275**, 363-382.
- De Bonis, A., Grifa, C., Cultrone, G., De Vita, P., Langella, A., & Morra, V. (2013): Raw Materials for Archaeological Pottery from the Campania Region of Italy: A Petrophysical Characterization. *Geoarchaeology*, **28**, 478-503.
- De Bonis, A., Cultrone, G., Grifa, C., Langella, A., & Morra, V. (2014): Clays from the Bay of Naples (Italy): New insight on ancient and traditional ceramics. *J. Eur. Ceram. Soc.* **34**, 3229-3244.
- De Bonis, A., Arienzo, I., D'Antonio, M., Franciosi, L., Geminario, C., Grifa, C., Guarino, V., Langella, A., & Morra, V., (2018): Sr-Nd isotopic fingerprinting as a tool for ceramic provenance: its application on raw materials, ceramic replicas and ancient pottery. *J. Archaeol. Sci.* **94**, 51-59.
- Galli, P., Giaccio, B., Messina, P., Peronace, E., Amato, V., Naso, G., Nomade, S., Pereira, E., Piscitelli, S., Bellanova, J., Billi, A., Blamart, D., Galderisi, A., Giocoli, A., Stabile, T., & Thil, F. (2017): Middle to Late Pleistocene activity of the northern Matese fault system (southern Apennines, Italy). *Tectonophysics*, **699**, 61-81.
- Giaccio, B., Hajdas, I., Isaia, R., Deino, A., & Nomade, S. (2017): High-precision ^{14}C and $^{40}\text{Ar}/^{39}\text{Ar}$ dating of the Campanian Ignimbrite (Y-5) reconciles the time-scales of climatic-cultural processes at 40 ka. *Sci. Rep.*, **7(1)**, 1-10.
- Guarino, V., De Bonis, A., Grifa, C., Langella, A., Morra, V., & Pedroni, L. (2011): Archaeometric study on terra sigillata from Cales (Italy). *Period. Mineral.*, **80**, 455-470.
- Makarona, C., Nys, K., & Claeys, P., (2014): Sr isotope analysis for the provenance study of ancient ceramics: an integrated approach. In: Scott, R.B., Braekmans, D., Carremans, M., & Degryse, P. (Eds.), *Proceedings of the 39th International Symposium for Archaeometry*, ISA 2012, Leuven (Belgium), pp. 149-156.
- Peccerillo, A., (2017): The Roman Province, in: Peccerillo, A. (Ed.), *Cenozoic Volcanism in the Tyrrhenian Sea Region. Advances in Volcanology*. Second ed., Springer, New York, USA, pp. 399-pp. 81-124.
- Pedroni, L. (1993): Problemi di topografia e urbanistica calena. *Samnium*, **66**, 208-230.
- Pedroni, L. (2001): Ceramica calena a vernice nera. Produzione e diffusione. Napoli, IT: Petrucci Editore.
- Pedroni, L., & Soricelli, G. (1996): Terra Sigillata da Cales. *Archeologia Classica*, **48**, 180-188.
- Renson, V., Jacobs, A., Coenaerts, J., Mattielli, N., Nys, K., & Claeys, Ph. (2013): Using lead isotopes to determine pottery provenance in Cyprus: Clay source Signatures and comparison with Late Bronze Age Cypriote pottery. *Geoarchaeology*, **28(6)**, 517-530.
- Rispoli, C., De Bonis, A., Guarino, V., Graziano, S.F., Di Benedetto, C., Esposito, R., Morra, V., & Cappelletti, P. (2019): The ancient pozzolanitic 154 mortars of the Thermal complex of Baia (Campi Flegrei, Italy). *J. Cult. Herit.* **40**, 143-154.
- Rouchon, V., Gillot, P.Y., Quidelleur, X., Chiesa, S., & Floris, B., (2008): Temporal evolution of the Roccamonfina volcanic complex (Pleistocene), Central Italy. *J. Volcanol. Geotherm. Res.*, **177**, 500-514.
- Ruffo, F. (2010): La Campania antica. Appunti di storia e di topografia. Parte I dal Massico-Roccamonfina al Somma-Vesuvio. (Vol. 1,). Il Denaro Libri. Napoli, pp. 9-336.
- Verde, M., De Bonis, A., Tomeo, A., Renson, V., Geminario, C., D'Uva, F., Rispoli, C. & Morra, V. (2023): Differently Calenian: A multi-analytical approach for the characterization of coarse ware from Cales (South Italy). *J. Archaeol. Sci. Rep.*, **49**, 103941.
- Williams, D.F. (1990): The study of ancient ceramics: the contribution of the petrographic method. In: T. Mannoni, & A. Molinari (Eds.), *Scienze in archeologia. Quaderni del Dipartimento di Archeologia e Storia delle Arti*; Università di Siena, All'insegna del Giglio, Firenze, pp. 43-64.

BeGEO Extended Abstract

111 | Scanu et alii | North African amphorae from Cumae. *Mineralogical-petrographic analysis for the provenance of North African amphorae from Cumae (South-Italy)*

North African amphorae from Cumae

Mineralogical-petrographic analysis for the provenance of North African amphorae from Cumae (South-Italy)

Michela Scanu¹, Carmela Capaldi¹, Antonella Ciotola¹, Francesco D'Uva², Maria Verde², Alberto De Bonis^{2,3}

¹Dipartimento di Studi Umanistici, Università degli Studi di Napoli Federico II, via Porta di Massa, 1, Napoli, Italia

²Dipartimento di Scienze della Terra, dell'Ambiente e delle Risorse (DiSTAR), Università degli Studi di Napoli Federico II, via Vicinale Cupa Cintia, 26, Napoli, Italia

³CRACS, Center for Research on Archaeometry and Conservation Science, Complesso Universitario di Monte Sant'Angelo, via Vicinale Cupa Cintia, 26, Napoli, Italia

DOI:10.19276/plinius.2023.02.001

INTRODUCTION

The target of this work is a selected sample of African amphorae found in the Forum of Cumae, which were examined in order to define their precise areas of origin.

This work is a preliminary analysis that aims to define the trade that the ancient city of Cumae had with North Africa. The samples were analyzed with a mineralogical-petrographic method, as well as a previous archaeological study.

The regions involved in amphoras production are Zeugitania and Byzacena, located in the south-central Tunisia, Tripolitania, located between southern Tunisia and western Libya, and *Mauretania Caesarensis*, located between Morocco and Algeria (Fig. 1a). These regions were also known for the production of other items, including cooking and fine ware (Bonifay, 2004). With the aim of defining the precise areas of production, nineteen samples of amphorae were selected from the most common types at the Cumae site, dated from the 2nd to the 6th centuries CE.

In this period, the trade with the North African regions became more intense and frequent, because of the crisis in the local trade, which led to a change in the trading system: from the provinces to Rome. North African amphorae are known to have carried liquid goods, such as high-quality oil, *garum* and fish sauces, with the occasional association of wine, which is restricted to a few defined types: Dressel 30 and Africana III (Di Giovanni, 2010; Rizzo, 2018).

From the 3rd century CE onward, the trade from North Africa became more and more dense, to the stage of almost total control of the markets. Due in part to the fact that the North African peoples experienced no internal crises, as had been the case in western regions, and due to their enduring prosperity given by agriculture based on settler *families* living in villages (Rizzo, 2014).

The Forum of Cumae

This area, located in the lower part of the city, is the center of political and commercial activities. It has been

investigated with archaeological survey and excavations since 1994, with the Kyme project, that involves the Soprintendenza Archeologica di Napoli e Caserta, the University of Naples Federico II, the University of Naples "L'Orientale" and the *Centre Jean Berard* (Capaldi, 2021).

The Forum area (Fig. 1b) in the roman period was surrounded by a double-order *portico*, with Doric order columns at the bottom and Ionic order columns at the top. It was decorated with stone theatrical masks on the eastern side and with stacks of weapons on the western side (Capaldi, 2016). Behind the arcade of the *portico*, there were places used for commerce and craft activities, known as *tabernae* (Gasparri, 2008, 2009). The forum was dominated by the main temple on a high podium, the *Capitolium*, from the Flavian era, located on the western side and dedicated to the Capitoline triad (Gasparri, 2008). Another major temple is the one incorporated in the building known as the "*Masseria del Gigante*," built in the classic *porticus triplex* pattern, it is devoted to *Divus Vespasianus* (Gasparri, 2008, 2009).

Geological setting

North Africa is an area affected by a long history of transformations, both geopolitical and geological. Geologically, Africa is divided into two zones separated by the Southern Atlassic Front: the first is the mountainous zone bearing the imprint of Alpine tectonics, consisting of Cenozoic sedimentary tectonics; the second is the Saharan region, consisting of a Precambrian basement with a Phanerozoic sedimentary cover (Capelli-Bonifay, 2014; Gallala et al., 2009).

Sedimentary rocks are dominant in North Africa (especially in the Tunisian area), but they are not the only features of the entire area: metamorphic rocks are widespread on the coast of Algeria (Baghdad et al., 2017), and in Libya volcanic rocks are present, albeit in smaller percentages. Some areas of North Africa then show similar lithology, having a similar geologic history, as well as can find even driven similarities with deposits scattered throughout the Mediterranean (an example is north-cen-

tral Sicily).

THE ARCHAEOLOGICAL MATERIALS AND ANALYTICAL METHODS

The materials examined are the result of an archaeological type sampling. The nineteen amphora samples were selected as representative among the African amphorae found at the Cumae site in the excavation campaigns between 1994 and 2018. Seven types of amphoras were selected (Fig. 1c).

North African amphorae consistently turn out to be the most attested type at Cumae, in line with the trade situation.

The Macroscopic analysis of the ceramic body was performed with a precision lense (30X) to determine a visual comparison between the colours (compared with the Munsell Soil Colour Chart) and the hardness (Cuomo di Caprio, 2007).

The archaeometric investigation was performed via mineralogical-petrographic techniques.

Polarized light microscopy (PLM) in thin section was used to investigate the textural and petrographic features of ceramic pastes with an OPTIKA V-600 POL microscope and a ZEISS Axiocam 105 color camera (ZEN 2.3 Lite software) for capturing the images (Terry-Chilingar, 1995; Quinn, 2013).

X-ray Powder Diffraction (XRPD) was used to determine the bulk mineralogical composition of samples on random powders. A diffractometer PANalytical X'Pert PRO 3040/60 PW, equipped with a CuK α generator operating at 40 kV, 40 mA, was used for measuring the samples at a scanning interval from 4-70° 2 θ (step interval of 0.020° 2 θ , a step counting time 120 s, with RTMS X'Cellerator detector). The mineral standards used are reported in Guarino et al. (2019) and Franciosi et al. (2019); precision and accuracy of EDS analyses are reported in Rispoli et al. (2019).

X-ray fluorescence spectrometry (XRF), performed with an AXIOS PANalytical Instrument (Malvern Panalytical Ltd., Marvel, UK), on pressed powder pellets was used to analyze the bulk chemical composition of the samples, expressed by the concentration of 10 major oxides (SiO₂, TiO₂, Al₂O₃, Fe₂O₃, MnO, MgO, CaO, Na₂O, K₂O, P₂O₅ in wt%) and 10 trace elements (Rb, Sr, Y, Zr, Nb, Ba, Cr, Ni, Sc, V in ppm). The analytical uncertainty was of 1-2 % for the major elements and 5-10 % for trace elements (Cucciniello et al., 2017). The standards employed are described in Guarino et al. (2021).

RESULTS AND DISCUSSION

The colors of the pastes vary from bright red tending to dark orange (Munsell 10R3/10 and Munsell 10R4/10), to dark orange-yellowish (Munsell 2.5YR5/10 and Munsell 10YR7/8). A group of amphorae with two-tone paste,

bright red and gray, stands out (Munsell 10R4/10 and Munsell 10R3/2).

The pastes are mostly coarse, with quartz inclusions visible even with only a precision lens. Samples with finer textured pastes are also present, which do not show large enough inclusions to be easily observed at the lense.

Polarized light microscopy (PLM) highlights two different groups (Fig. 1.d) of samples and some outliers according to their petrographic composition, which shows affinity with the geological features of the supposed area of production. The first group presents a coarse paste, with mostly inactive matrix, composed of not very well sorted inclusions of quartz, both rounded and angular, of large size, followed by inclusions of calcite, probably microfossils not always identifiable, and sporadic pyroxene; the second group shows a finer paste, with matrix maintaining traces of optical activity, and well sorted inclusions of smaller quartz (even 200 μ m); absent almost entirely are calcite and microfossils. Four outlier samples are also identified, for their unique characteristics.

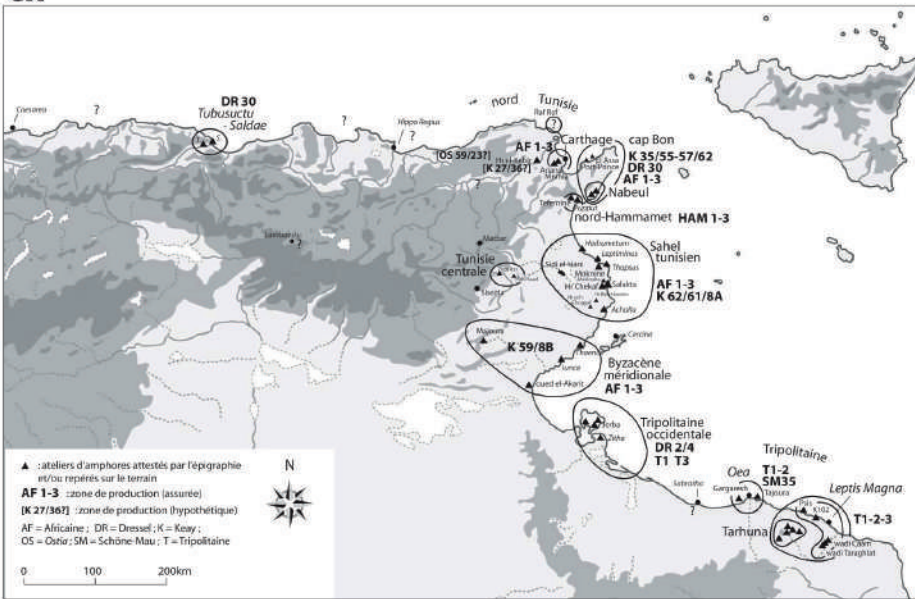
X-ray powder diffraction (XRPD) revealed, consistent with petrographic analyses, quartz as the most abundant mineralogical phase in all samples. Great homogeneity with thin section observations is also found for calcite: for samples showing abundant calcite in diffractograms, the presence of microcrystalline calcite inclusions and microfossils is equally visible in thin section. Slight diffuse presence of feldspar was also identified, found in thin section (with sporadic feldspar crystals). Pyroxene, found in thin section, was also found in mineralogical analysis, except for seven samples, which show in diffractograms this mineralogical phase, not visible in thin section. Therefore, pyroxene in these specimens is identified as a neoformed mineralogical phase.

XRPD also shows in most samples other neoformed phases represented by hematite and gehlenite. Residual clay minerals represented by illite/mica was also detected in most of the samples.

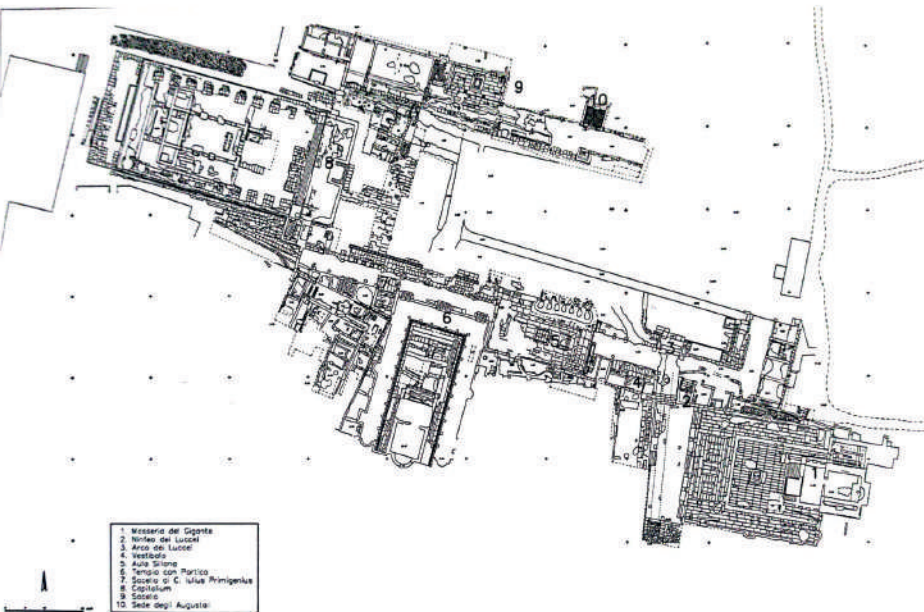
The X-ray fluorescence (XRF) chemical analysis shows high average values in SiO₂, Al₂O₃, Fe₂O₃, and lower values in MgO, K₂O, Na₂O. The majority of samples also have high concentrations of CaO (> 6 wt%); only three samples are low in CaO (with a CaO concentration of \leq 5 wt%).

Thanks to the color of the ceramic body and the mineralogical-petrographic characteristics provided by archaeometric analysis, it was possible to identify the firing atmosphere and relative temperatures, based on the presence or absence of particular mineralogical phases. Therefore, the temperature is estimated to range from a minimum of 800°C to a maximum of 950°C (Maritan et al., 2006; Cultrone et al., 2001; Nodari et al., 2007.). With mostly oxidant firing atmosphere, only three samples show characteristics of a reducing atmosphere at

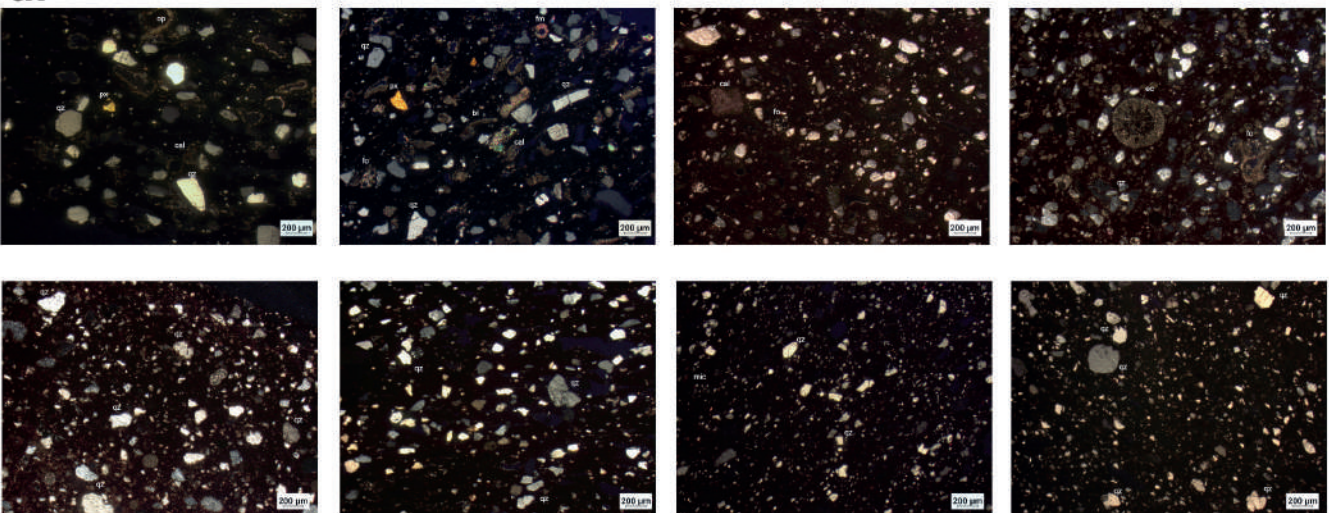
a.



b.



d.



c.



Figure 1 a) Main production areas of African amphorae; b) Chart of the Forum of Cumae; c) Seven archaeological types of the amphorae examined; d) Thin-section photographs

the beginning of the firing process and oxidizing at the end (Molera et al., 1998; Maritan et al., 2006).

CONCLUSIONS

The study of the technological characteristics showed the wide use of the oxidizing atmosphere during firing in the kiln; a fact derived from the paste color, between red and orange, of the majority of the samples. Only three samples (AA101, AA107 and AA108) deviate from this by presenting a two-tone paste: with sandwich coloring, with dark gray core and outer sections in red (black core). This highlights a particular firing atmosphere: started with reducing process and ended with oxidizing atmosphere (Molera et al., 1998; Maritan et al., 2006; De Bonis et al., 2017).

The estimation of firing temperatures was possible through the joint analysis of petrographic, mineralogical and chemical results. These analysis showed a predilection for high firing temperatures and high CaO clays. The estimated temperatures were between 850°C and 950°C (for AA102, AA107, AA108, AA111) and between 900°C and 1050°C (for AA101, AA103, AA104, AA110, AA112, AA115 and AA116). Only samples AA100, AA106, AA117 and AA118 show lower temperatures (Cultrone et al., 2001; De Bonis et al., 2014).

As for the low CaO samples, AA113 and AA114 show high firing temperatures (between 900°C and 1000°C), while AA105 shows lower temperatures (between 700°C and 750°C).

The study concerning the provenance of the samples was carried out by comparison with previous literature, either by considering the mineralogical-petrographic studies of Capelli and Bonifay (Capelli-Bonifay, 2016; Capelli-Bonifay et al., 2016), or by attempting a comparison with local clays through data found in specific publications on the study of North African sediments.

It was possible to define the provenance of the samples examined from four defined areas of North Africa: the *Mauretania Caesarensis* (present-day Algeria), Zeugitania (north-central Tunisia), Byzacena (south-central Tunisia) and Tripolitania (between southern Tunisia and Libya).

The types examined in the nineteen samples analyzed demonstrated a provenance of amphorae consistent with the archaeological literature; delineating a presence at the site of Cumae of African amphorae not only from Byzacena (thus from the producing area gravitating around the port of Hadrumentum), but also from Zeugitania (Africana I, Africana II, Africana III, and Ostia XXIII), Tripolitania (Tripolitana III and Dressel 2-4 North African), and the Algerian coast (Keay Ib).

REFERENCES

Baghdad, A., Bouazi, R., Bouftouha, Y., Bouabsa, & L.,

Fagel, N. (2017): Mineralogical characterization of Neogene clay areas from the Jijel basin for ceramic purposes (NE Algeria - Africa), *Appl. Clay Sci.*, **136**, 176-183.

Bonifay, M. (2004): Etudes sur la céramique romaine tardive d'Afrique. Archaeopress, Oxford, pp. 533.

Capaldi, C. (2016): Die Portikenfassade des Forums von Cumae, *Kampanien, Jdl*, **130**, 183-239.

Capaldi, C. (2021): Il Foro di Cuma, *Puteoli Cumae Miscellanea Rivista di studi. Notiziario del parco archeologico campi flegrei*, **Vol. 1**, 213-224.

Capelli, C., & Bonifay, M. (2014): Archéométrie et archéologie des céramiques africaines: une approche Pluridisciplinaire, 2. Nouvelles données sur la céramique culinaire et les Amphores, *LRCW 4*, **Vol. I**, 235-253.

Capelli, C., & Bonifay, M. (2016): Archeologia e archeometria delle anfore dell'Africa romana. Nuovi dati e problemi aperti, *Le regole del gioco: tracce, archeologi, racconti. Studi in onore di Clementina Panella*, 535-557.

Capelli, C., Bonifay, M., Franco, C., Huguet, C., Leitch, V., & Mukai, T. (2016): Étude archéologique et archéométrique intégrée, *La ceramica Africana della Sicilia Romana*, **Tomo I**, 273-297.

Cucciniello, C., Melluso, L., le Roex, A.P., Jourdan, F., Morra, V., de Gennaro, R., & Grifa, C. (2017): From nepheline, basanite and basalt to peralkaline trachyphonolite and comendite in the Ankaratra volcanic complex, Madagascar: $^{40}\text{Ar}/^{39}\text{Ar}$ ages, phase compositions and bulk-rock geochemical and isotopic evolution. *Lithos* **274-275**, 363-382.

Cultrone, G., Rodriguez-Navarro, C., Sebastian, E., Ca-zalla, O., & De La Torre, M.J. (2001): Carbonate and silicate phase reactions during ceramic firing, *Eur. J. Mineral.*, **13**, 621-634.

Cuomo di Caprio, N. (2007): Ceramica in archeologia, 2, Antiche tecniche di lavorazione e moderni metodi di indagine (Vol. 2). L'Erma di Bretschneider, Roma, pp. 752.

De Bonis, A., Cultrone, G., Grifa, C., Langella, A., & Morra, V. (2014): Clays from the Bay of Naples (Italy): New insight on ancient and traditional ceramics, *J. Eur. Ceram. Soc.*, **34**, 3229-3244.

De Bonis, A., Cultrone, G., Grifa, C. (2017): Different shades of red: The complexity of mineralogical and physico-chemical factors influencing the colour of ceramics, *Ceram. Int.*, **43**, 617-635.

Di Giovanni, V. (2010): Le dinamiche degli scambi economici nella Campania in età imperiale. Circolazione delle produzioni africane: ceramiche fini, anfore da trasporto e ceramiche da cucina, *L'Africa Romana. Trasformazione dei paesaggi del potere nell'Africa settentrionale fino alla fine del mondo antico. Atti del XIX Convegno di studio, Sassari, 16-19 dicembre 2010*,

- 1511-1538.
- Franciosi, L., D'Antonio, M., Fedele, L., Guarino, V., Tassinari, C.C.G., de Gennaro, R., & Cucciniello, C. (2019): Petrogenesis of the Solanas gabbro-granodiorite intrusion, S'arrabus (southeastern Sardinia, Italy): implications for Late. *Int. J. Earth Sci.*, **108**, 989-1012.
- Gallala, W., Gaied, M. E., & Montacer, M. (2009): Detrital mode, mineralogy and geochemistry of the Sidi Aïch Formation (Early Cretaceous) in central and southwestern Tunisia: Implications for provenance, tectonic setting and paleoenvironment, *J. Afr. Earth Sci.*, **53**, 159-170.
- Gasparri, C. (2008): Il Foro di *Cumae*, *Museo archeologico dei Campi Flegrei. Catalogo generale. Cuma*, 88-91.
- Gasparri, C. (2009): Il Foro di *Cumae*: un bilancio preliminare, *Cuma. Indagini archeologiche e nuove scoperte. Atti della Giornata di Studi (Napoli 12 dicembre 2007), Quaderni del Centro Studi Magna Grecia 7 - Studi Cumani 2*, 131-145.
- Guarino, V., de' Gennaro, R., Melluso, L., Ruberti, E., & Azzone, R.G. (2019): The transition from miaskitic to agpaitic rocks as marked by the accessory mineral assemblages, in the Passa Quatro alkaline complex (southeastern Brazil). *Can. Mineral.*, **57**, 339-361.
- Guarino, V., Bonis, D.e., Peña, J.T., Verde, M., & Morra, V. (2021): Multianalytical investigation of wasters from the Tower 8/Porta di Nola refuse middens in Pompeii: Sr-Nd isotopic, chemical, petrographic, and mineralogical analyses. *Geoarchaeology*, **36**, 712-739.
- Maritan, L., Nodari, L., Mazzoli, C., Milano, A., & Ruzzo, U. (2006): Influence of firing conditions on ceramic products: Experimental study on clay rich in organic matter, *Appl. Clay Sci.*, **31**, 1-15.
- Molera, J., Pradell, T., & Vendrell-Saz, M. (1998): The colours of Ca-rich ceramic pastes: origin and characterization, *Appl. Clay Sci.*, **13**, 187-202.
- Munsell Color (Firm) (2010): Munsell Soil Color Charts: with Genuine Munsell Color Chips. Grand Rapids, MI: Munsell Color.
- Nodari, L., Marcuz, E., Maritan, L., Mazzoli, C., & Russo, U. (2007): Hematite nucleation and growth in firing of carbonate-rich clay for pottery production, *J. Eur. Ceram. Soc.*, **27**, 4665-4673.
- Quinn, P.S. (2013): Ceramic Petrography. The interpretation of Archaeological Pottery and related artefacts in thin section.
- Rispoli, C., De Bonis, A., Guarino, V., Graziano, S.F., Di Benedetto, C., Esposito, R., Morra, V., & Cappelletti, P. (2019): The ancient pozzolan mortar of the Thermal complex of Baia (Campi Flegrei, Italy). *J. Cult. Herit.*, **40**, 143-154.
- Rizzo, G. (2014): Anfore nordafricane, *Ostia IV. Le terme del Nuotatore. Scavo dell'ambiente XVI e dell'area XXV, StMisc* **23**, 260-295.
- Rizzo, G. (2018): Ostia, le anfore e i commerci mediterranei. Un bilancio preliminare, *ArchCl.*, **Vol. 69**, 223-266.
- Terry, R.D., & Chilingarian, G.V. (1955): Summary of "Concerning some additional aids in studying sedimentary formations", in *J. Sediment. Petrol.*, **25**, 229-234.



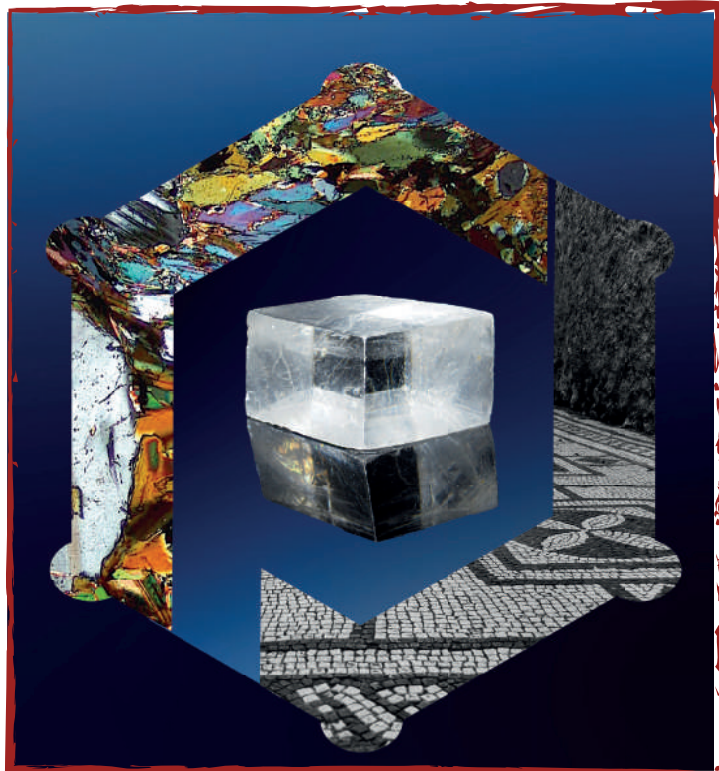
Photo Contest Submissions

Here are all the submissions of the SIMP members to the photo contest held to decide the image that is being featured on the cover of this issue.

A commission of experts has appointed
"Sfalerite su Sulvanite" by **Matteo Chinellato**
 as the winner of the contest.

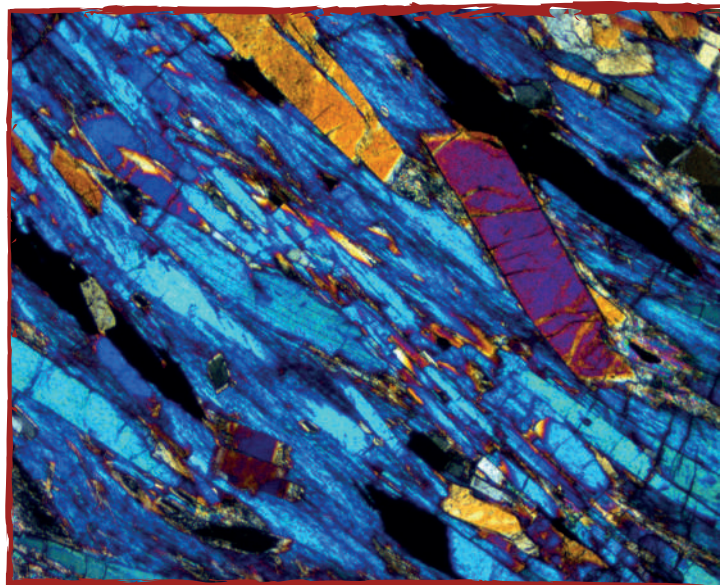
Here onward, the photos are displayed according to the submission order

P in a glance



#1 Sossio Fabio Graziano

Sea-Ilimanite (mare di sillimanite)



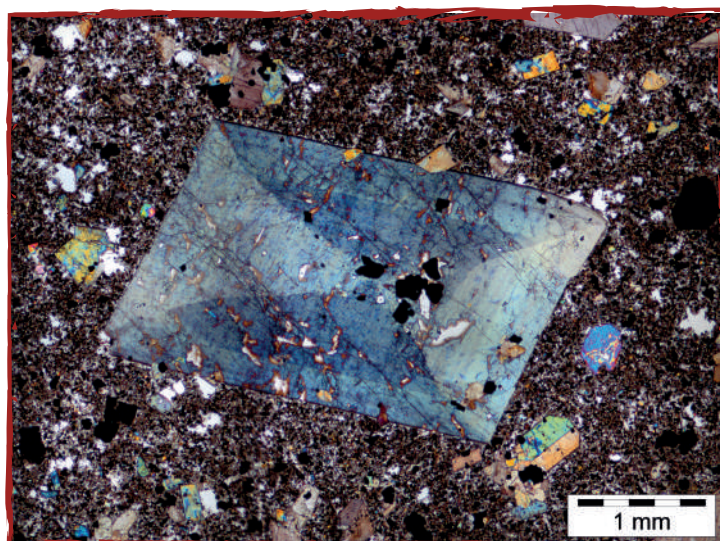
#2 Fabiola Caso

From magma mixing to faulting



#3 Antonio Langone

La scienza una clessidra, i giovani la sabbia



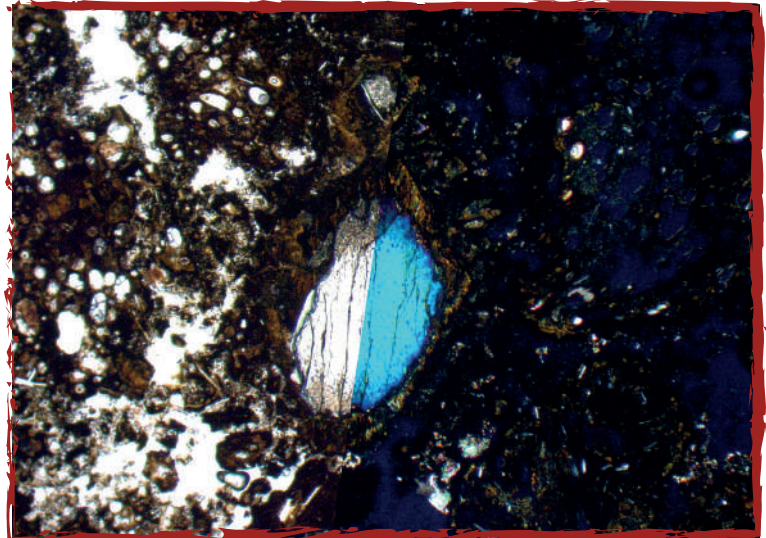
#4 Francesco Maria Lo Forte

Piromorfite Fiore di Piombo della Valsassina



#5 Fabrizio Vergani

Zoned olivine in Surtsey tuff



#6 Giovanna Montesano

Micashist Trio



#7 Lorenzo Dulcetta

Geodi di quarzo nelle Miniere Etrusche



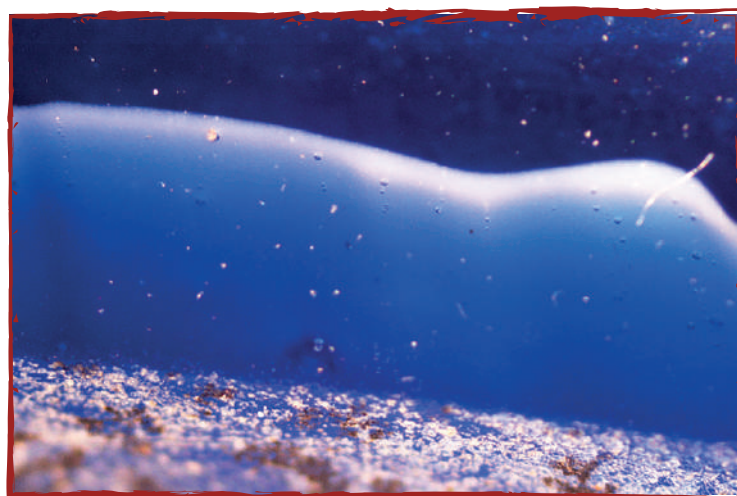
#8 Luca Tinagli

Tramonto da un mondo lontanissimo



Manfredo Capriolo

Universo di Vetro



#10 *Martina Cristina Caggiani*

Sfalerite con Sulvanite



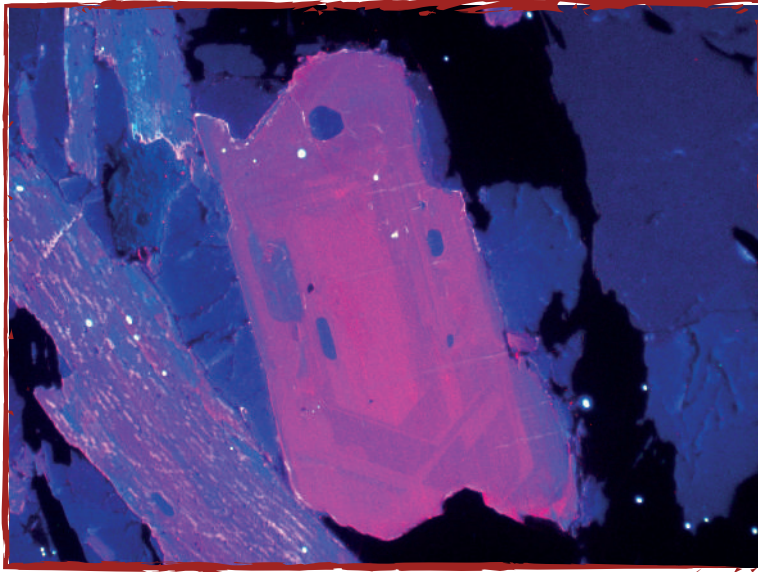
#11 *Matteo Chinellato*

This is where Ocean Petrology starts...



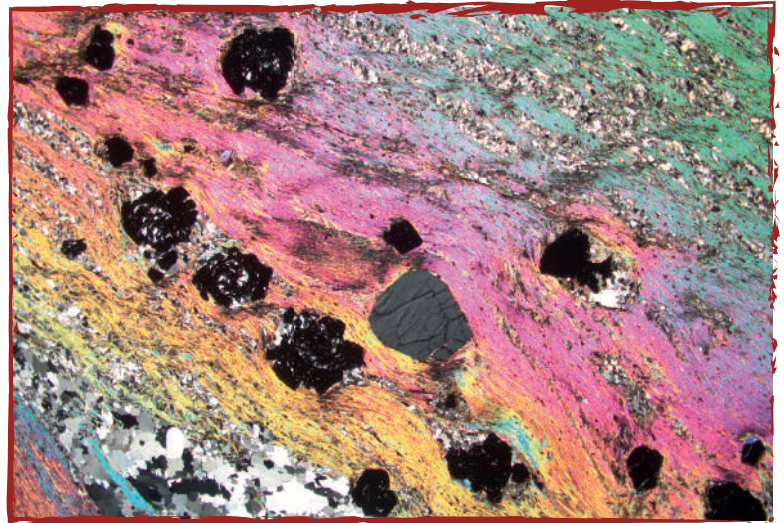
#12 *Valentin Basch*

Interlocking Planes



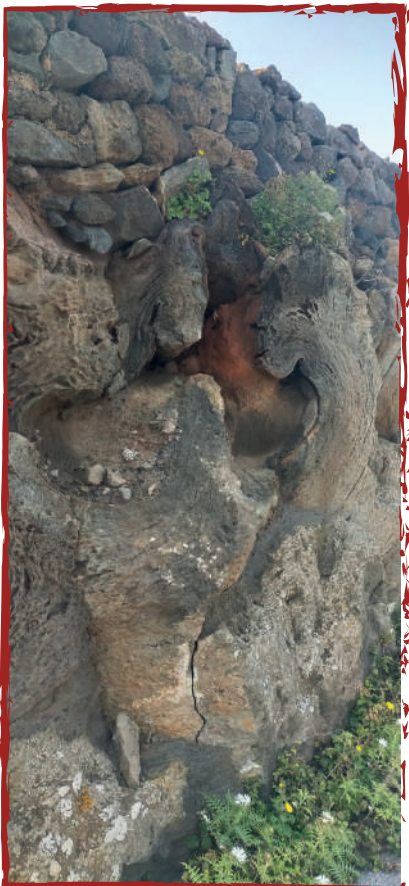
#13 Sara Nerone

You spin me round



#14 Sara Nerone

Lava Lovers



#15 Alessandra Cinquegrani

Sossio Fabio Graziano (*Università di Napoli Federico II*) - **P in a glance** - Nella sagoma di una cella elementare cubica, il corpo centrale è rappresentato da un cristallo di calcite, fotografato con ottica macro. L'elemento definisce la P di Plinius insieme al bordo, nel cui spessore sono rappresentate due immagini inerenti le tematiche della SIMP: una microfotografia di sezione sottile ottenuta al microscopio polarizzatore e una pavimentazione a mosaico rinvenuta in una domus pompeiana. Immagine di : Sossio Fabio Graziano e Claudia Di Benedetto.

Fabiola Caso (*Università di Milano*) - **Sea-Ilmanite (mare di sillimanite)** - Non è sempre facile comprendere le microstrutture delle migmatiti. A volte infatti, ci si perde in mare di sillimanite. Cristalli prismatici di sillimanite che marcano la foliazione principale all'interno di gneiss migmatitici dell'Unità della Valpelline (Dent-Blache Nappe). Foto in XPL (polarizzatori incrociati).

Antonio Langone (*Università di Pavia*) - **From magma mixing to faulting**

Francesco Maria Lo Forte (*Università degli Studi di Palermo*) - **La scienza una clessidra, i giovani la sabbia** - Zonatura a clessidra in clinopirosseno (diopside), rinvenuto in una lava basanitica ricca in alcali dell'ultima eruzione del vulcano Pico do Fogo, Capo Verde. La zonatura è stata generata dall'arrivo di nuovo magma in camera magmatica.

Fabrizio Vergani (*Università di Milano Bicocca*) - **Piomorfite - fiore di piombo della Valsassina** - Immagine di alcuni cristalli di piomorfite verde (dimensione massima 2 mm), ottenuta a partire da 30 foto processate con il metodo del focus stacking. Le foto originali sono state acquisite mediante l'utilizzo di uno stereo-microscopio. Il campione proviene da una vecchia miniera di solfuri della Valsassina (LC); il sito in oggetto è stato descritto in Vergani et al. (2021) "I minerali del sito di Ombrega e della miniera Corno (Introbio, LC)" RMI, 45, 4, 274-287. La vecchia ricerca mineraria di Ombrega, che ha interessato una serie di sottili filoncelli a galena e sfalerite in ganga baritica, è caratterizzata dalla presenza di splendidi campioni di piomorfite, annoverabili fra i migliori della Lombardia. Lo studio della paragenesi secondaria dei filoni a solfuri della Valsassina ha portato alla scoperta, da parte dell'autore di questa foto, di numerosi minerali di nuova segnalazione per la Lombardia e di alcune fasi di assoluta rarità quali la brindleyite della miniera Faidallo (quarto ritrovamento mondiale).

Giovanna Montesano (*Dipartimento di Scienze della Terra, dell'Ambiente e delle Risorse (DiSTAR), Università degli studi di Napoli Federico II*) - **Zoned olivine in Surtsey tuff** - This euhedral zoned olivine, with a fresh core and an altered rim, is in a basaltic tuff sample from Surtsey, a very young volcanic island located at the SW of Iceland, the type locality for the Surtseyan volcanism, grew up in 1963. The olivine, of about 2 mm length, is inside an altered pyroclast.

Lorenzo Dulcetta (*Università di Cagliari*) - **Micaschist trio** - The picture groups three types of micaschists recently studied and mapped in the Variscan basement of Corsica. Starting from the upper-left corner and moving in a clockwise sense, the three rocks show an increase in grain size of garnet consistent with the increase in the metamorphic grade recognized in the metamorphic complex; the first picture shows small, spessartine-rich garnets, the second shows larger Mn-rich almandines with biotite, plagioclase and white mica, while the last one has cm-sized almandines with chloritoid and rutile inclusions, associated with matrix staurolite, white mica, chlorite and ilmenite.

Luca Tinagli - **Geodi di quarzo nelle miniere etrusche** - La foto mostra una geode di quarzo con geminazioni e patine di ossidi/idrossidi di Fe formatesi all'interno dello skarn a hedenbergite-ilvaite. La foto è stata scattata a -95 m nel salone di coltivazione di una miniera di epoca etrusco-romano sfruttata per l'estrazione di solfuri di Pb-Cu associati allo skarn. Grazie alla verticalità e alle piccole dimensioni del giacimento questi antichi siti estrattivi si sono conservati intatti fino ad oggi, rappresentando un unicum nel panorama italiano, consentendo lo studio delle mineralizzazioni nelle aree periferiche del giacimento a skarn a Fe-Cu-Zn-Pb(-Ag) della miniera Temperino-Lanzi (Campiglia Marittima, LI) ma anche degli aspetti archeo-minerari dello sfruttamento.

Manfredo Capriolo (*University of Birmingham*) - **Tramonto da un mondo lontanissimo** - Sunset on Mauna Loa shield volcano and Mauna Kea volcanic craters, Big Island (Hawaii, US).

Maria Cristina Caggiani (*Università di Catania*) - **Universo di vetro** - Frammento di vetro Romano ritrovato a Pompei e conservato presso il Museo Archeologico Nazionale di Napoli, inglobato in resina, lucidato e osservato al microscopio ottico in riflessione presso l'Università degli Studi di Bari "Aldo Moro". Si nota il distacco cromatico fra le differenti bacchette usate nella tecnica del vetro cosiddetto "a nastro".

Matteo Chinellato (*Gruppo Mineralogico Lombardo - Rivista Mineralogica Italiana*) - **Sfalerite con Sulvanite** - Epitassia da 0,77 mm di micro-cristalli scuri di sulvanite su cristalli gialli di sfalerite. Località: Colonnata, Bacino estrattivo di Colonnata, Carrara, Alpi Apuane, Massa-Carrara, Toscana, Italia. Collezione privata foto Matteo Chinellato.

Valentin Basch (*CNR-Istituto di Geoscienze e Georisorse Pavia*) - **This is where ocean petrology starts...** - Campionamento del fondale oceanico nel Mar delle Filippine (Shikoku Basin) - A bordo del sottomarino Shinkai 6500: Yasuhiko Ohara, Valentin Basch.

Sara Nerone (*Università di Torino*) - **Interlocking planes** - Interlocked planes of oscillatory chemical zoning in kyanite under cold-cathode cathodoluminescence.

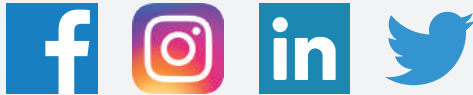
Sara Nerone (*Università di Torino*) - **You spin me round** - Snowball garnets spinning in a matrix made of white mica and quartz under cross-polarized light.

Alessandra Cinquegrani (*Università degli Studi di Palermo*) - **Lava lovers** - Piega reomorfica in ignimbrite Tufo Verde di Pantelleria.

Plinius is the official SIMP bulletin,
printed under the auspices of the
Consiglio Nazionale delle Ricerche (CNR)
and of the Ministero dei Beni Culturali



Follow SIMP on social media



For any communication and
news write to
comunicazione@socminpet.it

